

Doctoral Dissertation (Shinshu University)

**A basic study on the microstructure and
mechanical properties of ultrahigh-strength
TRIP-aided martensitic steel**

March 2014

Junya Kobayashi

Index

Chapter 1. Introduction..... 1

1.1 Background of this study 1

 1.1.1 Current state and issues of automobiles 1

 1.1.2 Efforts to reduce automobile weight and improve impact safety..... 2

1.2 Advanced high-strength steels 6

 1.2.1 Dual-phase (DP) steel 7

 1.2.2 Twinning induced plasticity (TWIP) steel 8

 1.2.3 Complex phase (CP) steel 9

 1.2.4 Martensitic (MS) steel..... 9

 1.2.5 Transformation-induced plasticity (TRIP) steel..... 9

 1.2.6 TRIP-aided bainitic ferrite (TBF) steel 10

 1.2.7 Quench & Partitioning (Q&P) steel 11

 1.2.8 Hot-stamping steel..... 12

1.3 Transformation-induced plasticity 13

1.4 Scope and structure of this thesis..... 17

REFERENCES 19

Chapter 2. Microstructure and Retained Austenite Characteristics of C-Si-Mn TRIP-aided Martensitic Steel..... 26

2.1 Introduction..... 26

2.2 Experimental Procedure..... 26

2.3 Result 28

 2.3.1 Vickers hardness 28

 2.3.2 Retained austenite characteristics..... 28

 2.3.3 Microstructure and carbide..... 30

2.4 Discussion..... 34

 2.4.1 Microstructural change on quenching 34

 2.4.2 Carbon-enrichment mechanism during partitioning 36

2.5 Summary 37

REFERENCES 39

Chapter 3. Effects of Microalloying on Retained Austenite Characteristics of TRIP-aided Martensitic Steel	41
3.1 Introduction.....	41
3.2 Experimental procedure	41
3.3 Result	43
3.3.1 Vickers hardness	43
3.3.2 Retained austenite characteristics.....	44
3.3.3 Microstructure and carbide.....	45
3.4 Discussion	
Effects of alloying elements on retained austenite characteristics.....	47
3.5 Summary	48
REFERENCES	49
Chapter 4. Effects of Partitioning and Isothermal Transformation Temperature on Tensile Properties and Formabilities of TRIP-aided Martensitic Steel.....	50
4.1 Introduction.....	50
4.2 Experimental procedure	50
4.3 Results.....	56
4.3.1 Microstructure	56
4.3.2 Retained austenite characteristics.....	57
4.3.3 Tensile properties	58
4.3.4 Formabilities.....	58
4.4 Discussion.....	61
4.4.1 Carbon-enrichment mechanism of TM steel subjected to isothermal transformation process at 200–250°C.	61
4.4.2 Excellent stretch-flangeability.....	62
4.5 Summary	63
REFERENCES	64
Chapter 5. Effects of Partitioning Temperature after Isothermal Transformation Process on Stretch-flangeability and Bendability of a 0.2C-1.5Si-1.5Mn-0.05Nb Ultrahigh-strength TRIP-aided Martensitic Sheet Steel	65

Index

5.1 Introduction.....	65
5.2 Experimental procedure	65
5.3 Results.....	68
5.3.1 Microstructure	68
5.3.2 Retained austenite characteristics.....	69
5.3.3 Tensile properties	70
5.3.4 Stretch-formability, stretch-flangeability and bendability	71
5.4 Discussion.....	73
5.4.1 Yield stress	73
5.4.2 Stretch-flangeability	73
5.5 Summary	74
REFERENCES	75
Chapter 6. Effects of microalloying on stretch-flangeability of Ultrahigh-strength TRIP-aided martensitic steel sheets	76
6.1 Introduction.....	76
6.2 Experimental procedure	77
6.3 Results.....	80
6.3.1 Microstructure and Retained Austenite Characteristics	80
6.3.2 Tensile Properties	85
6.3.3 Stretch-flangeability and Stretch-formability.....	87
6.4 Discussion.....	90
6.4.1 Microstructure Formation and Carbon Enrichment into Retained Austenite in TM Steel with High Hardenability.....	90
6.4.2 The Increase of Yield Stress and Yield Ratio with Alloying	93
6.4.3 The Effects of Alloying Elements on Stretch-flangeability	94
6.5 Summary	96
REFERENCES	97
Chapter 7. Effects of Microalloying on the Impact Toughness of Ultrahigh-strength TRIP-aided Martensitic Steels.....	99
7.1 Introduction.....	99
7.2 Experimental procedure	99

Index

7.3 Results.....	103
7.3.1 Microstructures and carbide	103
7.3.2 Retained austenite characteristics and tensile properties	108
7.3.3 Charpy impact toughness	109
7.4 Discussion.....	114
7.4.1 High upper-shelf charpy impact absorbed values	114
7.4.2 Low ductile-brittle fracture appearance transition temperature	119
7.5 Summary.....	120
REFERENCES	122
Chapter 8. Notch-fatigue strength of advanced TRIP-aided martensitic steels	124
8.1 Introduction.....	124
8.2 Experimental procedure	124
8.3 Results.....	127
8.3.1 Microstructure and retained austenite characteristics	127
8.3.2 Vickers hardness and tensile properties	130
8.3.3 Notch-fatigue limit and notch sensitivity for fatigue	131
8.4 Discussion.....	133
8.4.1 Microstructure and retained austenite characteristics of steels B through D ..	133
8.4.2 Low notch-tensile strength ratios of steels B through D.....	136
8.4.3 High notch-fatigue limits of steels B through D	137
8.5 Summary.....	138
REFERENCES	139
Chapter 9. Conclusions	141
List of Papers	144
Acknowledgement	148

Summary

In the present study, the microstructure, tensile properties, formabilities, impact toughness, and fatigue properties of transformation-induced plasticity (TRIP)-aided martensitic (TM) steel were investigated and are discussed in this thesis. The results obtained in this study are summarized below:

In Chapter 1, the background of advanced high-strength steels (AHSSs) and the aim of this study are introduced. AHSSs have been developed to improve the fuel efficiency and impact safety of automobiles. For the production of vehicles made primarily of steel in the future, light-weight automobile bodies can be fabricated by the application of newly developed AHSSs (e.g., TRIP steels). Focusing on the TRIP effect that improves the mechanical properties of steels, the mechanism of TRIP was introduced.

In Chapter 2, the effect of partitioning temperature after quenching on the microstructure and retained austenite characteristics of 0.2%C-1.5%Si-1.5%Mn (in mass%) TM steel are presented and discussed. The presence of a carbon-enrichment mechanism during partitioning is proposed in this chapter. TM steel consisting of wide and narrow lath-martensite structures contained about 3 vol% of retained austenite after quenching in oil, with 1.7–2.0 vol% of carbides only in wider lath-martensite structures. With partitioning at temperatures lower than 250°C for times shorter than 1000 s, the volume fractions of the retained austenite and carbide were maintained, although the carbon concentration of the retained austenite increased.

In Chapter 3, the effect of alloying elements on the microstructure and retained austenite characteristics of 0.2%C-1.5%Si-1.5%Mn TM steel are given and discussed. Addition of Cr and Mo to the base steel raised the upper limit of partitioning temperature to 400°C, although the carbon concentration in retained austenite decreased slightly. Further, Ni addition decreased the volume fraction of retained austenite and increased the carbon concentration.

In Chapter 4, the effects of quenching or isothermal transformation processes on the tensile properties and formability of 0.2%C-1.5%Si-1.5%Mn-0.05%Nb TM steels are presented and discussed. When isothermally transformed at temperatures below M_f , TM steel showed a tensile strength of 1.5 GPa and a total elongation of 8%. The hole-expanding ratio ($\lambda = 30\text{--}50\%$) was higher than that in steel obtained after quench and partitioning (QP). As a result, steel obtained after the IT process possessed a superior combination of tensile strength and stretch flangeability. It is considered that the excellent combination of IT process steel is mainly caused by a uniform and fine martensite lath structure matrix and a smaller amount of carbides that suppress the damage caused by punching and cracking on hole expanding, as well as by the presence of metastable retained austenite.

Summary

In Chapter 5, the effect of partitioning temperature after the IT process on the tensile properties and formabilities of 0.2%C-1.5%Si-1.5%Mn-0.05%Nb TM steel are presented and discussed. Partitioning after the IT process significantly enhanced the formability, especially stretch flangeability, of TM steel as compared to that obtained from partitioning after the quenching process. The excellent stretch flangeability was associated with softening of a mixed uniform wide and narrow lath martensitic structure matrix and an increase in the stability of the retained austenite, which suppressed the damage caused by punching and crack propagation on hole expansion through the partitioning process.

In Chapter 6, the effect of the addition of Cr, Mo, and/or Ni on the tensile properties and formabilities of 0.2%C-1.5%Si-1.5%Mn-0.05%Nb TM steel are given and discussed. The addition of 0.5%Cr and 1.0%Cr significantly improved the combination of tensile strength and stretch flangeability of TM steel. This was mainly caused by the refinement of the size of voids and cracks at the interface of an MA-like phase upon punching and suppression of void coalescence on hole expanding.

In Chapter 7, the effects of the addition of Cr, Mo, and/or Ni on the Charpy impact absorbed value and ductile-brittle fracture appearance transition temperature of 0.2%C-1.5%Si-1.5%Mn-0.05%Nb TM steel are presented and discussed, and are compared with those for TRIP-aided bainitic ferrite (TBF) steel and conventional martensitic steel. When Cr, Cr-Mo, or Cr-Mo-Ni was added to the base steel, TM steel exhibited a high upper-shelf Charpy impact absorbed value that ranged from 100 J/cm² to 120 J/cm² and a low fracture appearance transition temperature that ranged from -150°C to -130°C, while also exhibiting a tensile strength of about 1.5 GPa. This impact toughness of the alloyed steel was far superior to that of conventional martensitic steel and was caused by the presence of a softened wide lath-martensite matrix. This matrix contained only a small amount of carbide and hence had a lower carbon concentration, a large amount of finely dispersed martensite-retained austenite complex phase, and a metastable retained austenite phase of 2–4 vol% in the complex phase, which led to plastic relaxation via a strain-induced transformation and played an important role in the suppression of the initiation and propagation of voids and/or cleavage cracks.

In Chapter 8, notch-fatigue strengths and notch sensitivities of 0.1–0.6%C-1.5%Si-1.5%Mn TM steel are given and discussed. If TM steel containing 0.2%, 0.3% or 0.4%C were subjected to an ITP process, comprising isothermal transformation and partitioning processes, much higher notch-fatigue limits and lower notch sensitivities than those in the case of conventional martensitic steels (SCM steels) without retained austenite were achieved. It was expected that high notch-fatigue limits were principally associated with the plastic relaxation of localized stress concentration as a result of the strain-induced transformation of metastable retained austenite and a large

Summary

amount of a finely dispersed MA-like phase along prior austenitic, packet, and block boundaries, as well as a small amount of carbide only in the wide lath-martensite structure, which contributed to difficult fatigue crack initiation and/or propagation.

In Chapter 9, the conclusions of this thesis are summarized. TM steel showed not only ultrahigh strength but also high formability, impact energy absorption capacity, and fatigue strength that are necessary to improve the fuel efficiency and impact safety of automobiles. It can be expected that the applications of TM steel would improve the global environment and our lives in the future.

Chapter 1. Introduction

1.1 Background of this study

1.1.1 Current state and issues of automobiles

Nowadays, automobiles play an essential role in our lives. In Japan, the production of automobiles in 2012 was 9.94 million units, higher than that in the past 3 years (**Fig. 1-1(a)**).¹⁾ In addition, the registration of automobiles in 2012 increased significantly in comparison to that in 2011 (**Fig. 1-1(b)**). In countries all over the world, including those in America, Asia-Oceania, Africa, and other countries, the production of passenger automobiles increased in 2012 more than that in 2011. Hidden behind this trend is the fact that automakers are developing “eco cars” (low-emission automobiles) with high fuel efficiency. These economical automobiles are becoming popular all over the world.

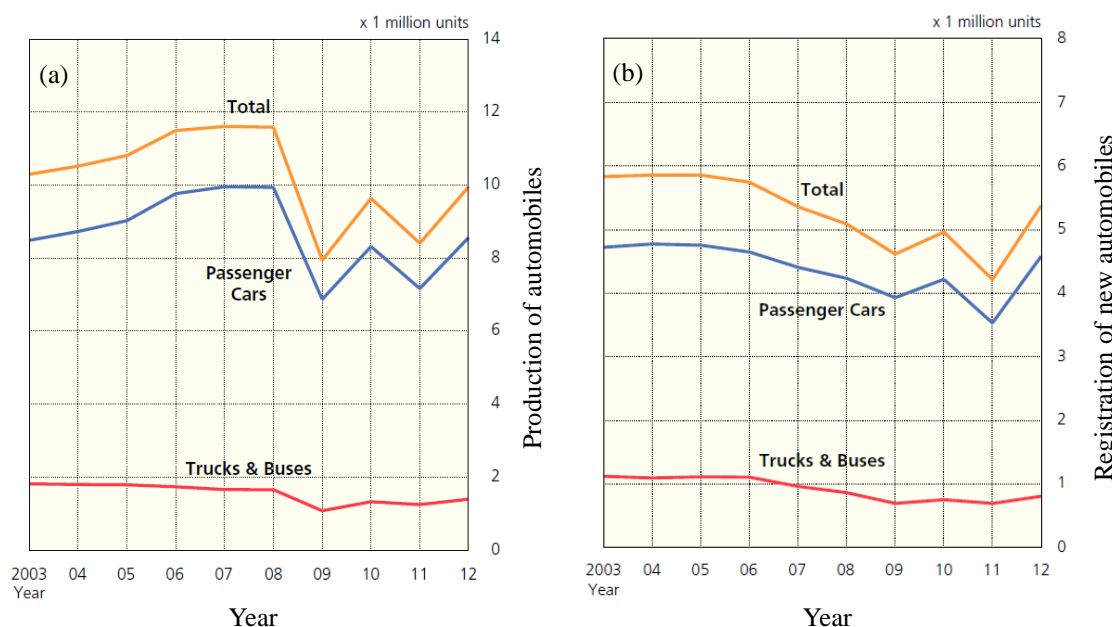


Fig. 1-1. Trends in (a) production and (b) registration of automobiles in Japan.¹⁾

However, there are some issues pertaining to automobiles owing to a large number of automobiles in the world, such as CO₂ reduction and improvement in the impact safety of automobiles.

It is well known that global warming is caused by greenhouse gas emissions. The increasing number of automobiles is leading to increased gas emissions. Further, an increase in the automobile body weight also leads to increased gas emissions and lower fuel efficiency. **Fig. 1-2** shows trends in global fuel economy/automobile emissions regulations. According to Fig. 1-2, strict CO₂ emissions legislation has been passed for achieving further reduction in emissions by 2020. Therefore, the automobile body weight is needed to be reduced for future automobiles. On the other hand, the reduction

in the automobile body weight has to be compensated for, for achieving safety improvements. Thus, it is necessary to develop advanced high-strength sheet steels (AHSSs) in order to improve the safety of light-weight automobiles (such as future low-emission automobiles).

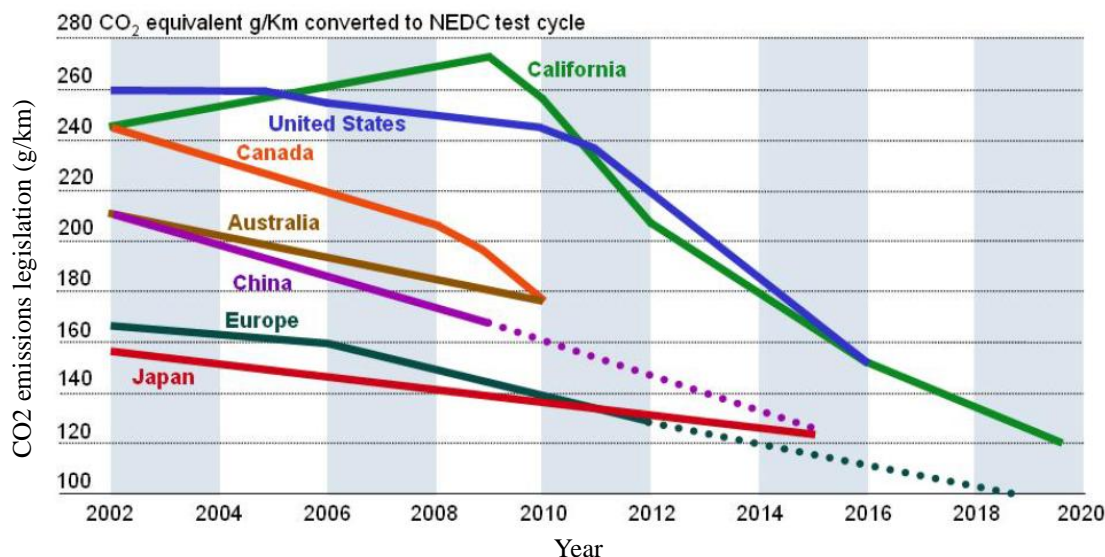


Fig. 1-2. Trends in global fuel economy/automobile emissions regulations.^{2,3)}

1.1.2 Efforts to reduce automobile weight and improve impact safety

The FutureSteelVehicle^{2,3)} (FSV) program is the most recent addition to the global steel industry's series of initiatives offering steel solutions to the challenges facing automakers around the world, such as to increase the fuel efficiency of automobiles and to reduce greenhouse gas emissions while improving safety and performance as well as maintaining affordability. The FSV addresses the increased weight reduction in automobiles with solutions that demonstrate steel as the material of choice for the automobile structure.

The FSV program has the following key features:

1. State-of-the-future design innovations that exploit the versatility and strength of steel
2. Body structure mass savings of 35% as compared to a benchmark vehicle
3. Uses 97% high-strength steel (HSS) and advanced high-strength steel (AHSS)
4. Uses nearly 50% GPa steels
5. Enables 5-star safety ratings
6. Reduces total lifetime emissions by nearly 70%
7. Reduces mass and emissions at no cost penalty

The FSV program helped in achieving 35% body structure mass savings as compared to a benchmark vehicle (point 2 above). This significant reduction in the body weight has been realized through the use of a wide range of AHSS grades combined with a large number of steel technologies and the FSV design optimization methodology. **Figure 1-3** shows the FSV body (battery electric vehicle type) and its steel grade use. In this figure, AHSS with a tensile strength of 1.0 GPa or more were used for the FSV body. These steels are dual phase (DP), complex phase (CP), transformation-induced plasticity (TRIP), twinning-induced plasticity (TWIP), martensitic (MS), and hot forming (HF) steels. The rates of DP, CP, TRIP, and HF steels are high in the FSV body. AHSS are primarily applied to the A, B, and C pillars and underbody of an automobile.

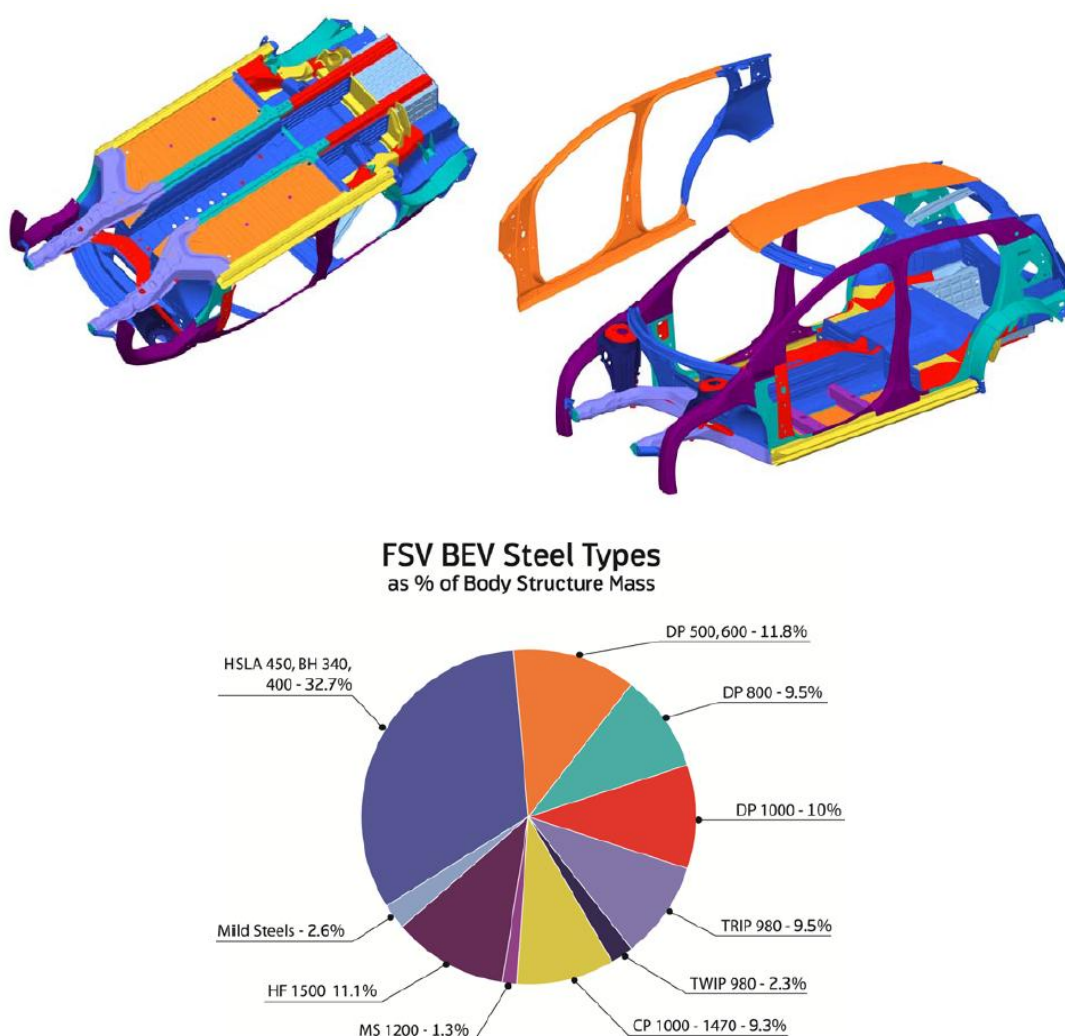


Fig. 1-3. FSV body (battery electric vehicle type) and its steel grade use.³⁾

Figure 1-4 shows a comparison of the tensile strength of FSV materials and those of ultralight steel auto body (ULSAB)^{4,5)} and ultralight steel auto body-advanced vehicle concept (ULSAB-AVC)^{6,7)}. **Figure 1-5** shows a comparison of the grade mix of

FSV materials and those of ULSAB and ULSAB-AVC. ULSAB and ULSAB-AVC are previous programs undertaken for improving the fuel consumption and impact safety of automobiles. Figs. 1-4 and 1-5 show that steels with a tensile strength of 340–450 MPa, which are high-strength low alloy (HSLA)^{8,9)} and bake hardening (BH)^{10–12)} steels, are mainly used in ULSAB. The rate of use of these steels in ULSAB is approximately 90%. In ULSAB-AVC, DP steel^{11–15)} with the tensile strength between 500 and 1000 MPa and TRIP steel^{12,16)} are newly applied to automobile bodies. AHSS with a tensile strength of 1.0 GPa grade or more, such as TRIP, TWIP, CP, MS, and HF steels, are applied to the FSV body in the FSV program, as mentioned above.

Table 1-1 shows a comparison of the average tensile strength of the FSV material mix with that of ULSAB and ULSAB-AVC. The increase in the tensile strength of ULSAB-AVC is significantly larger than that in the case of ULSAB. For the FSV-battery electric vehicle, the tensile strength is higher than that of ULSAB-AVC, and the average material thickness decreases upon the application of AHSS. The decrease in the automobile body weight and improvement of crash safety are achieved by the application of AHSS.

As mentioned above, AHSS decreases the weight of an automobile body and improves crash safety, as summarized in **Fig. 1-6**. However, owing to the strict CO₂ emissions legislation and the increasing demands for improving fuel efficiency, further weight reduction is required in the future.

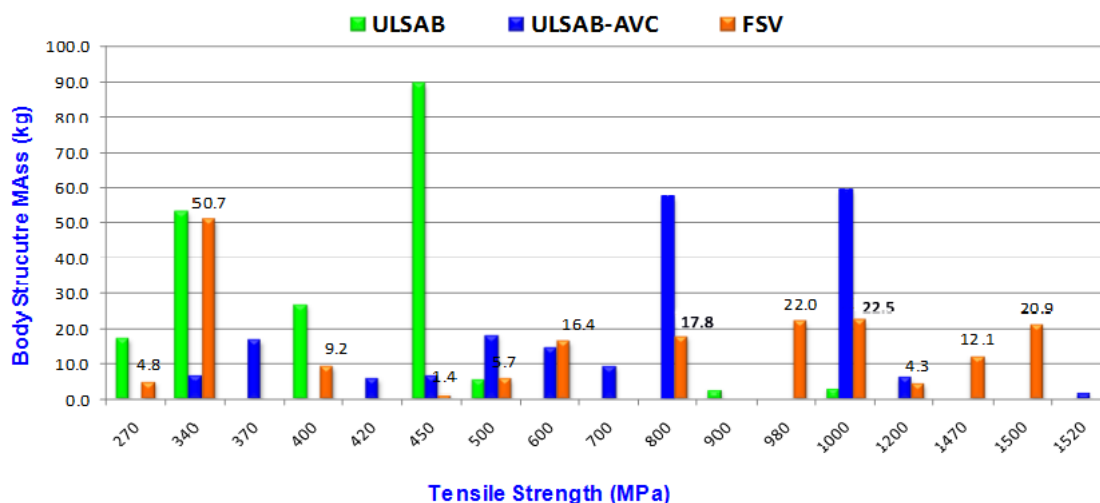


Fig. 1-4. FSV materials tensile strength compared to ULSAB and ULSAB-AVC.³⁾

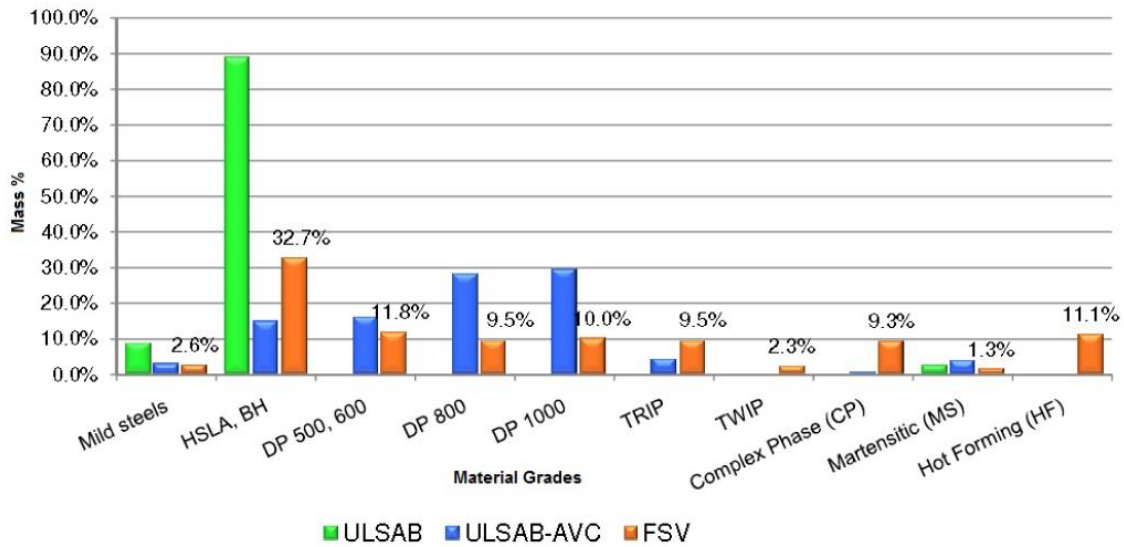


Fig. 1-5. Comparison between grade mix of FSV material and that of ULSAB and ULSAB-AVC.³⁾

Table. 1-1. Comparison between average tensile strength of FSV material mix and that of ULSAB and ULSAB-AVC.³⁾

Vehicle	Tensile Strength (MPa)	Average Material Thickness (mm)
ULSAB	413	1.16
ULSAB-AVC	758	1.0
FSV-BEV	789	0.98

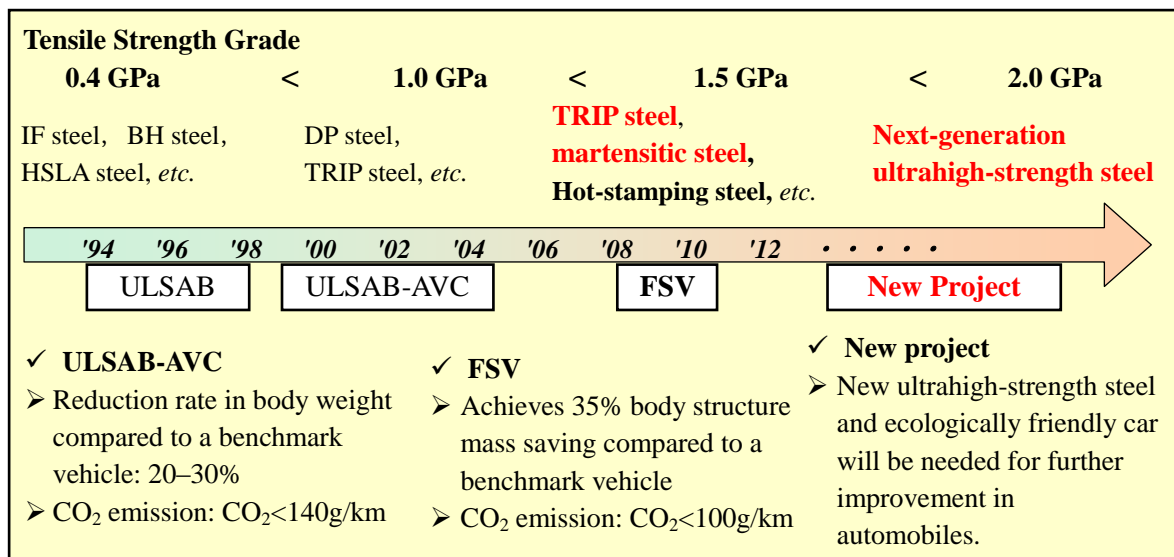


Fig. 1-6. Process and summary of ULSAB, ULSAB-AVC, and FSV programs.

1.2 Advanced high-strength steels

In order to reduce the body weight and improve the crash safety of automobiles, various types of AHSS have been developed. De Cooman¹⁶⁾ mentioned the following three principal reasons for the current trend of using more AHSS in automobile applications:

1. Reduction in passenger car weight by increased use of high-strength thinner gauge sheet steel, leading to reduced fuel consumption and emissions.
2. Improvement in the passive safety of vehicles, leading to better passenger safety via improved crash-worthiness.
3. Strong competition from light-weight materials, particularly Al and Mg alloys, and plastics.

In addition, a safety-based car body design requires an intensive use of the following two main types of high strength steels, as shown in **Fig. 1-7**.

1. High-strength steel grades with a high energy absorption potential, typically DP and TRIP steel grades with tensile strengths <1000 MPa, for dynamic loading occurring during car crashes or collisions, and
2. Very high-strength steels, typically martensitic steel grades with exceptional tensile strengths (>1200 MPa), which provide high-stiffness, anti-intrusion and load-transferring barriers for the protection of automotive passengers.

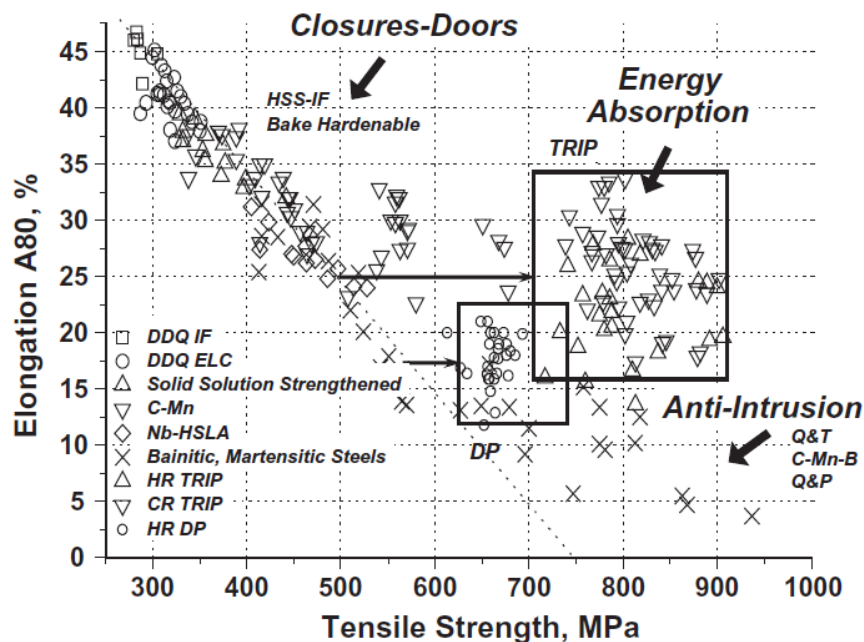


Fig. 1-7. Elongation vs. tensile strength diagram for conventional steels showing the fact that the multiphase DP and TRIP AHSS have a much improved strength-ductility balance. The current trend in automobile part steel selections are also indicated.¹⁶⁾

In general, the increase in the steel strength leads to a decrease in elongation and impact energy absorption. As shown in Fig. 1-7, conventional high-strength steels such as interstitial-free (IF)¹⁷⁻²⁰, bake-hardened (BH) and high-strength low-alloy (HSLA) steels have inferior ductility, which almost linearly decreases with increasing strength. In contrast, AHSS (such as DP and TRIP steels shown in Fig. 1-7) shows improved tensile strength without much loss in total elongation. In fact, AHSS is characterized by superior strain hardening properties and large uniform elongation. Since AHSS possesses a combination of high strength and large elongation, these steels are highly attractive for the automobile industry. In stretch-forming applications for automobiles and in high-energy impact situations (e.g., in a crash), formability and energy-absorbing capacities are especially important for manufacturing and safety considerations, respectively.

1.2.1 Dual-phase (DP) steel

The microstructure of DP steel consists of soft ferrite and hard martensite (**Fig. 1-8**).^{11-15,21-25} DP steel is subjected to quenching from intercritical annealing. The strength of DP steel can be varied by controlling the balance between ferrite and martensite fractions. When DP steel is deformed, the strain is concentrated in the soft ferrite phase. Therefore, DP steel possesses a higher work hardening rate, uniform elongation, higher tensile strength, and a lower yield ratio (yield stress/tensile strength) than conventional steels (e. g., HSLA steel) with comparable tensile strength. As mentioned above, since DP steel has a good combination of tensile strength and elongation, it can be used in automobile applications that require high impact energy absorbing capacities and press formability, such as front-side members. However, the hole-expanding property of DP steel under high local deformation is low, because voids and cracks easily form at the soft ferrite/hard martensite structure interface (**Fig. 1-9**).

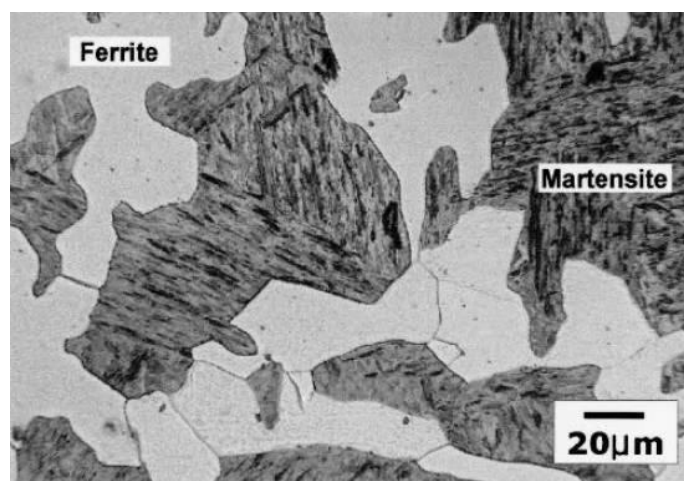


Fig. 1-8. Optical micrograph of DP steel.²¹⁾ The specimen was nital etched.

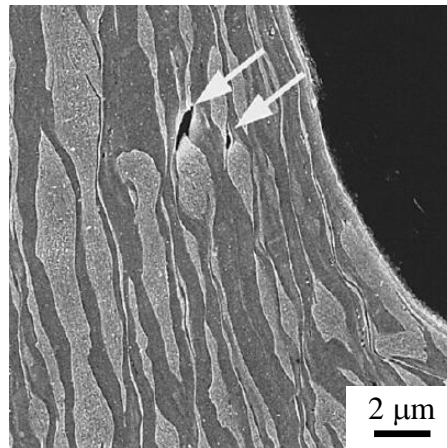


Fig. 1-9. Microstructure of DP steel after hole-punching.²²⁾ Voids are shown with arrows.

1.2.2 Twining induced plasticity (TWIP) steel

TWIP steel is high-Mn austenitic steel containing 20–30% Mn.^{26–31)} TWIP steel possesses a high work hardening rate, high tensile strength, uniform elongation, and low yield strength because of lower stacking fault energy (SFE) and deformation twinning. Fine twin lamellae can be regarded as extra obstacles within a grain that inhibit the dislocation movement. **Figure 1-10** shows an example of a steel exhibiting deformation twinning.

Although TWIP steel has superior mechanical properties resulting from deformation twinning, it has some disadvantages such as high cost and formation of cracked edges during hot rolling because of a high Mn content.

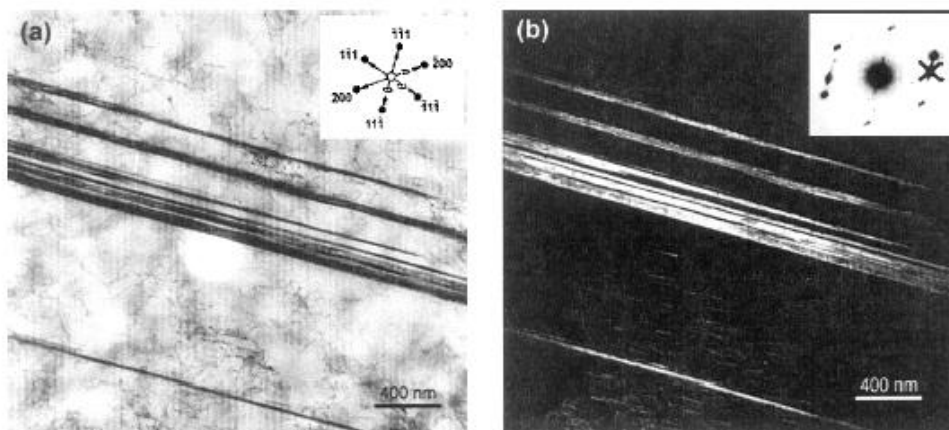


Fig. 1-10. TEM images of TWIP steel after a tensile test ($\epsilon = 10\%$).²⁶⁾

1.2.3 Complex phase (CP) steel

CP steel consists of ferrite and bainite and/or martensite.^{32,33)} The chemical composition of CP steel is similar to that of DP or TRIP steels. CP steel possesses a tensile strength of over 800 MPa, good formability, high impact energy absorption, and good hole-expansion capacity.

1.2.4 Martensitic (MS) steel

Martensitic steel^{34–38)} is manufactured by quenching at austenitizing temperature. The microstructure of martensitic steel consists of a lath-martensite single structure. The strength of martensitic steel is over 1200 MPa because of hard lath martensite containing supersaturated carbon and high dislocation density. In order to improve the elongation and impact energy absorption capacity of martensitic steel, it is often subjected to tempering after quenching. In this case, carbide present in the lath-martensite structure precipitates (**Fig. 1-11**).

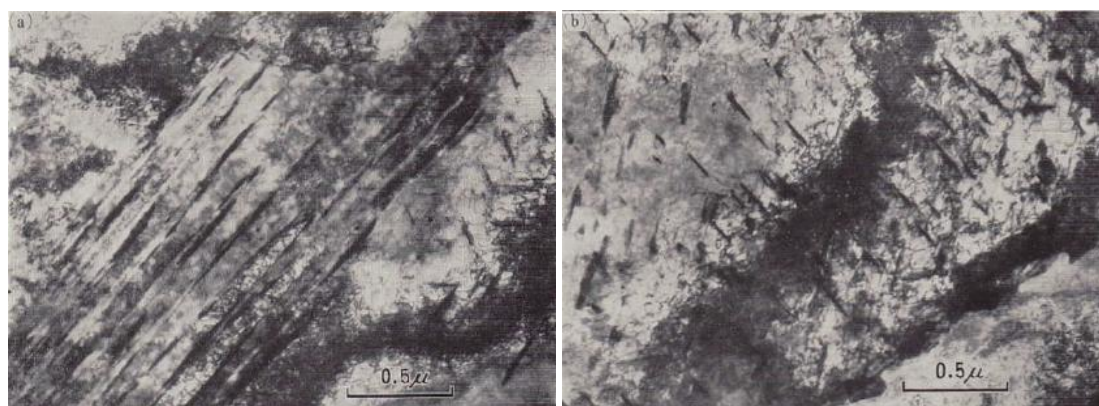


Fig. 1-11. TEM images of 0.15% C martensitic steel tempered at 300°C for 3600 s.³⁵⁾

1.2.5 Transformation-induced plasticity (TRIP) steel

TRIP³⁹⁾ steel is manufactured by austempering or isothermal bainitic transformation after austenitizing or intercritical annealing. Recently, low-alloy TRIP steel (TRIP-aided steel)^{16,40–67)} has been developed (it will be mentioned in section 1.2.6), and is different from the high-alloy TRIP steel reported by Zackay et al.³⁹⁾ The microstructure of TRIP steel consists of ferrite, bainite, martensite, and retained austenite. The volume fraction of retained austenite is usually 15 vol%. TRIP steel possesses high strength and superior elongation due to the TRIP effect of retained austenite that is formed from martensite transformation during deformation. Although the retained austenite is a minor phase in the microstructure, it significantly affects the mechanical properties of TRIP steel. In TRIP steel, Si is added in order to suppress carbide formation during austempering. This allows the remaining austenite to become enriched in C, which results in its room

temperature stabilization. The details of transformation-induced plasticity will be discussed in section 1.3.

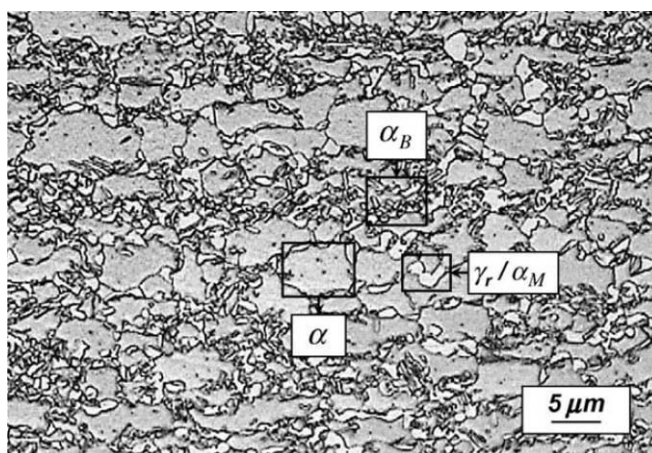


Fig. 1-12. Light optical micrograph of color-etched TRIP steel.¹⁶⁾ α , α_B , α_M , and γ_r denote ferrite, bainite, martensite, and retained austenite, respectively.

1.2.6 TRIP-aided bainitic ferrite (TBF) steel

TBF steel was developed as low-alloy TRIP steel by Sugimoto et al. who performed an isothermal transformation at temperatures higher than the martensite-start temperature after austenitization.^{44–48,50–54,58–67)} The microstructure of TBF steel consists of lath bainitic ferrite and filmy metastable retained austenite (**Figs. 1-13** and **1-14**). TBF steel possesses 1000–1200 MPa grade tensile strength, excellent stretch flangeability, high fatigue strength, and high hydrogen brittle performance. Since TBF steel has superior mechanical properties and few alloying elements, it has been applied in some automotive applications.

Recently, TBF steel with a matrix structure consisting of martensite and bainitic ferrite and fine metastable retained austenite as a second phase has been developed by Sugimoto et al.^{65–67)} This steel showed a tensile strength of 1470 MPa and superior formability owing to a fine lath martensite and bainitic ferrite complex matrix structure and the TRIP effect of metastable retained austenite. The use of this TBF steel will further decrease the body weight and improve crash safety for next-generation automobiles.

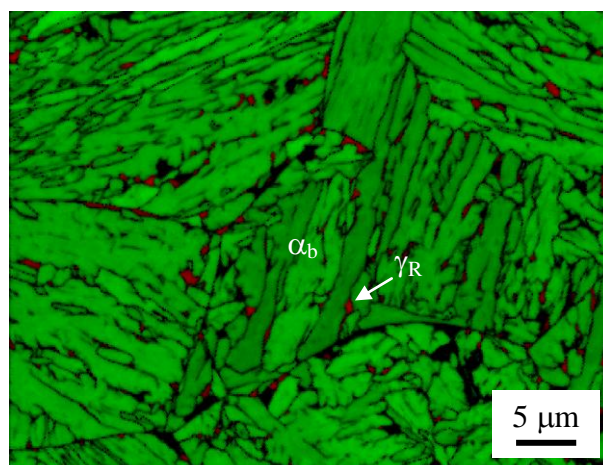


Fig. 1-13. EBSD analysis results for a 0.2C-1.5Si-1.5Mn system TBF steel subjected to austempering at 400°C for 1000 s. In this figure, green and red phases show the matrix (BCC phase: bainitic ferrite, α_{bf}) and secondary phase (FCC phase: retained austenite, γ_R), respectively.

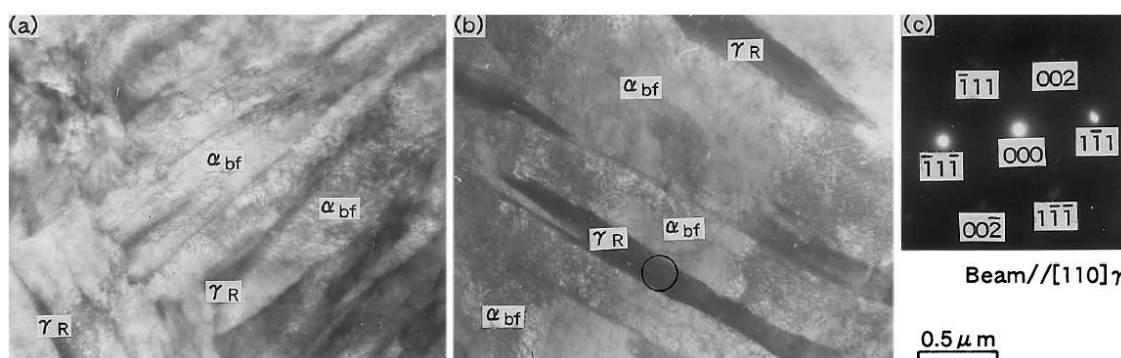


Fig. 1-14. TEM images of interlath retained austenite films (γ_R) along with a bainitic ferrite lath structure (α_{bf}) in TBF steel austempered at (a) 375°C or (b) 450°C for 200 s; (a) and (b): bright-field images, (c): selected area diffraction pattern of the encircled area in (b).⁵²⁾

1.2.7 Quench & Partitioning (Q&P) steel

Q&P steel⁶⁸⁻⁷¹⁾ is manufactured by a heat process illustrated in **Fig. 1-15**; in this process, the steel is quenched to temperatures between martensite transformation start (M_S) and finish temperature (M_f) after austenitizing, and is then isothermally held at a temperature near or over M_S for the carbon enrichment of retained austenite. The microstructure of Q&P steel usually consists of martensite, bainite, and retained austenite. Q&P steel possesses a high combination of tensile strength and elongation, similar to TRIP-aided steel.

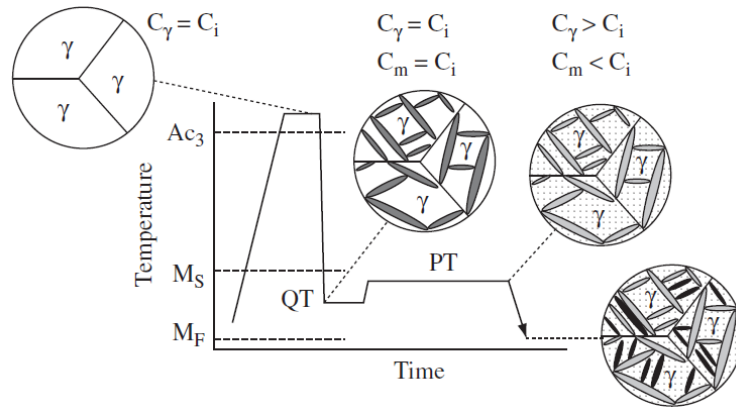


Fig. 1-15. Schematic illustration of the Q&P process for producing austenite-containing microstructures.⁷⁰⁾ C_i , C_γ , and C_m represent carbon concentration in the initial alloy, austenite, and martensite, respectively. QT and PT are the quenching and partitioning temperatures.

1.2.8 Hot-stamping steel

Hot-stamping steel⁷²⁻⁷⁵⁾ is manufactured through a thermomechanical treatment shown in **Fig. 1-16**. In this process, steel is formed by pressing performed using a press machine after austenitizing, and is then quenched to room temperature in the die. The pressed steel is descaled and trimmed. The final product possesses a superior shape-fitting property. The tensile strength of hot-stamping steel is over 1470 MPa owing to the martensite matrix structure.

Although hot-stamping steel has ultrahigh strength and shape-fitting property, its productivity is low because of the complex thermomechanical treatment. Recently, in order to improve its productivity, forming, trimming, and punching processes are combined during the hot-stamping process.⁷⁵⁾

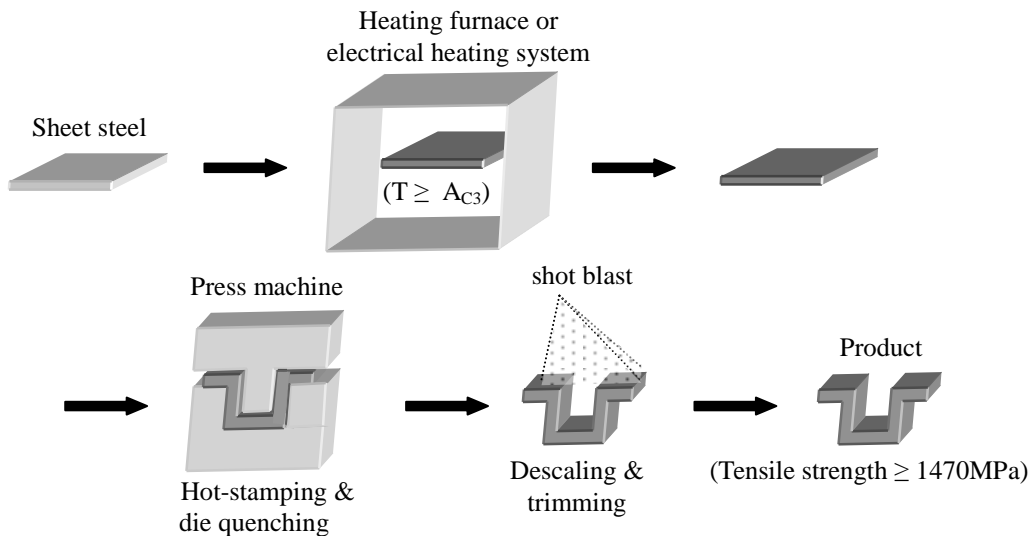


Fig. 1-16. Schematic illustration of the hot-stamping process.

1.3 Transformation-induced plasticity

Zackay et al.³⁹⁾ reported that superior elongation of high-alloy metastable austenitic steel can be obtained by transformation-induced plasticity (TRIP) of austenite. Further, Matsumura et al. developed low-alloy C-Si-Mn TRIP steel by employing austempering after intercritical annealing.⁴⁰⁻⁴³⁾ In addition, Matsumura et al. reported that austenite stabilization occurs during isothermal bainitic transformation (austempering).

In general, the austenite phase is an unstable phase at room temperature, and it transforms into the ferrite phase. However, if the stability of austenite is increased by isothermal bainitic transformation or austempering, austenite remains as metastable retained austenite at room temperature. The retained austenite transforms into martensite by stress or strain during deformation (**Fig. 1-17**). Thus, when tensile stress is applied to TRIP steel, the retained austenite in the strain concentration region will transform into martensite. Since the carbon content of the retained austenite is high, the transformed martensite possesses high strength. This transformation results in plastic deformation and work hardening of the ferrite structure matrix. This effect propagates further in the deformation area, and martensitic transformation occurs in neighboring areas subsequently to disperse strain. This TRIP effect leads to a high combination of strength and elongation.

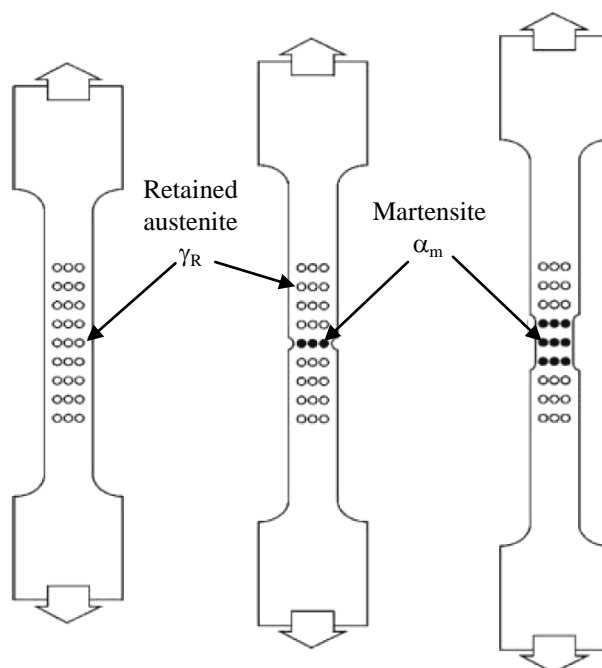


Fig. 1-17. Schematic representation of the TRIP-aided plasticity mechanism in low-alloy TRIP steels.¹⁶⁾ During straining, retained austenite transforms into martensite. Austenite is replaced by high-strength high-C martensite, and the transformation is associated with volume expansion. Both effects suppress plastic instability and extend the range of uniform elongation.

The behavior of martensitic transformation of retained austenite is explained as following on the basis of M_S , M_S^σ , and M_d related to the martensitic transformation temperature (**Fig. 1-18**).^{16,76-81)} The M_S^σ temperature is the temperature at which the stress-induced transformation is converted to strain-induced transformation. The M_d temperature is the temperature above which no martensitic transformation occurs.

- (1) M_S – M_S^σ range: When the retained austenite is loaded with stress lower than the yield stress of retained austenite, stress-induced transformation of austenite to martensite occurs at a pre-existing nucleation site. Since the chemical driving force of the transformation of austenite to martensite is high in the range of M_S – M_S^σ (**Fig. 1-19**), the transformation occurs because of stress. The stress required for martensitic transformation increases with increasing temperature, because the chemical driving force decreases.
- (2) M_S^σ – M_d range: When the retained austenite is subjected to plastic deformation, a new nucleation site for martensitic transformation originates because of slip. Martensite transformation occurs at the intersection of strain-induced deformation bands.
- (3) Above M_d : Strain-induced transformation does not occur, because a higher temperature results in higher stacking fault energy and lower driving force for transformation.

Generally, the retained austenite that possesses the transformation temperature between M_S^σ and M_d leads to high strength, large elongation, and high impact energy absorption capacity. The retained austenite is formed because of the high carbon concentration of fine (or filmy) retained austenite.

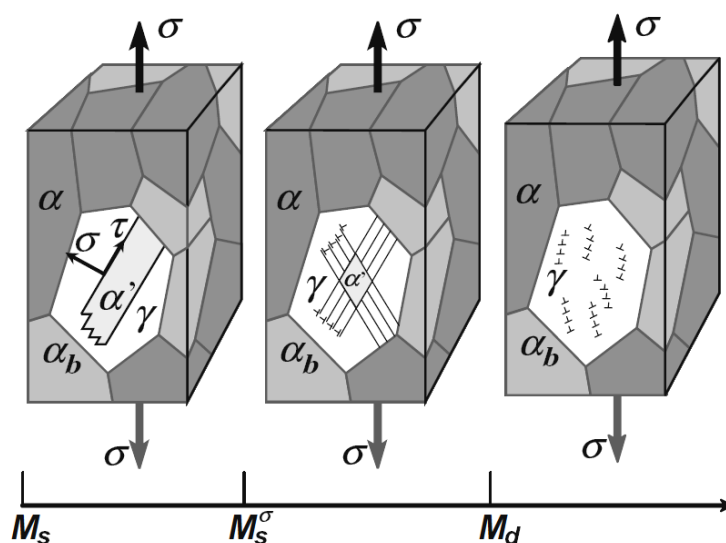


Fig. 1-18. Schematic illustrating the dominant deformation mechanisms in different temperature ranges in retained austenite in TRIP steel: (from left to right) stress-induced plasticity, strain-induced plasticity, and dislocation glide plasticity.¹⁶⁾

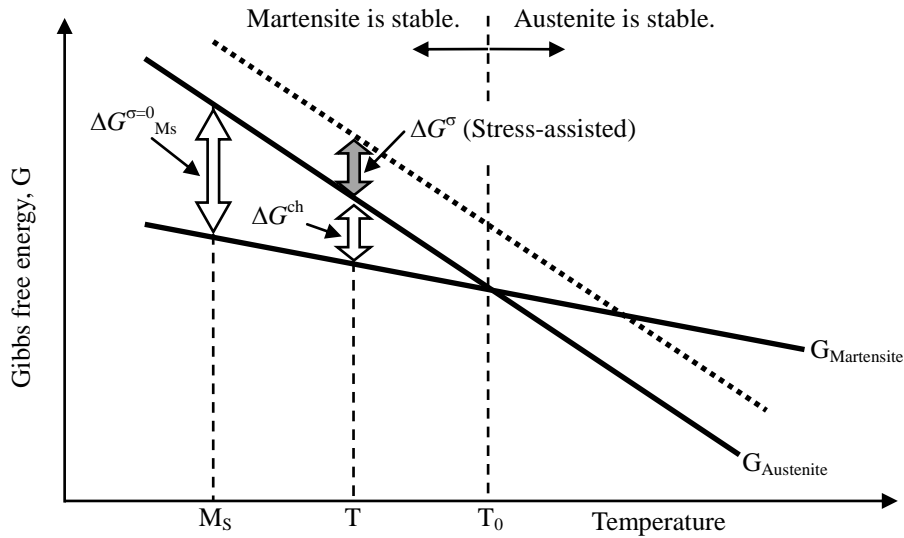


Fig. 1-19. Schematic illustration of chemical (ΔG^{ch}) and mechanical driving forces (ΔG^{ch}) of TRIP-aided steel.⁷⁷⁾

With respect to stacking fault energy (SFE), TRIP easily occurs in steel with low stacking fault energy of austenite. Saeed-Akbari et al.⁸²⁾ reported that the stacking fault energy increases with increase in the C and Mn content, as illustrated in **Fig. 1-20**. If the stacking fault energy of steels increases, the deformation mechanism of the steel converts from TRIP to TWIP as shown in **Fig.1-21** and as reported by Lee et al.⁸³⁾ In Fig. 1-21, ϵ -martensite transformation is favored in SFE below 20 mJ/m². The mixed deformation mechanism associated with the simultaneous occurrence of strain-induced martensite formation and TRIP appears in intermediate SFE ranging from 12 to 18 mJ/m² at a low strain rate. In steel with significantly high stacking fault energy, the deformation mechanism of steel is only slip deformation.

In order to effectively utilize the TRIP effect, it is necessary that SFE be controlled by the alloying and heating of TRIP steel.

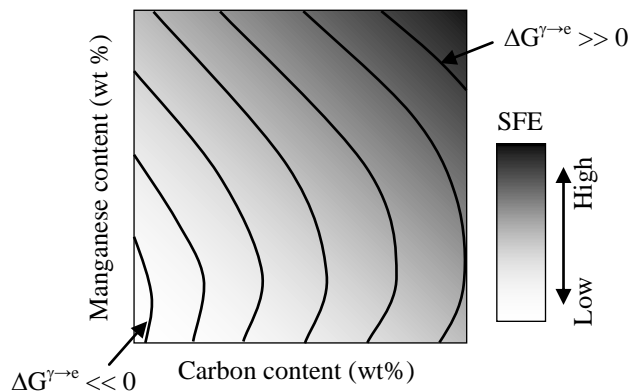


Fig. 1-20. Schematic illustration of a composition-dependent SFE map.⁸²⁾ $\Delta G^{\gamma \rightarrow \epsilon}$ and SFE show free energy for the $\gamma \rightarrow \epsilon$ phase transformation and stacking fault energy.

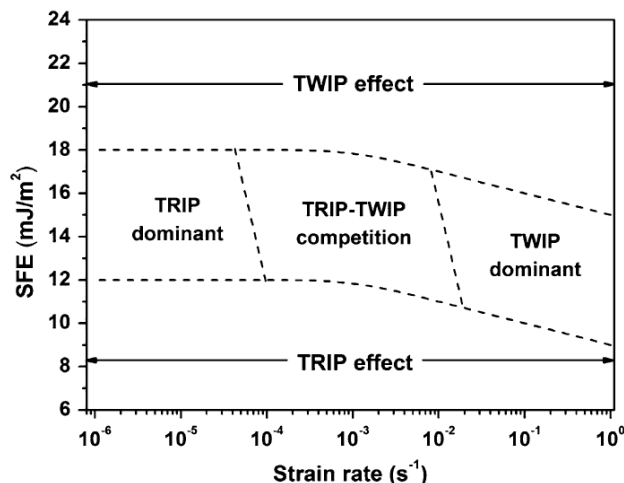


Fig. 1-21. Effect of strain rate on the plasticity-enhancing mechanism in Fe-12Mn-0.6C with SFE ranging from 12 to 18 mJ/m².⁸³⁾

TRIP-aided steel can be expected to further improve the tensile strength, formability, fatigue strength, impact toughness, hydrogen embrittlement performance, and other properties of third-generation steels, as mentioned by Matlock et al.⁸⁴⁾ (**Fig. 1-22**). In addition, Sugimoto has explained that a combination of tensile strength and total elongation in some steels improves with increasing volume fractions of austenite or retained austenite (**Fig. 1-23**). In order to improve the mechanical properties of low-alloy steels, it is important that the volume fraction of retained austenite is increased by new heating or thermomechanical processes.

In the future, the requirements for steels with excellent combinations of strength, elongation, and toughness will further increase for achieving higher levels of fuel efficiency and impact safety of automobiles and for reducing greenhouse gas emissions. Therefore, the development of TRIP-aided steels with superior mechanical properties and studies on such steels are necessary.

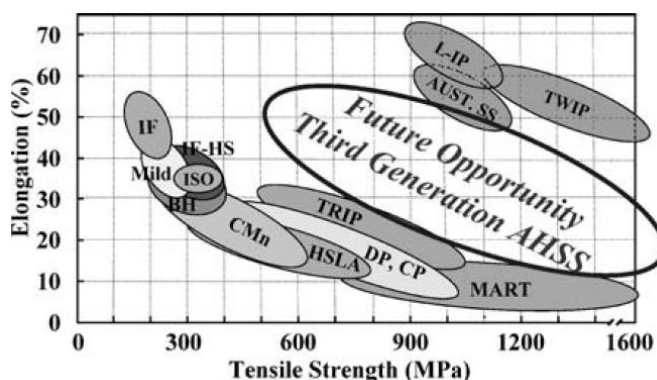


Fig. 1-22. Summary of tensile strength and tensile elongation data for various classes of conventional and advanced high-strength sheet steels.⁸²⁾

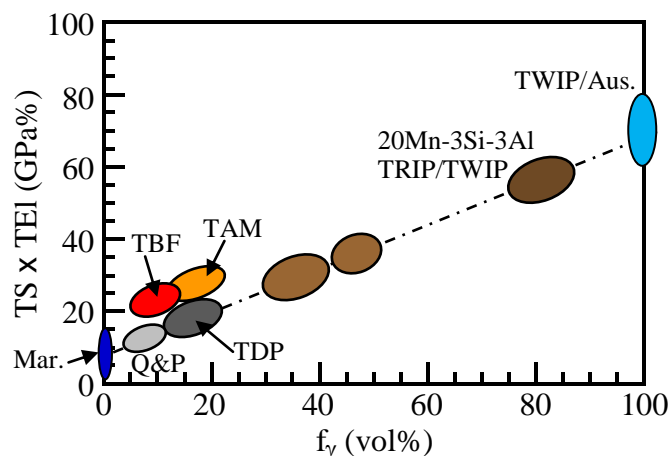


Fig. 1-23. Relationship between a combination of tensile strength and total elongation ($TS \times TEI$) and volume fractions of austenite or retained austenite (f_γ).⁷⁶⁾ Mar.: martensitic steel, Q&P: quench and partitioning steel, TDP: TRIP-aided dual-phase steel, TBF: TRIP-aided bainitic ferrite steel, TAM: TRIP-aided annealed martensitic steel, Aus.: austenitic steel.

1.4 Scope and structure of this thesis

The scope of the present study is to develop and investigate high-strength TRIP-aided steels. It will be realized by utilizing ultrahigh-strength TRIP-aided martensitic (TM) steel. TM steel possesses an ultrahigh strength of over 1470 MPa, high formability, high impact toughness, and high fatigue strength. The microstructure of this steel is characterized by fine lath martensite with ultrahigh strength and a martensite metastable retained austenite mixed phase. TM steel can be expected to improve the fuel efficiency and impact safety of automobiles.

In this thesis, results of investigation on the microstructure and mechanical properties of ultrahigh-strength TM steel, which was developed in this study, are presented and discussed. In Chapter 1 (this chapter), the background of advanced high-strength steels and the aim of this study are introduced. In Chapter 2, In Chapter 2, the effect of partitioning temperature after quenching on the microstructure and retained austenite characteristics of 0.2%C-1.5%Si-1.5%Mn (in mass%) TM steel are given and discussed. In Chapter 3, the effect of alloying elements on the microstructure and retained austenite characteristics of 0.2%C-1.5%Si-1.5%Mn TM steels are given and discussed. In Chapter 4, the effects of quenching or isothermal transformation processes on the tensile properties and formability of 0.2%C-1.5%Si-1.5%Mn-0.05%Nb TM steels are presented and discussed. In Chapter 5, the effect of partitioning temperature after the IT process on the tensile properties and formabilities of 0.2%C-1.5%Si-1.5%Mn-0.05%Nb TM steel are presented and discussed. In Chapter 6, the effect of the addition of Cr, Mo, and/or Ni on the tensile properties and formabilities

Chapter 1. Introduction

of 0.2%C-1.5%Si-1.5%Mn-0.05%Nb TM steel are given and discussed. In Chapter 7, the effects of the addition of Cr, Mo, and/or Ni on the Charpy impact absorbed value and ductile-brittle fracture appearance transition temperature of 0.2%C-1.5%Si-1.5%Mn-0.05%Nb TM steel are presented and discussed, and are compared with those for TRIP-aided bainitic ferrite (TBF) steel and conventional martensitic steel. In Chapter 8, notch-fatigue strengths and notch sensitivities of 0.1–0.6%C-1.5%Si-1.5%Mn TM steel are given and discussed. In Chapter 9, the conclusions of this thesis are summarized.

REFERENCES

- (1) “The Motor Industry of Japan 2013”, Japan Automobile Manufacturers Association, Inc., 2013.
- (2) “Future Steel Vehicle Phase 1”, World Auto Steel, 2011.
- (3) “Future Steel Vehicle -Nature's Way to Mobility- Overview Report – Future Steel Vehicle Phase 2”, World Auto Steel, 2011.
- (4) S. Itoh, K. Kishida and Y. Kuriyama: Steels Contributing to the Weight of Automobile - Mainly ULSAB Project -, *Feramu*, **4** (1999), pp. 367–372 (in Japanese).
- (5) World Auto Steel, ULSAB, ULSAB Program Reports. Available: <http://www.worldautosteel.org/projects/ulsab/ultralight-steel-auto-body-ulsab-programme/> [Accessed 15 Oct. 2013]
- (6) Y. Kuriyama, K. Yamazaki, K. Hashimoto and H. Ohhashi: Progress of Subsequent ULSAB project, Text of Materials Forum 2002, Society of Automotive Engineers of Japan, pp. 16–21 (in Japanese).
- (7) World Auto Steel, ULSAB-AVC, ULSAB-AVC Program Reports. Available: <http://www.worldautosteel.org/projects/ulsab-avc-2/ulsab-avc/> [Accessed 15 Oct. 2013]
- (8) J.Y. Yoo, W.Y. Choo, T.W. Park and Y.M. Kim: Microstructures and Age Hardening Characteristics of Direct Quenched Cu Bearing HSLA Steel, *ISIJ Int.*, **35** (1995), pp. 1034–1040.
- (9) R. Riva, C. Mapell and R. Venturini: Effect of Coiling Temperature on Formability and Mechanical Properties of Mild Low Carbon and HSLA Steels Processed by Thin Slab Casting and Direct Rolling, *ISIJ Int.*, **47** (2007), pp. 1204–1213.
- (10) Y. Hosoya: Evolution of Automobile Panel for Sheet Steel, *Feramu*, **11** (2006), pp. 773–778 (in Japanese).
- (11) T. Senuma: Physical Metallurgy of Modern High Strength Steel Sheets, *ISIJ Int.*, **41** (2001), pp. 520–532.
- (12) M. Takahashi: Development of High Strength Steels for Automobiles, *Nippon Steel Technical Report*, **88** (2003), pp. 2–7.
- (13) D. Kondo, K. Kunishige and R. Ueji: Effects of the Grain Size and Volume Fraction of Second Hard Phase on Mechanical Properties of DP Steel, *CAMP-ISIJ*, **18** (2005), p. 548.
- (14) K-T. Park, Y.K. Lee and D.H. Shin: Fabrication of Ultrafine Grained Ferrite/Martensite Dual Phase Steel by Severe Plastic Deformation, *ISIJ Int.*, **45** (2005), pp. 750–755.
- (15) M. Calcagnotto, D. Ponge and D. Raabe: Ultrafine Grained Ferrite/Martensite Dual Phase Steel Fabricated by Large Strain Warm Deformation and Subsequent

- Intercritical Annealing, *ISIJ Int.*, **48** (2008), pp. 1096–1101.
- (16) B.C. De Cooman: Structure-properties Relationship in TRIP Steels Containing Carbide-free Bainite, *Current Opinion in Solid State Mater. Sci.*, **8** (2004), pp. 285–303.
- (17) S. Ikeda, K. Makii, Y. Shindo and S. Hashimoto: Effect of Precipitates on Ductility of High Tensile Strength IF Sheet Steel, *Materia*, **12** (2000), p. 944 (in Japanese).
- (18) B. Hutchinson and D. Artymowicz: Mechanisms and Modelling of Microstructure/Texture Evolution in Interstitial-free Steel Sheets, *ISIJ Int.*, **41** (2001), pp. 533–541.
- (19) S-H. Lee, Y. Saito, K-T. Park and D.H. Shin: Microstructures and Mechanical Properties of Ultra Low Carbon IF Steel Processed by Accumulative Roll Bonding Process, *Mater. Trans.*, **43** (2002), pp. 2320–2325.
- (20) N. Narasaiah, P.C. Chakraborti, R. Maiti and K.K. Ray: Fatigue Crack Initiation in an Interstitial Free Steel, *ISIJ Int.*, **45** (2005), pp. 127–132.
- (21) H.S. Lee, B. Hwang, S. Lee, C.G. Lee and S-J. Kim: Effects of Martensite Morphology and Tempering on Dynamic Deformation Behavior of Dual-phase Steels, *Metall. Mater. Trans. A*, **35A** (2004), pp. 2371–2382.
- (22) K. Hasegawa, K. Kawamura, T. Urabe and Y. Hosoya: Effects of Microstructure on Stretch-flange-formability of 980 MPa Grade Cold-rolled Ultra High Strength Steel Sheets, *ISIJ Int.*, **44** (2004), pp. 603–609.
- (23) A. Murugaiyan, A. Saha Prodder, A. Pandit, S. Chandra, D. Bhattacharjee and R.K. Ray: Phase Transformations in Two C–Mn–Si–Cr Dual Phase Steels, *ISIJ Int.*, **46** (2006), pp. 1489–1494.
- (24) M.A. Asadabad, M. Goodaezi and S. Kheirandish: Kinetics of Austenite Formation in Dual Phase Steels, *ISIJ Int.*, **48** (2008), pp. 1251–1255.
- (25) H.A. Alizamini, M. Militzer and W.J. Poole: Formation of Ultrafine Grained Dual Phase Steels through Rapid Heating, *ISIJ Int.*, **51** (2011), pp. 958–964.
- (26) O. Grässel, L. Krüger, G. Frommeyer and L.W. Meyer: High Strength Fe-Mn-(Al, Si) TRIP/TWIP Steel Development–Properties-application, *Int. J. Plasticity.*, **16** (2000), pp. 1391–1409.
- (27) S. Vercammen, B. Blanpain, B.C. De Cooman and P. Wollants: Cold Rolling Behaviour of an Austenitic Fe-30Mn-3Al-3Si TWIP-steel: The Importance of Deformation Twinning, *Acta Mater.*, **52** (2004), pp. 2005–2012.
- (28) B.X. Huang, X.D. Wang, L. Wang and Y.H. Rong: Effect of Nitrogen on Stacking Fault Formation Probability and Mechanical Properties of Twinning-induced Plasticity Steels, *Metall. Mater. Trans. A*, **39A** (2008), pp. 717–724.
- (29) S. Kang, J-G. Jung and Y-K. Lee: Effect of Niobium on Mechanical Twinning and Tensile Properties of a High Mn Twinning-induced Plasticity Steel, *Mater. Trans.*, **53**

- (2012), pp. 2187–2190.
- (30) L. Chen, S-J. Lee and B.C. De Cooman: Mechanical Properties of H-charged Fe–18Mn–1.5Al–0.6C TWIP Steel, *ISIJ Int.*, **52** (2012), pp. 1670–1677.
- (31) M. Koyama, T. Sawaguchi and K. Tsuzaki: TWIP Effect and Plastic Instability Condition in an Fe–Mn–C Austenitic Steel, *ISIJ Int.*, **53** (2013), pp. 323–329.
- (32) K. Sugimoto, T. Sakaki, T. Kuribayashi and O. Miyagawa: Strength and Ductility of Ferrite-Bainite-Martensite Steels, *Tetsu-to-Hagane*, **72** (1986), pp. 2101–2108 (in Japanese).
- (33) A.S. Podder, D. Bhattacharjee and R.K. Ray: Effect of Martensite on the Mechanical Behavior of Ferrite–Bainite Dual Phase Steels, *ISIJ Int.*, **47** (2007), pp. 1058–1064.
- (34) Z. Nishiyama: *Martensitic Transformation–Basic Edition–*, Maruzen Co., Tokyo (1971), (in Japanese).
- (35) Z. Nishiyama: *Martensitic Transformation–Applied Edition–*, Maruzen Co., Tokyo (1974), (in Japanese).
- (36) K. Sugimoto, T. Sakaki, T. Fukusato and O. Miyagawa: Deformation and Strain Hardening of Martensite in 1.4%Mn Steels, *Tetsu-to-Hagane*, **70** (1984), pp. 1712–1718 (in Japanese).
- (37) G. Krauss: Heat Treated Martensitic Steels: Microstructural Systems for Advanced Manufacture, *ISIJ Int.*, **35** (1995), pp. 349–359.
- (38) Y. Nagataki, S. Tsuyama and Y. Hosoya: Effect of Tempering Temperature on the Bendability of Martensitic Steels, *Tetsu-to-Hagane*, **99** (2013), pp. 245–253 (in Japanese).
- (39) V.F. Zackay, E.R. Parker, D. Fahr and B. Bush: The Enhancement of Ductility in High-strength Steels, *Trans. Am. Soc. Met.*, **60** (1967), pp. 252–259.
- (40) O. Matsumura, Y. Sakuma and H. Takechi: Enhancement of Elongation by Retained Austenite in Intercritical Annealed 0.4C-1.5Si-0.8Mn Steel, *ISIJ Int.*, **27** (1987), pp. 570–579.
- (41) O. Matsumura, Y. Sakuma and H. Takechi: Retained Austenite in 0.4%C-Si-1.2%Mn Steel Sheet Annealed in Intercritical Range and Austempered, *Tetsu-to-Hagane*, **77** (1991), pp. 1304–1311 (in Japanese).
- (42) O. Matsumura, Y. Sakuma and H. Takechi: Retained Austenite in 0.4C-Si-1.2Mn Steel Sheet Intercritically Heated and Austempered, *ISIJ Int.*, **32** (1992), pp. 1014–1020.
- (43) O. Matsumura, Y. Sakuma, H. Takechi and J. Zhao: Effect of Retained Austenite on Formability of High Strength Sheet Steels, *ISIJ Int.*, **32** (1992), pp. 1110–1116.
- (44) K. Sugimoto, N. Usui, M. Kobayashi and S. Hashimoto: Effects of Volume Fraction and Stability of Retained Austenite on Ductility of TRIP-aided Dual-phase

- Steels, *ISIJ Int.*, **32** (1992), pp. 1311–1318.
- (45) K. Sugimoto, M. Misu, M. Kobayashi and H. Shirasawa: Effects of Second Phase Morphology on Retained Austenite Morphology and Tensile Properties in a TRIP-aided Dual-phase Steel Sheet, *ISIJ Int.*, **33** (1993), pp. 775–782.
- (46) K. Sugimoto, M. Kobayashi, A. Nagasaka and S. Hashimoto: Warm Stretch-formability of TRIP-aided Dual-phase Sheet Steels, *ISIJ Int.*, **35** (1995), pp. 1407–1414.
- (47) K. Sugimoto, S.X. Dong, M. Kobayashi, T. Haga and H. Shirasawa: Fatigue Properties of TRIP-aided Dual-phase Sheet Steel, *Trans. JSME. A*, **63** (1997), pp. 717–724 (in Japanese).
- (48) K. Sugimoto, A. Nagasaka, M. Kobayashi and S. Hashimoto: Effects of Retained Austenite Parameters on Warm Stretch-flangeability in TRIP-aided Dual-phase Sheet Steels, *ISIJ Int.*, **39** (1999), pp. 56–63.
- (49) M. De Meyer, D. Vanderscheren and B.C. De Cooman: The Influence of the Substitution of Si by Al on the Properties of Cold Rolled C-Mn-Si TRIP Steels, *ISIJ Int.*, **39** (1999), pp. 813–822.
- (50) A. Nagasaka, K. Sugimoto, M. Kobayashi, Y. Kobayashi and S. Hashimoto: Effects of Structure and Stability of Retained Austenite on Deep Drawability of TRIP-aided Dual-phase Sheet Steels, *Tetsu-to-Hagane*, **85** (1999), pp. 885–890 (in Japanese).
- (51) S-M. Song, K. Sugimoto, M. Kobayashi, H. Matsubara and T. Kashima: Impact Properties of Low Alloy TRIP Steels, *Tetsu-to-Hagane*, **86** (2000), pp. 563–569 (in Japanese).
- (52) K. Sugimoto, T. Iida, J. Sakaguchi and T. Kashima: Retained Austenite Characteristics and Tensile Properties in a TRIP Type Bainitic Sheet Steel, *ISIJ Int.*, **40** (2000), pp. 902–908.
- (53) K. Sugimoto, J. Sakaguchi, T. Iida and T. Kashima: Stretch-flangeability of a High-strength TRIP Type Bainitic Sheet Steel, *ISIJ Int.*, **40** (2000), pp. 920–926.
- (54) K. Sugimoto, K. Nakano, S-M. Song and T. Kashima: Retained Austenite Characteristics and Stretch-flangeability of High-strength Low-alloy TRIP Type Bainitic Sheet Steels, *ISIJ Int.*, **42** (2002), pp. 450–455.
- (55) K. Sugimoto, A. Kanda, R. Kikuchi, S. Hashimoto, T. Kashima and S. Ikeda: Ductility and Formability of Newly Developed High Strength Low Alloy TRIP-aided Sheet Steels with Annealed Martensite Matrix, *ISIJ Int.*, **42** (2002), pp. 910–915.
- (56) K. Sugimoto, R. Kikuchi, M. Tsunazawa, S. Hashimoto, T. Kashima and S. Ikeda: The Effects of Heat-treatment Conditions on Stretch-flangeability and Bendability of High-strength Low Alloy TRIP-aided Sheet Steels with Annealed Martensitic

- Matrix, *Tetsu-to-Hagane*, **89** (2003), pp. 1065–1070 (in Japanese).
- (57) K. Sugimoto, A. Hayakawa, T. Hojo, S. Hashimoto and S. Ikeda: Grain Refinement of High Strength Low Alloy TRIP-aided Ferrous Steels by Thermomechanical Processing in $\alpha+\gamma$ Region, *Tetsu-to-Hagane*, **89** (2003), pp. 1233–1239 (in Japanese).
- (58) T. Hojo, S-M. Song, K. Sugimoto, A. Nagasaka, S. Ikeda, H. Akamizu and M. Mayuzumi: Hydrogen Embrittlement of Ultra High Strength Low Alloy TRIP-aided Steels, *Tetsu-to-Hagane*, **90** (2004), pp. 177–182 (in Japanese).
- (59) S. Hashimoto, S. Ikeda, K. Sugimoto and S. Miyake: Effects of Nb and Mo Addition to 0.2%C-1.5%Si-1.5%Mn Steel on Mechanical Properties of Hot Rolled TRIP-aided Steel Sheets, *ISIJ Int.*, **44** (2004), pp. 1590–1598.
- (60) K. Sugimoto, M. Tsunazawa, T. Hojo and S. Ikeda: Ductility of 0.1-0.6C-1.5Si-1.5Mn Ultra High-strength TRIP-aided Sheet Steels with Bainitic Ferrite Matrix, *ISIJ Int.*, **44** (2004), pp. 1608–1614.
- (61) M. Mukherjee, O.N. Mohanty, S. Hashimoto, T. Hojo and K. Sugimoto: Strain-induced Transformation Behaviour of Retained Austenite and Tensile Properties of TRIP-aided Steels with Different Matrix Microstructure, *ISIJ Int.*, **46** (2006), pp. 316–324.
- (62) M. Mukherjee, O.N. Mohanty, S. Hashimoto, T. Hojo and K. Sugimoto: Acoustic Emission Technique to Study the Effect of Strain Rate on the Deformation Behaviour of TRIP Aided Steels with Different Matrix Microstructures, *ISIJ Int.*, **46** (2006), pp. 1241–1250.
- (63) K. Sugimoto, M. Murata, T. Muramatsu and Y. Mukai: Formability of C–Si–Mn–Al–Nb–Mo Ultra High-strength TRIP-aided Sheet Steels, *ISIJ Int.*, **47** (2007), pp. 1357–1362.
- (64) T. Hojo, K. Sugimoto, Y. Mukai and S. Ikeda: Effects of Aluminum on Delayed Fracture Properties of Ultra High Strength Low Alloy TRIP-aided Steels, *ISIJ Int.*, **48** (2008), pp. 824–829.
- (65) K. Sugimoto, M. Murata and S-M. Song: Formability of Al–Nb Bearing Ultra High-strength TRIP-aided Sheet Steels with Bainitic Ferrite and/or Martensite Matrix, *ISIJ Int.*, **50** (2010), pp. 162–168.
- (66) M. Murata, J. Kobayashi and K. Sugimoto: Stretch-flangeability of Ultra High-strength Low Alloy TRIP-aided Sheet Steels with Mixed Structure Matrix of Bainitic Ferrite and Martensite, *Tetsu-to-Hagane*, **96** (2010), pp. 84–92 (in Japanese).
- (67) K. Sugimoto: New Types of High-strength Low Alloy TRIP-aided Sheet Steels, *Feramu*, **15** (2010), pp. 183–188 (in Japanese).
- (68) J. Speer, D.K. Matlock, B.C. De Cooman and J.G. Schroth: Carbon partitioning

- into austenite after martensite transformation, *Acta Mater.*, **51** (2003), pp. 2611–2622.
- (69) A.M. Streicher, J.G. Speer, D.K. Matlock and B.C. De Cooman: Quenching and Partitioning Response of a Si-added TRIP Sheet Steel, *Proc of Int. Conf. on Advanced High Strength Sheet Steels for Automotive Applications*, AIST, Warrendale, PA, (2004), pp. 51–62.
- (70) J.G. Speer, F.C. Rizzo Assuncao, D.K. Malock and D.V. Edmonds: The “Quenching and Partitioning” Process: Background and Recent Progress, *Materials Research*, **8** (2005), pp. 417–423.
- (71) B.C. De Cooman and J.G. Speer: Quench and Partitioning Steel: a New AHSS Concept for Automotive Anti-intrusion Applications, *Steel Res. Int.*, **77** (2006), pp. 634–640.
- (72) T. Senuma and T. Takeshita: Recent Research and Development of Modern Steel Sheet for Automobiles, *J. Japan Inst. Metals*, **70** (2006), pp. 858–864 (in Japanese).
- (73) T. Senuma, H. Magome, A. Tanabe and Y. Takemoto: Effect of Press Forming Conditions on Shape Fixability of Hot Stamped Hat-type Parts, *J. Jpn. Soc. Tech. Plast.*, **49** (2008), pp. 321–325 (in Japanese).
- (74) T. Senuma, H. Magome, K. Haga, T. Fujioka, Y. Takemoto and K. Shimizu: Highly Efficient Hot Stamping Technology, *J. Jpn. Soc. Tech. Plast.*, **51** (2010), pp. 680–684 (in Japanese).
- (75) K. Hidaka, Y. Takemoto and T. Senuma: Microstructural Evolution of Carbon Steels in Hot Stamping Processes, *ISIJ. Int.*, **52** (2012), pp. 688–696.
- (76) K. Sugimoto and J. Kobayashi: Advanced Ultrahigh-strength TRIP-aided Sheet Steel with Excellent Cold Formability, *J. Jpn. Soc. Tech. Plast.*, **54** (2013), pp. 949–953 (in Japanese).
- (77) M. Azuma, N. Fujita and M. Takahashi: Model for the Prediction of Microstructures and Mechanical Properties of Cold-rolled High Strength Steels, *Nippon Steel Technical Report*, **102** (2013), pp. 44–50.
- (78) V. Raghavan and A.R. Entwisle: Physical Properties of Martensite and Bainite, *J. Iron Steel Inst.*, **93** (1965), 110.
- (79) G.B. Olson and M. Cohen: Kinetics of Strain-induced Martensitic Nucleation, *Metall. Trans.*, **6A** (1975), pp. 791–795.
- (80) G.B. Olson and M. Cohen: Stress-assisted Isothermal Martensitic Transformation: Application to TRIP Steels, *Metall. Trans.*, **13A** (1982), pp. 1907–1914.
- (81) G. Stringfellow, D.M. Parks and G.B. Olson: A Constitutive Model for Plasticity Accompanying Strain-induced Martensitic Transformation in Metastable Austenitic Steel, *Acta Metall. Mater.*, **40** (1992), pp. 1703–1716.
- (82) A. Saeed-Akbari, J. Imlau, U. Prahl and W. Bleck: Derivation and Variation in

Composition-dependent Stacking Fault Energy Maps Based on Subregular Solution Model in High-manganese Steels, *Metall. Mater. Trans. A*, **40A** (2009), pp. 3076–3090.

- (83) S. Lee, Y. Estrin and B.C. De Cooman: Effect of the Strain Rate on the TRIP-TWIP Transition in Austenitic Fe-12 pct Mn-0.6 pct C TWIP Steel, *Metall. Mater. Trans. A*, Published online: 12 October 2013, 14 pages.
- (84) D.K. Matlock and J.G. Speer: Third Generation of AHSS: Microstructure Design Concepts, *Proc. of the Int. Conf. on Microstructure and Texture in Steels and Other Materials*, A. Haldar, S. Suwas and D. Bhattacharjee (Eds.), Springer, London, (2009), pp. 185–204.

Chapter 2. Microstructure and Retained Austenite Characteristics of C-Si-Mn TRIP-aided Martensitic Steel

2.1 Introduction

In the past two or three decades, many advanced high-strength sheet steels for automobile parts have been developed to reduce the body weight of automobiles. According to De Cooman,¹⁾ first-generation advanced high-strength steels (AHSSs), such as dual-phase steel, *Transformation-Induced Plasticity-aided steel* (TRIP-aided steel) with a polygonal ferrite matrix, and so on, have contributed considerably to the weight reduction and crash safety of recent automobiles because of their good combination of formability and tensile strength. Although second-generation AHSSs such as *Twinning-Induced Plasticity steel* (TWIP steel)²⁾ have not been applied so widely to automotive parts, third-generation advanced AHSSs such as *TRIP-aided bainitic ferrite steel* (TBF steel)³⁻⁹⁾ and *quenching and partitioning steel* (Q&P steel),¹⁰⁾ with good formability (stretch-flangeability and bendability) and ultra-high strength (980–1470 MPa) are expected for future automotive applications. For the achievement of a tensile strength of more than 2.0 GPa, quenching-partitioning-tempering (Q-P-T) steel with a martensite matrix was developed by Wang et al.¹¹⁾ They reported that ultra-high-strength TRIP-aided steel can be developed through the utilization of the martensite structure.

Further ultra-high strength may be achieved by changing the matrix structure into martensite with carbon-enriched metastable retained austenite. However, such a “*TRIP-aided martensitic steel* (TM steel)” has not yet been developed. Moreover, there have been no reports on the microstructural formation mechanism and carbon-enrichment mechanism of retained austenite in martensitic steels such as TM steel. In this section, TM steel with a chemical composition of 0.2% C, 1.5% Si, and 1.5% Mn (in mass%) is developed by means of quenching (to temperatures lower than M_f) and partitioning processes. In addition, the microstructural formation mechanisms and retained austenite characteristics are investigated and discussed.

2.2 Experimental Procedure

In this study, a 100-kg steel ingot was prepared by vacuum melting followed by hot forging to produce a bar of 32 mm in diameter. Then, the bars were heated to 1200°C and hot-rolled to 13 mm in diameter with a finishing rolling temperature of 850°C, and cooled in air to room temperature. The chemical composition is detailed in **Table 2-1**. The measured CCT diagram is shown in **Fig. 2-1**, indicating a martensite start temperature M_S of about 420°C. In addition, the martensite finish temperature M_f is estimated to be 277°C.⁹⁾

Table 2-1. Chemical composition (mass%) of a steel used.

C	Si	Mn	P	S	Al	N	O
0.20	1.50	1.50	0.015	0.0008	0.041	0.0005	0.0008

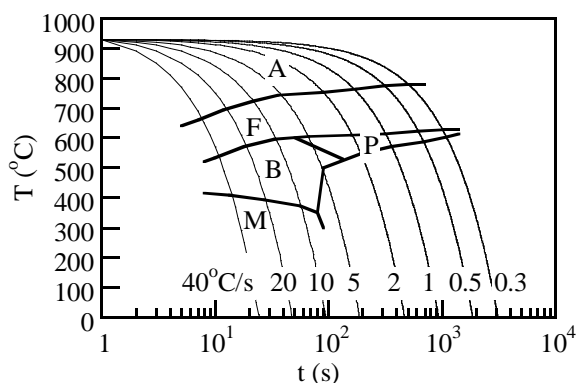


Fig. 2-1. Measured CCT diagram of steel used, in which A, F, P, B and M represent austenite, ferrite, pearlite, bainite and martensite, respectively.

The heat-treatment diagram of TM steel is shown in **Fig. 2-2**. TM steel was partitioned at 200–500°C after quenching to room temperature in oil or ice-brine.

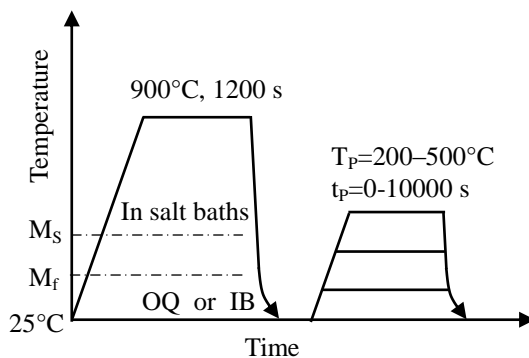


Fig. 2-2. Heat treatment diagram for TM steel, in which OQ and IB represent quenching in oil and ice-brine, respectively.

The retained austenite characteristics of the steel were investigated by X-ray diffractometry (XRD; Rigaku Co., RINT2100). Specimens were electropolished after grinding with Emery paper (#1200). The volume fraction of retained austenite (f_{γ} , vol%) was quantified from the integrated intensity of the $(200)_{\alpha}$, $(211)_{\alpha}$, $(200)_{\gamma}$, $(220)_{\gamma}$ and $(311)_{\gamma}$ peaks obtained by X-ray diffractometry using Mo-K α radiation.¹²⁾ The carbon concentration (C_{γ} , mass%) was estimated from the equation below. In this case, the lattice constant (a_{γ} , $\times 0.1$ nm) was measured from the $(200)_{\gamma}$, $(220)_{\gamma}$ and $(311)_{\gamma}$ peaks of

Cu-K α radiation.¹³⁾

$$a_{\gamma} = 3.5780 + 0.0330C_{\gamma} + 0.00095Mn_{\gamma} + 0.0056Al_{\gamma} + 0.0220N_{\gamma} \quad (2-1)$$

where Mn_{γ} , Al_{γ} , and N_{γ} represent the concentrations of the respective individual elements (mass%) in the retained austenite. For convenience, the contents of added alloying elements were substituted for these concentrations in this study.

The microstructure was observed by field-emission scanning electron microscopy with electron backscatter diffraction pattern (FE-SEM; Hitachi Co., S-4100 and FE-SEM-EBSP; JEOL Ltd., JSM-6500F) equipment and transmission electron microscopy (TEM; JEOL Ltd., JEM-2010). Specimens for FE-SEM-EBSP analysis were ground with colloidal silica after grinding with alumina. The volume fraction of the carbide precipitation was measured through carbon extraction replicas.

Vickers hardness tests were carried out using a Vickers microhardness machine (Shimadzu Co., DUH-201H) at 25°C, with a load of 0.98 N (HV0.1). The surface of the specimen was polished with Emery paper (#600).

2.3 Result

2.3.1 Vickers hardness

Figure 2-3 shows the Vickers hardnesses of the TM steels. The TM steels subjected to quenching in oil and ice-brine have Vickers hardnesses of about 450HV at partitioning temperatures in the range 25–350°C. When the TM steels are partitioned at temperatures above 400°C, the Vickers hardness decreases with increasing partitioning temperature.

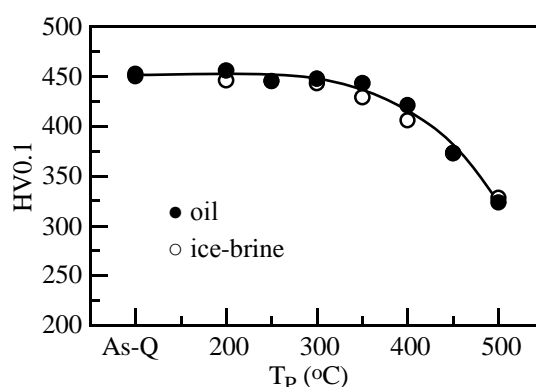


Fig. 2-3. Variations in Vickers hardness of TM steel as a function of partitioning temperature (T_p). Partitioning time (t_p) = 1000 s.

2.3.2 Retained austenite characteristics

Figure 2-4 shows the typical change in the X-ray diffraction pattern of the retained

austenite with partitioning temperature in the TM steel quenched in oil. **Figures 2-5** and **2-6** show the variations in the initial volume fraction and carbon concentration of the retained austenite of TM steels quenched in oil or ice-brine as a function of partitioning time and temperature, respectively. The TM steel quenched in oil contains retained austenite of a maximum of about 3 vol%. This amount decreases with increasing partitioning time in the range 100–10000 s (Fig. 2-5) and with increasing partitioning temperature in the range 250–450°C (Fig. 2-6). On the other hand, the carbon concentration of the retained austenite increases considerably with increasing partitioning temperature and time. If the TM steel is quenched in ice-brine, the amount of retained austenite and its carbon concentration are reduced to about 1.6 vol% and 0.3 mass%, respectively.

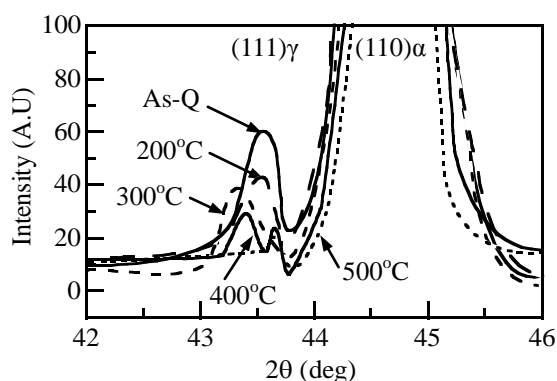


Fig. 2-4. Typical changes in X-ray diffraction patterns in TM steels as-quenched (As-Q) and partitioned at 200–500°C for 1000 s after oil quenching.

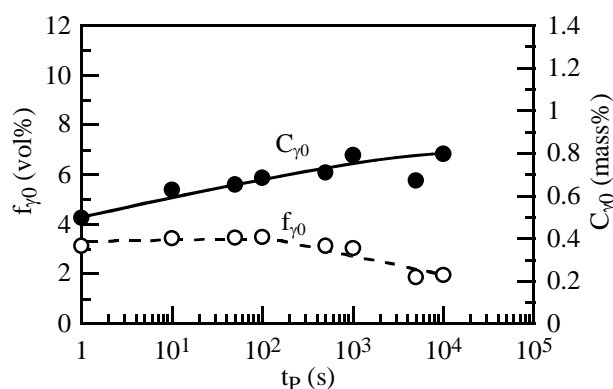


Fig. 2-5. Variations in initial volume fraction (f_{γ_0}) and initial carbon concentration (C_{γ_0}) of retained austenite as a function of partitioning time (t_p) in TM steel (quenching in oil). $T_p = 250^\circ\text{C}$.

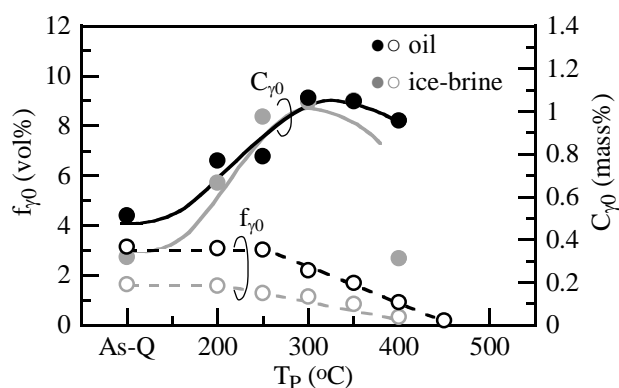


Fig. 2-6. Variations in initial volume fraction (f_{γ_0}) and initial carbon concentration (C_{γ_0}) of retained austenite as a function of partitioning temperature (T_P) in TM steel. $t_P = 1000$ s.

2.3.3 Microstructure and carbide

Figure 2-7 shows typical SEM images of the TM steel quenched in oil. **Figure 2-8** shows typical FE-SEM-EBSP analysis results for TM steel, and **Figure 2-9** shows typical TEM images. From Figs. 2-7 and 2-8, the matrix structure of the present TM steel is found to consist of wide and narrow lath martensite structures, and hardly seems to change with partitioning temperature. It is also found that the wider lath martensite structure in TM steel gives a higher image quality than the narrower lath martensite structure, which means that the narrow lath martensite structure possesses a higher dislocation density.¹⁴⁾ It is noteworthy that there is no twin in the narrow lath martensite, or the narrow martensite is α' -martensite and not ϵ -martensite. As shown in Figs. 2-8(d), 2-8(e), and 2-9(c), most of the retained austenite phases are fine, and are located on the interlath boundary of the narrow martensite lath structure, which is yellowish green in Fig. 2-8(d).

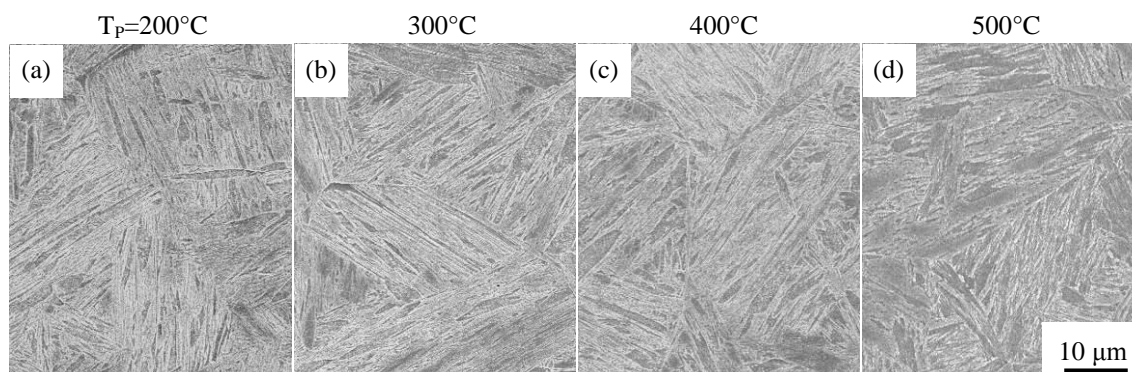


Fig. 2-7. Typical SEM images of TM steel subjected to partitioning process at (a) 200°C, (b) 300°C, (c) 400°C or (d) 500°C for 1000 s.

In Figs. 2-9(a), 2-9(b), and 2-9(e)–2-9(h), a large amount of fine and needle-shaped carbide seems to precipitate only in the wider martensite lath structure. This means that the needle-shaped carbides are already precipitated through auto-tempering upon quenching. According to De Cooman and Speer,¹⁾ the martensite structure in Q&P steel includes transition ϵ - or η -carbide. In this study, some carbides were observed in the TM steel (Fig. 2-9), but the precipitates were not detected as ϵ - or η -carbide, so the carbides are considered as cementites.

The volume fraction of carbide in the present TM steel was too low to be measured by X-Ray diffractometry (Fig. 2-4). Therefore, in order to measure the carbide volume fraction accurately, we observed it through carbon extraction replicas for TM steels partitioned at 25–500°C. As an example, a typical TEM image of the extraction replicas is shown in Fig. 2-9(h). The measured volume fraction of carbide is shown in **Fig. 2-10**. The amount of carbide in the TM steel hardly changes when it is partitioned at temperatures below 250°C ($f_{\theta} = 1.7\text{--}2.0$ vol%). The carbide fraction appears to increase with increasing partitioning temperature at temperatures above 250°C, accompanied by coarsening of the carbide. In the partitioning range above 450°C, the amount of carbide increases further ($f_{\theta} = 5.2$ vol%). The carbide fraction of the TM steel quenched in ice-brine and then partitioned at 200°C ($f_{\theta} = 1.2$ vol%) is lower than that of TM steel quenched in oil. Note that the amount of carbide in TM steel partitioned at 300°C for 1000 s is considerably lower than that ($f_{\theta} = 5.7$ vol%) of SCM420 steel (0.21%C-0.21%Si-0.77%Mn-1.02%Cr-0.18%Mo-0.06%Ni, in mass%) quenched in oil and then tempered at 300°C for 3600 s.

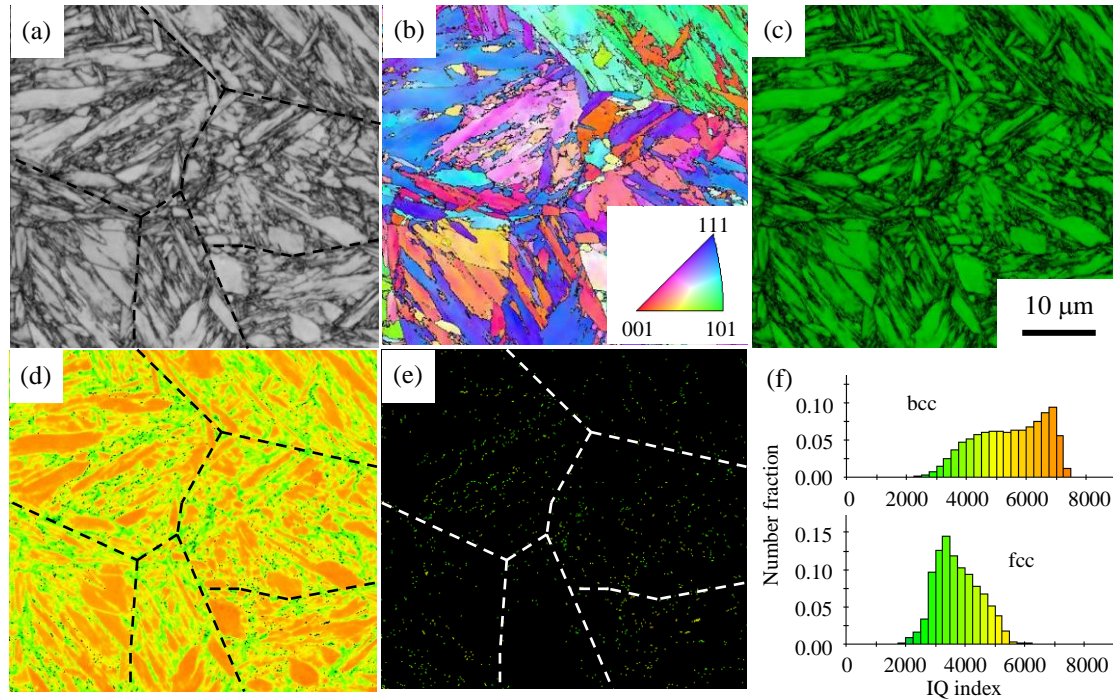


Fig. 2-8. (a) Image quality map, (b) inverse pole figure map, (c) phase map, (d) image quality distribution map of bcc phase, (e) image quality distribution map of fcc phase and (f) number fraction of image quality (IQ) of bcc and fcc phases in TM steel partitioned at 250°C for 1000 s. In (c), green and red phases denote matrix structure (bcc) and retained austenite (fcc), respectively. In (d), darker yellow and yellowish green regions represent martensite lath structures with higher and lower image quality index, respectively. Black phases are other ones such as retained austenite phases. Dotted lines in (a), (d) and (e) represent prior austenitic grain boundary.

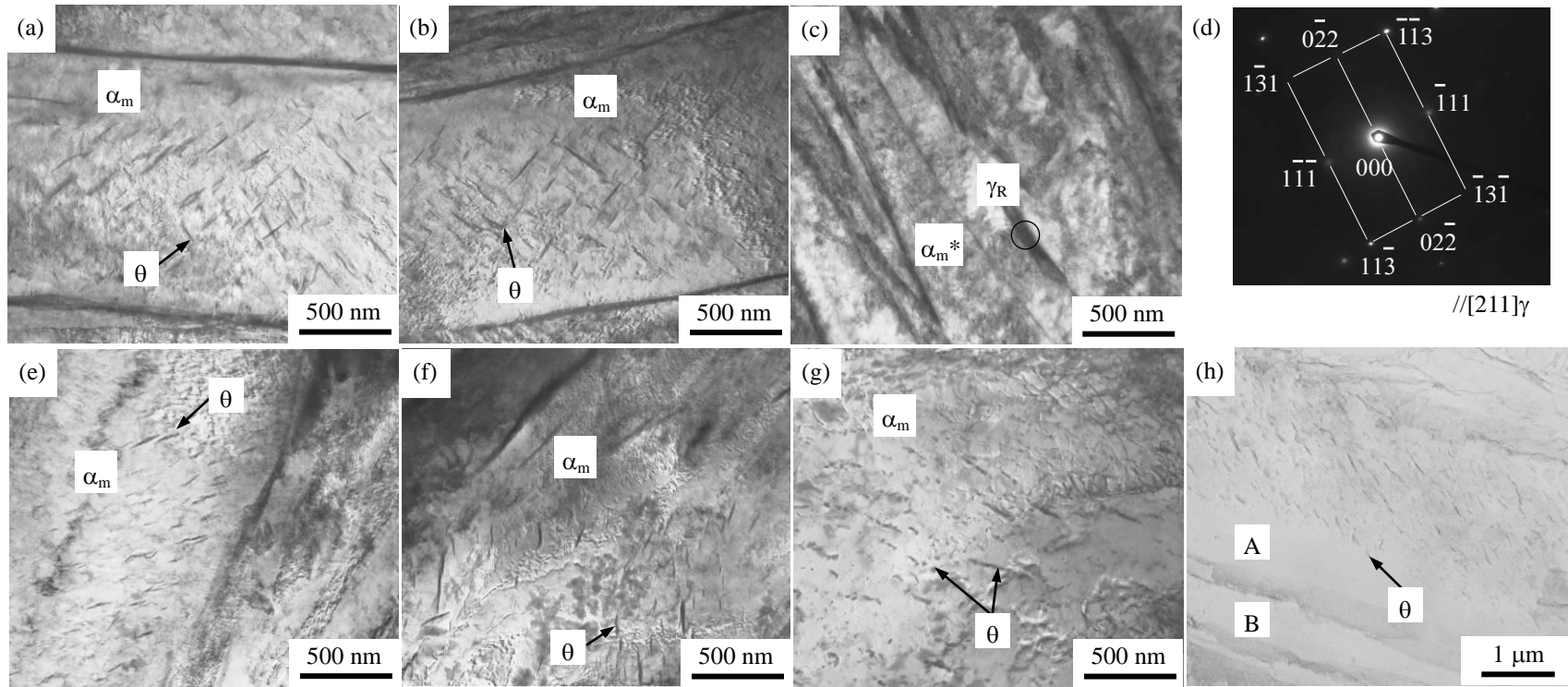


Fig. 2-9. TEM images of lath martensite structure in TM steel subjected to partitioning at (a) 25°C (as quenched), (b-d, h) 200°C, (e) 300°C, (f) 400°C or (g) 500°C for 1000 s. (a), (b), (e), (f) and (g): wide lath martensite structure (α_m) with carbides (θ). (c): narrow lath martensite structure (α_m^*) and interlath retained austenite (γ_R), (d): selected area diffraction pattern of circle in (c). (h): carbides observed by extraction replicas, in which A and B represent wide lath martensite structure with carbides ($f_\theta = 1.7$ vol%) and narrow lath martensite structure without carbides, respectively.

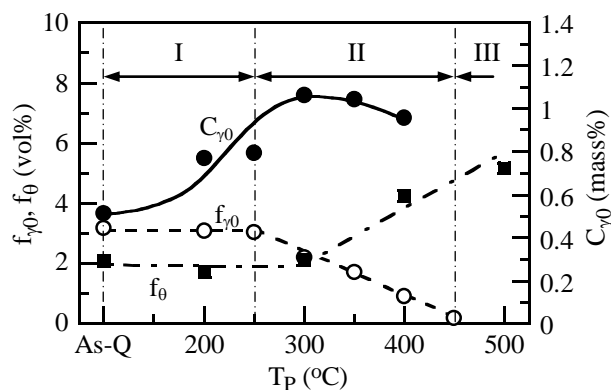


Fig. 2-10. Variations in volume fraction of carbide (f_{θ} : ■) and volume fraction (f_{γ_0} : ○) and carbon concentration (C_{γ_0} : ●) of retained austenite as a function of partitioning temperature (T_P) of TM steel quenched in oil.

2.4 Discussion

Figures 2-7–2-9 showed that TM steel subjected to the quenching and partitioning process consists of a wide and narrow lath martensite structure matrix and retained austenite located along the narrow martensite lath boundary, with precipitation of a small amount of carbide in the wide lath martensite structure. In general, Si suppresses carbide formation in steel,^{5,15)} similarly to Al.⁹⁾ Thus, it is considered that Si addition of 1.5 mass% results in such microstructural characteristics. In this case, a high shearing stress or free energy is required in the retained austenite for martensite transformation, because most of the retained austenite films are fine and surrounded by a hard martensite lath structure.

In the following, the transformation and carbide precipitation behavior of such a microstructure during the quenching and partitioning processes is discussed.

2.4.1 Microstructural change on quenching

The microstructural change and the retained austenite characteristics during the quenching process are illustrated in **Fig. 2-11**. On quenching, the austenite is transformed into two kinds of lath martensite structure matrices. The transformation behavior can be summarized as follows.

Stages 1–3: When the steel is cooled to temperatures below M_S after heating in the γ region, the wide martensite structure is first formed preferentially (stages 1–2 in Fig. 2-11(c)). Carbides are not yet precipitated in the wide martensite structure.

Stages 3–4: On continuous cooling to room temperature below M_f , the untransformed austenite is transformed to the narrow martensite structure and retained as retained austenite (stages 3–4 in Fig. 2-11(c)). At the same time, the wide martensite structure is tempered through auto-tempering, and therefore, carbide is precipitated only

in the wider martensite lath structure because of carbon diffusion.

According to Koistinen and Marburger,¹⁶⁾ the amount of martensite structure ($f\alpha_m$) increases with decreasing isothermal transformation temperature (T_{IT}) in conventional structural steel as follows:

$$f\alpha_m = 1 - \exp\{-1.1 \times 10^{-2}(M_s - T_{IT})\} \quad (2-2)$$

If the present steel is subjected to the isothermal transformation process at temperatures between M_f and room temperature, the volume fractions of narrow martensite and retained austenite may increase. In fact, the above forecast was verified by Kobayashi et al.¹⁷⁾ with an investigation of the mechanical properties of TM steel.

In Fig. 2-6, it is seen that the volume fraction and carbon concentration of the retained austenite decrease more with decreasing carbide content when the TM steel is quenched in ice-brine than when it is quenched in oil. This is because of the increasing volume fraction of martensite due to the lower quenching temperature in ice-brine. It may also be associated with the shorter diffusion time that results from rapid quenching.

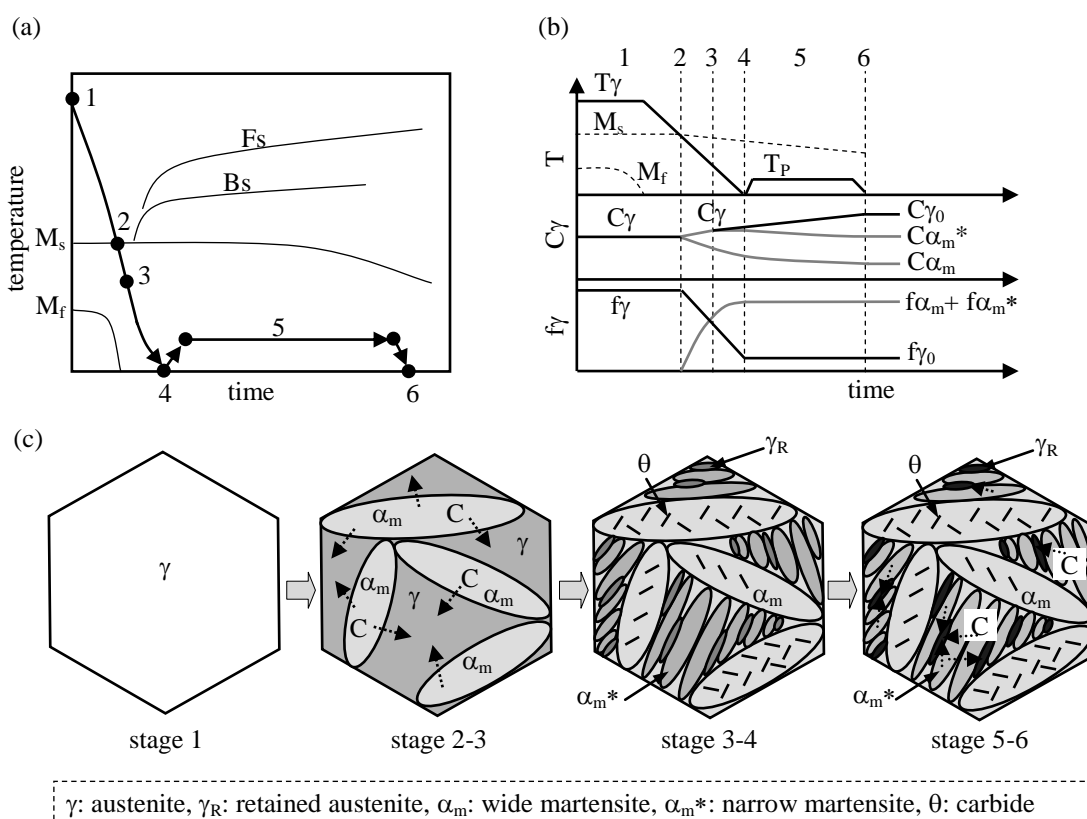


Fig. 2-11. Illustrations of (a) heat treatment diagram, (b) changes in carbon concentrations (C_γ , C_{α_m} and $C_{\alpha_m^*}$) and volume fractions (f_γ , f_{α_m} and $f_{\alpha_m^*}$) and (c) microstructural change at stages 1 through 6 of TM steel during partitioning process at 200°C.

2.4.2 Carbon-enrichment mechanism during partitioning

The microstructural changes in the behavior of this TM steel during the partitioning process (stages 5–6 in Fig. 2-11(c)) at temperatures between 200 and 500°C are illustrated in **Fig. 2-12**, and are classified into three partitioning ranges: Range I, Range II, and Range III, as follows:

Range I (200–250°C): When the quenched TM steel is partitioned at temperatures lower than 250°C, the carbon concentration of the retained austenite increases considerably with increasing partitioning temperature (Fig. 2-10). Because the volume fractions of retained austenite and carbide are both constant (Fig. 2-10), supersaturated carbon in the martensite may move into the retained austenite (Fig. 2-12(a)).

Range II (250–450°C): When the steel is partitioned at temperatures higher than 300°C, the carbon concentration of the retained austenite increased to 1.0–1.1 mass%. The volume fraction of retained austenite decreases and the carbide content increases with increasing partitioning temperature (Fig. 2-10). Thus, it is thought that the retained austenite shrinks and the excess solute carbon causes the further precipitation or coarsening of the carbide (Fig. 2-12(b)).

Range III (above 450°C): When the steel is partitioned at temperatures above 450°C, most of the retained austenite phase decomposes into ferrite and carbide (Fig. 2-12(c)). In the wide martensite lath structure, spheroidal carbides coexist with coarsened needle-shaped carbides (Fig. 2-9(g)).

According to Nishiyama,¹⁸⁾ the decomposition of retained austenite into ferrite and cementite begins upon tempering at over 140°C in plain carbon steel. In this study, no retained austenite was decomposed into ferrite and carbide even in Range II. Therefore, we confirm that the retained austenite was shrunk in Range II.

Figure 2-13 shows a plot of the carbon concentration of the retained austenite of TM steel in an equilibrium diagram calculated for the C-1.5%Si-1.5%Mn (in mass%) system. The carbon concentrations at $T_p = 350$ and 400°C agree well with the T_0 line where austenite and ferrite with the same chemical composition have identical free energies.¹⁹⁾ However, the carbon concentration at 250°C is significantly lower than the T_0 line because of the low diffusion rate of carbon. From these results, it is expected that the upper limit of the carbon concentration of the retained austenite is the T_0 line, in the same way as for TBF steel.

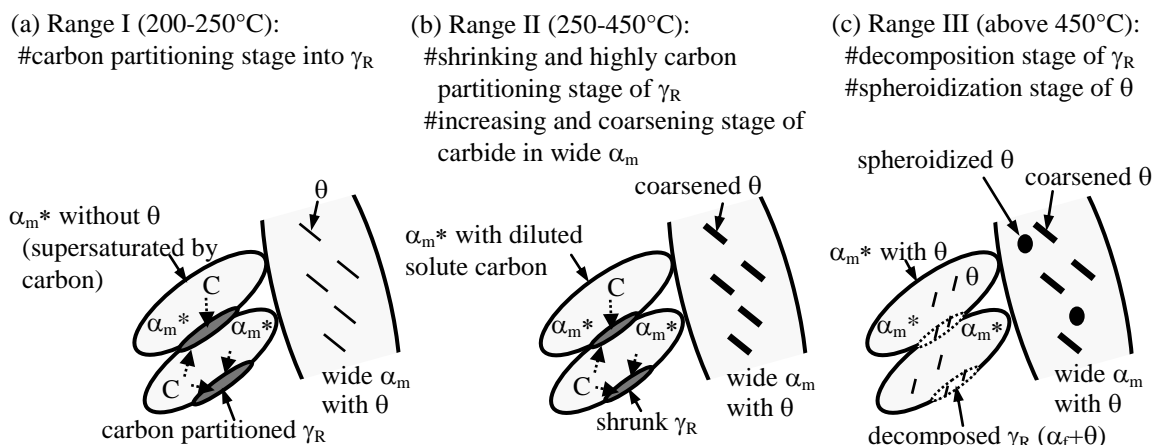


Fig. 2-12. Illustrations of (a) heat treatment diagram, (b) changes in carbon concentrations (C_γ , C_{α_m} and $C_{\alpha_m^*}$) and volume fractions (f_γ , f_{α_m} and $f_{\alpha_m^*}$) and (c) microstructural change at stages 1 through 6 of TM steel during partitioning process at 200°C.

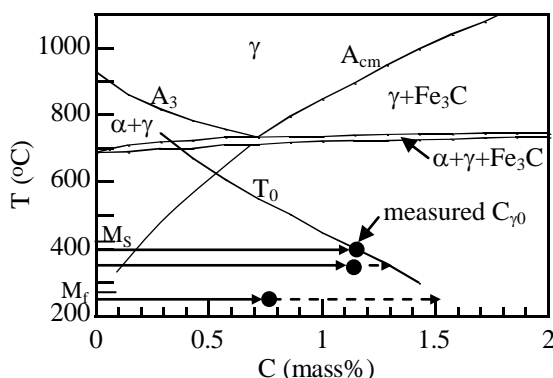


Fig. 2-13. Illustration of T_0 and A_{cm} temperatures in C-1.5%Si-1.5%Mn system, in which solid circle marks represent measured carbon concentration of retained austenite in TM steel quenched in oil.

2.5 Summary

The effects of partitioning after quenching in oil or ice-brine on the microstructure and retained austenite characteristics of 0.2%C-1.5%Si-1.5%Mn (in mass%) TM steel were investigated.

- (1) The TM steel consisting of wide and narrow lath martensite structures contained retained austenite of about 3 vol% after quenching in oil, with carbides of 1.7–2.0 vol% only in the wider martensite lath structure. When the steel was quenched in ice-brine, the volume fraction of retained austenite decreased to 1.8 vol% with a decrease in the carbide volume fraction.

Chapter 2. Microstructure and Retained Austenite Characteristics of C-Si-Mn TRIP-aided Martensitic Steel

- (2) With partitioning at temperatures lower than 250°C for times shorter than 1000 s, the volume fractions of the retained austenite and carbide were maintained, although the carbon concentration of the retained austenite increased. In this case, high mechanical properties of TM steel for automotive application can be expected due to a superior TRIP effect.
- (3) On the other hand, partitioning at 300–400°C for 1000 s after quenching caused a considerable increase in the carbon concentration of the retained austenite, although the volume fraction of retained austenite decreased and the volume fraction of carbide increased with increasing partitioning temperature.

REFERENCES

- (1) B.C. De Cooman and J.G. Speer: Quench and Partitioning Steel: a New AHSS Concept for Automotive Anti-Intrusion Applications, *Steel Res. Int.*, **77** (2006), pp. 634–640.
- (2) U. Brux, G. Frommeyer, O. Grassel, L.W. Meyer and A. Weise: Development and characterization of high strength impact resistant Fe-Mn-(Al, Si) TRIP/TWIP steels, *Steel Res.*, **73** (2002), pp. 294–298.
- (3) K. Sugimoto, T. Iida, J. Sakaguchi and T. Kashima: Retained Austenite Characteristics and Tensile Properties in a TRIP Type Bainitic Sheet Steel, *ISIJ Int.*, **40** (2000), pp. 902–908.
- (4) K. Sugimoto, J. Sakaguchi, T. Iida and T. Kashima: Stretch-flangeability of a High-strength TRIP Type Bainitic Sheet Steel, *ISIJ Int.*, **40** (2000), pp. 920–926.
- (5) K. Sugimoto, K. Nakano, S-M. Song and T. Kashima: Retained Austenite Characteristics and Stretch-flangeability of High-strength Low-alloy TRIP Type Bainitic Sheet Steels, *ISIJ Int.*, **42** (2002), pp. 450–455.
- (6) K. Sugimoto, M. Tsunazawa, T. Hojo and S. Ikeda: Ductility of 0.1-0.6C-1.5Si-1.5Mn Ultra High-strength TRIP-aided Sheet Steels with Bainitic Ferrite Matrix, *ISIJ Int.*, **44** (2004), pp. 1608–1614.
- (7) K. Sugimoto, M. Murata, T. Muramatsu and Y. Mukai: Formability of C–Si–Mn–Al–Nb–Mo Ultra High-strength TRIP-aided Sheet Steels, *ISIJ Int.*, **47** (2007), pp. 1357–1362.
- (8) K. Sugimoto, M. Murata and S-M. Song: Formability of Al–Nb Bearing Ultra High-strength TRIP-aided Sheet Steels with Bainitic Ferrite and/or Martensite Matrix, *ISIJ Int.*, **50** (2010), pp. 162–168.
- (9) M. Murata, J. Kobayashi and K. Sugimoto: Stretch-flangeability of Ultra High-strength Low Alloy TRIP-aided Sheet Steels with Mixed Structure Matrix of Bainitic Ferrite and Martensite, *Tetsu-to-Hagane*, **96** (2010), pp. 84–92 (in Japanese).
- (10) B.C. De Cooman: Structure-properties relationship in TRIP steels containing carbide-free bainite, *Current Opinion in Solid State Mater. Sci.*, **8** (2004), pp. 285–303.
- (11) X.D. Wang, N. Zhong, Y.H. Rong, T.Y. Hsu (Z.Y. Xu) and L. Wang: Novel ultrahigh-strength nanolath martensitic steel by quenching–partitioning–tempering process, *J. Mater. Res.*, **24** (2009), pp. 260–267.
- (12) H. Maruyama: X-ray measuring method of retained austenite, *J. Jpn. Soc. Heat Treat.*, **17** (1977), pp. 198–204 (in Japanese).
- (13) D.J. Dyson and B. Holmes: Effect of Alloying Additions on the Lattice Parameter of Austenite, *J. Iron Steel Inst.*, **208** (1970), pp. 469–474.

Chapter 2. Microstructure and Retained Austenite Characteristics of C-Si-Mn TRIP-aided Martensitic Steel

- (14) O. Umezawa: Practical application of SEM-EBSF analysis, *J. Jpn. Inst. Light Met.*, **50** (2000), pp. 86–93 (in Japanese).
- (15) D. Liu, B. Bai, H. Fang, W. Zhang, J. Gu and K. Chang: Effect of tempering temperature and carbide free bainite on the mechanical characteristics of a high strength low alloy steel, *Mater. Sci. Eng. A*, **371** (2004), pp. 40–44.
- (16) D.P. Koistinen and R.E. Marburger: A general equation prescribing the extent of the austenite-martensite transformation in pure iron-carbon alloys and plain carbon steels, *Acta Metall.*, **7** (1959), pp. 59–60.
- (17) J. Kobayashi, D.V. Pham and K. Sugimoto: Stretch-flangeability of 1.5GPa Grade TRIP-aided Martensitic Cold Rolled Sheet Steels, *Steel Res. Int.* **2011**, (2011), pp. 598–603.
- (18) Z. Nishiyama: *Martensitic Transformation –applied edition–*, Maruzen Co., Tokyo, (1974), 114 (in Japanese).
- (19) M. Takahashi and H.K.D.H. Bhadeshia: A Model for the Microstructure of Some Advanced Bainitic Steels, *Mater. Trans. JIM*, **32** (1991), pp. 689–696.

Chapter 3. Effects of Microalloying on Retained Austenite Characteristics of TRIP-aided Martensitic Steel

3.1 Introduction

For the past two or three decades, many advanced high-strength sheet steels have been developed to reduce the weight of automobile body structures. According to De Cooman and Speer¹⁾, first-generation advanced high-strength steels (AHSSs) such as dual-phase steel and TRIP-aided steel with polygonal ferrite matrix, considerably contributed to weight reduction of recent automobiles due to a good combination of formability and tensile strength. Although second-generation AHSS such as twinning induced plasticity (TWIP) steel has not been generally applied to automotive parts, third generation advanced AHSSs such as TRIP-aided bainitic ferrite (TBF) steel²⁻⁵⁾ and quenching and partitioning (Q&P) steel⁶⁾ with good formability (stretch-flangeability and bendability) and ultra high tensile strength of 980-1470 MPa are expected to be used in automotive applications.

Higher tensile strengths may be achieved by changing the matrix structure to martensite, while maintaining carbon-enriched retained austenite. Recently, a TRIP-aided martensitic steel (TM steel), has been developed by means of quenching at temperatures below M_f after austenitizing.⁷⁾ In this study, effects of partitioning temperature on retained austenite characteristics and microstructure in TM steel with chemical composition of 0.2C, 1.5Si and 1.5Mn (in mass%) are introduced. Also, effects of Cr, Mo and Ni additions on the retained austenite characteristics and microstructure were examined to improve hardenability.

3.2 Experimental procedure

In this study, five kinds of vacuum melted and hot-rolled steel bars of 13 mm diameter with different Cr, Mo, Ni and Nb contents were prepared. The chemical composition, calculated martensite-start temperature (M_s)⁸⁾ and hardenability of the steels A through E are listed in **Table 3-1**. Nb was added to refine prior austenitic grain size.

Hardenability was defined by a product of multiplying factors and the Grossman pearlitic hardenability factor (Πf_i)^{9,10)} measured from the following equation.

$$\begin{aligned} D_I/D_I^* = \Pi f_i = & (1 + 0.64\%Si) \times (1 + 4.10\%Mn) \times (1 + 2.83\%P) \times (1 - 0.62\%S) \\ & \times (1 + 2.33\%Cr) \times (1 + 0.52\%Ni) \times (1 + 3.14\%Mo) \times (1 + 0.27\%Cu) \\ & \times (1 + 1.5(0.9 - \%C)) \end{aligned} \quad (3-1)$$

where D_I and D_I^* are critical diameter and ideal critical diameter for hardenability,

Chapter 3. Effects of Microalloying on Retained Austenite Characteristics of TRIP-aided Martensitic Steel

respectively, and, %Si, %Mn, %P, %S, %Cr, %Ni, %Mo, %Cu and %C represent added content (in mass%) of individual alloying elements.

Table 3-1. Chemical composition (mass%), martensite-start and -finish temperatures (M_s , M_f , °C) and hardenability factors (Πf_i) of a steel used.

Steel	C	Si	Mn	P	S	Al	Nb
A	0.20	1.50	1.51	0.0030	0.0023	0.044	-
B	0.21	1.49	1.50	0.0019	0.0040	0.040	0.050
C	0.20	1.49	1.50	0.0019	0.0040	0.040	0.050
D	0.18	1.48	1.49	0.0029	0.0040	0.043	0.050
E	0.21	1.49	1.49	0.0019	0.0030	0.034	0.049

Steel	Cr	Mo	Ni	N	O	M_s	M_f	Πf_i
A	-	-	-	0.0013	0.0007	409	289	14.2
B	0.50	-	-	0.0012	0.0012	408	292	30.6
C	1.00	-	-	0.0012	0.0012	406	261	47.0
D	1.02	0.20	-	0.0010	0.0015	392	258	76.8
E	1.00	0.20	1.52	0.0014	0.0009	357	245	135.8

A hot-rolling process and heat-treatment schematic for the TM steel are presented in **Fig. 3-1**. To produce the TM steel, 13 mm diameter \times 10 mm long bars were annealed at 900°C for 1200 s in austenite region and then quenched in oil, followed by partitioning at $T_p = 200\text{--}500^\circ\text{C}$ for $t_p = 1000$ s in salt baths. The partitioning time corresponds to peak carbon concentration of retained austenite.⁷⁾

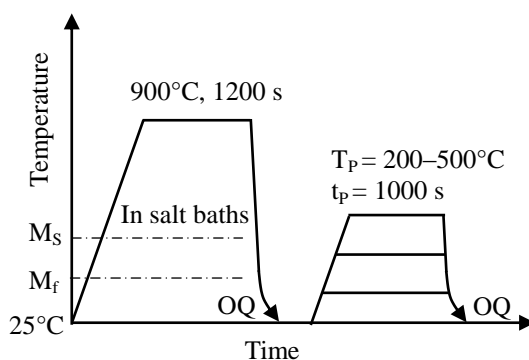


Fig. 3-1. Heat treatment diagram for TM steel, in which OQ resents quenching in oil.

The retained austenite characteristics of the TM steels were investigated by X-ray diffractometry (XRD; Rigaku Co., RINT2100). The specimen surfaces were electropolished after grinding with Emery paper (#1200). The volume fraction of retained austenite (f_γ , vol%) was quantified from the integrated intensity of the $(200)_\alpha$,

$(211)_\alpha$, $(200)_\gamma$, $(220)_\gamma$ and $(311)_\gamma$ peaks obtained by X-ray diffractometry using Mo-K α radiation.¹⁰⁾ The carbon concentration (C_γ , mass%) was estimated from the equation below. In this case, the lattice constant (a_γ , $\times 10^{-1}$ nm) was measured from the $(200)_\gamma$, $(220)_\gamma$ and $(311)_\gamma$ peaks with Cu-K α radiation.¹¹⁾

$$\begin{aligned}
 a_\gamma = & 3.5780 + 0.0330C_\gamma + 0.00095Mn_\gamma - 0.0002Ni_\gamma + 0.0006Cr_\gamma \\
 & + 0.0220N_\gamma + 0.0056Al_\gamma - 0.0004Co_\gamma + 0.0015Cu_\gamma + 0.0031Mo_\gamma \\
 & + 0.0051Nb_\gamma + 0.0039Ti_\gamma + 0.0018V_\gamma + 0.0018W_\gamma \quad (3-2)
 \end{aligned}$$

where Mn_γ , Ni_γ , Cr_γ , N_γ , Al_γ , Co_γ , Cu_γ , Mo_γ , Nb_γ , Ti_γ , V_γ and W_γ represent the concentrations of the respective individual elements (mass%) in the retained austenite. As an approximation, the contents of added alloying elements were substituted for these concentrations in this study.

The microstructures were observed by TEM (transmission electron microscopy), field-emission scanning electron microscopy (FE-SEM; Hitachi Co., S-4100) and FE-SEM electron backscatter diffraction pattern (FE-SEM-EBSP; JEOL Ltd., JSM-6500F) analysis. Specimens for FE-SEM were etched with 5% nital etchant. Specimens for FE-SEM-EBSP were finished with colloidal silica after polishing with γ -alumina particles.

Vickers hardness tests were carried out using a Vickers microhardness machine (Shimadzu Co., DUH-201H) at 25°C with a load of 0.98 N (HV0.1). The surface of the specimen was polished with Emery paper (#600).

3.3 Result

3.3.1 Vickers hardness

Figure 3-2 shows Vickers hardness ($HV0.1$) of steels A through E which are partitioned at $T_P = 200\text{--}500^\circ\text{C}$ for $t_P = 1000$ s. These TM steels possess Vickers hardness above 430HV in a partitioning temperature range between 20 and 400°C. By partitioning at 450 and 500°C the hardness rapidly decreases in all the steels. Cr, Mo and Ni additions increased hardness.

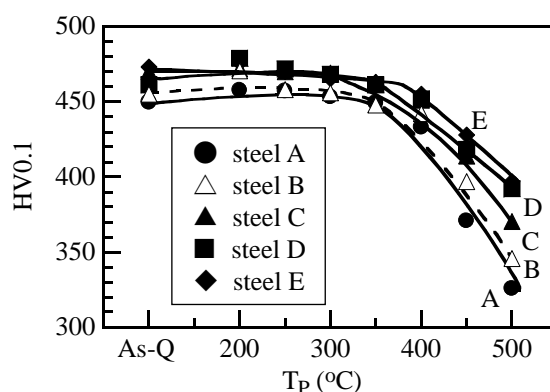


Fig. 3-2. Variations in Vickers hardness of steels A through E as a function of partitioning temperature (T_P). Partitioning time (t_P) = 1000 s.

3.3.2 Retained austenite characteristics

Figure 3-3 shows the variations in retained austenite volume fraction (f_{γ_0}), carbon concentration (C_{γ_0}) and total carbon concentration ($f_{\gamma_0} \times C_{\gamma_0}$) as a function of partitioning temperature (T_P) in steels A through E. The base steel (A) contains a maximum volume fraction of retained austenite of 3 vol%. The amount is decreased by partitioning at temperatures higher than 250°C. It is noteworthy that the maximum carbon concentration is obtained by partitioning at 300°C. Alloying element additions such as Cr, Mo and Ni change the retained austenite volume fraction, carbon concentration and total carbon concentration, as well as these partitioning temperature dependences.

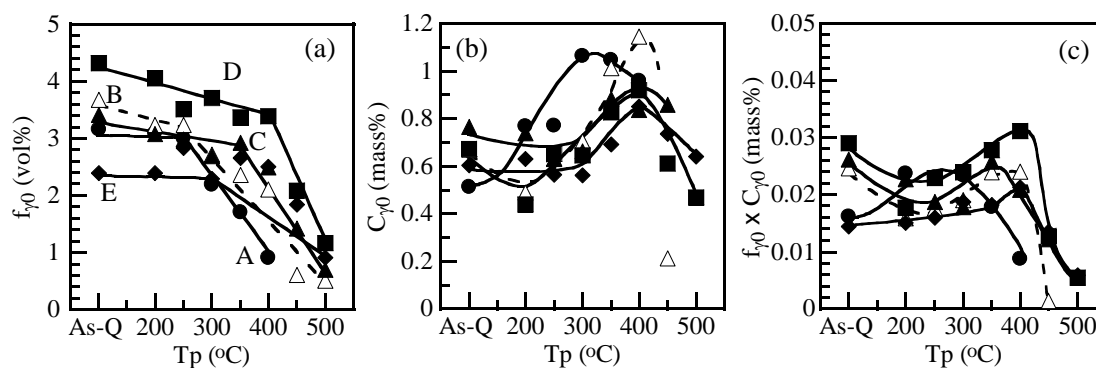


Fig. 3-3. Variations in (a) initial volume fraction (f_{γ_0}), (b) initial carbon concentration (C_{γ_0}) and (c) initial total carbon concentration ($f_{\gamma_0} \times C_{\gamma_0}$) of retained austenite as a function of partitioning temperature (T_P) in steels A (●), B (△), C (▲), D (■) and E (◆).

Figure 3-4 shows variations in retained austenite characteristics as a function of hardenability (Π_{f_i}) in steels A through E partitioned at 300 or 350°C. Addition of Cr and Mo (steels B, C and D) increases volume fraction and total carbon concentration of the

retained austenite and decreases the carbon concentration, particularly when partitioned at 300°C. On the contrary, further addition of Ni (steel E) decreases the volume fraction and total carbon concentration, while increasing the austenite carbon concentration.

Figure 3-5 shows that critical partitioning temperature (T_{CP}) above which volume fraction of retained austenite rapidly decreases varies with alloy element addition. The critical partitioning temperature increases with Cr and Mo additions. Ni does not seem to affect it.

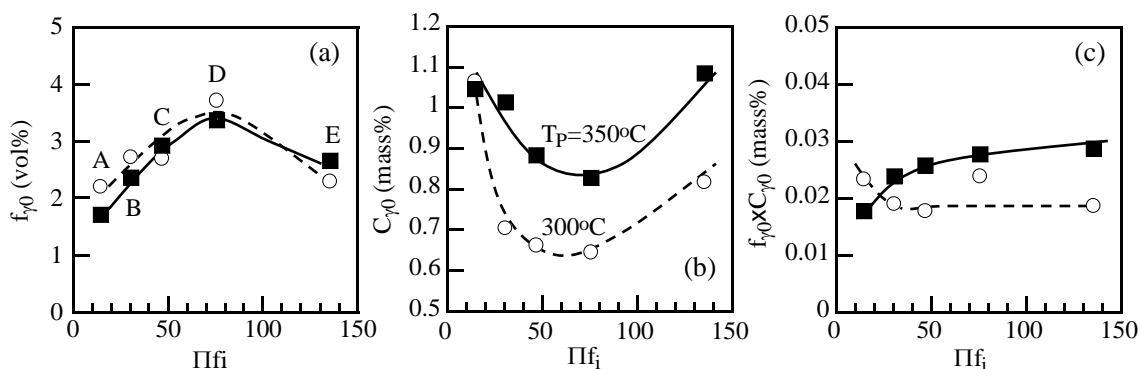


Fig. 3-4. Variations in (a) initial volume fraction ($f_{\gamma 0}$), (b) initial carbon concentration ($C_{\gamma 0}$) and (c) initial total carbon concentration ($f_{\gamma 0} \times C_{\gamma 0}$) of retained austenite with hardenability (Πf_i) in steels A through E at partitioned at $T_p = 300^\circ\text{C}$ (○) or 350°C (■).

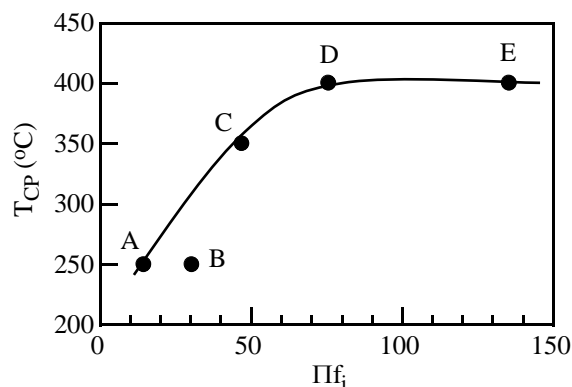


Fig. 3-5. Variation in critical partitioning temperature (T_{CP}) for volume fraction of retained austenite as a function of hardenability (Πf_i).

3.3.3 Microstructure and carbide

Figure 3-6 shows typical SEM images of steels A through E. Microstructures of all the steels consist of martensite lath structure matrix and retained austenite. As shown in **Fig. 3-7**, a large amount of fine, needle shaped cementite precipitates were evident only in the martensite lath structure, especially in larger lath structure. The cementite appears to coarsen with increasing partitioning temperature. Because cementite appears even in

Chapter 3. Effects of Microalloying on Retained Austenite Characteristics of TRIP-aided Martensitic Steel

as-quenched steel (Fig. 3-7(a)), the cementite may be precipitated by auto-tempering. The amount of the cementite precipitates seems to increase with increasing temperature in a partitioning range above 250°C. In a partitioning range above 450°C, the amount of cementite increases further, with spheroidized ones. Most of the retained austenite appears to occur as films between lath structures (Fig. 3-7(a)). Nb addition is found to refine the prior austenitic grain size.

Figure 3-8 shows TEM images of steels C, D and E subjected to partitioning at 400°C. If the cementite fraction was measured by extraction replica technique, the amount decreases in steels B through E, relative to steel A.

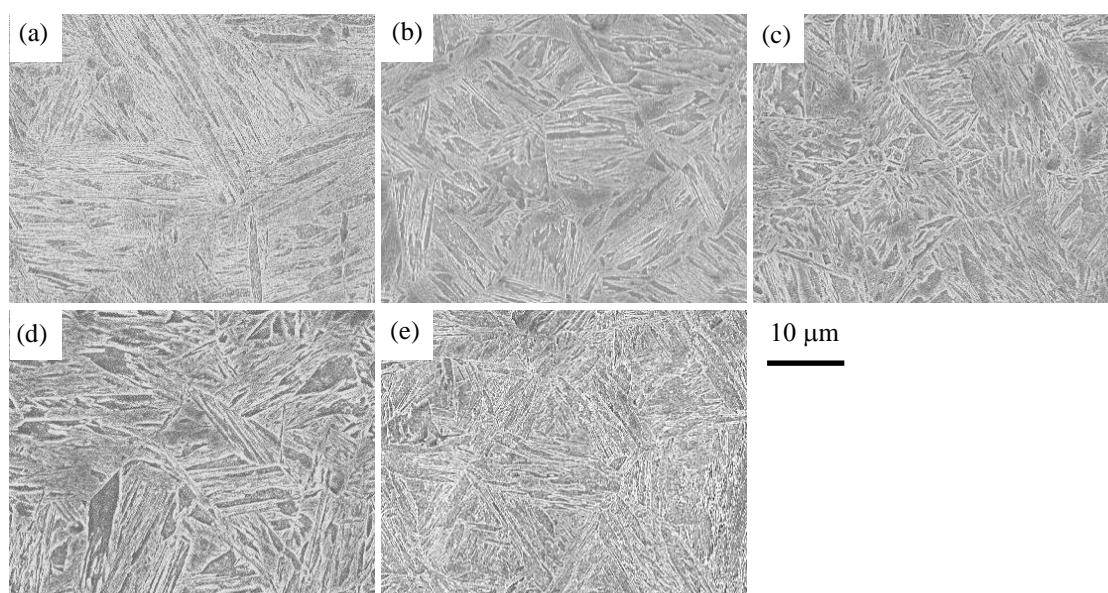


Fig. 3-6. Typical SEM images of steels (a) A, (b) B, (c) C, (d) D and (e) E subjected to partitioning at 200°C.

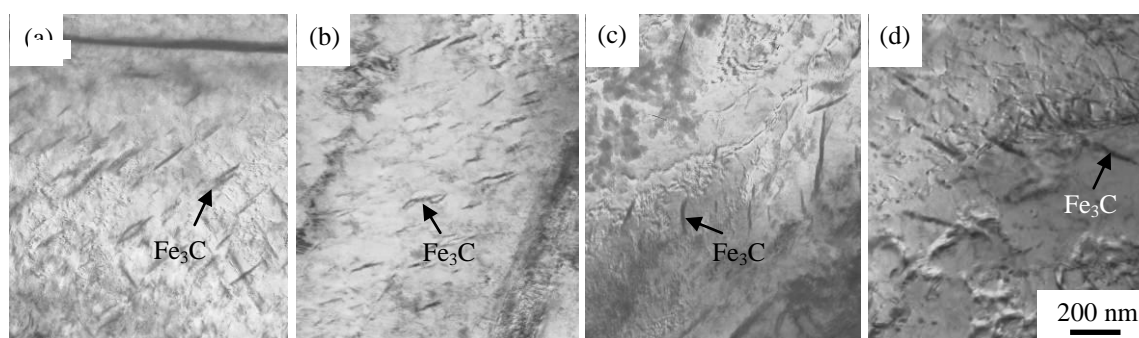


Fig. 3-7. TEM images of steel A subjected to partitioning at (a) 25°C (as-quenched), (b) 300°C, (c) 400°C or (d) 500°C. Cementite volume fractions measured by extraction replica technique are 2.1, 2.1, 4.3 and 5.2 vol% in (a), (b), (c) and (d), respectively.

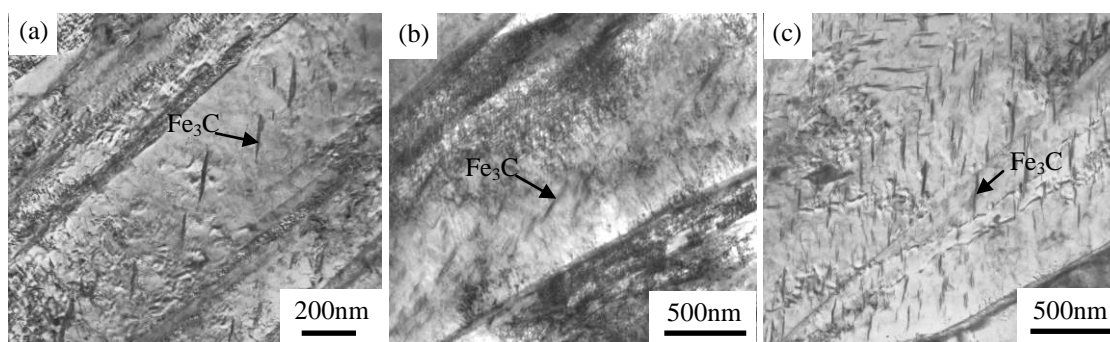


Fig. 3-8. TEM images of steels (a) C, (b) D and (c) E subjected to partitioning at 400°C.

3.4 Discussion

Effects of alloying elements on retained austenite characteristics

In this study, volume fraction and total carbon of retained austenite increased with increasing hardenability in a range of $\Pi f_i = 0-80$, which is associated with addition of Cr and Mo, not addition of Nb (Fig. 3-4). On the other hand, these values decreased at the factor of $\Pi f_i = 140$ or with Ni addition. Hardenability dependence of the carbon concentration exhibited the opposite tendency. From Fig. 3-8, volume fraction of cementite considerably increased in steel E. From these results, hardenability dependences of volume fractions of cementite and retained austenite characteristics may be illustrated as shown in **Fig. 3-9**.

In general, Cr, Mo and Ni enhance the hardenability of the steel. Therefore, it is expected that these elements suppress cementite precipitation on quenching just after austenitizing. This leads to an increase in solute carbon on quenching. Also, these elements suppress carbon diffusion in martensite, which suppresses the carbon enrichment and increases the volume fraction of retained austenite. Cr and Mo hardly influence to T_0 temperature where austenite and ferrite of the same chemical composition have identical free energies¹³⁾, different from Ni, as shown in **Fig. 3-10**. Thus, Cr and Mo increase volume fraction of retained austenite and decrease the carbon concentration through the suppressed diffusion of carbon.

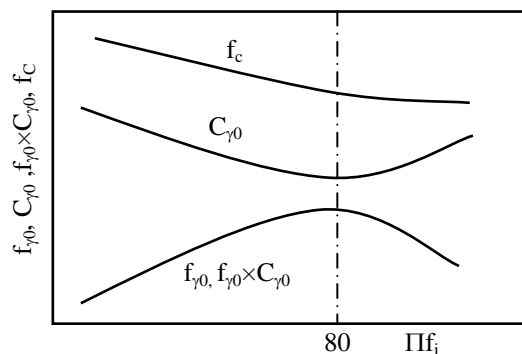


Fig. 3-9. Illustration of variations in volume fraction of cementite (f_c) and retained austenite characteristics (f_{γ_0} , C_{γ_0} , $f_{\gamma_0} \times C_{\gamma_0}$) with hardenability (Πf_i).

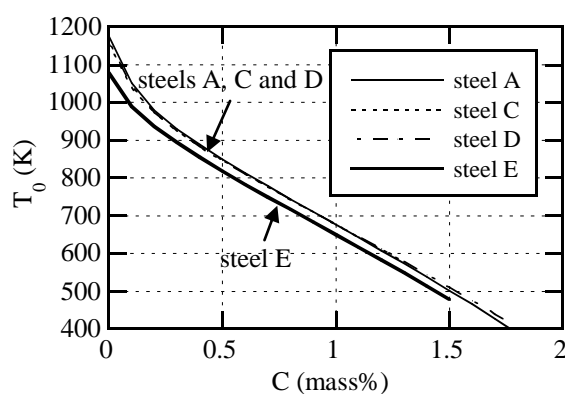


Fig. 3-10. T_0 temperatures of steels A, C, D and E which were calculated from Thermo-Calc.

3.5 Summary

The effects of partitioning after quenching in oil on microstructure and retained austenite characteristics of 0.2C-1.5Si-1.5Mn (in mass%) TM steel (base steel, A) were investigated. In addition, effects of alloying element additions to the base steel were examined.

- (1) Addition of Cr and Mo into the base steel raised upper limit partitioning temperature to 400°C, although carbon concentration of the retained austenite was decreased somewhat. Cr and Mo increase volume fraction of retained austenite and decrease the carbon concentration through the suppressed diffusion of carbon. If Cr and Mo add into the base steel, superior mechanical properties of TM steel can be expected.
- (2) Ni addition decreased volume fraction of retained austenite and increased the carbon concentration. This might be caused by the decrease of T_0 temperature through addition of Ni. Addition of Nb changed hardly retained austenite characteristics, although it played a role of refining the prior austenitic grain.

REFERENCES

- (1) B.C. De Cooman and J.G. Speer: Quench and Partitioning Steel: a New AHSS Concept for Automotive Anti-Intrusion Applications, *Steel Res. Int.*, **77** (2006), pp. 634–640.
- (2) K. Sugimoto, T. Iida, J. Sakaguchi and T. Kashima: Retained Austenite Characteristics and Tensile Properties in a TRIP Type Bainitic Sheet Steel, *ISIJ Int.*, **40** (2000), pp. 902–908.
- (3) K. Sugimoto, J. Sakaguchi, T. Iida and T. Kashima: Stretch-flangeability of a High-strength TRIP Type Bainitic Sheet Steel, *ISIJ Int.*, **40** (2000), pp. 920–926.
- (4) K. Sugimoto: Fracture strength and toughness of ultra high strength TRIP aided steels, *Mater. Sci. Technol.*, **25** (2009), pp. 1108–1117.
- (5) K. Sugimoto, M. Murata and S-M. Song: Formability of Al–Nb Bearing Ultra High-strength TRIP-aided Sheet Steels with Bainitic Ferrite and/or Martensite Matrix, *ISIJ Int.*, **50** (2010), pp. 162–168.
- (6) B.C. De Cooman: Structure-properties relationship in TRIP steels containing carbide-free bainite, *Current Opinion in Solid State Mater. Sci.*, **8** (2004), pp. 285–303.
- (7) J. Kobayashi and K. Sugimoto: Retained Austenite Characteristics of TRIP-aided Martensitic Steels, *CAMP-ISIJ*, **22** (2009), 635.
- (8) I. Tamura: *Steel Material Study on the Strength*, Nikkan Kogyo Shinbun Ltd., Tokyo, (1970), p. 40 (in Japanese).
- (9) M.A. Grossman: Hardenability Calculated from Chemical Composition, *Trans. Am. Inst. Min. Metall. Eng.*, **150** (1942), pp. 227–257.
- (10) J.H. Hollomon and L.D. Jaffe: The Hardenability Concept, *Trans. Am. Inst. Min. Metall. Eng.*, **167** (1946), pp. 601–616.
- (11) H. Maruyama: X-ray measuring method of retained austenite, *J. Jpn. Soc. Heat Treat.*, **17** (1977), pp. 198–204 (in Japanese).
- (12) D.J. Dyson and B. Holmes: Effect of Alloying Additions on the Lattice Parameter of Austenite, *J. Iron Steel Inst.*, **208** (1970), pp. 469–474.
- (13) M. Takahashi and H.K.D.H. Bhadeshia: A Model for the Microstructure of Some Advanced Bainitic Steels, *Mater. Trans. JIM*, **32** (1991), pp. 689–696.

Chapter 4. Effects of Partitioning and Isothermal Transformation Temperature on Tensile Properties and Formabilities of TRIP-aided Martensitic Steel

4.1 Introduction

According to Sugimoto et al.¹⁻³⁾, a Transformation-Induced Plasticity-aided sheet steel with a mixed structure matrix of bainitic ferrite and martensite lath structures (*TRIP-aided bainitic ferrite/martensite steel*; TBF steel) produced by austempering or isothermal transformation holding at temperatures between martensite-start (M_S) and martensite-finish temperature (M_f) possesses a good combination of tensile strength and stretch-flangeability due TRIP effect of metastable retained austenite to reduce the body weight of automobiles. In this case, the more stable the retained austenite films, the higher the combination because the retained austenite suppresses a void or crack formation on hole-punching and crack propagation on hole-expanding. An increase in volume fraction of the retained austenite also plays the same role as an increase in retained austenite stability. The resultant low damage on hole-punching and difficult crack propagation behavior lead to good stretch-flangeability.

If the steel was quenched to room temperature and then partitioned at 250°C, matrix structure changes to martensite single phase, as well as changes of retained austenite characteristics and carbide precipitation behavior, as reported by Sugimoto et al.⁴⁾ Also, such a steel or *TRIP-aided martensitic steel* (TM steel) was developed by Kobayashi et al.⁵⁾ by means of isothermal transformation holding at temperatures below M_f after austenitizing. These heat treatments closely resemble the quench and partitioning (Q&P) process described by De Cooman and Speer^{6,7)} and the austempering process described by Sugimoto et al. However, the steel described herein is very different from the TM steels that are produced by cooling to temperatures lower than the M_f temperature and holding at temperatures that are not between M_S and M_f or higher than M_S , and there is not any research which investigates the formability and a relationship between the formability and metallurgical properties in both TM steels.

In this section, stretch-flangeability of two kinds of TM steels was examined, as well as stretch-formability. In addition, the stretch-flangeability was related to metallurgical properties.

4.2 Experimental procedure

In this study, vacuum melted and hot-rolled sheet steel (3.2 mm thickness) with a chemical composition of **Table 4-1** was prepared. The CCT diagram is shown in **Fig. 4-1**, showing martensite-start temperature of about 420°C. After cold rolling to a thickness of 1.2 mm, tensile specimens of gauge length of 50 mm and gauge width of

Chapter 4. Effects of Partitioning and Isothermal Transformation Temperature on Tensile Properties and Formabilities of TRIP-aided Martensitic Steel

12.5 mm (JIS13B) and stretch-forming and hole-expanding specimens of 50 mm by 50 mm were machined. The specimens were subjected to isothermal transformation holding at $T_{IT} = 200\text{--}450^\circ\text{C}$ for 200 s after austenitizing at 900°C (IT process) or partitioning at $200\text{--}450^\circ\text{C}$ for 1000 s after quenching from 900°C (QP process), as shown in **Fig. 4-2**. The characteristics of the retained austenite in the steel were quantified by X-ray diffractometry (XRD; Rigaku Co., RINT2100). Specimens were electropolished after being ground with Emery paper (#2000). As described by Maruyama, the volume fraction of the retained austenite (f_γ , vol%) was calculated from the integrated intensity of the $(200)_\alpha$, $(211)_\alpha$, $(200)_\gamma$, $(220)_\gamma$, and $(311)_\gamma$ peaks resulting from X-ray diffractometry using Mo-K α radiation.⁸⁾ The carbon concentration (C_γ , mass%) was estimated by substituting the lattice constant (a_γ , 10^{-10} m) measured from the $(200)_\gamma$, $(220)_\gamma$ and $(311)_\gamma$ peaks of Cu-K α radiation into the equation proposed by Dyson and Holmes.⁹⁾

$$a_\gamma = 3.5780 + 0.0330C_\gamma + 0.00095Mn_\gamma + 0.0056Al_\gamma + 0.0220N_\gamma, \quad (4-1)$$

where Mn_γ , Al_γ , and N_γ represent the concentrations of the respective individual elements (mass%) in the retained austenite. For convenience, the contents of added alloying elements were substituted for these concentrations in this study.

Table 4-1. Chemical composition (mass%) of a steel used.

C	Si	Mn	P	S	Al	Nb	N
0.21	1.50	1.50	0.015	0.0023	0.042	0.05	0.0012

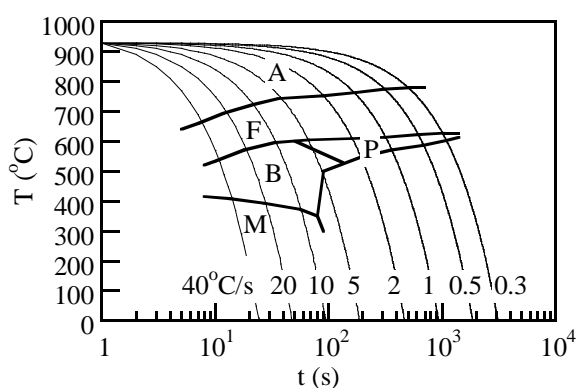


Fig. 4-1. Measured CCT diagram of steel used, in which A, F, P, B and M represent austenite, ferrite, pearlite, bainite and martensite, respectively.

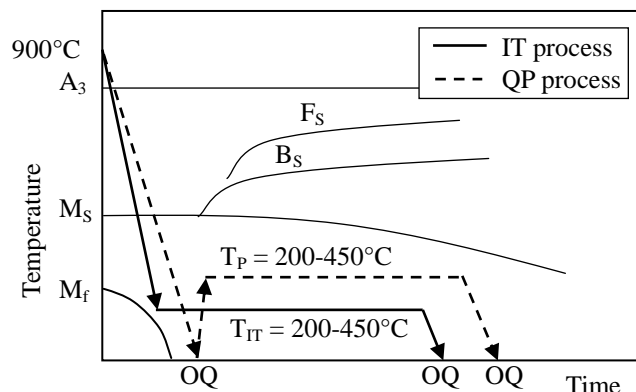


Fig. 4-2. Heat treatment diagrams of IT and QP process, in which F_s , B_s and OQ represent ferrite-start temperature, bainite-start temperature and quenching in oil.

According to a previous study by Sugimoto et al.¹⁾, retained austenite stability against straining of TRIP-aided steel can be evaluated by “*strain-induced transformation factor; k*” defined by the following equation, rather than the carbon concentration, if retained austenite morphology changes so much.

$$\log f_{\gamma} = \log f_{\gamma 0} - k \varepsilon_p, \quad (4-2)$$

where f_{γ} is a volume fraction of retained austenite after strained by plastic strain ε_p and $f_{\gamma 0}$ is an initial volume fraction of retained austenite.¹⁻³⁾

The microstructure of the steel was examined by transmission electron microscopy (TEM; JEOL Ltd., JEM-2010) and electron backscatter diffraction pattern analysis using field emission scanning electron microscopy (FE-SEM; Hitachi Co., S-4100 and FE-SEM-EBSP; JEOL Ltd., JSM-6500F). The volume fraction of carbide was measured using carbon extraction replicas.

Tensile tests were carried out on a hard type of testing machine (Shimadzu Co., AD-10TD, **Fig. 4-3(b)**). The strain rate was $3.3 \times 10^{-3} \text{ s}^{-1}$. The hole-punching and hole-expanding tests were conducted with a graphite-type lubricant. First, a hole with 4.76 mm diameter was punched out at a punching rate of 10 mm/min, with a clearance of 10% between the die and the punch (**Fig. 4-4**). The successive hole-expansion tests were performed at a punching rate of 1 mm/min using the hole-expanding die and the flat-bottom cylindrical punch (**Figs. 4-5(a)** and **4-5(b)**). In the expansion tests, the punch made contact with the roll-over section of the hole-punched specimens. The hole-expansion ratio (λ) was determined by the following equation:

$$\lambda = \{(d_f - d_0)/d_0\} \times 100\%, \quad (4-3)$$

Chapter 4. Effects of Partitioning and Isothermal Transformation Temperature on Tensile Properties and Formabilities of TRIP-aided Martensitic Steel

where d_0 and d_f are the initial hole diameter and the hole diameter on cracking, respectively. Stretch-forming tests were also performed using the same specimens as used for the stretch-flanging tests, to measure the maximum stretch height H_{max} without cracking. The punching rate was 1 mm/min. The stretch-forming die and a cylindrical punch with a diameter of 17.4 mm and a curvature radius of 8.7 mm was used (Figs. 4-5(c) and 4-5(d)).²⁾

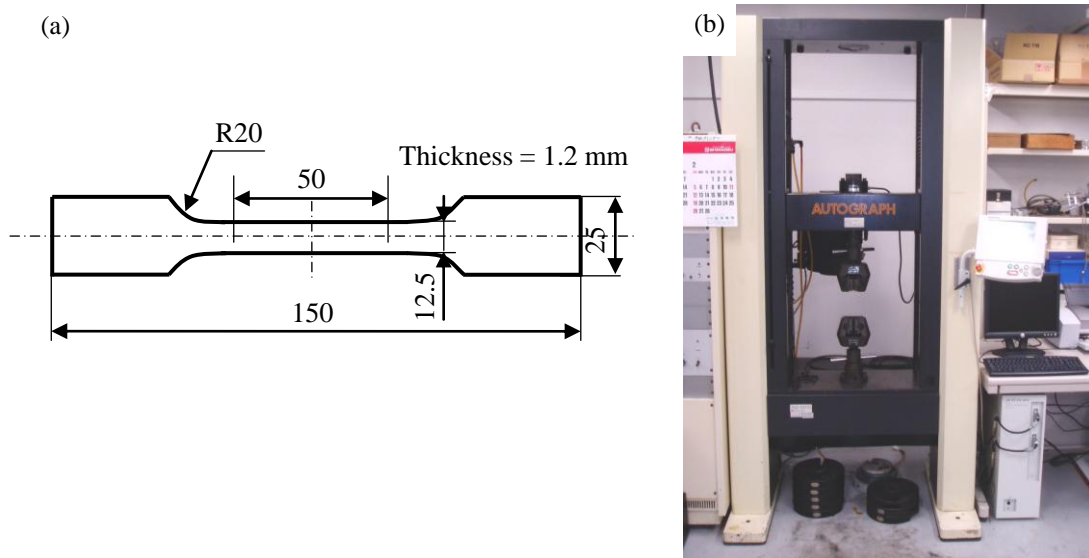


Fig. 4-3. (a) Illustration of tensile specimen and (b) image of a hard type of testing machine (Shimadzu Co., AD-10TD).

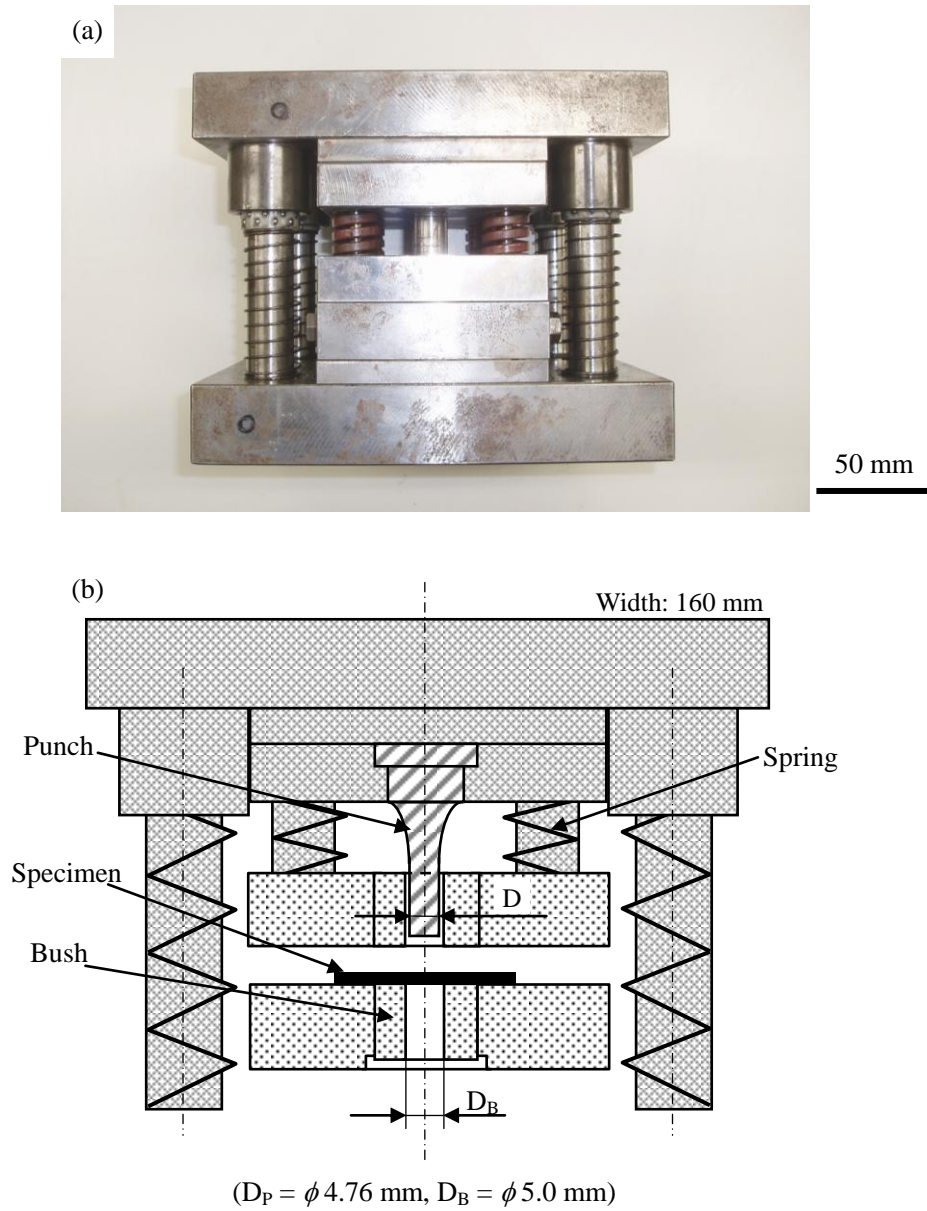


Fig. 4-4. (a) Image of a hole-punching die and (b) illustration of the hole-punching system.

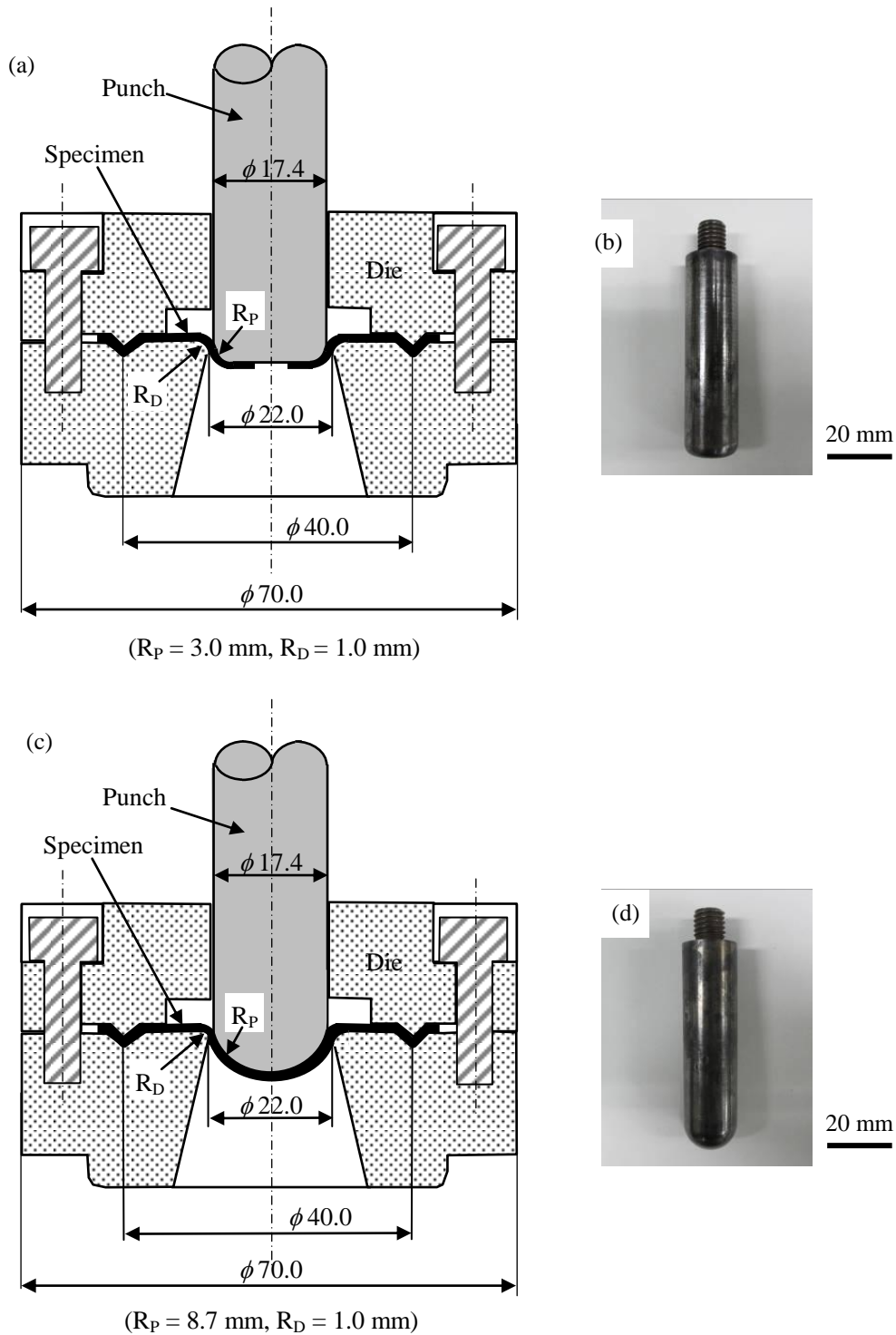


Fig. 4-5. Illustrations of (a) hole-expanding and (c) stretch-forming systems. (b) and (d) show flat-bottom and hemispherical-bottom cylindrical punches, respectively.

4.3 Results

4.3.1 Microstructure

Typical microstructures of IT and QP process steels are shown in **Fig. 4-6**. Both steels apparently exhibit the same microstructure. The matrix structure consists of wide and narrow martensite lath structures.

Carbides precipitate only in the wider martensite lath structure (**Fig. 4-7**). The volume fraction of carbide in IT process is 0.47 vol% and is smaller than that (1.08 vol%) of QP process steel when the steel was isothermally held at 200°C after austenitizing. However, these carbide amounts are so much smaller than that of SCM420 steel, which was reported by Sugimoto et al.⁴⁾ According to De Cooman et al.¹⁰⁾, the carbides are transition carbides or cementites. On the other hand, most of retained austenite phases are surrounded by or adjacent to the fine martensite lath structure.

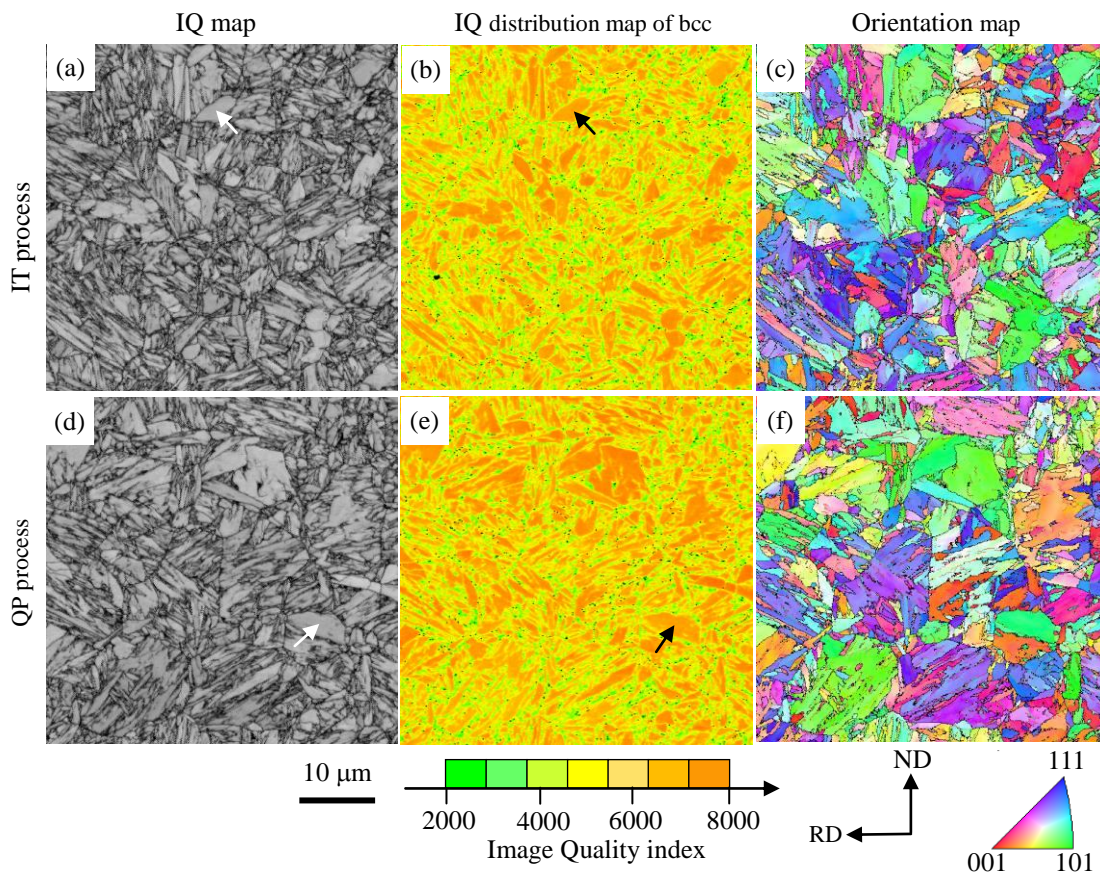


Fig. 4-6. EBSD analysis results of steels subjected to isothermal transformation holding (IT process) or partitioning (QP process) at 200°C. Arrows represent wider martensite lath structure.

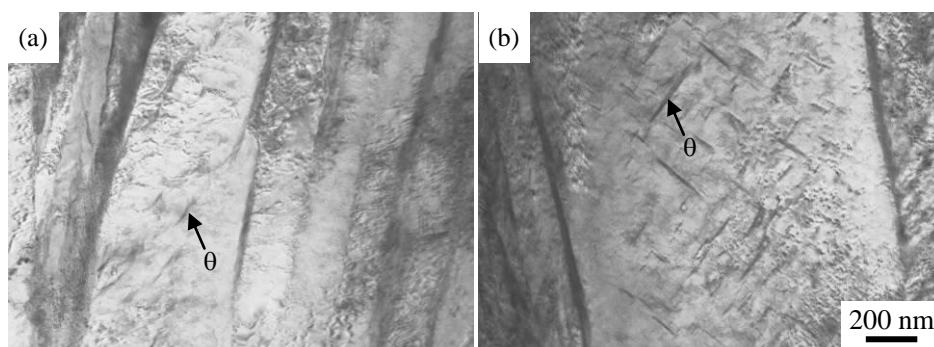


Fig. 4-7. TEM images of steels subjected to (a) isothermal transformation holding (IT process) or (b) partitioning (QP process) at 200°C, in which θ is cementite or transition carbide. Volume fraction of carbide in IT and QP process steels are $f_{\theta} = 0.47$ and 1.08 vol%, respectively.

4.3.2 Retained austenite characteristics

Volume fraction and carbon concentration of retained austenite of IT and QP process steels are shown in **Fig. 4-8**. A larger amount of retained austenite was observed in IT process steels, although the carbon concentration was lower than that of QP process steel. The carbon concentration of IT process steel is significantly low at isothermal transformation temperatures below 250°C. According to Kobayashi et al.⁵⁾, if the IT process steel isothermally held at 200°C after austenitizing was subjected to partitioning at 250–450°C (called ITP process), the carbon concentration of retained austenite increases, in the same way as QP process steel. It is noteworthy in the QP process steel that the volume fraction of retained austenite gradually decreased with increasing partitioning temperature in a temperature range higher than 300°C.

The k value shows opposite tendency carbon concentration of retained austenite (**Fig. 4-9**). Namely, k values of IT process steel are higher than that of QP process steel. It is noteworthy that k value of IT process steel are considerably low when isothermally held at 350–450°C.

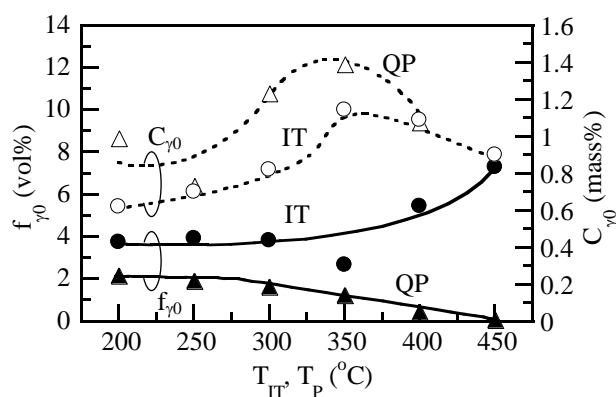


Fig. 4-8. Variations in initial volume fraction (f_{γ_0}) and carbon concentration (C_{γ_0}) of retained austenite as a function of isothermal transformation or partitioning temperature (T_{IT} , T_P) in IT and QP process steels.

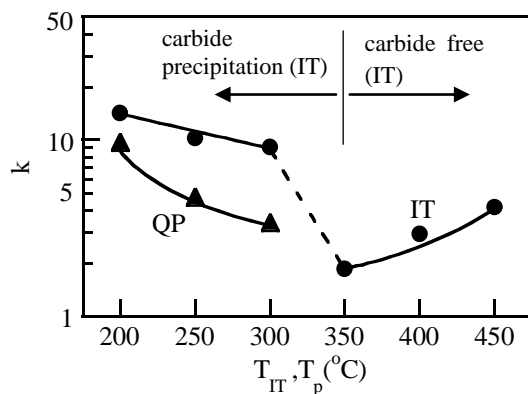


Fig. 4-9. Variations in k values as a function of isothermal transformation or partitioning temperature (T_{IT} , T_P) in IT and QP process steels.

4.3.3 Tensile properties

Tensile properties of IT and QP process steels are shown in **Fig. 4-10**. The IT process steel exhibits lower tensile strength and yield stress than QP process steel. Since the yield stress is considerably lowered by IT process, IT process steel possesses lower yield ratio.

In contrast, uniform and total elongations are increased by IT process. When a combination of tensile strength and total elongation of IT process steel was compared with that of QP process steel, the IT process steel exhibits better combination than QP process steel.

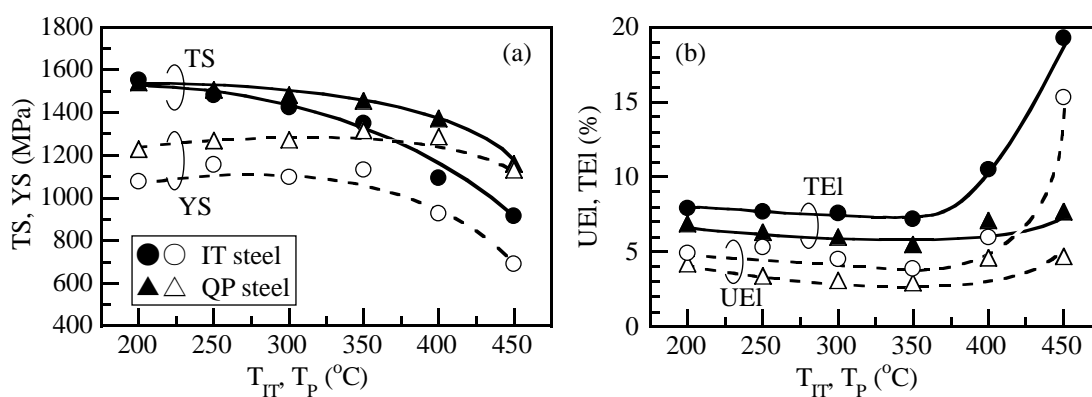


Fig. 4-10. Variations in (a) tensile strength (TS) and yield stress or 0.2% offset proof stress (YS) and (b) total elongation (TEI) and uniform elongation (UEI) as a function of isothermal transformation or partitioning temperature (T_{IT} , T_P) in IT and QP process steels.

4.3.4 Formabilities

Figure 4-11 shows maximum stretch-height and hole-expanding ratio as a function

Chapter 4. Effects of Partitioning and Isothermal Transformation Temperature on Tensile Properties and Formabilities of TRIP-aided Martensitic Steel

of isothermal transformation or partitioning temperature in steels subjected to IT or QP process. The IT process steel possesses higher maximum stretch-height and hole-expanding ratio than QP process steel, although these values of both steels increase with increasing isothermal transformation and partitioning temperatures.

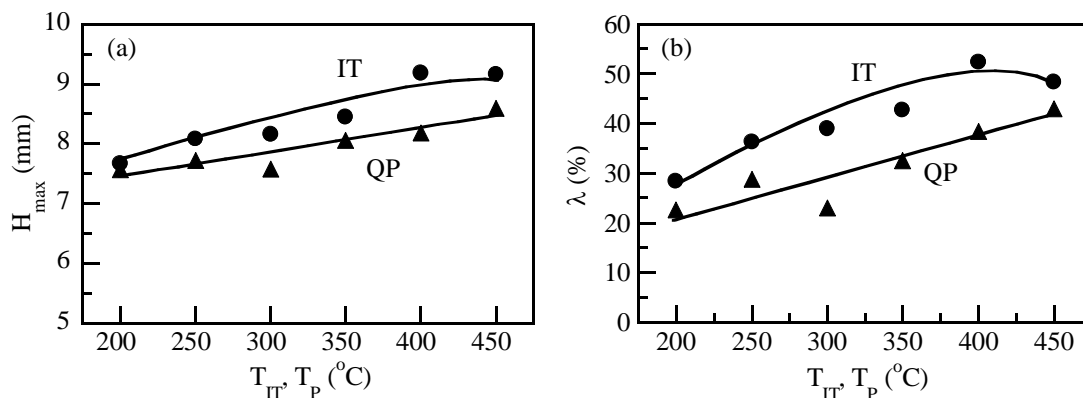


Fig. 4-11. Variations in (a) maximum stretch-height (H_{max}) and (b) hole-expanding ratio (λ) as a function of isothermal transformation or partitioning temperature (T_{IT} , T_P) in IT and QP process steels.

Figure 4-12 compares maximum stretch-height and hole-expanding ratio of IT and QP process steels and ferrite- martensite dual-phase steel as a function of tensile strength.

IT process steel exhibits higher combinations of tensile strength and stretch-flangeability than QP process steel and dual-phase steel. According to Kobayashi et al.⁵⁾, when the IT process steel was partitioned at 250–450°C, both the stretch formability and stretch-flangeability are further improved.

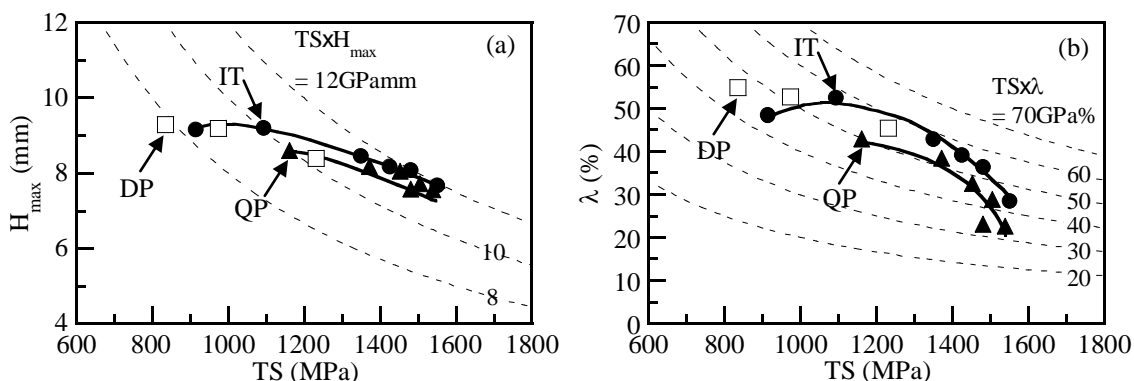


Fig. 4-12. Variations in combinations of (a) tensile strength and maximum stretch-height ($TS \times H_{max}$) and (b) tensile strength and hole-expanding ratio ($TS \times \lambda$) in IT and QP process steels. DP: 0.082%C-0.88%Si-2.0%Mn (in mass%) ferrite-martensite dual-phase steel with different volume fraction of second phase.

Figure 4-13 shows appearance of steels after stretch-forming or stretch-flanging tests. **Figure 4-14** shows SEM images of break section of punched hole in IT and QP process steels. It is found that punching damage such as void or crack in IT process steel is smaller than that in QP process steel (Fig. 4-14). In addition, IT process steel is characterized by longer shearing section than QP process steel, as shown in **Fig. 4-15**. These results indicate that IT process suppresses punching damage for the TM steel, compared with QP process. It is very important that isothermal transformation temperature dependence of shear section length resembles to that of hole-expanding ratio.

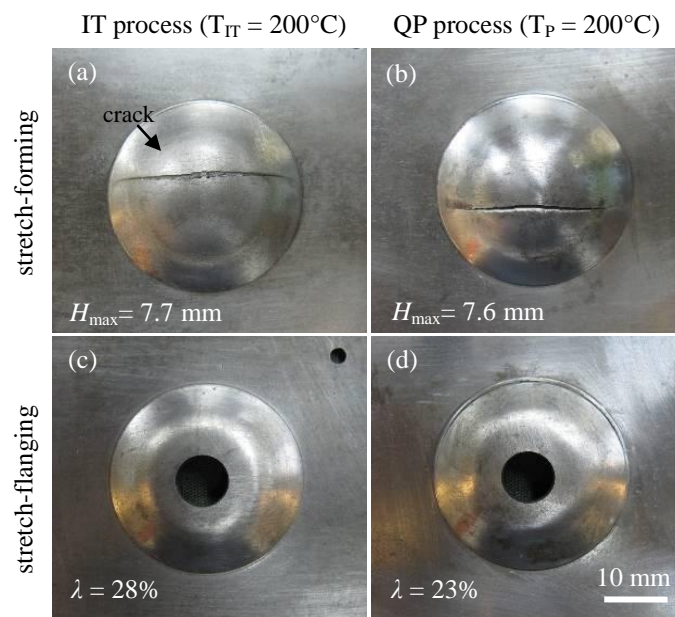


Fig. 4-13. Appearance of IT and QP process steels subjected to stretch-forming or stretch-flanging. ($T_{IT} = T_P = 200^{\circ}\text{C}$)

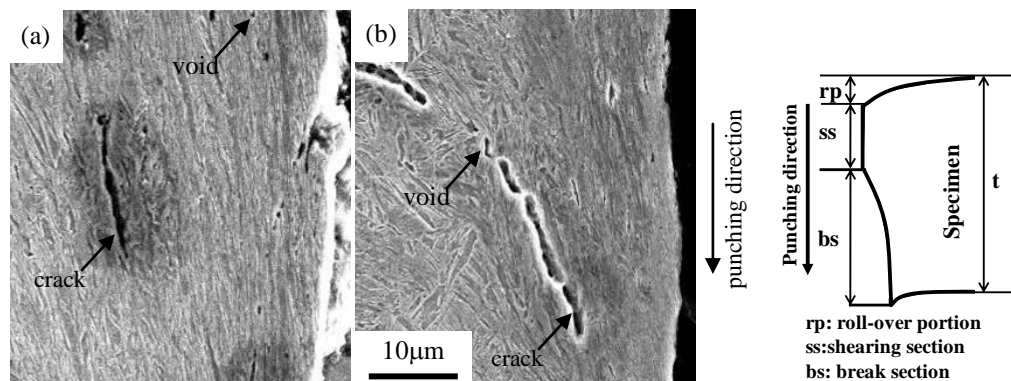


Fig. 4-14. Scanning electron micrographs of break section of punched hole surface in (a) IT and (b) QP process steels isothermally held and partitioned at 200°C , respectively.

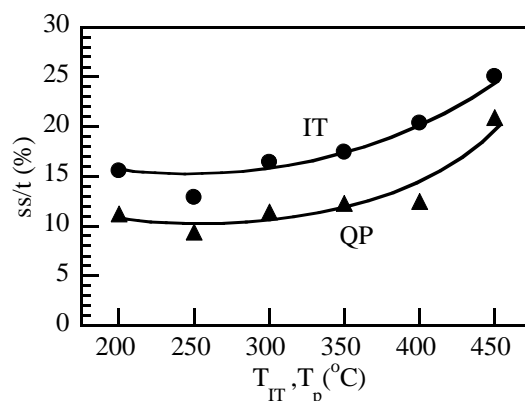


Fig. 4-15. Variations in ratio of shearing section length (ss) to sheet thickness (t) as a function of isothermal transformation (T_{IT}) or partitioning temperature (T_P) of steels.

4.4 Discussion

4.4.1 Carbon-enrichment mechanism of TM steel subjected to isothermal transformation process at 200–250°C.

According to Sugimoto et al.²⁾, Si addition of 1.5 mass% promotes carbon enrichment in retained austenite and an increase in the volume fraction in TM steel due to suppressing the carbide precipitation. They proposed that when QP process steel was subjected to partitioning at 25–250°C after quenching in oil, volume fraction of carbide and retained austenite characteristics vary during partitioning as illustrated in **Fig. 4-16**.

Namely, first auto-tempering on quenching takes place on during quenching or martensitic transformation, particularly in the wider martensite lath structure (stage 1–2 in Fig. 4-16(b)). Simultaneously, some of supersaturated solute carbon in martensite is enriched in retained austenite to about 0.4 mass% through carbon diffusion from the wider martensite. Next, when the quenched steel is partitioned at temperatures higher than 250°C, carbon concentration of retained austenite considerably increases with increasing partitioning time (stage 2–3), because supersaturated carbon in narrow martensite may diffuses into retained austenite, with decrease in volume fractions of retained austenite and increase in carbide fraction.

It is supposed that a similar microstructural change takes place in IT process steel, with different volume fractions of retained austenite and carbide, because both steels possessed the similar microstructure (Fig. 4-6). The high volume fraction of retained austenite and low volume fraction of carbide of IT process steel may be associated with (i) incomplete martensite transformation and (ii) delayed carbon-enrichment in retained austenite from transformed martensite during isothermal transformation holding.

When IT process steel was held at 200–300°C, the mechanical stability was lower than that of QP process steel (Fig. 4-9). This result may be caused by lower carbon concentration of retained austenite because size and location of the retained austenite

are nearly the same in both steels.

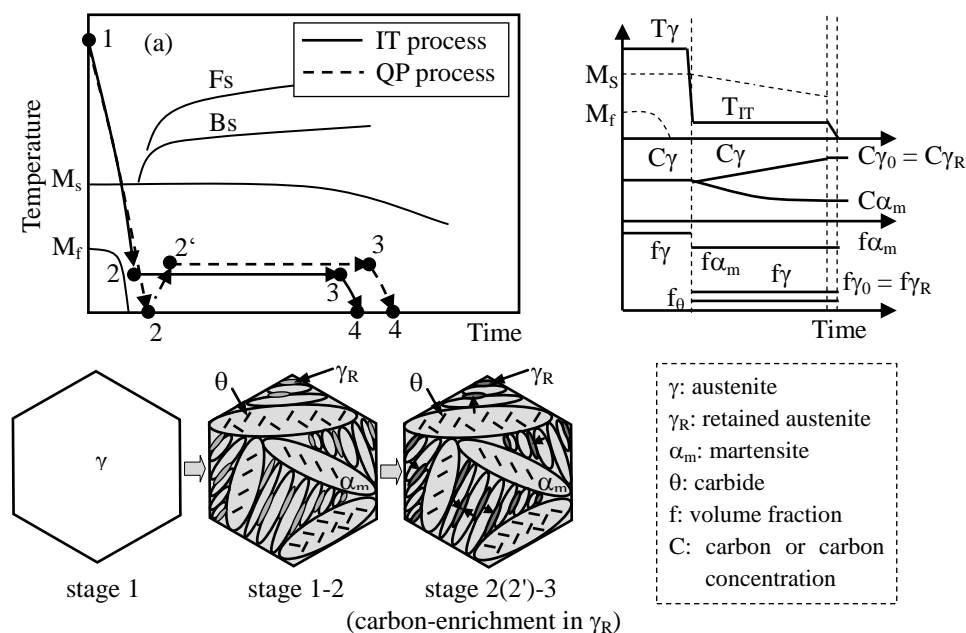


Fig. 4-16. Illustration of (a) heat treatment diagram, (b) microstructural change at stages 1 through 3 and (c) change in carbon concentrations (C_γ , $C_\gamma = C_{\gamma_R}$ and C_{α_m}) and volume fractions (f_γ , $f_\gamma = f_{\gamma_R}$, f_θ and f_{α_m}) of each phase during isothermal transformation holding at 200°C in IT process steel. (b) is also applied to QP process steel.

4.4.2 Excellent stretch-flangeability

Sugimoto et al.^{2,3)} have reported that stretch-flangeability of TBF steel is controlled by (i) volume fraction and stability of retained austenite and uniformity and (ii) size of matrix microstructure which influence both hole-surface layer damage on punching and localized ductility on expanding. The present IT process steel also exhibited an excellent stretch-flangeability, when isothermally held at temperatures below M_f (Fig. 4-11(b)), despite high tensile strength of about 1.5GPa.

As shown in Figs. 4-14 and 4-15, IT process steel was characterized by a small damage of punched hole-surface, or a small amount of void and long shear section. This may lead to higher stretch-flangeability in IT process steel, as well as a larger amount of retained austenite which contributes to a large strain on stretch-flanging. Also, the small punching damage may be associated with uniform and fine lath martensite matrix structure and a smaller amount of carbide, reducing localized stress concentration.

In Fig. 4-9, IT process steel exhibited higher k value or lower mechanical stability of retained austenite than QP process steel. Because the stretch-flangeability was better than that of QP process steel, the mechanical stability of retained austenite is expected to hardly influence the stretch-flangeability in this study.

According to Kobayashi et al.⁵⁾, partitioning at 250–350°C after isothermal transformation at 200°C improves retained austenite characteristics and a combination of tensile strength and stretch flangeability. This result will be reported in chapter 5.

4.5 Summary

Stretch-flangeability of TM steel subjected to IT process was compared with that of previously developed TM steel subjected to QP process. In addition, the stretch-flangeability was related to some metallurgical properties. Main results are summarized as follows,

- (1) Microstructure of the TM steel subjected to IT process at 200–250°C below M_f consisted of wide and narrow martensite lath structures and interlath retained austenite surrounded by narrow martensite lath structure, similar to the steel subjected to QP process. A small amount of carbide precipitated only in wider martensite lath structure of both the steels although the carbide fraction was smaller than that of QP process. It is noteworthy that the volume fraction of retained austenite of IT process steel was higher than that of QP process steel, with lower carbon concentration of retained austenite. This is expected to be associated with incomplete martensite transformation and delayed carbon enrichment in retained austenite during isothermal transformation holding.
- (2) When isothermally transformed at temperatures below M_f , the IT process steel possessed tensile strength of 1.5 GPa and total elongation of 8%. The hole-expanding ratio ($\lambda = 30\text{--}50\%$) was higher than that of QP process steel. Resultantly the IT process steel possessed a superior combination of tensile strength and stretch-flangeability. It is considered that the excellent combination of IT process steel is mainly caused by uniform and fine martensite lath structure matrix and a smaller amount of carbides which suppress the damage on punching and cracking on hole-expanding, as well as metastable retained austenite.

REFERENCES

- (1) K. Sugimoto, T. Iida, J. Sakaguchi and T. Kashima: Retained Austenite Characteristics and Tensile Properties in a TRIP Type Bainitic Sheet Steel, *ISIJ Int.*, **40** (2000), pp. 902–908.
- (2) K. Sugimoto, J. Sakaguchi, T. Iida and T. Kashima: Stretch-flangeability of a High-strength TRIP Type Bainitic Sheet Steel, *ISIJ Int.*, **40** (2000), pp. 920–926.
- (3) K. Sugimoto, M. Murata and S-M. Song: Formability of Al–Nb Bearing Ultra High-strength TRIP-aided Sheet Steels with Bainitic Ferrite and/or Martensite Matrix, *ISIJ Int.*, **50** (2010), pp. 162–168.
- (4) K. Sugimoto and J. Kobayashi: Newly developed TRIP-aided martensitic steels, Materials Science & Technology 2010 Conference & Exhibition (Recent Developments in Steel Processing) October 17-21, 2010, Houston, Texas, pp. 1639–1649.
- (5) D.V. Pham, J. Kobayashi and K. Sugimoto: Effects of Microalloying on Stretch-flangeability of TRIP-aided Martensitic Sheet Steel, *Tetsu-to-Hagane*, **99** (2013), pp. 659–668.
- (6) J.G. Speer, D.V. Edmonds, F.C. Rizzo and D.K. Matlock: Partitioning of carbon from supersaturated plates of ferrite, with application to steel processing and fundamentals of the bainite transformation, *Solid State Mater. Sci.*, **8** (2004), pp. 219–237.
- (7) B.C. De Cooman and J.G. Speer: Quench and Partitioning Steel: A New AHSS Concept for Automotive Anti-Intrusion Applications, *Steel Research Int.*, **77** (2006), pp. 634–640.
- (8) H. Maruyama: X-ray measuring method of retained austenite, *J. Jpn. Soc. Heat Treat.*, **17** (1977), pp. 198–204 (in Japanese).
- (9) D.J. Dyson and B. Holmes: Effect of Alloying Additions on the Lattice Parameter of Austenite, *J. Iron Steel Inst.*, **208** (1970), pp. 469–474.
- (10) B.C. De Cooman: Structure-properties relationship in TRIP steels containing carbide-free bainite, *Current Opinion in Solid State Mater. Sci.*, **8** (2004), pp. 285–303.

Chapter 5. Effects of Partitioning Temperature after Isothermal Transformation Process on Stretch-flangeability and Bendability of a 0.2C-1.5Si-1.5Mn-0.05Nb Ultrahigh-strength TRIP-aided Martensitic Sheet Steel

5.1 Introduction

To reduce the body weight of automobiles, an ultrahigh-strength transformation-induced-plasticity (TRIP)-aided sheet steel with two kinds of lath martensite structure matrices and metastable retained austenite, also called TRIP-aided martensitic or TM steel, has been developed in terms of quenching or isothermal transformation process after austenitizing.¹⁻³⁾ These heat treatments closely resemble the quench and partitioning (Q&P) process described by De Cooman and Speer^{4,5)} and the austempering process described by Sugimoto et al.^{6,7)} However, the steel described herein is very different from the TM steels that are produced by cooling to temperatures lower than the M_f temperature and holding at temperatures that are not between M_S and M_f or higher than M_S .

According to a previous study, high tensile strength and stretch flangeability in 0.2%C-1.5%Si-1.5%Mn-0.05%Nb (in mass%) TM steel is achieved by an isothermal transformation (IT) process after austenitizing, a different from the quenching process.³⁾ Metastable retained austenite phases suppress void or crack formation on hole-punching and crack propagation on hole-expansion. The small degree of damage on hole-punching and the reduction in crack propagation lead to good formability.

Recently, Sugimoto and Kobayashi reported that partitioning after the IT process promotes carbon enrichment of the retained austenite.²⁾ Thus, partitioning is expected to improve the formability of TM steel through the stabilization of the retained austenite or an increased TRIP effect.

In this section, in order to further improve the formability of TM steel, the effects of partitioning after the IT process (ITP process) on the formability were investigated. Also, the formability was compared with that of TM steel subjected to partitioning after the quenching process.

5.2 Experimental procedure

Vacuum melted and hot-rolled sheet steel (3.2 mm in thickness) with the chemical composition listed in **Table 5-1** was used in this study. The continuous cooling transformation (CCT) diagram in **Fig. 5-1** shows the martensite-start temperature of about 420°C. After cold rolling to a thickness of 1.2 mm, tensile, stretch-forming and hole-expansion, and bending specimens with a gauge length and gauge width of 50 mm and 12.5 mm, 50 mm and 50 mm, and 70 mm and 40 mm, respectively, were machined.

The specimens were heat-treated for the ITP process, as shown in **Fig. 5-2**. The partitioning temperatures were between 200 and 450°C for the ITP process. For comparison, heat treatment for the QP process was also done.

The characteristics of the retained austenite in the steel were quantified by X-ray diffractometry (XRD; Rigaku Co., RINT2100). Specimens were electropolished after being ground with Emery paper (#2000). As described by Maruyama, the volume fraction of the retained austenite (f_γ , vol%) was calculated from the integrated intensity of the $(200)_\alpha$, $(211)_\alpha$, $(200)_\gamma$, $(220)_\gamma$, and $(311)_\gamma$ peaks resulting from X-ray diffractometry using Mo-K α radiation.⁸⁾ The carbon concentration (C_γ , mass%) was estimated by substituting the lattice constant (a_γ , $\times 10^{-1}$ nm) measured from the $(200)_\gamma$, $(220)_\gamma$ and $(311)_\gamma$ peaks of Cu-K α radiation into the equation proposed by Dyson and Holmes.⁹⁾

$$a_\gamma = 3.5780 + 0.0330C_\gamma + 0.00095Mn_\gamma + 0.0056Al_\gamma + 0.0220N_\gamma, \quad (5-1)$$

where Mn_γ , Al_γ , and N_γ represent the concentrations of the respective individual elements (mass%) in the retained austenite. For convenience, the contents of added alloying elements were substituted for these concentrations in this study.

Table 5-1. Chemical composition (mass%) of a steel used.

C	Si	Mn	P	S	Al	Nb	N
0.21	1.50	1.50	0.015	0.0023	0.042	0.050	0.0012

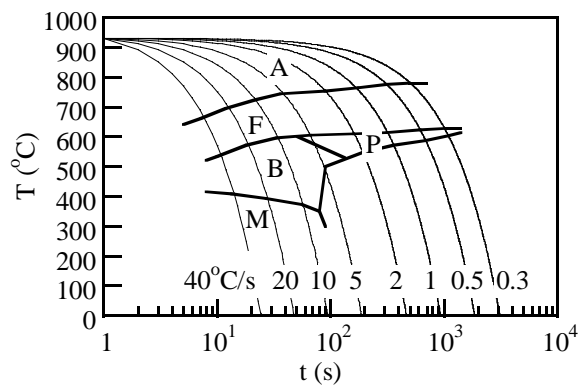


Fig. 5-1. Measured CCT diagram of steel used, in which A, F, P, B and M represent austenite, ferrite, pearlite, bainite and martensite, respectively.

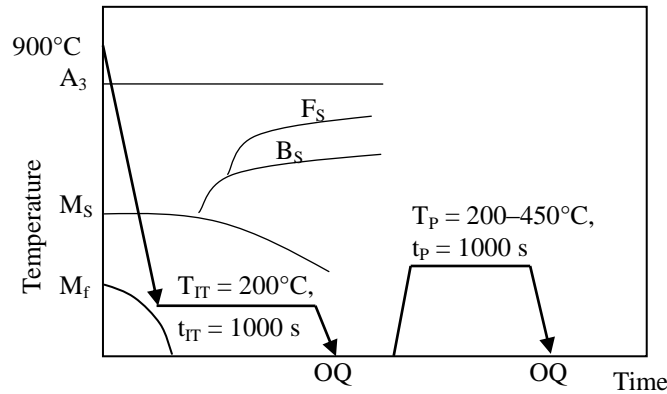


Fig. 5-2. Heat treatment diagram of ITP process, in which F_s, B_s and OQ represent ferrite-start temperature, bainite-start temperature and quenching in oil.

The stability of the retained austenite against the strain-induced martensite transformation or k value was defined by the following equation:

$$\log f_{\gamma} = \log f_{\gamma 0} - k \varepsilon_P, \quad (5-2)$$

where f_{γ} is a volume fraction of retained austenite after strained by plastic strain ε and $f_{\gamma 0}$ is an initial volume fraction of retained austenite.^{6,7)}

The microstructure of the steel was examined by transmission electron microscopy (TEM; JEOL Ltd., JEM-2010) and electron backscatter diffraction pattern analysis using field emission scanning electron microscopy (FE-SEM; Hitachi Co., S-4100 and FE-SEM-EBSP; JEOL Ltd., JSM-6500F). The volume fraction of carbide was measured using carbon extraction replicas.

Tensile tests were carried out on a hard type of testing machine (as shown in Fig. 4-3 in Chapter 4.). The strain rate was $3.3 \times 10^{-3} \text{ s}^{-1}$. The hole-punching and hole-expanding tests were conducted with a graphite-type lubricant. First, a hole with 4.76 mm diameter was punched out at a punching rate of 10 mm/min, with a clearance of 10% between the die and the punch (as shown in Fig. 4-4 in Chapter 4.). The successive hole-expansion tests were performed at a punching rate of 1 mm/min using the hole-expanding die and the flat-bottom cylindrical punch (as shown in Fig. 4-5(a) in Chapter 4.). In the expansion tests, the punch made contact with the roll-over section of the hole-punched specimens. The hole-expansion ratio (λ) was determined by the following equation:

$$\lambda = \{(d_f - d_0)/d_0\} \times 100\%, \quad (5-3)$$

where d_0 and d_f are the initial hole diameter and the hole diameter on cracking,

respectively. Stretch-forming tests were also performed using the same specimens as used for the stretch-flanging tests, to measure the maximum stretch height H_{max} without cracking. The punching rate was 1 mm/min and a cylindrical punch with a diameter of 17.4 mm and a curvature radius of 8.7 mm was used (as shown in Fig. 4-5(c) in Chapter 4.).³⁾ Bendability was assessed in terms of the minimum bending radius (R_{min}) bendable to 90° without cracking using a bending die and punches with bending radius of 0.5–5.0 mm (Fig. 5-3). All tests were conducted at 20°C.

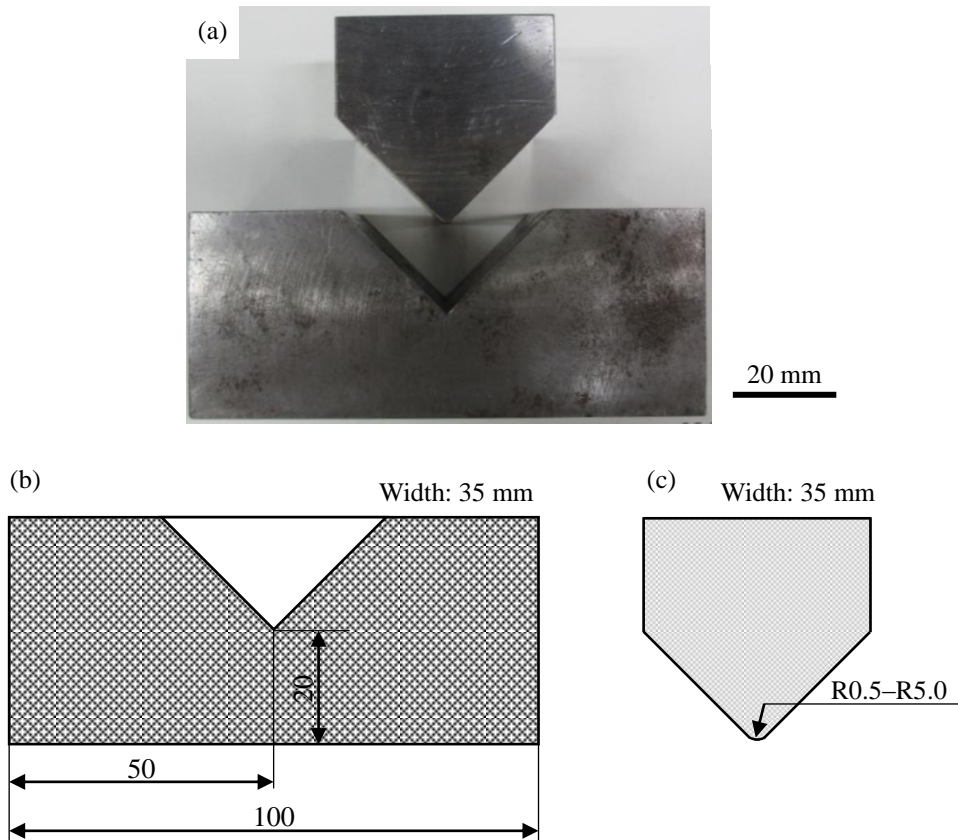


Fig. 5-3. (a) Image and (b, c) illustrations of the bending die and punch, respectively.

5.3 Results

5.3.1 Microstructure

The typical microstructure of ITP process steel is shown in Fig. 5-4. The matrix consists of wide and narrow lath martensite structures. The volume fraction of the narrow lath martensite is about 17 vol%. Most of the retained austenite is located along the narrow lath martensite structures and on the prior grain boundary and packet one, as well as TM steel subjected to IT process in Chapter 3. A small amount of needle-like carbide precipitates in multi angle only in wide lath martensite. The volume fraction increases with increasing partitioning temperature, as shown in Fig. 5-5. At a partitioning temperature of 200°C, the amount of carbides in ITP process steel ($f_{\theta} = 0.64$

vol%) is much lower than that in QP process steel ($f_{\theta} = 1.08$ vol%). These carbides precipitate due to auto-tempering on isothermal transformation or quenching.

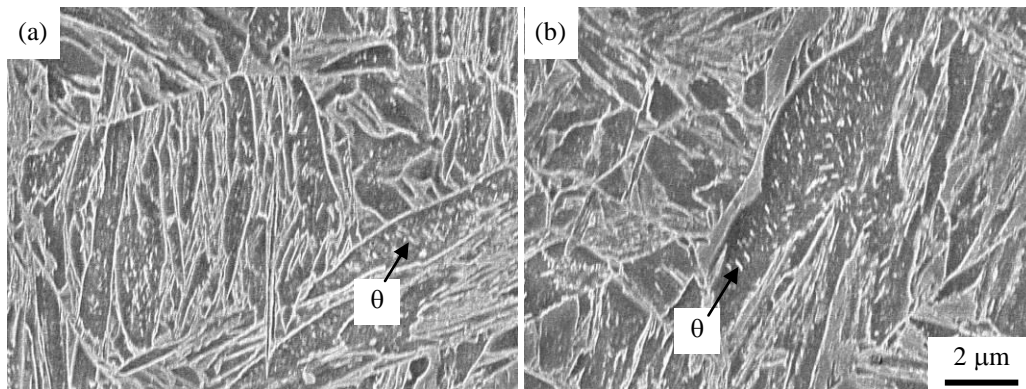


Fig. 5-4. Typical SEM images of steels subjected to partitioning process at 200°C and 400°C after isothermal transformation holding. θ denotes carbide.

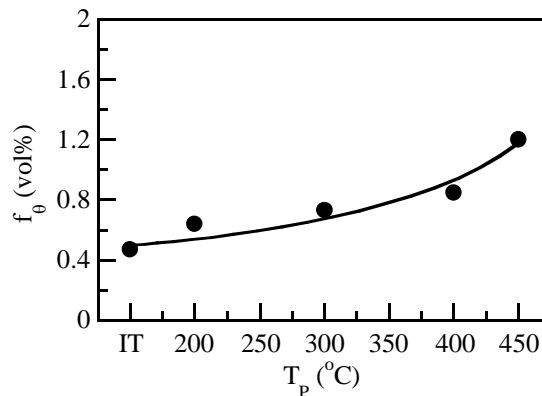


Fig. 5-5. Variation in volume fraction of carbide (f_{θ}) as a function of partitioning temperature (T_p).

5.3.2 Retained austenite characteristics

Figure 5-6 shows the initial volume fraction ($f_{\gamma 0}$) and initial carbon concentration ($C_{\gamma 0}$) of the retained austenite, and the k value as a function of the partitioning temperature in the ITP process steel. The initial volume fraction of the retained austenite decreases with an increase in the partitioning temperature. When partitioned at 450°C, all retained austenite phases decompose into carbide and ferrite. On the other hand, the initial carbon concentration increases from 0.6 to 1.2 mass% on partitioning. Corresponding to the carbon concentration, the k value decreases (or the stability of the retained austenite increases) with an increase in the partitioning temperature.

When these characteristics were compared with those of QP process steel, the ITP process steel was seen to possess a larger amount of retained austenite.

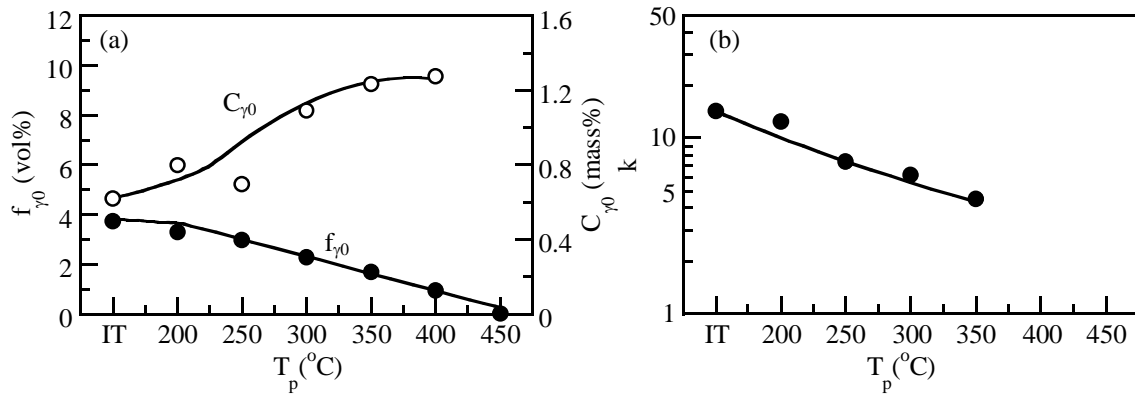


Fig. 5-6. Variations in (a) initial volume fraction (f_{γ_0}), carbon concentration (C_{γ_0}) of retained austenite and (b) the stability of the retained austenite against the strain-induced martensite transformation or k value as a function of partitioning temperature (T_p).

5.3.3 Tensile properties

Figure 5-7 shows typical nominal stress - strain curves for ITP process steel partitioned at 200–400 °C. Table 5-2 shows the tensile properties of ITP process steel. When the steel was partitioned at 200–350 °C, the yield stress increased and the tensile strength decreased with an increase in the partitioning temperature. The reduction of area increases with increasing partitioning temperature, with decreases in uniform and total elongations. These tensile properties are superior to those of QP process steel.

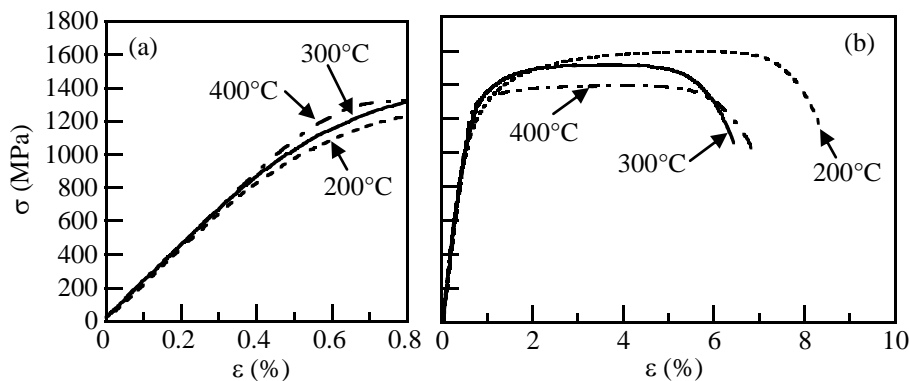


Fig. 5-7. (a) Initial and (b) total nominal stress–strain curves of ITP process steels partitioned at 200 °C, 300 °C and 400 °C.

Table 5-2. Tensile properties of steels subjected to partitioning after the IT process.

T_p	YS	TS	YR	UEI	TEI	RA
200	1225	1609	0.76	5.1	7.5	50
250	1277	1556	0.82	3.7	6.5	57
300	1322	1552	0.85	3.0	5.9	55
350	1342	1517	0.88	2.8	6.1	61
400	1325	1425	0.93	3.5	6.5	63
450	1140	1225	0.93	5.2	8.7	66

T_p (°C): partitioning temperature; YS (MPa): 0.2% proof stress or yield strength; TS (MPa): tensile strength; YR : yield ratio; UEI (%): uniform elongation; TEI (%): total elongation; RA (%): reduction of area.

5.3.4 Stretch-formability, stretch-flangeability and bendability

Figure 5-8 shows the variations in the maximum stretch height, minimum bending radius, and hole-expansion ratio as a function of the partitioning temperature for ITP process steel. The stretch formability and stretch flangeability increase with increasing partitioning temperature. On the other hand, bendability is improved by partitioning at temperatures above 400°C.

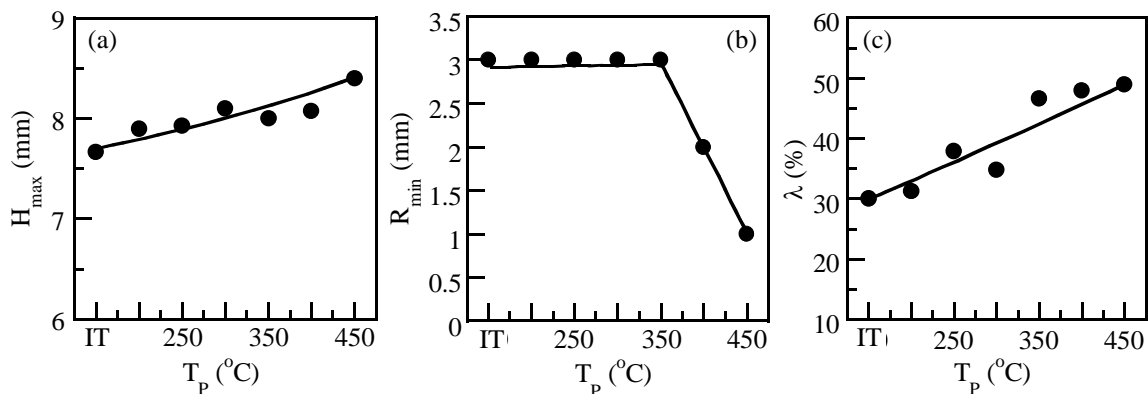


Fig. 5-8. (a) Maximum stretch height (H_{max}), (b) minimum bending radius (R_{min}), and (c) hole-expansion ratio (λ) of ITP process steel as a function of partitioning temperature.

Figure 5-9 shows the relationship between the tensile strength and the maximum stretch height, the minimum bending radius, and the hole-expansion ratio for ITP process steel. For comparison, the experimental data for QP process steel³⁾ with the same chemistry are also plotted in the figure. It is found that ITP process steel partitioned at 200–350°C possesses superior stretch flangeability as well as stretch

formability and bendability, as compared to QP process steel.

Figure 5-10 shows the ratio of shearing section length to sheet thickness (ss/t) as a function of the partitioning temperature for ITP process steel. The shear section length increases with increasing partitioning temperature. From SEM observations, it is found that the size and the number of voids and cracks are reduced by partitioning at higher temperatures. The damage on punching is smaller than that in QP process steel. These results show that partitioning after the IT process, rather than after the quenching process, considerably reduces punching damage.

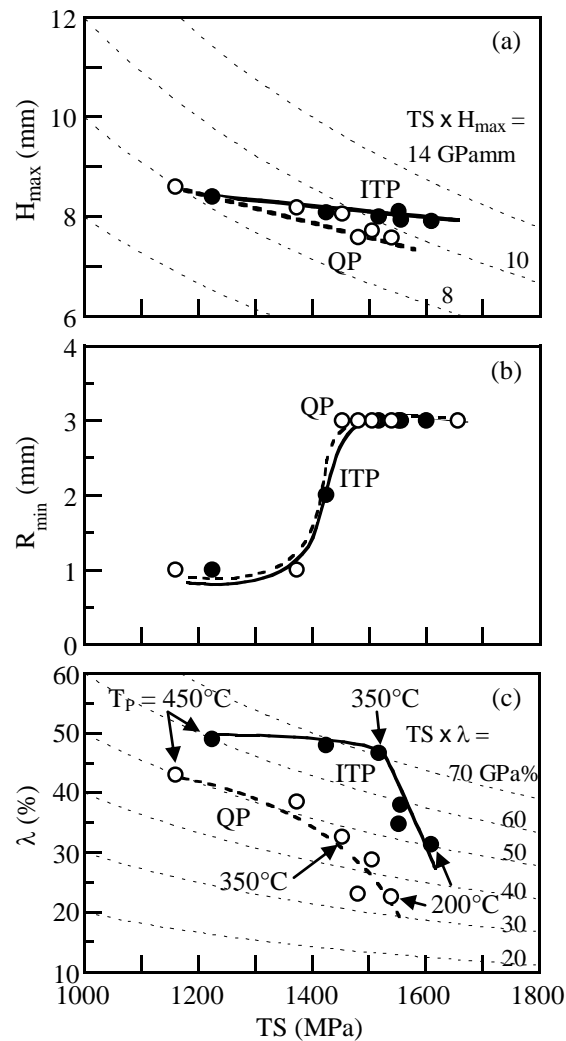


Fig. 5-9. Relationships between the tensile strength (TS) and the (a) maximum stretch height (H_{max}), (b) minimum bending radius (R_{min}), and (c) hole-expansion ratio (λ) in ITP process and QP process¹²⁾ steels.

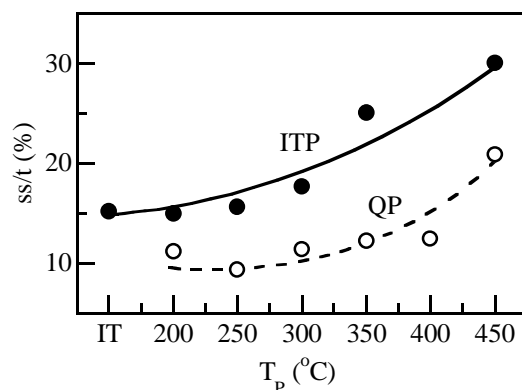


Fig. 5-10. Ratios of shearing section length to sheet thickness (ss/t) in ITP and QP process steels as a function of partitioning temperature.

5.4 Discussion

5.4.1 Yield stress

In general, the yield stress and yield ratio of TM steel are low. Kobayashi et al.³⁾ have reported that low yield stress or "continuous yielding" is associated with spherically symmetric internal stress due to martensitic transformation strain.^{10,11)} This feature is favourable for cold-stamping because the sheet attaches well to dies in the early stage of forming.

In this study, partitioning at 200–350°C after IT process increased yield stress and yield ratio. In addition, the yield stress and yield ratio increased with increasing partitioning temperature although the tensile strength decreased only a little (Table 5-2). From Fig. 5-7, it is found that the increase in yield stress is responsible for flow stress increased in an early strain range. In this case, the abovementioned spherically symmetric internal stress is expected to be relaxed by partitioning. Thus, relaxation of the internal stress by partitioning may increase the flow stress despite softening by the recovered matrix structure and coarsening of the carbides.

5.4.2 Stretch-flangeability

Partitioning at 200–350°C after the IT process considerably improved the stretch flangeability in ITP process steel, as shown in Fig. 5-8. Also, as shown in Fig. 5-9, the ITP process steel was characterized by a small degree of damage to the punched hole-surface with a long shear section and a small number of tiny cracks. So, such a small punching damage by partitioning mainly brought on the excellent stretch flangeability, as well as a large reduction of area or a good localized ductility leading to difficult crack propagation on hole-expanding.

According to Kobayashi et al., both the damage to the hole-surface layer on punching and the localized ductility on expansion are controlled by the volume fraction

and stability of the retained austenite as well as the uniformity and size of the matrix structure in TM steel.¹²⁾ In addition, when the IT process was carried out, the excellent stretch flangeability was associated with (i) a mixed structure matrix of uniform wide and narrow lath martensite, (ii) a larger amount of metastable retained austenite, and (iii) decreased cementite content, which suppress both damage due to punching as well as crack propagation on hole-expansion.

In the studied ITP process steel, partitioning at 200–350°C lead to the (1) carbon-enrichment or stabilization of the retained austenite and (2) softening of the narrow and wide lath martensite, although carbides in the wide lath martensite were coarsened and increased. Thus, it can be concluded that (1) and (2) reduced the surface damage on punching and improved the localized ductility on hole-expansion, and consequently enhanced the stretch flangeability.

5.5 Summary

The effects of partitioning after the IT process on formability of a 0.2%C-1.5%Si-1.5%Mn-0.05%Nb (in mass%) TM steel were investigated.

- (1) Partitioning at 200–350°C after the IT process promoted carbon-enrichment in the retained austenite in the TM steel, with a small decrease in the fraction of retained austenite. The partitioning softened a mixed lath structure matrix, with a coarsening of and an increase in the carbides.
- (2) The partitioning increased the yield stress and yield ratio of the TM steel, accompanied by small declines in the tensile strength as well as the uniform and total elongations.
- (3) Partitioning after the IT process significantly enhanced the formability, especially stretch-flangeability, as compared to that from partitioning after the quenching process.
- (4) The excellent stretch-flangeability was associated with (i) a softening of a mixed uniform wide and narrow lath martensitic structure matrix and (ii) an increase in the stability of the retained austenite, which suppressed the damage on punching and crack propagation on hole-expansion through partitioning process.
- (5) In case of partitioning above 400°C after the IT process, the volume fraction of retained austenite was too low to effectively use TRIP effect.

REFERENCES

- (1) V.F. Zackay, E.R. Parker, D. Fahr and B. Bush: The Enhancement of Ductility in High-strength Steels, *Trans. Am. Soc. Met.*, **60** (1967), pp. 252–259.
- (2) K. Sugimoto and J. Kobayashi: Newly developed TRIP-aided martensitic steels, Materials Science & Technology 2010 Conference & Exhibition (Recent Developments in Steel Processing) October 17-21, 2010, Houston, Texas, pp. 1639–1649.
- (3) J. Kobayashi, D.V. Pham and K. Sugimoto: Stretch-flangeability of 1.5GPa Grade TRIP-aided Martensitic Cold Rolled Sheet Steels, *Steel Res. Int.* **2011**, (2011), pp. 598–603.
- (4) J.G. Speer, D.V. Edmonds, F.C. Rizzo and D.K. Matlock: Partitioning of carbon from supersaturated plates of ferrite, with application to steel processing and fundamentals of the bainite transformation, *Solid State Mater. Sci.*, **8** (2004), pp. 219–237.
- (5) B.C. De Cooman and J.G. Speer: Quench and Partitioning Steel: a New AHSS Concept for Automotive Anti-Intrusion Applications, *Steel Research Int.*, **77** (2006), pp. 634–640.
- (6) K. Sugimoto, J. Sakaguchi, T. Iida and T. Kashima: Stretch-flangeability of a High-strength TRIP Type Bainitic Sheet Steel, *ISIJ Int.*, **40** (2000), pp. 920–926.
- (7) K. Sugimoto, M. Murata and S-M. Song: Formability of Al–Nb Bearing Ultra High-strength TRIP-aided Sheet Steels with Bainitic Ferrite and/or Martensite Matrix, *ISIJ Int.*, **50** (2010), pp. 162–168.
- (8) H. Maruyama: X-ray measuring method of retained austenite, *J. Jpn. Soc. Heat Treat.*, **17** (1977), pp. 198–204 (in Japanese).
- (9) D.J. Dyson and B. Holmes: Effect of Alloying Additions on the Lattice Parameter of Austenite, *J. Iron Steel Inst.*, **208** (1970), pp. 469–474.
- (10) T. Sakaki, K. Sugimoto, T. Fukuzato: Role of internal stress for continuous yielding of dual-phase steels, *Acta Metall.*, **31** (1983), pp. 1737–1746.
- (11) K. Sugimoto, T. Sakaki, T. Fukuzato, O. Miyagawa: Influence of Martensite Morphology on Initial Yielding and Strain Hardening in a 0.11C-1.36Mn Dual-phase Steel, *Tetsu-to-Hagane*, **71** (1985), pp. 994–1001 (in Japanese).

Chapter 6. Effects of microalloying on stretch-flangeability of Ultrahigh-strength TRIP-aided martensitic steel sheets

6.1 Introduction

Recently, third generation advanced high-strength steel sheets (3rd generation AHSSs) have been developed for reducing body weight of automobiles, suppression of global warming, and improvement in impact safety. Typical AHSSs include C-Si-Mn “Transformation-induced plasticity (TRIP)¹⁾-aided bainitic ferrite” (TBF) steel and “Quench and Partitioning” (Q&P) steel, which possess superior formability owing to transformation-induced plasticity (TRIP) of the metastable retained austenite. TBF steel is produced by an isothermal transformation (IT) process at temperatures higher than the martensite transformation-start temperature (M_s) (when the matrix structure is bainitic ferrite) or between the M_s and martensite transformation-finish temperature (M_f) temperatures (when the matrix structure is a mixture of bainitic ferrite and martensite) after austenitizing.^{2,3)} Q&P steel is fabricated by first quenching at a temperature below the M_s temperature after austenitizing and then by partitioning (P) at a temperature higher than the M_s temperature (matrix structure is the same mixture of bainitic ferrite and martensite as in the case of TBF steel).⁴⁻⁶⁾

In order to increase the strength of TBF steel, Sugimoto et al. recently developed a C-Si-Mn “TRIP-aided martensitic” (TM) steel with a wide lath-martensite structure and a narrow lath-martensite/metastable-austenite-retained complex phase (MA-like phase).⁷⁻¹⁰⁾ The TM steel was manufactured by the following two-step heat treatment ITP process:

(1) IT process for 1000 s at temperatures below M_f temperature after austenitizing.

(2) P process at temperatures between 200–350°C for 1000 s after the IT process, which further enriches the carbon concentration of the retained austenite.

The TM steel achieved superior stretch-flangeability compared to TBF steel because of its unique microstructure.⁷⁾ As the microstructure and retained austenite characteristics of TM steel are affected by Cr, Mo, and Ni alloying⁷⁾, press-formability of TM steel sheet can be also expected to be improved by microalloying with Cr, Mo and Ni; however, the effects of alloying elements on the press-formability of TM steel have not yet been reported.

In the present study, the effects of Cr, Mo and/or Ni alloying on the microstructure, retained austenite characteristics, tensile properties, stretch-formability and stretch-flangeability of TM steel subjected only to an IT process at temperatures below the M_f temperature were investigated in order to further improve the press-formability of TM steel. It was discovered that the tensile properties and stretch-flangeability were also related to some metallurgical factors.

6.2 Experimental procedure

Five kinds of steels, with varying Cr, Mo and Ni contents listed in **Table 6-1**, were prepared in the form of 100 kg ingots by vacuum melting, which were then hot-forged into slabs. The slabs were then heated to 1200°C and hot-rolled into thin plates (3 mm in thickness) with a finishing rolling temperature at 850°C, followed by cooling in air to room temperature and subsequent annealing at 650°C. Finally, the plates were cold-rolled to 1.2 mm after acid pickling.

In general, carbon equivalent (C_{eq}) is used in the evaluation of hardenability of steels. Some of the plates contained boron at a concentration of ~20 ppm, along with the other alloying elements, for increasing hardenability; however, C_{eq} does not include the effects of boron. Therefore, hardenability defined as the product of the various Grossman pearlitic hardenability factors¹¹⁾ (Πf_i s) was used in this study. The value of Πf_i was calculated using the following equation:

$$\begin{aligned} \Pi f_i = D_1/D_1^* = & (1 + 0.64\%Si) \times (1 + 4.1\%Mn) \times (1 + 2.83\%P) \\ & \times (1 - 0.62\%S) \times (1 + 2.33\%Cr) \times (1 + 0.52\%Ni) \\ & \times (1 + 3.14\%Mo) \times (1 + 0.27\%Cu) \times (1 + 1.5(0.9 - \%C)), \end{aligned} \quad (6-1)$$

where D_1 and D_1^* are the ideal critical diameters for the hardenability of alloyed and carbon steels, respectively. The effect of the prior austenite grain size is not considered in Eq. (6-1). The last term on the right-hand side of Eq. (6-1) was included only in the case of the steel containing boron, because the hardenability of boron-bearing steel is more sensitive to carbon contents than boron contents. Hereafter, Πf_i is called the “hardenability factor” or “hardenability”. The continuous cooling transformation (CCT) diagrams of steels A through E are shown in **Fig. 6-1**.

Tensile specimens with a gauge length of 50 mm and gauge width of 12.5 mm (JIS13B), and stretch-forming and hole-expansion specimens of 50 mm length and width were machined from the cold-rolled steel sheets. These specimens were subjected to an IT process, as shown in **Fig. 6-2**. Similar to previous studies⁶⁻⁸⁾, the austenitizing was performed at 900°C for 1200 s, and then the IT process was performed at 200°C for 1000 s.

The microstructure of the steels was examined by transmission electron microscopy (TEM; JEOL Ltd., JEM-2010) and electron backscatter diffraction pattern analysis using field emission scanning electron microscopy (FE-SEM; Hitachi Co., S-4100 and FE-SEM-EBSP; JEOL Ltd., JSM-6500F). The volume fraction of carbide in the specimens was measured as follows. First the specimens were etched in 5%-nital etchant, and then a carbon film was coated on the specimen. The carbon replicas with

carbides were then peeled off from the specimens in an ethanol solution including 30% nitric acid, followed by TEM examination and image analysis in an area of about 560 μm^2 .

The characteristics of the retained austenite in the steels were quantified by X-ray diffraction (XRD; Rigaku Co., RINT2100). Specimens were electropolished after being ground with emery paper (#2000). As described by Maruyama¹²⁾, the volume fraction of the retained austenite (f_γ , vol%) was calculated from the integration of intensities of the $(200)_\alpha$, $(211)_\alpha$, $(200)_\gamma$, $(220)_\gamma$ and $(311)_\gamma$ peaks from the XRD studies performed using Mo-K α radiation. The carbon concentration (C_γ , mass%) was estimated by substituting the lattice constant (a_γ , units of 10^{-1} nm) measured from the $(200)_\gamma$, $(220)_\gamma$ and $(311)_\gamma$ peaks of Cu-K α radiation into the following equation proposed by Dyson and Holmes.¹³⁾

$$a_\gamma = 3.5780 + 0.0330\%C_\gamma + 0.00095\%Mn_\gamma - 0.0002\%Ni_\gamma + 0.0006\%Cr_\gamma + 0.0220\%N_\gamma + 0.0056\%Al_\gamma - 0.0004\%Co_\gamma + 0.0015\%Cu_\gamma + 0.0031\%Mo_\gamma + 0.0051\%Nb_\gamma + 0.0039\%Ti_\gamma + 0.0018\%V_\gamma + 0.0018\%W_\gamma, \quad (6-2)$$

where $\%Mn_\gamma$, $\%Ni_\gamma$, $\%Cr_\gamma$, $\%N_\gamma$, $\%Al_\gamma$, $\%Co_\gamma$, $\%Cu_\gamma$, $\%Mo_\gamma$, $\%Nb_\gamma$, $\%Ti_\gamma$, $\%V_\gamma$ and $\%W_\gamma$ represent the concentrations of the respective individual elements (mass%) in the retained austenite phase. For convenience, the contents of added alloying elements were substituted for these concentrations in this study.

Table 6-1. Chemical composition (mass%), measured martensite-start and -finish temperatures (M_s , M_f , °C) and hardenability factor (Πf_i) of steels used.

Steel	C	Si	Mn	P	S	Al	Nb
A	0.20	1.50	1.50	0.0015	0.002	0.042	0.048
B	0.21	1.49	1.50	0.0019	0.004	0.040	0.050
C	0.20	1.49	1.50	0.0019	0.004	0.040	0.050
D	0.18	1.48	1.49	0.0029	0.004	0.043	0.050
E	0.21	1.49	1.49	0.0019	0.003	0.034	0.049

Steel	Cr	Mo	Ni	O	N	M_s	M_f	Πf_i
A	-	-	-	0.0010	0.0012	409	289	14.6
B	0.50	-	-	0.0012	0.0012	408	292	30.6
C	1.00	-	-	0.0014	0.0012	406	261	47.0
D	1.02	0.20	-	0.0015	0.0010	368	250	76.8
E	1.00	0.20	1.52	0.0009	0.0014	357	245	135.8

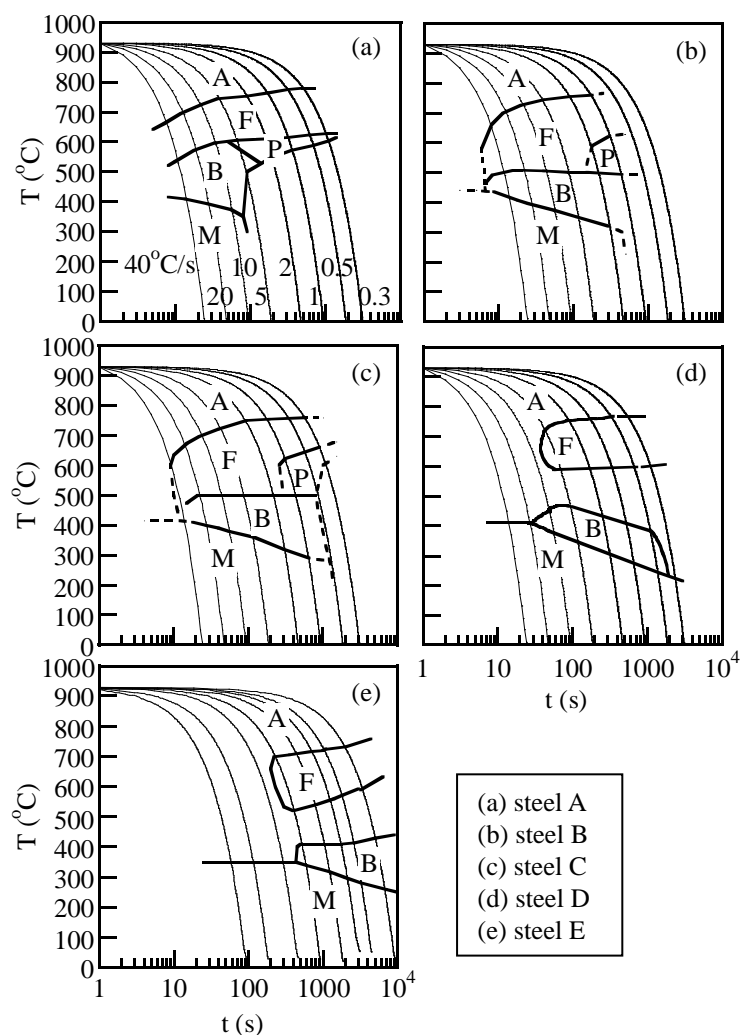


Fig. 6-1. Measured CCT diagrams of steels A through E, in which A, F, P, B and M represent austenite, ferrite, pearlite, bainite and martensite, respectively.

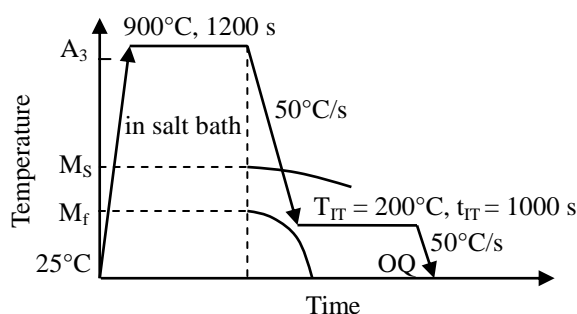


Fig. 6-2. Heat treatment diagram of ITP process, in which OQ represents quenching in oil.

Tensile tests were carried out on a hard type of testing machine (Shimadzu Co., AD-10TD, as shown in Fig. 4-3 in Chapter 4.). The strain rate was $3.3 \times 10^{-3} \text{ s}^{-1}$ and the tensile direction was parallel to the rolling direction of the sheet. In order to investigate the initial yield behavior, a strain gauge (Kyowa Electronic Instruments Co., Ltd, KFG-10-120-C1) was attached to the gauge section of the specimen. The hole-punching and hole-expanding tests were conducted with a graphite-type lubricant. First, a hole with 4.76 mm diameter was punched out at a punching rate of 10 mm/min, with a clearance of 10% between the die and the punch (as shown in Fig. 4-4 in Chapter 4.). The successive hole-expansion tests were performed at a punching rate of 1 mm/min using the hole-expanding die and the flat-bottom cylindrical punch (as shown in Fig. 4-5(a) in Chapter 4.). In the expansion tests, the punch was contacted with the roll-over section of the hole-punched specimens. The hole-expansion ratio (λ) was determined by the following equation:

$$\lambda = \{(d_f - d_0)/d_0\} \times 100\%, \quad (6-3)$$

where d_0 and d_f are the initial hole diameter and the hole diameter upon cracking, respectively. Stretch-forming tests were also performed to measure the maximum stretch height, H_{\max} , without cracking. The punching rate was 1 mm/min and a cylindrical punch with a diameter of 17.6 mm and a curvature radius of 8.7 mm was used (as shown in Fig. 4-5(c) in Chapter 4.).¹⁰⁾ The forming tests were carried out twice in this study. The error margins in the hole-expanding ratio and maximum stretch height were 1–3% and 0.05–0.2 mm, respectively. All tests were conducted at 25°C.

6.3 Results

6.3.1 Microstructure and Retained Austenite Characteristics

Figure 6-3 shows SEM images of the microstructure in steels A through E. The results from EBSD analysis in steels A and D are shown in **Fig. 6-4**. Based on these results, the body centered cubic (Fe- α , bcc) structures of the TM steel consisted of high image quality (IQ) index or low IQ index structures. According to Kobayashi et al.³⁾, the martensitic and bainitic ferrite matrices possess a high IQ index whereas the MA phase in TBF steel possesses a low IQ index. Thus, the high IQ index structure in Fig. 6-4 seems to be a soft wide lath-martensite structure with low dislocation density¹⁴⁾. It is proposed that this wide lath-martensite structure was auto-tempered during cooling after austenitizing. The width of the lath-martensite was 0.5–1.0 μm . As shown in Figs. 6-3(f)–6-3(j), needle-like carbides were observed in the wide lath-martensite structures. The low IQ index structure was a blocky phase composed of fine martensite and retained austenite. The blocky second phase appears to be a martensite-austenite

constituent or phase, which was observed in martensitic steel in a previous study¹⁵). Hereafter, the blocky second phase is referred to as an “MA-like phase”. The MA-like phase was primarily located on the prior austenite, packet, and martensite block boundaries. The fraction of the MA-like phase increased with increasing hardenability. In addition, these MA-like phases were also finely dispersed with increasing hardenability (Figs. 6-4(b) and 6-4(e)).

TEM images of steels A (base steel) and D (Cr-Mo-bearing steel) are shown in **Fig. 6-5**. In Fig. 6-5, the blocky second phase was found to possess a narrow lath-martensite structure (α_m^*) with high dislocation density. Considering the IQ map distribution of Figs. 6-4(b) and 6-4(e), the retained austenite appears to be located on a narrow lath-martensite boundary. Carbides in Figs. 6-3 and 6-5, which were precipitated only in wide lath-martensite, were detected to be cementite (Fe_3C). The length of the carbide was about 200 nm. The sizes of the carbides in steels B through D were slightly smaller than that of steel A. It was hypothesized that these carbides were precipitated by auto-tempering during cooling after austenitizing.

Figure 6-6 shows the initial volume fraction and carbon concentration of retained austenite, volume fractions of the MA-like phase and carbide, and the stability of the retained austenite against the strain-induced martensite transformation “ k value” as a function of hardenability factor in steels A through E. The k value or “*strain-induced transformation factor*” was defined by the following equation¹⁶):

$$\log f_\gamma = \log f_{\gamma 0} - k\varepsilon, \quad (6-4)$$

where f_γ is the volume fraction of retained austenite after applying plastic strain ε and $f_{\gamma 0}$ is the original volume fraction of retained austenite. In Fig. 6-6(a), the initial volume fraction of the retained austenite had only a slight dependence on the hardenability factor. On the other hand, the initial carbon concentration of the retained austenite clearly decreased with increasing hardenability. Although the k value of steel E (Cr-Mo-Ni bearing steel) slightly increased (retained austenite became unstable), the hardenability dependence of the k value was small (Fig. 6-6(c)).

The carbide fraction in steels A through E was between 0.8 and 1.2 vol%, and it minimally depended on the hardenability (Fig. 6-6(b)). The volume fractions of the MA-like phase in steels A through E were 11–18 vol% and increased with increasing hardenability.

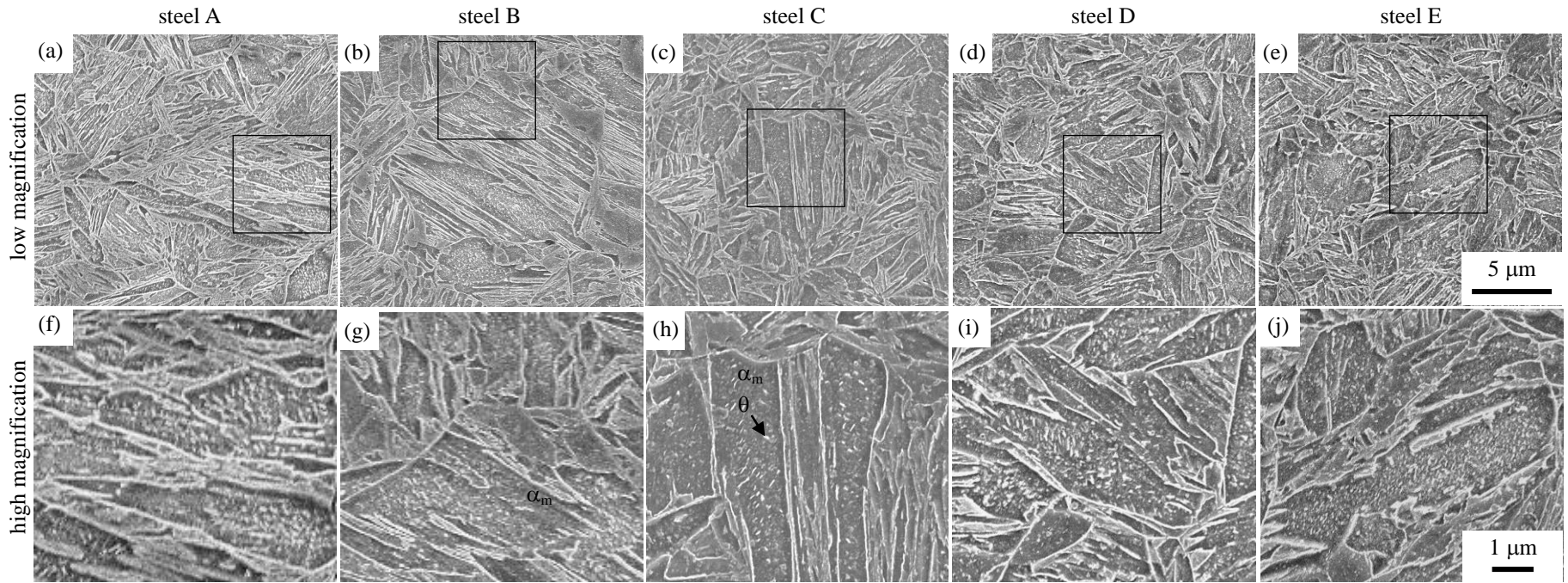


Fig. 6-3. SEM images of steels A through E, in which α_m and θ represent wide lath-martensite and carbide, respectively. Bottom images are responsible to square region in upper images.

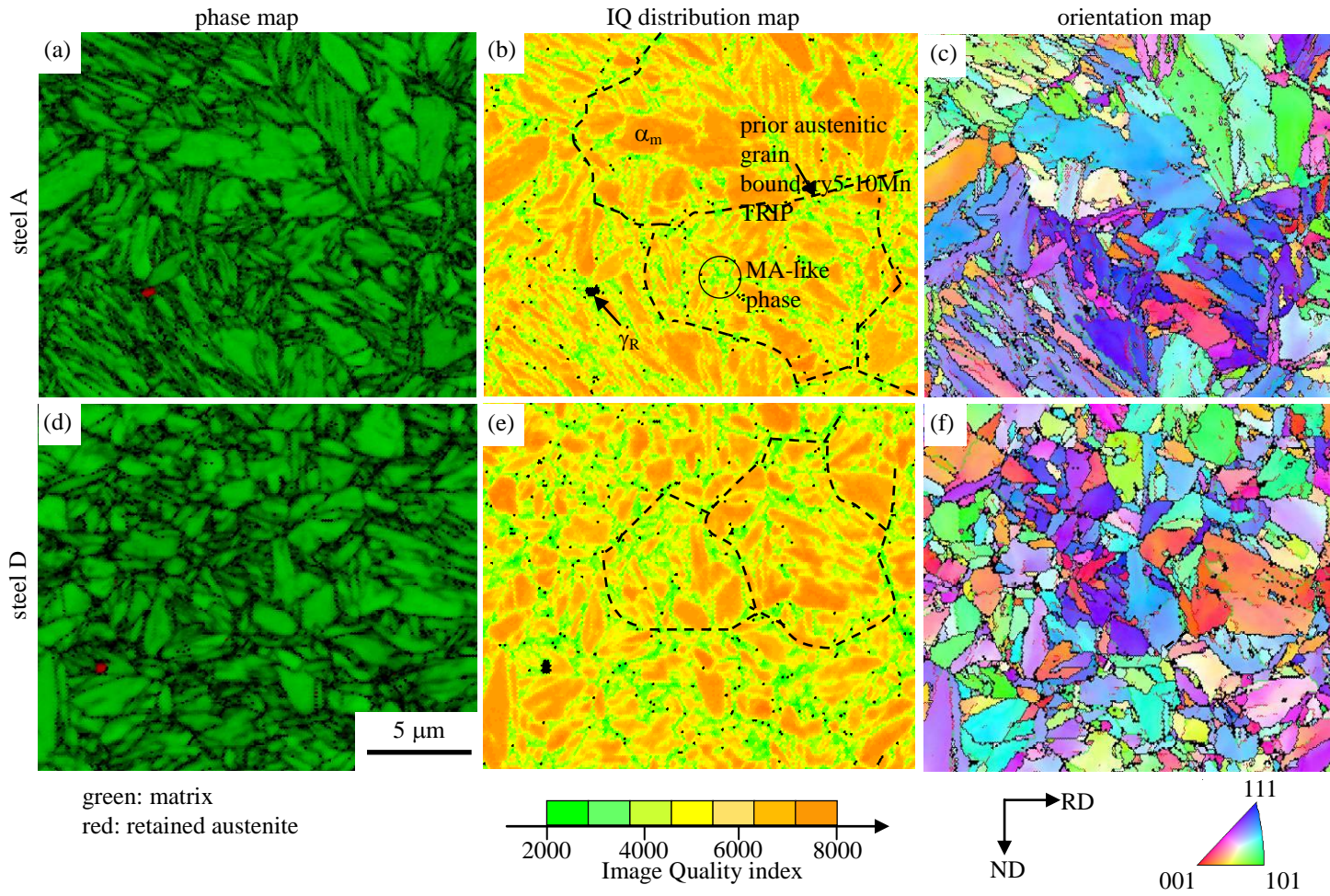


Fig. 6-4. Phase maps and image quality (IQ) distribution maps and orientation maps of Fe- α (bcc) in steels A and D.

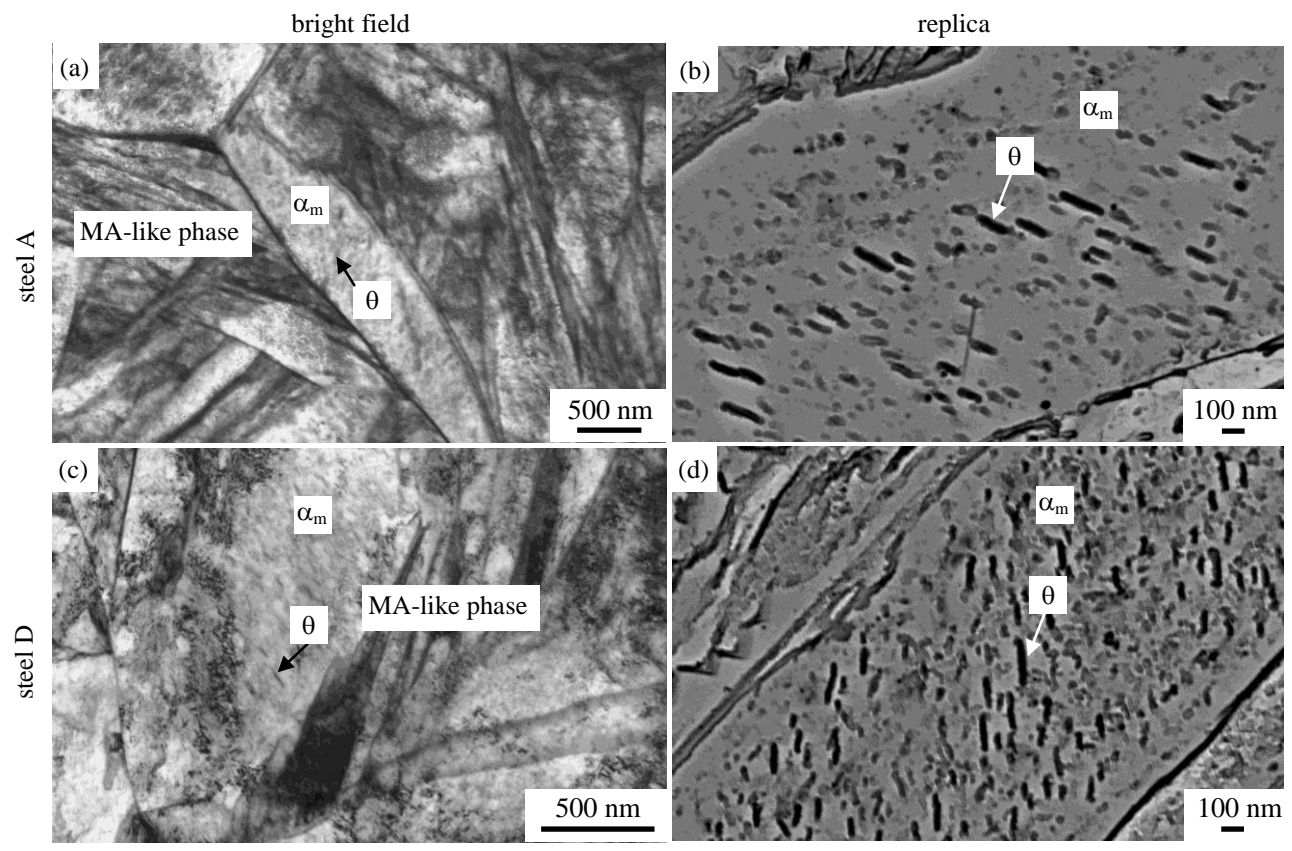


Fig. 6-5. TEM images of bright field and replica of steels A and D, in which α_m and θ represent wide lath-martensite and carbide, respectively.

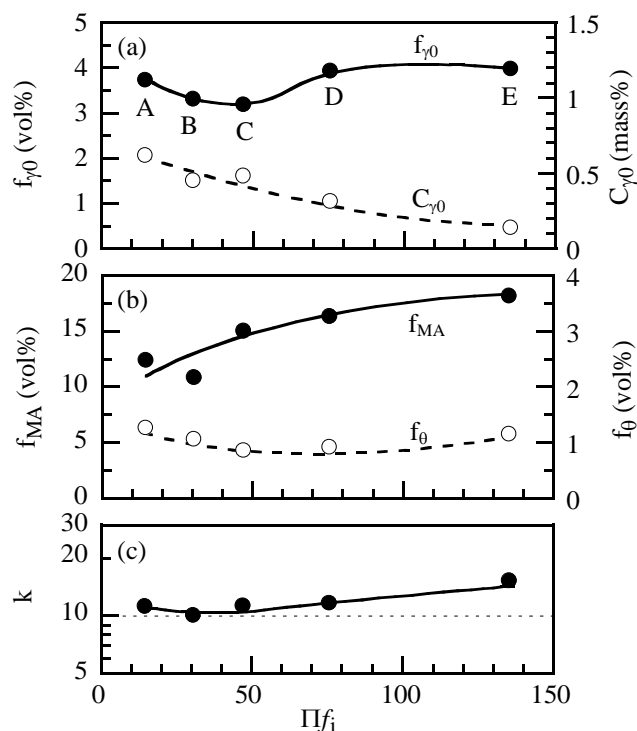


Fig. 6-6. Variations in (a) initial volume fraction ($f_{\gamma 0}$) and carbon concentration ($C_{\gamma 0}$) of retained austenite, (b) volume fractions of MA-like phase (f_{MA}) and carbide (f_{θ}) and (c) strain-induced transformation factor (k) as a function of hardenability factor (Πf_i) in steels A through E.

6.3.2 Tensile Properties

Figure 6-7 shows the engineering stress-strain curves of steels A, C, and D. The tensile properties of steels A through E are shown in Fig. 6-8. The tensile strengths of steels A through E were of an ultrahigh strength grade, at 1.5 GPa. The tensile strength, yield stress (or 0.2% offset proof stress), and yield ratio of steels A through E increased with increasing hardenability (Figs. 6-8(a) and 6-8(b)). In particular, the yield stress and yield ratio were significantly dependent on hardenability.

The total elongation and a combination of the tensile strength and total elongation slightly decreased with increasing hardenability (Fig. 6-8(c)). The reductions of area in steels D and E were lower than those of steels A, B, and C (Fig. 6-8(d)).

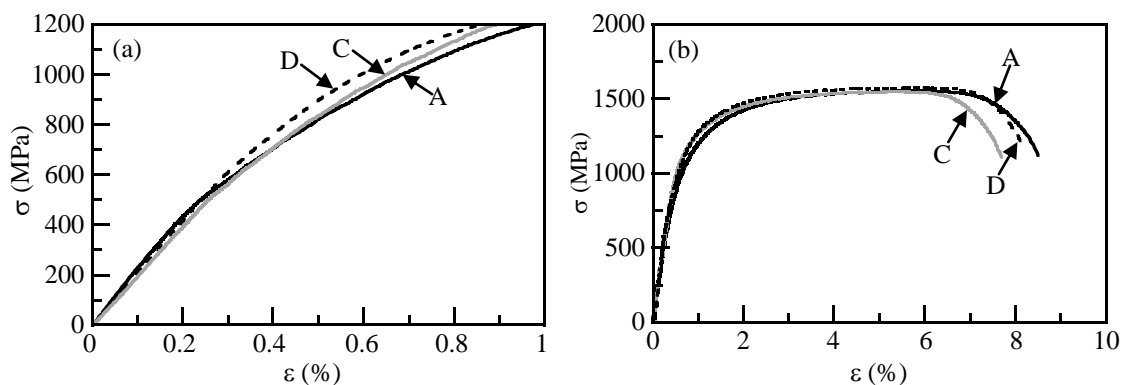


Fig. 6-7. Typical engineering stress (σ) - strain (ϵ) curves of steels A, C and D. (a) is curves in early stage of (b).

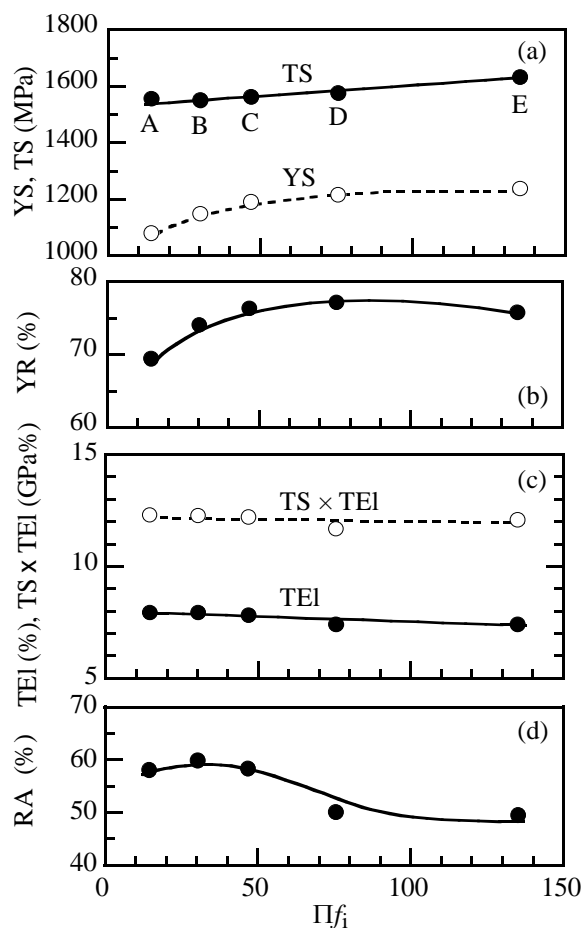


Fig. 6-8. Variations in (a) yield stress or 0.2% offset proof stress (YS) and tensile strength (TS), (b) yield ratio ($YR = YS/TS$), (c) total elongation (TEI) and combination of tensile strength and total elongation ($TS \times TEI$) and (d) reduction of area (RA) as a function of hardenability factor (Πf_i) in steels A through E.

6.3.3 Stretch-flangeability and Stretch-formability

The hole-expanding ratio, a combination of tensile strength and hole-expanding ratio, maximum stretch-height, and a combination of tensile strength and maximum stretch-height in steels A through E as a function of hardenability are shown in **Fig. 6-9**. The hole-expanding ratio of steel A was 28.4%. The hole-expanding ratios of steels B and C (Cr-bearing steels) increased respectively to 35.7% and 38.3%, which were approximately 10% higher than that of steel A. On the other hand, the hole-expanding ratio of steels D and E were roughly equal to that of steel A. The combination of tensile strength and hole-expanding ratio of steel C was highest of all steels. Although the hole-expanding ratio and combination of tensile strength and hole-expanding ratio changed with hardenability factor, the maximum stretch-height and combination of tensile strength and maximum stretch-height in steels A through E were nearly constant.

Figure 6-10 shows the ratio of shear section length to sheet thickness and punching shear stress as a function of hardenability factor. The ratio of shear section length to sheet thickness decreased with increasing hardenability. In contrast, the punching shear stresses of the steels increased with increasing hardenability.

SEM images of the break section of hole-surface pierced by punch in steels A, C, and D are shown in **Fig. 6-11**. Dimple fractures appeared on the fracture surface of steels A through E. The dimple size on fracture surface decreased with increasing hardenability (Figs. 6-11(a)–6-11(c)). In cross-sectional images of Figs. 6-11(d)–6-11(f), a small number of fine voids and cracks were observed in steel C. The punching damage was lowest of all steels. The voids of steel C appear to be formed at the wide lath-martensite structure matrix/MA-like phase interface.

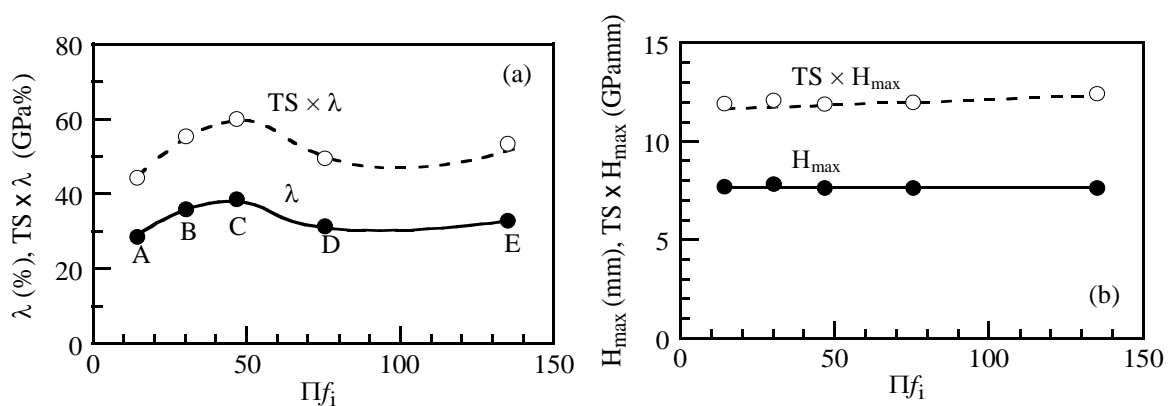


Fig. 6-9. Variations in (a) hole-expanding ratio (λ) and combination of tensile strength and hole-expanding ratio ($TS \times \lambda$) and (b) maximum stretch-height (H_{max}) and combination of tensile strength and maximum stretch-height ($TS \times H_{max}$) as a function of hardenability factor (Πf_i) in steels A through E.

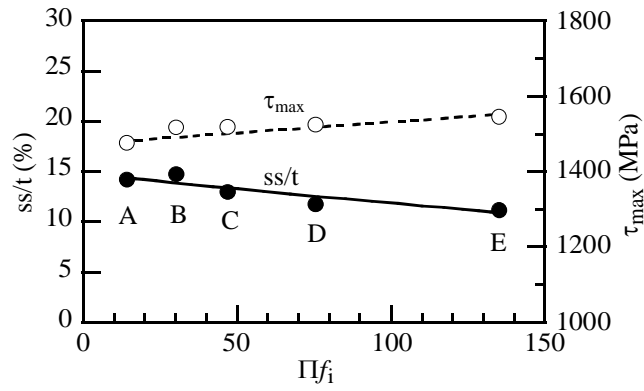


Fig. 6-10. Variations in ratio of shear section length to sheet thickness (ss/t) and punching shear stress (τ_{max}) as a function of hardenability factor (Πf_i) in steels A through E.

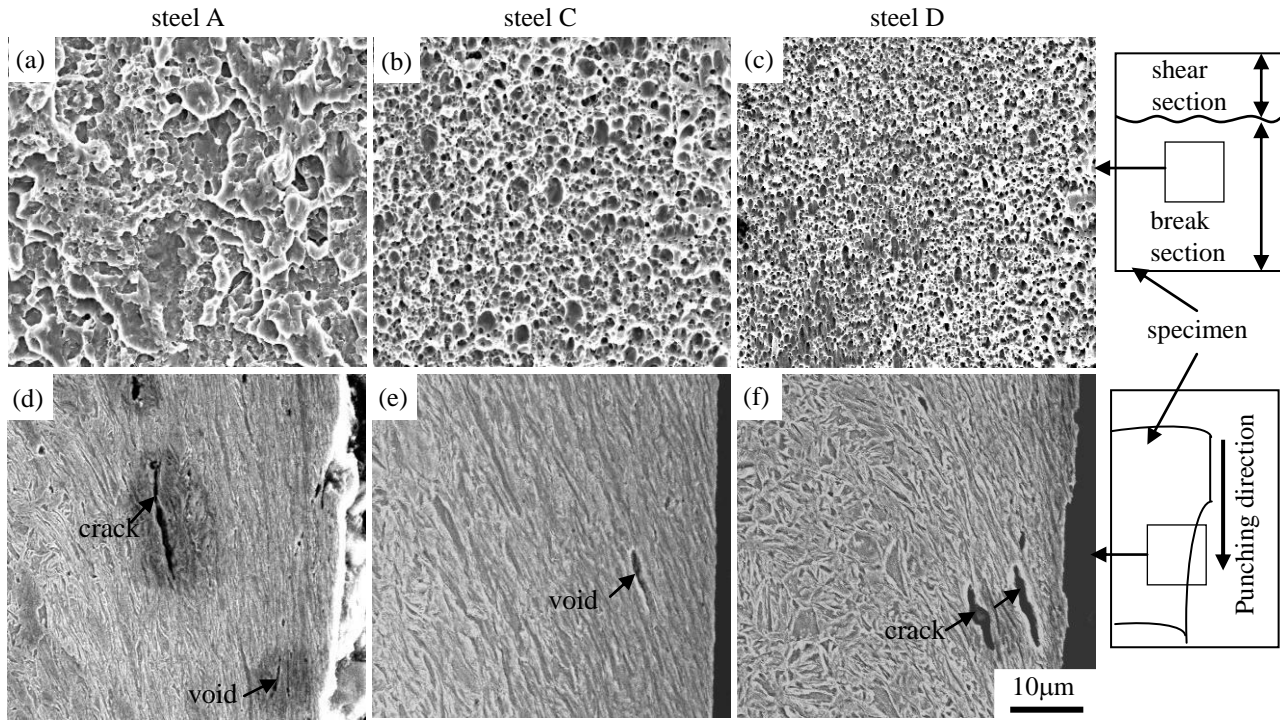


Fig. 6-11. SEM images of break section of hole-surface pierced by punch in steels (a, d) A, (b, e) C and (c, f) D.

6.4 Discussion

6.4.1 Microstructure Formation and Carbon Enrichment into Retained Austenite in TM Steel with High Hardenability

The microstructure of steels B through E consisted of fine, uniform lath-martensite structure matrix and the MA-like phase (Fig. 6-4). The volume fractions of MA-like phase were increased by additions of Cr, Mo and/or Ni (Fig. 6-6(b)). On the other hand, the volume fractions of the retained austenite in steels B and C (Cr-bearing steels) were the smallest of all steels, although the carbon concentration of the retained austenite in steels A through E decreased with increasing hardenability factor (Fig. 6-6(a)). In order to investigate the change in these retained austenite characteristics, the dilatometry curves of steels A through E were plotted. The typical dilatometer curves of steels A and D are shown in Fig. 6-12(a). Figure 6-12(b) shows these martensite transformation fraction-temperature curves. The martensite transformation fraction was fitted using the volume fraction of each phase resulting from SEM observation, EBSD and X-ray diffraction analyses. In Fig. 6-12, martensitic transformation of steel D was shifted to a lower temperature, compared to steel A.

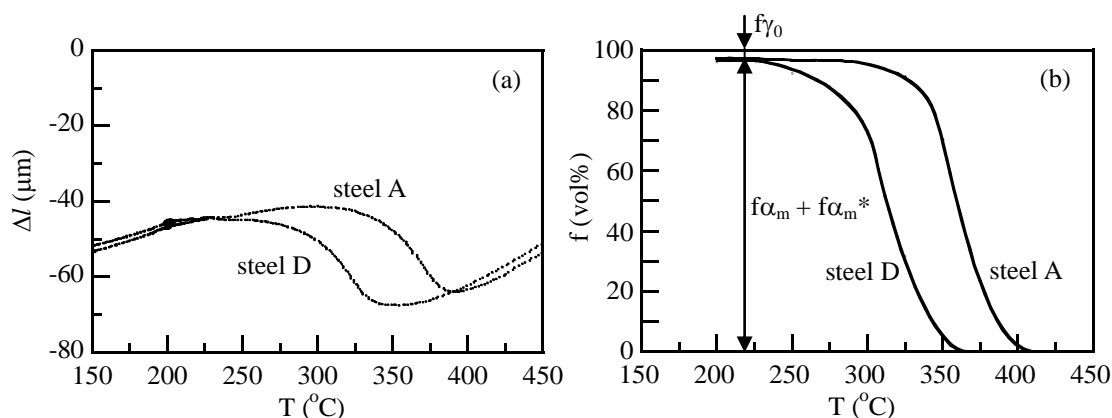


Fig. 6-12. Typical (a) dilatometer (Δl) - temperature (T) curves and (b) martensite transformation fraction ($f\alpha_m + f\alpha_m^*$) - temperature (T) curves of steels A and D, in which $f\alpha_m$, $f\alpha_m^*$ and $f\gamma_0$ represent volume fractions of wide lath-martensite, narrow lath-martensite and initial retained austenite, respectively.

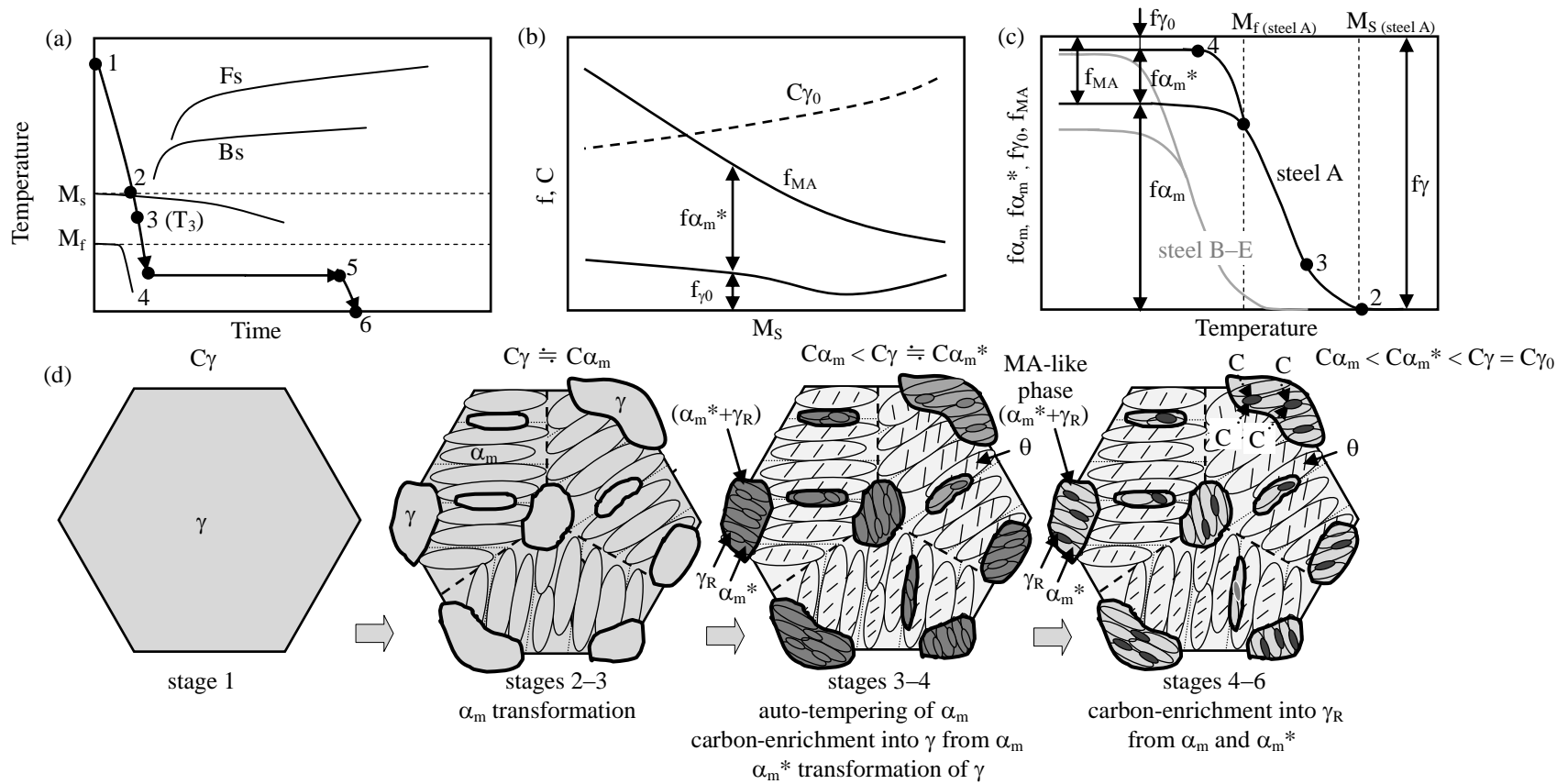


Fig. 6-13. Illustration of (a) heat treatment diagram, (b) martensite-start temperature (M_s) dependences of initial volume fraction (f_{γ_0}) and carbon concentration (C_{γ_0}) of retained austenite and volume fractions of MA-like phase (f_{MA}) and narrow lath-martensite ($f_{\alpha_m^*}$), (c) variation in volume fraction of wide lath-martensite (f_{α_m}), $f_{\alpha_m^*}$, f_{MA} and f_{γ_0} with temperature and (d) microstructural change at stages 1 through 6 during heat treatment in steel D, in which α_m , α_m^* , γ , γ_R , θ , MA and C represent wide lath-martensite, narrow lath-martensite, austenite, retained austenite, carbide, MA-like phase and solute carbon, respectively. C_{γ} , C_{α_m} and $C_{\alpha_m^*}$ are carbon concentrations of austenite, wide lath-martensite and narrow lath-martensite, respectively.

Based on Figs. 6-4–6-6 and 6-12(b), the microstructural changes of steels B through E are schematically illustrated in **Fig. 6-13**. First, we will discuss the mechanism of microstructural formation in steel A. According to Kobayashi et al.⁸⁾, the microstructure of steel A changes as follows.

Stage 1: The microstructure was austenite.

Stage 2–3: When the steel was quenched to temperature T_3 , lower than M_S , a large amount of austenite phase transformed to wide lath-martensite (α_m). The untransformed austenite was located on the prior austenitic grain, packet, and block boundaries. In this situation, the volume fraction of wide lath-martensite ($f\alpha_m$) increased with decreasing quenching temperature according to the following equation reported by Koistinen and Marburger¹⁷⁾:

$$f\alpha_m = 1 - \exp\{-1.1 \times 10^{-2}(M_S - T_3)\} \quad (6-5)$$

Namely, the wide lath-martensite fraction increases with increasing M_S temperature because $(M_S - T_3)$ increases.

Stage 3–4: Carbide precipitated only in the wide lath-martensite with supersaturated carbon by auto-tempering during cooling. At the same time, the carbon in the martensite partitioned to untransformed austenite. Most of untransformed austenite transformed to narrow lath-martensite, and a small amount of untransformed austenite was retained. This complex phase was confirmed as the MA-like phase. The retained austenite was mainly located on the narrow lath-martensite boundaries. Carbides did not precipitate in the narrow lath-martensite since auto-tempering was suppressed by the lowered M_S temperature or the increased carbon concentration of untransformed austenite.

Stage 4–6: Supersaturated carbon in wide and narrow lath-martensite further partitioned into untransformed austenite during the IT process. As a result, the carbon concentration of untransformed austenite increased. The size and volume fraction of carbide in the wide lath-martensite were only slightly affected.

In this study, the microstructural changes of steels B through E were nearly the same as that of steel A (Figs. 6-3–6-5), although the carbon concentration of retained austenite decreased and the volume fraction of the MA-like phase increased with increasing hardenability in steels B through E (Figs. 6-6(a) and 6-6(b)). The reason why the carbon concentration of retained austenite decreased with increasing hardenability factor can be considered as follows: the volume fractions of untransformed austenite at stage 3–4 in steels B through E increased with the decrease in M_S temperature shown in Fig. 6-13(c). Thus, carbon enrichment in the retained austenite was suppressed because the supersaturated carbon of the wide lath-martensite did not move in the untransformed austenite as a result of an increase in the volume fractions of the untransformed

austenite. In steels B through E, the above decrease in M_s temperature may also lead to refining of the martensite block structure and suppression of carbide precipitation. It is hypothesized that the volume fractions of carbide in steels B and C were low because Cr addition suppresses the carbide coarsening.¹⁸⁾

6.4.2 The Increase of Yield Stress and Yield Ratio with Alloying

In Fig. 6-8, the yield stress and yield ratio of steels B through E were increased, compared to those of steel A. According to the initial yield model of Sakaki et al.¹⁹⁾ and Sugimoto et al.²⁰⁾, the elastic limit Y_e ¹⁹⁾ and strain hardening increment $\Delta\sigma$ ²⁰⁾ in a dual phase steel containing of martensite second phase are estimated by the following equations (see **Fig. 6-14**).

$$Y_e = Y [-1/2 \times (Y_0/Y) + \{1 - 3/4 \times (Y_0/Y)^2\}^{1/2}] \quad (6-6)$$

$$\Delta\sigma = f_s K E \varepsilon_0, \quad (6-7)$$

where Y and Y_0 are the yield strengths of the soft matrix structure at room temperature and upon martensitic transformation, respectively (in this case, $Y > Y_0$). The f_s , K , E , and ε_0 are volume fraction, morphological coefficient of the second phase, Young's modulus of the matrix and second phase, and plastic strain in the matrix, respectively. In this case, it was assumed that the second phase deforms elastically. In the present study, the f_s and soft matrix structure can be replaced by the volume fraction of the MA-like phase, f_{MA} , and wide lath-martensite matrix structure. If Y_0/Y is approximately 0.8, Y_e is 0.32 Y . Thus, the lower yield strength of steel A may have been caused by a low elastic limit at initial yielding. Although the elastic limits of steels B through E may be equal to that of steel A, their strain hardening increments are higher than that of steel A because of an increase in the volume fractions of the MA-like phase in steels B through E. From a microstructure perspective, although the volume fraction of carbide in steel C was slightly lower than that of steel A, the volume fraction of the MA-like phase increased (Fig. 6-6(b)). In spite of the decrease in carbon concentrations of the retained austenite in steels B through E, the stabilities of the retained austenite against straining were equal to that of steel A (Fig. 6-6(c)). Therefore, higher yield strengths of steels B through E are considered to be caused by larger hardening increment flow stress with increasing volume fraction of the MA-like phase in a strain range from the elastic limit to 0.2% strain (Fig. 6-14). High yield ratios of steels B through E may be caused by relatively high yield stress compared to tensile strength.

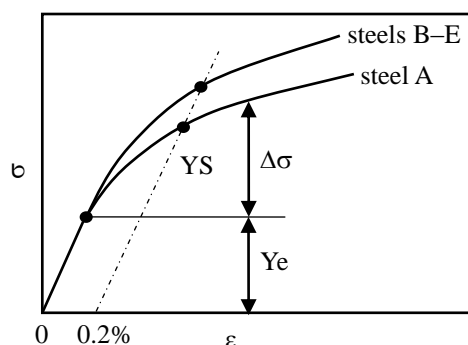


Fig. 6-14. Illustration of stress (σ) - strain (ε) curves in early stage and definition of elastic limit (Y_e), 0.2% offset proof stress (YS) and strain hardening increment ($\Delta\sigma$) in steel A and steels B through E.

In steels D and E, the total elongation and the combination of tensile strength and total elongation were slightly lower than those of steel A. In addition, the reductions of area were significantly decreased (Fig. 6-8(d)). The microstructure of steels D and E became fine, and the volume fraction of MA-like phase was significantly increased. Mechanical stability of the retained austenite in steels D and E slightly decreased, compared to steel A. From these results, the decreases in reduction of area in steels D and E may be caused by the increase in volume fraction of the MA-like phase. On the other hand, the decrease in total elongation may be caused by the decrease in mechanical stability of the retained austenite.

6.4.3 The Effects of Alloying Elements on Stretch-flangeability

The best combination of tensile strength and stretch-flangeability was achieved by adding 0.5%Cr and 1.0%Cr (Fig. 6-9(a)). According to Sugimoto et al.¹⁶⁾, stretch-flangeability of TRIP-aided steel with lath-type structure matrix is mainly controlled by the punching damage in the hole-surface layer and the localized ductility upon expansion. The punching damage is controlled by the following metallurgical factors.

- (1) Matrix: Fine and uniform packet, block, and lath structures suppress the void and crack initiations.
- (2) Second phase: A small difference of flow stress between the matrix and second phase and low second phase fraction suppress the void and crack initiations at the matrix/second phase interface.
- (3) Retained austenite: Higher stability of the retained austenite suppresses crack initiation through the plastic relaxation of localized stress concentration resulting from the strain-induced transformation to martensite.
- (4) Carbide: Carbides located on prior austenitic grain, packet, block, and lath boundaries play a role in crack nucleation sites. If the carbide size in wide

lath-martensite structure is relatively large, voids and cracks initiate near the carbide.

In the present study, the retained austenite characteristics and the volume fraction of carbide in steels A through E changed minimally (Fig. 6-6). On the other hand, the volume fraction of the MA-like phase increased and the MA-like phase was finely dispersed (by decreasing the size of the martensite block) with increasing hardenability factor. The hardenability dependence of metallurgical properties and the stretch-flangeability are illustrated in **Fig. 6-15**. Based on roles (1)–(4) described above and Fig. 6-15, the highest stretch-flangeability of steels B and C can be explained as follows.

If the volume fraction of the MA-like phase increases, stretch-flangeability is reduced by easy void initiation at the matrix/MA-like phase interface, as line (i) in Fig. 6-15(b) shows. In contrast, the stretch-flangeability is increased by a fine microstructure resulting from the short interparticle path of the MA-like phase (d_{MA}). Such a theory is compatible with the results of Figs. 6-11(b), 6-11(e), namely, that the punching damage in the hole-surface layer was lowest in steel C. Therefore, superior stretch-flangeability of steels B and C may be associated with a good balance of (i) volume fraction and (ii) interparticle path of the MA-like phase.

The combinations of tensile strength and stretch-flangeability of steels D and E were not improved, in spite of their finer microstructures than steels B and C. This may be caused by low local elongation and easy void and crack initiation at the matrix/second phase interface by increases in volume fraction of the MA-like phase.

Note that the retained austenite in steels A through E also played a role in enhancing the stretch-flangeability through suppression of void initiation and coalescence upon hole expansion due to plastic relaxation of localized stress concentration resulting from the strain-induced transformation.^{2,16)}

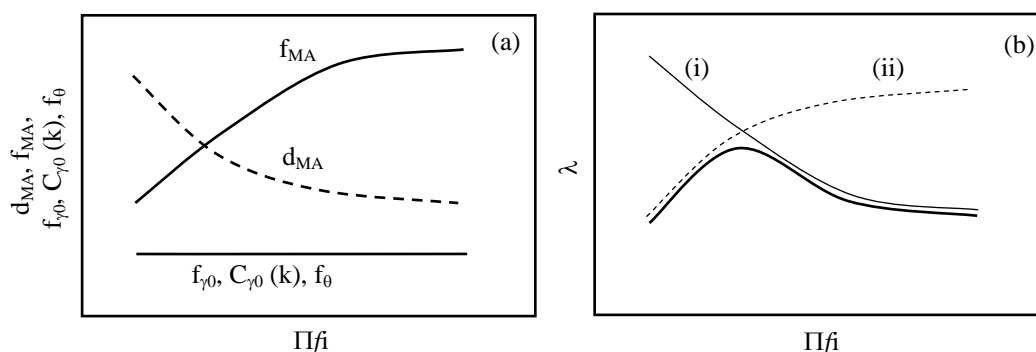


Fig. 6-15. Illustrations of variations in (a) volume fraction (f_{MA}) and interparticle path (d_{MA}) of MA-like phase, retained austenite characteristics (f_{γ_0} , $C_{\gamma_0}(k)$) and carbide fraction (f_{θ}) and (b) stretch-flangeability (λ) as a function of hardenability factor (Πf_i). In Fig. 6-15(b), line (i) decreases stretch-flangeability due to increasing of f_{MA} . Line (ii) increases stretch-flangeability due to decreasing of d_{MA} .

6.5 Summary

The effects of alloying elements on the microstructure, retained austenite characteristics, tensile properties, and formabilities of 0.2%C-1.5%Si-1.5%Mn-0.05%Nb (in mass%) TM steels subjected to an isothermal transformation process at temperatures below M_f were investigated. In addition, relationships between tensile properties, stretch-flangeability, and metallurgical factors were discussed. Primary results can be summarized as follows.

- (1) The microstructures of alloyed TM steels consisted of a wide lath-martensite structure and a uniform, fine MA-like phase on the prior austenitic grain, packet, and block boundaries. It was supposed that the retained austenite was mainly located on the narrow lath-martensite boundaries in the MA-like phase. The volume fraction and interparticle path of the MA-like phase respectively increased and decreased with addition of alloying elements. On the other hand, retained austenite characteristics and carbide volume fractions were minimally changed by alloying.
- (2) The addition of Cr increased tensile strength, yield strength, and yield ratio. This was caused by the increase in strain hardening rate resulting from the increase in volume fraction of the MA-like phase. The total elongation and combination of tensile strength and total elongation were slightly decreased by alloying. The reduction of area was significantly decreased by the additions of Cr-Mo and Cr-Mo-Ni.
- (3) The additions of 0.5%Cr and 1.0%Cr significantly improved the combination of tensile strength and stretch-flangeability of TM steel. This was mainly caused by a good balance of (i) volume fraction and (ii) interparticle path of the MA-like phase, which refined the size of voids and cracks at the matrix/MA-like phase interface on punching and suppressed the void coalescence on hole-expanding.

REFERENCES

- (1) V.F. Zackay, E.R. Parker, D. Fahr and B. Bush: The Enhancement of Ductility in High-strength Steels, *Trans. Am. Soc. Met.*, **60** (1967), pp. 252–259.
- (2) M. Murata, J. Kobayashi and K. Sugimoto: Stretch-flangeability of Ultra High-strength Low Alloy TRIP-aided Sheet Steels with Mixed Structure Matrix of Bainitic Ferrite and Martensite, *Tetsu-to-Hagane*, **96** (2010), pp. 84–92 (in Japanese).
- (3) J. Kobayashi, D. Ina, N. Yoshikawa and K. Sugimoto: Effects of the Addition of Cr, Mo and Ni on the Microstructure and Retained Austenite Characteristics of 0.2% C-Si-Mn-Nb Ultrahigh-Strength TRIP-Aided Bainitic Ferrite Steels, *ISIJ Int.*, **52** (2012), pp. 1894–1901.
- (4) J.G. Speer, D.V. Edmonds, F.C. Rizzo and D.K. Matlock: Partitioning of carbon from supersaturated plates of ferrite, with application to steel processing and fundamentals of the bainite transformation, *Solid State Mater. Sci.*, **8** (2004), pp. 219–237.
- (5) B.C. De Cooman and J.G. Speer: Quench and Partitioning Steel: A New AHSS Concept for Automotive Anti-Intrusion Applications, *Steel Research Int.*, **77** (2006), pp. 634–640.
- (6) W. Cao, J. Shi, C. Wang, L. Xu, M. Wang, Y. Weng and H. Dong: The 3rd Generation Automobile Sheet Steels Presenting with Ultrahigh Strength and High Ductility, *Proc. of ICAS 2010*, Metall. Ind. Press, Beijing, (2010), pp. 196–215.
- (7) K. Sugimoto and J. Kobayashi: Newly developed TRIP-aided martensitic steels, Materials Science & Technology 2010 Conference & Exhibition (Recent Developments in Steel Processing) October 17-21, 2010, Houston, Texas, pp. 1639–1649.
- (8) J. Kobayashi, S. Song and K. Sugimoto: Microstructure and Retained Austenite Characteristics of Ultra High-Strength TRIP-aided Martensitic Steels, *ISIJ Int.*, **52** (2012), pp. 1124–1129.
- (9) J. Kobayashi, K. Sugimoto and G. Arai: Effects of Hot-Forging Process on Combination of Strength and Toughness in Ultra High-Strength TRIP-Aided Martensitic Steels, *Adv. Mat. Res.*, **409** (2012), pp. 696–701.
- (10) J. Kobayashi, D.V. Pham and K. Sugimoto: Stretch-flangeability of 1.5GPa Grade TRIP-aided Martensitic Cold Rolled Sheet Steels, *Steel Res. Int. 2011*, (2011), pp. 598–603.
- (11) J.H. Hollomon and L.D. Jaffe: The Hardenability Concept, *Trans. Am. Inst. Min. Metall. Eng.*, **167** (1946), pp. 601–616.
- (12) H. Maruyama: X-ray measuring method of retained austenite, *J. Jpn. Soc. Heat Treat.*, **17** (1977), pp. 198–204 (in Japanese).

Chapter 6. Effects of microalloying on stretch-flangeability of Ultrahigh-strength TRIP-aided martensitic sheet steels

- (13) D.J. Dyson and B. Holmes: Effect of Alloying Additions on the Lattice Parameter of Austenite, *J. Iron Steel Inst.*, **208** (1970), pp. 469–474.
- (14) O. Umezawa: Practical application of SEM-EBSA analysis, *J. Jpn. Inst. Light Met.*, **50** (2000), pp. 86–93 (in Japanese).
- (15) C. Wang, Y. Zhang, W. Cao, J. Shi, M. Wang and H. Dong: Austenite/martensite structure and corresponding ultrahigh strength and high ductility of steels processed by Q&P techniques, *Sci. China Technol. Sci.*, **55** (2012), pp. 1844–1851.
- (16) K. Sugimoto, T. Iida, J. Sakaguchi and T. Kashima: Retained Austenite Characteristics and Tensile Properties in a TRIP Type Bainitic Sheet Steel, *ISIJ Int.*, **40** (2000), pp. 902–908.
- (17) D.P. Koistinen and R.E. Marburger: A general equation prescribing the extent of the austenite-martensite transformation in pure iron-carbon alloys and plain carbon steels, *Acta Metall.*, **7** (1959), pp. 59–60.
- (18) T. Suzuki, Y. Ono, G. Miyamoto and T. Furuhashi: Effects of Si and Cr on Bainite Microstructure of Medium Carbon Steels, *ISIJ Int.*, **50** (2010), pp. 1476–1482.
- (19) T. Sakaki, K. Sugimoto, T. Fukuzato: Role of internal stress for continuous yielding of dual-phase steels, *Acta Metall.*, **31** (1983), pp. 1737–1746.
- (20) K. Sugimoto, T. Sakaki, T. Fukuzato, O. Miyagawa: Influence of Martensite Morphology on Initial Yielding and Strain Hardening in a 0.11C-1.36Mn Dual-phase Steel, *Tetsu-to-Hagane*, **71** (1985), pp. 994–1001 (in Japanese).

Chapter 7. Effects of Microalloying on the Impact Toughness of Ultrahigh-strength TRIP-aided Martensitic Steels

7.1 Introduction

It is known that the transformation-induced plasticity (TRIP¹⁾) of the metastable retained austenite phase in steels significantly improves the formability of the corresponding steels. Making use of this fact, third-generation advanced high-strength steels (AHSSs) such as a TRIP-aided bainitic ferrite steel (TBF steel)²⁻⁵⁾, medium Mn-TRIP steel⁶⁻⁸⁾, quenching and partitioning steel (Q&P steel)⁹⁾, and quenching-partitioning-tempering steel (Q-P-T steel)^{10,11)} have been developed, with the aim of reducing the weights of automobiles and improving their crash safety.

Recently, a 0.2%C-1.5%Si-1.5%Mn-0.05%Nb (in mass%) TRIP-aided steel with a lath-martensite structure and a fine retained austenite phase (TM steel) has been developed by Sugimoto *et al.*^{12,13)} This steel, which was subjected to an isothermal transformative heat treatment at temperatures lower than the martensite-finish temperature after the austenitizing process, possesses ultrahigh strength and good stretch-flangeability and stretch-formability.¹³⁾ To mass-produce the TM steel, high hardenability which results from microalloying of Cr, Mo, and/or Ni should be required because the lack of hardenability of steel causes degradation of the ductile-brittle fracture appearance transition temperatures (*FATTs*) due to the formation of pro-eutectoid ferrite on prior austenitic grain boundary. Also good impact toughness (high upper shelf energy and low ductile-brittle transition temperature) which is necessary for further improvement of automobile crash safety is required to apply the TM steel to automotive structural parts. However, there have been no studies on these impact properties of Cr, Mo, and/or Ni-containing TM steels.

In this section, the Charpy impact absorbed values (*CIAVs*) and *FATTs* of 0.2%C-1.5%Si-1.5%Mn-0.05%Nb TM steels microalloyed with Cr, Mo and/or Ni were investigated. In addition, the relationship between these parameters and some of the metallurgical characteristics of the steels were determined.

7.2 Experimental procedure

Five different TM steels with varying Cr, Mo, and Ni concentrations were prepared in the form of 100 kg ingots by vacuum melting, and the ingots were hot-forged into slabs. These slabs were then heated to 1200°C and hot-rolled into thin plates (3 mm in thickness) with the finishing rolling temperature being 850°C. The plates were allowed to cool in air to room temperature and then annealed at 650°C. The chemical compositions of the steel plates are listed in **Table 7-1**; the martensite-start and -finish temperatures (M_s and M_f , respectively; °C) were measured using a dilatometer.

Table 7-1. Chemical composition (mass%), martensite-start and -finish temperatures (M_s , M_f , °C) and hardenability factors (Πf_i) of a steel used.

Steel	C	Si	Mn	P	S	Al	Nb	
A	0.20	1.50	1.51	0.0030	0.0023	0.044	0.050	
B	0.21	1.49	1.50	0.0019	0.0040	0.040	0.050	
C	0.20	1.49	1.50	0.0019	0.0040	0.040	0.050	
D	0.18	1.48	1.49	0.0029	0.0040	0.043	0.050	
E	0.21	1.49	1.49	0.0019	0.0030	0.034	0.049	
SCM420	0.21	0.21	0.77	0.0200	0.0240	*	*	
Steel	Cr	Mo	Ni	N	O	M_s	M_f	Πf_i
A	-	-	-	0.0013	0.0007	409	289	14.2
B	0.50	-	-	0.0012	0.0012	408	292	30.6
C	1.00	-	-	0.0012	0.0012	406	261	47.0
D	1.02	0.20	-	0.0010	0.0015	392	258	76.8
E	1.00	0.20	1.52	0.0014	0.0009	357	245	135.8
SCM420	1.02	0.18	0.06	*	*	*	*	24.6

For the purpose of this study, the hardenability of the steel plates was defined as the product of the various Grossman pearlitic hardenability factors^{14,15)} (Πf_i s). The reason for applying Grossman pearlitic hardenability factor is that some of the other plates contained boron in a concentration of ~20 ppm, along with the other alloying elements, for increasing hardenability. The value of Πf_i was calculated using the following equation:

$$\begin{aligned}
 \Pi f_i = D_1/D_1^* = & (1 + 0.64\%Si) \times (1 + 4.1\%Mn) \times (1 + 2.83\%P) \\
 & \times (1 - 0.62\%S) \times (1 + 2.33\%Cr) \times (1 + 0.52\%Ni) \\
 & \times (1 + 3.14\%Mo) \times (1 + 0.27\%Cu) \\
 & \times (1 + 1.5(0.9 - \%C)),
 \end{aligned}
 \tag{7-1}$$

where D_1 and D_1^* are the ideal critical diameters for the hardenability of alloyed and carbon steels, respectively. The effect of the prior size of the austenite grains is not considered in Eq. (7-1). The last term on the right-hand side of Eq. (7-1) was included only in the case of the steel containing boron, because the hardenability of boron-bearing steel is very sensitive to carbon contents than boron contents. Hereafter, Πf_i is called the “hardenability factor”. The continuous cooling transformation (CCT) diagrams of the steels B through E are shown in **Fig. 7-1**. For comparison, commercial plates of the SCM420 steel were also prepared.

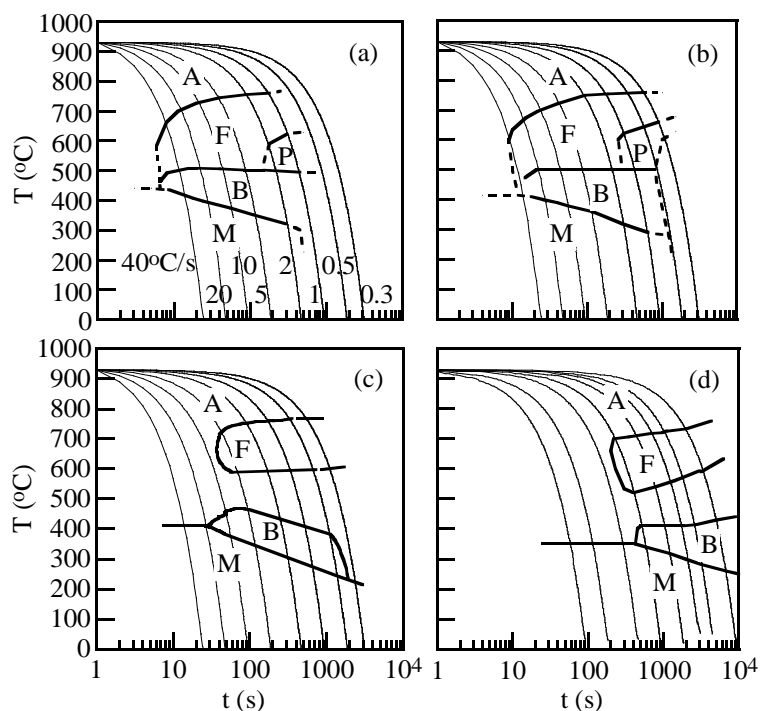


Fig. 7-1. CCT diagrams of the steels (a) B, (b) C, (c) D, and (d) E, in which A, F, P, B, and M represent the austenite, ferrite, pearlite, bainite, and martensite phases, respectively.

Specimens for tensile tests (JIS 14B; 2.5 mm in thickness; 25 mm gauge in length; 4 mm in width) and subsized specimens to determine the *CI*AVs and *FATT*s (JIS 4; 2.5 mm in thickness; 10 mm in width; 55 mm in length; V notch with a depth of 2 mm) were machined from the plates. These specimens were subjected to the heat treatment shown in **Fig. 7-2**, namely, an isothermal transformation at 50°C for 1000 s after being austenitized at 900°C for 1200 s, and partitioned at 300°C for 1000 s to enrich the carbon concentration of retained austenite. The partitioning time used was that reported previously.¹²⁾ The plates of SCM420 steel were quenched to room temperature after austenitizing at 900°C for 1200 s, and then tempered at temperatures ranging from 200°C to 600°C for 3600 s.

The microstructures of the steels were observed via field-emission scanning electron microscopy (FE-SEM; Hitachi Co., S-4100 and FE-SEM-EBSP; JEOL Ltd., JSM-6500F), which was performed using an instrument equipped with electron backscatter diffraction (EBSP) system. Transmission electron microscopy (TEM; JEOL Ltd., JEM-2010) was also used. The steel specimens for the FE-SEM-EBSP analyses were first ground with alumina powder and then with colloidal silica. The volume fraction of carbide in the specimens was measured using carbon extraction replicas and TEM.

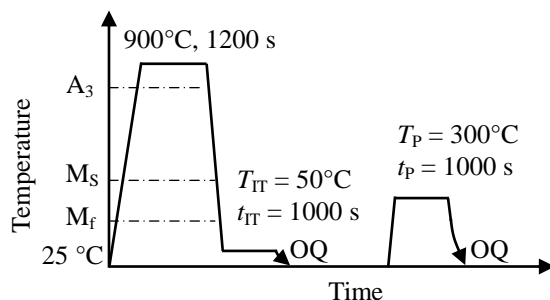


Fig. 7-2. Profile showing the heat treatment to which the steels were subjected. OQ: quenching in oil.

The retained austenite characteristics of the steels were evaluated via X-ray diffractometry (XRD; Rigaku Co., RINT2100). The surfaces of the specimens were electropolished after being ground with Emery paper (#1200). The volume fractions of the retained austenite phases (f_{γ} ; vol%) were quantified from the integrated intensity of the $(200)_{\alpha}$, $(211)_{\alpha}$, $(200)_{\gamma}$, $(220)_{\gamma}$, and $(311)_{\gamma}$ peaks, obtained via X-ray diffractometry using Mo-K α radiation.¹⁶⁾ The carbon concentrations (C_{γ} ; mass%) of the specimens were estimated from Eq. (7-2). For doing so, the lattice constant (a_{γ} ; $\times 10^{-1}$ nm) was determined from the $(200)_{\gamma}$, $(220)_{\gamma}$, and $(311)_{\gamma}$ peaks of the Cu-K α radiation.¹⁷⁾

$$\begin{aligned}
 a_{\gamma} = & 3.5780 + 0.0330\%C_{\gamma} + 0.00095\%Mn_{\gamma} - 0.0002\%Ni_{\gamma} \\
 & + 0.0006\%Cr_{\gamma} + 0.0220\%N_{\gamma} + 0.0056\%Al_{\gamma} - 0.0004\%Co_{\gamma} \\
 & + 0.0015\%Cu_{\gamma} + 0.0031\%Mo_{\gamma} + 0.0051\%Nb_{\gamma} + 0.0039\%Ti_{\gamma} \\
 & + 0.0018\%V_{\gamma} + 0.0018\%W_{\gamma}, \quad (7-2)
 \end{aligned}$$

where $\%Mn_{\gamma}$, $\%Ni_{\gamma}$, $\%Cr_{\gamma}$, $\%N_{\gamma}$, $\%Al_{\gamma}$, $\%Co_{\gamma}$, $\%Cu_{\gamma}$, $\%Mo_{\gamma}$, $\%Nb_{\gamma}$, $\%Ti_{\gamma}$, $\%V_{\gamma}$ and $\%W_{\gamma}$ represent the concentrations of the respective individual elements (mass%) in the retained austenite phase. As an approximation, the concentrations of the added alloying elements were substituted for these concentrations in this study.

The tensile tests were performed at 25 °C using a hard-type testing machine (Shimadzu Co., AD-10TD, as shown in Fig. 4-3 in Chapter 4.) with the crosshead speed being 1 mm/min (resulting in a strain rate of $6.67 \times 10^{-4} \text{ s}^{-1}$).

The impact tests were conducted on a Charpy impact testing machine (Tokyo Testing Machine Inc., CI-300, maximum energy: 300J, **Fig. 7-3**) over temperatures ranging from -196°C to 100°C . Liquid nitrogen, dry ice, ethyl alcohol and water were used to cool and warm the specimens. The specimens were held at the different testing temperatures for 1800 s before being tested. The impact test was carried out within 3 s after picking up the specimen from a regulator. The impact properties were evaluated by determining the upper-shelf Charpy impact absorbed value (*US-CIAVs*) and the *FATTs*

of the specimens. In the present study, the fractions of ductile/brittle fracture surface at each testing temperature were evaluated from digital camera image of fractured specimen. The *FATTs*, which were the 50% shear fracture ductile to brittle transition temperatures, were determined by interpolating the fraction of ductile/brittle fracture surface at testing temperatures between -196°C to -100°C with fitting the data to a hyperbolic tangent curve.



Fig. 7-3. Image of a Charpy impact testing machine (Tokyo Testing Machine Inc., CI-300, maximum energy: 300J).

7.3 Results

7.3.1 Microstructures and carbide

Figure 7-4 shows typical SEM images of the steels A through E and the SCM420 steel. **Figure 7-5** shows the results of the EBSD analyses of the steels A, C, D and E. The matrix structures of the steels B through E comprised phases of varying image qualities (*IQs*). Lower *IQ* phases were located on the prior austenitic grain, packet, and block boundaries and were similar to conventional martensite-retained austenite constituent (MA-like phase). On the other hand, the higher *IQ* phases seemed to be wider lath-martensite structure that was originally transformed. The volume fractions of the MA-like phases increased with an increase in the concentration of the alloying elements (**Table 7-2**). In the steel A (base steel), a pro-eutectoid ferrite was located on

the prior austenitic grain boundary (Fig. 7-4(a)).

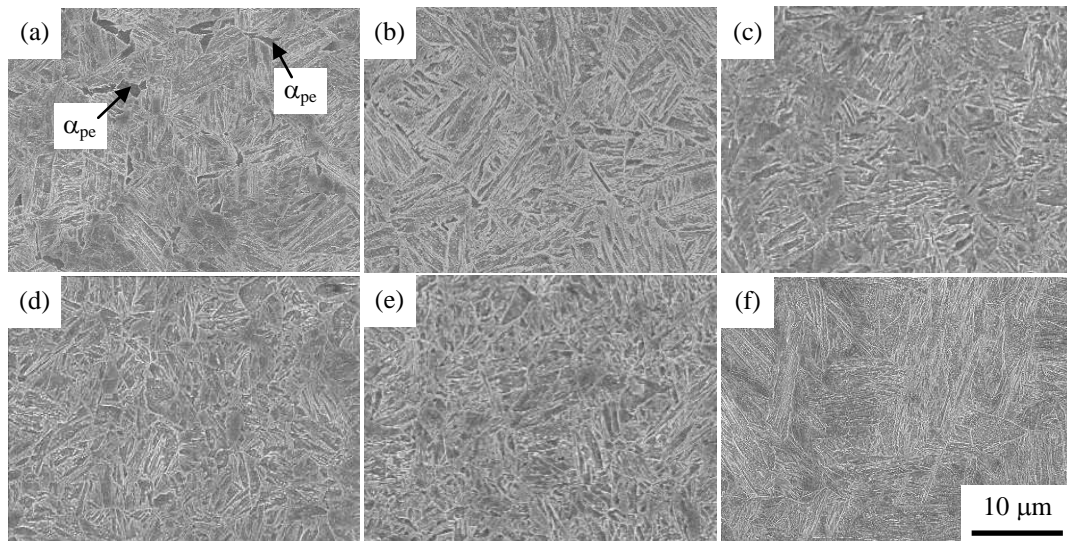


Fig. 7-4. Typical SEM images of the steels (a) A, (b) B, (c) C, (d) D, and (e) E, and (f) SCM420 steel tempered at 200°C. The α_{pe} in (a) is a pro-eutectoid ferrite.

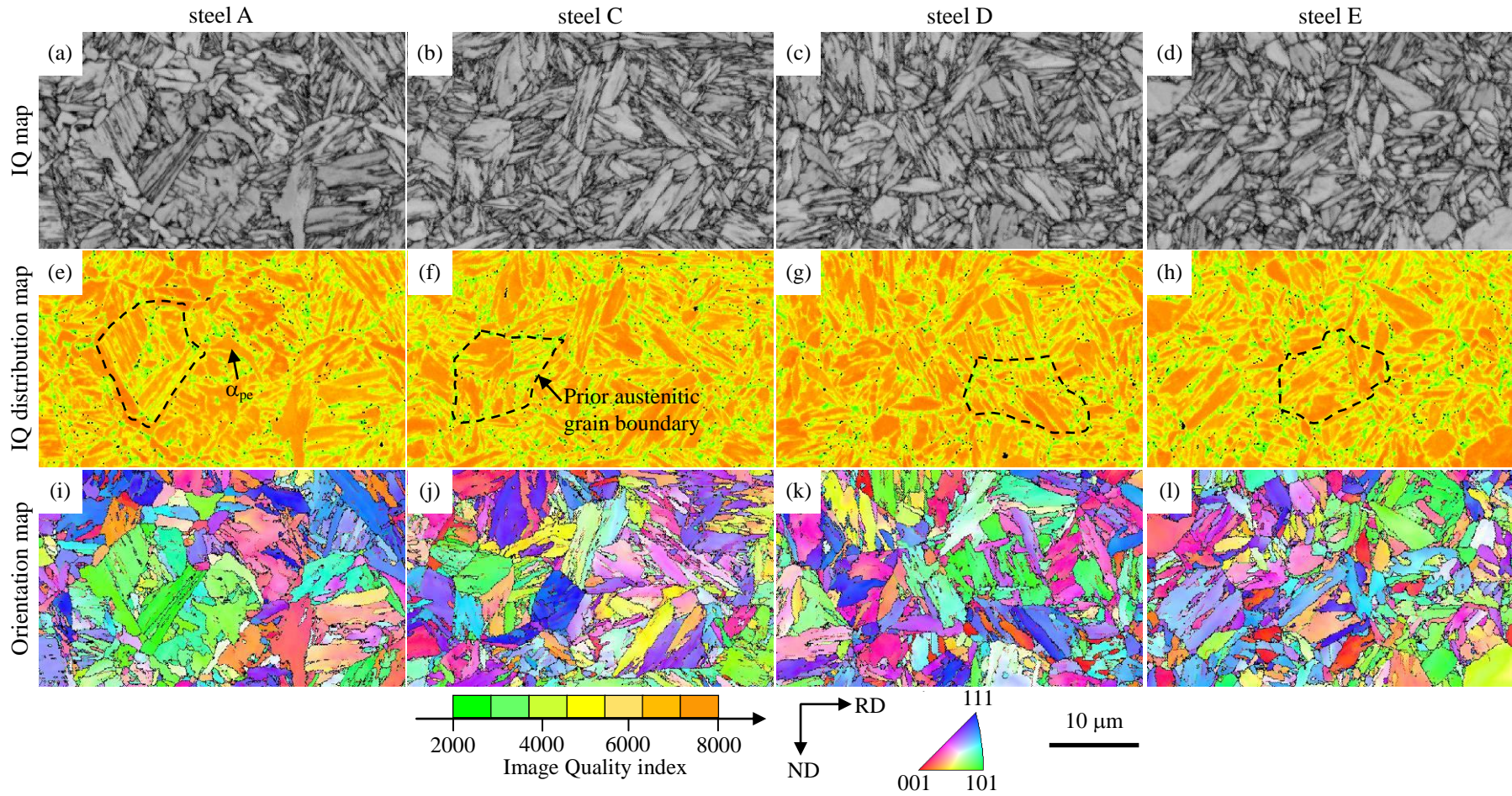


Fig. 7-5. (a–d) Image quality (IQ) maps, (e–h) IQ distribution maps of body centered cubic (bcc), and (i–l) orientation maps of bcc in the steels A, C, D, and E.

Table 7-2. Retained austenite characteristics, volume fractions of the carbide and MA-like phase, tensile properties of the steels A through E and of SCM420 steel. *: not measured

steel	T_P or T_T (°C)	$f_{\gamma 0}$ (vol%)	$C_{\gamma 0}$ (mass%)	f_{θ} (vol%)	f_{MA} (vol%)	YS (MPa)	TS (MPa)	UEl (%)	LEl (%)	TEl (%)	RA (%)	n_{4-7}	ε_f
A	300	3.66	1.07	1.00	14.5	1274	1463	5.9	7.8	13.7	51.9	0.54	0.73
B	300	2.71	0.70	1.62	*	1228	1474	4.6	7.3	11.9	53.9	0.46	0.77
C	300	2.69	0.66	1.43	18.0	1211	1420	4.7	9.1	13.8	56.2	0.52	0.83
D	300	3.70	0.64	0.90	15.6	1258	1476	4.7	7.8	12.5	50.3	0.52	0.70
E	300	2.30	0.56	0.86	18.7	1316	1527	6.1	7.3	13.4	56.0	0.59	0.82
SCM420	200	0.70	≥ 0.20	3.98	13.0	1142	1478	8.2	6.2	14.4	47.0	0.59	0.63
	300	0.31	*	5.14	*	1158	1389	5.3	6.2	11.5	46.2	0.50	0.62

T_P : partitioning temperature; T_T : tempering temperature; $f_{\gamma 0}$: initial volume fraction of the retained austenite phase; $C_{\gamma 0}$: initial carbon concentration of the retained austenite phase; f_{θ} : volume fraction of the carbide; f_{MA} : volume fraction of the MA-like phase; YS : yield stress or 0.2% offset proof stress; TS : tensile strength; UEl : uniform elongation; LEl : local elongation; TEl : total elongation; RA : reduction of area; n_{4-7} : strain hardening coefficient for true strains ranging from 4% to 7%; ε_f : fracture strain calculated from the RA values ($\varepsilon_f = \ln(1/(1 - RA))$).

Figure 7-6 shows typical TEM images of the steel C (1.0Cr steel). It was found that the MA-like phase in this steel was composed of narrow lath-martensite and fine retained austenite films, which were located on the block boundaries. The width of the narrow lath-martensite structure was 0.1–0.2 μm lesser than the width (0.5–1.0 μm) of the wide lath-martensite structure (or the higher *IQ* phase in Fig. 7-5).

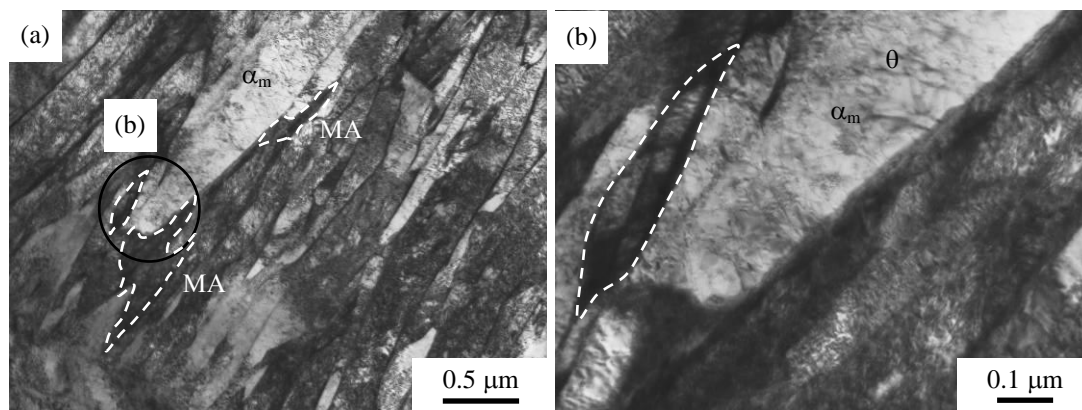


Fig. 7-6. Typical TEM images of the steel C, in which α_m , θ and MA are the wide lath-martensite structure, carbide, and narrow lath-martensite–metastable retained austenite complex phase, respectively. (b); high-magnification image of the area encircled in (a).

Figure 7-7 shows TEM images of the carbides in the steels A through E and the SCM420 steel, which were obtained using their extraction replicas. A large number of fine needle-shaped carbide precipitates were seen in the wide lath-martensite structures in all the steels. It was assumed that these needle-shaped carbide precipitates were formed through auto-tempering when the steel specimens were cooled to temperatures ranging from their corresponding M_s temperatures to 50°C. The volume fraction of the carbide in the steels A through E was between 0.86 vol% and 1.62 vol%, with the steels B and C (0.5Cr and 1.0Cr steels, respectively) possessing larger carbide fraction (Table 7-2). However, the volume fractions of the carbide of these steels were much lower than that of the SCM420 steel, as shown in Table 7-2. Note that the carbide precipitates in the steels A through E were oriented along a single orientation, while those in SCM420 steel exhibited multiple orientations.

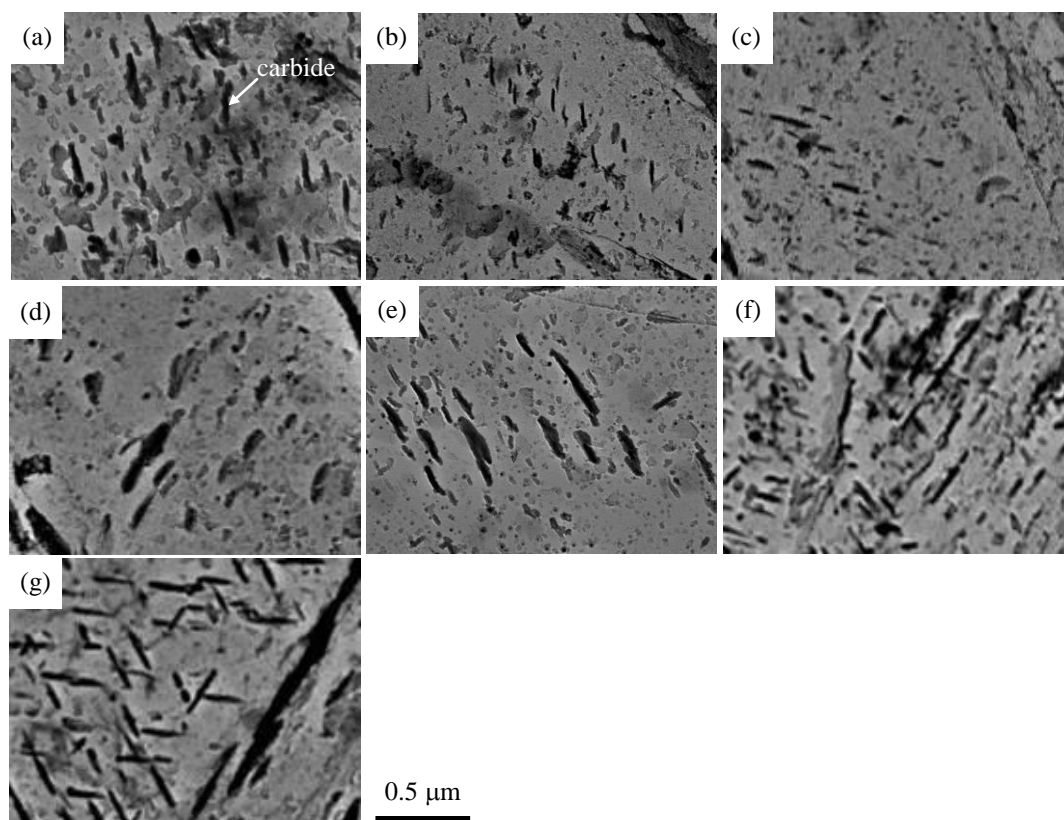


Fig. 7-7. TEM images of the extraction replicas of the wide lath-martensite phases in the steels (a) A, (b) B, (c) C, (d) D, and (e) E, and the SCM420 steel tempered at (f) 200°C and at (g) 300°C.

7.3.2 Retained austenite characteristics and tensile properties

Table 7-2 shows the initial volume fractions and carbon concentrations of retained austenite phase and the volume fractions of the carbide for the steels A through E and for the SCM420 steel. The tensile properties of these steels are also listed. The volume fractions and carbon concentrations of the retained austenite phases in the steels A through E ranged from 2.30 vol% to 3.70 vol% and from 0.56 mass% to 1.07 mass%, respectively. Except in the case of the steel D (1.0Cr-0.2Mo steel), the volume fraction of the retained austenite phase in all the steels tended to decrease with the addition of the respective alloying element. The carbon concentration also decreased slightly with the addition of the respective alloying element.

The yield stresses and tensile strengths of the steels A through E were between 1211 and 1316 MPa and between 1420 and 1527 MPa, respectively. The yield stress and tensile strength values of the steels increased significantly after the addition of Cr, Mo, and/or Ni, and were higher than those of SCM420 steel. The total elongations ranged from 11.9% to 13.8% and did not change significantly after the addition of the alloying elements.

7.3.3 Charpy impact toughness

Figure 7-8 shows the typical load-displacement curves for the steels A through E and for SCM420 steel. These were obtained from the results of the instrumental Charpy impact tests, performed at 25°C. The peak load for the steels increased after the addition of the alloying elements. It is found that the absorbed energies corresponding to the peak loads (E_i) for the steels A through E and for SCM420 steel were almost the same. It is worth noting that the steels A through E—and in particular, the steel D (1.0Cr-0.2Mo steel)—exhibited higher absorbed energies for crack propagation (E_p) than the SCM420 steel.

Figure 7-9 shows the typical *CI*AV-testing temperature curves for the steels A through E. **Figure 7-10** shows the variations in the *US-CI*AVs and the *FATT*s of these steels, where the *US-CI*AV is conveniently adopted by *CI*AV at 25°C at which the fracture surface is 100% fibrous, and the *FATT* is the temperature at which the fracture surface is 50-50% cleavage and fibrous. The steels A through E possessed much higher *US-CI*AVs (especially 1.0Cr-0.2Mo steel: steel D) and lower transition temperatures (except for base steel: steel A) than the SCM420 steel. The microalloying of the steels decreased their *FATT*s to some extent.

109

109

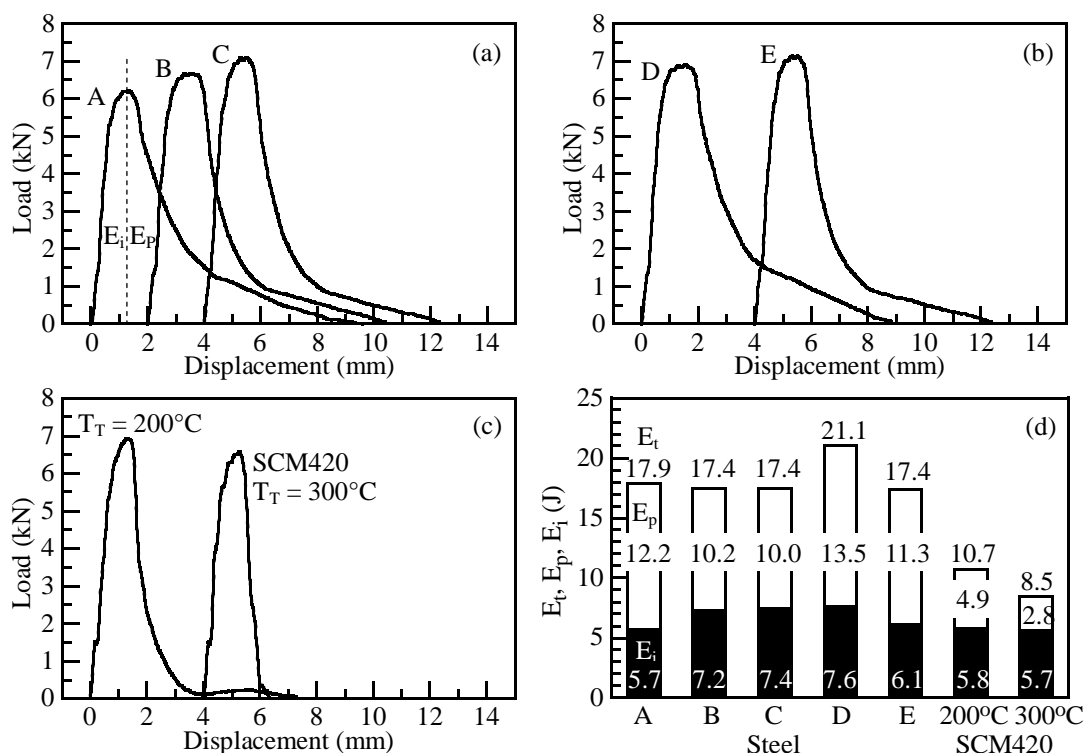


Fig. 7-8. (a–c) Load-displacement curves and (d) total absorbed energies (E_t), crack initiation energies (E_i), and crack propagation energies (E_p), determined at 25°C, of the steels A through E and of the SCM420 steels tempered at 200°C and at 300°C.

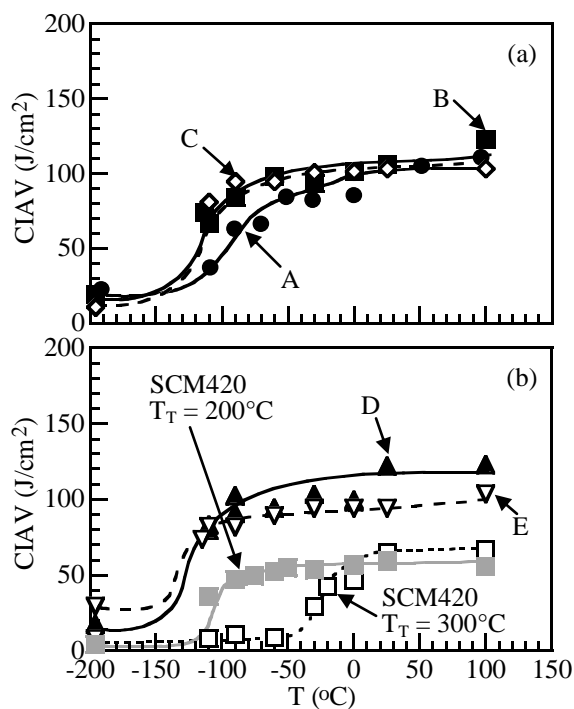


Fig. 7-9. Variations in the Charpy impact absorbed value (*CIAV*) with the testing temperature (*T*) for the steels A through E, and for the SCM420 steels tempered at 200°C and at 300°C.

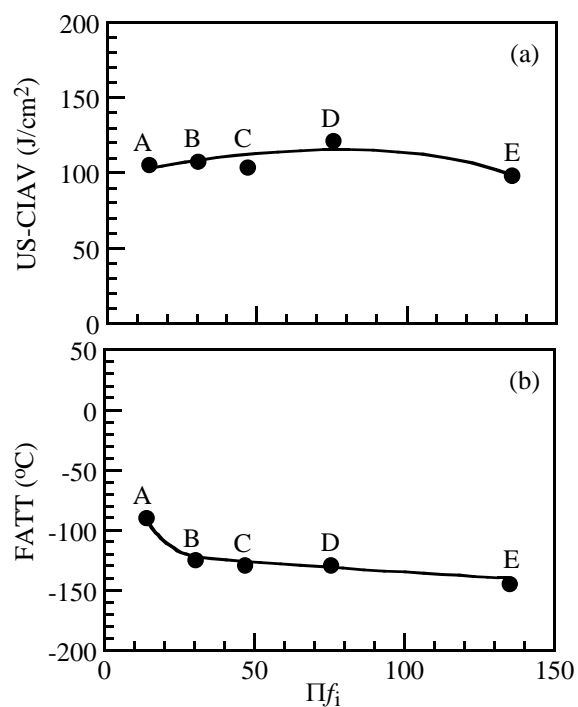


Fig. 7-10. Variations in (a) the upper-shelf Charpy impact absorbed value (*US-CIAV*) and (b) the ductile-brittle fracture appearance transition temperature (*FATT*) as a function of the hardenability factor (Πf_i) for the steels A through E.

The phenomenon of void or crack formation near the notch roots in the case of the steel D (1.0Cr-0.2Mo steel) and SCM420 steel after the impact tests is shown in **Fig. 7-11**. Most of the voids in the steel D appeared to originate at the interface between the wide lath-martensite structure and MA-like phase (Fig. 7-11(b)). On the other hand, in SCM420 steel, a few voids also originated at the lath-boundaries between the wide lath-martensite structures (Fig. 7-11(d)). Note that fewer voids or cracks were present in the steel D than in SCM420 steel.

Figure 7-12 shows typical fractographs of the steels A, C, and D (base steel, 1.0Cr and 1.0Cr-0.2Mo steels, respectively) and of SCM420 steel. Distinct dimple fractures, consisting of coarse and fine dimples, were formed near the fracture surfaces in the steels A, C, and D, which fractured at 25°C (Figs. 7-12(a)–7-12(c)). These fractures were different from those seen near the fracture surface in SCM420 steel, which contained only fine dimples (Fig. 7-12(d)). When the impact tests were performed at –196°C, quasi-cleavage fractures occurred in all the steels, except for SCM420 steel. It was tempered at 300°C, resulting in formation of a few large intergranular fracture facets. In contrast, there were many small river-like patterns in the quasi-cleavage fracture surfaces of the steels A through E. It was found that the unit sizes of the cleavage fractures in the steels C and D were somewhat smaller than those of the steel A and SCM420 steel.

III

III

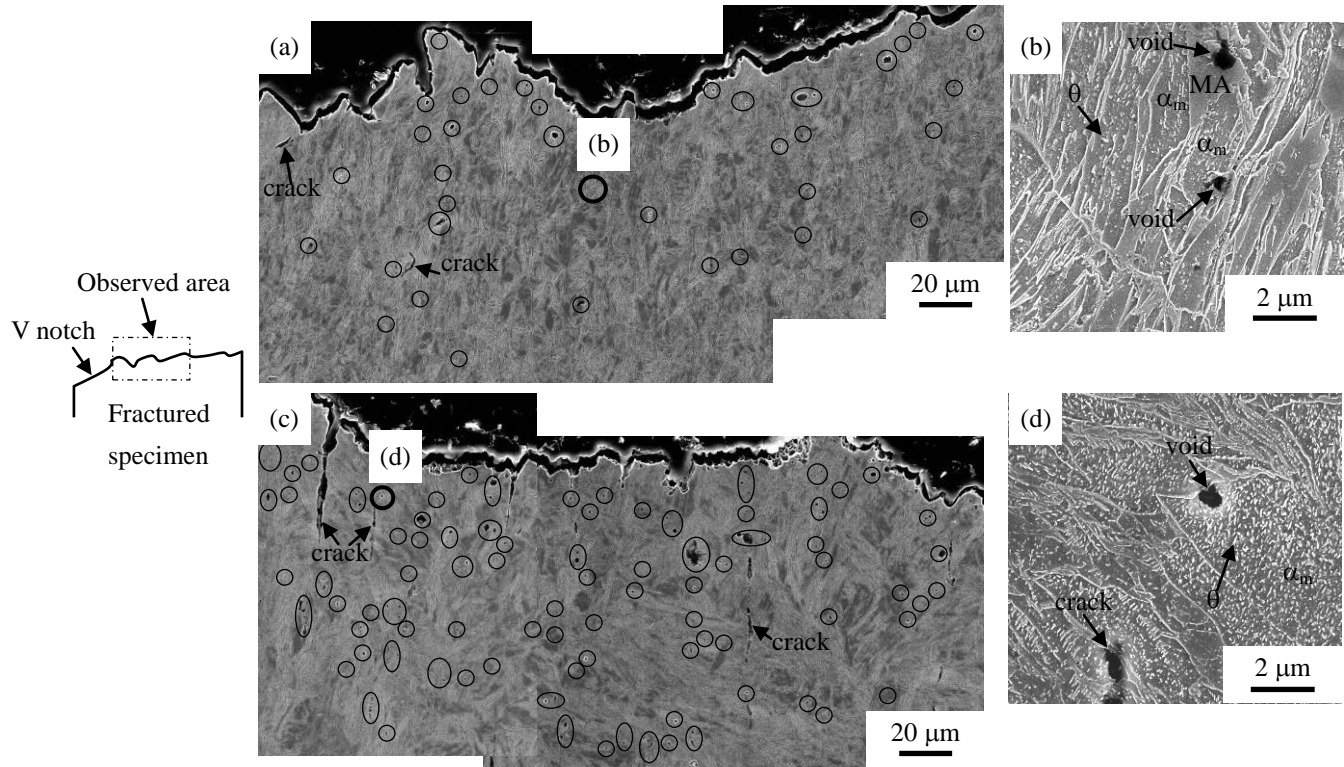


Fig. 7-11. Typical SEM images of the fracture surface located near a notch root for (a, b) the steel D and (c, d) the SCM420 steel tempered at 300°C. The SEM images were obtained at 25°C. (b, d) high-magnification images of the areas encircled in (a, c), respectively. α_m , θ and MA denote the wide lath-martensite structure, carbide and MA-like phase, respectively.

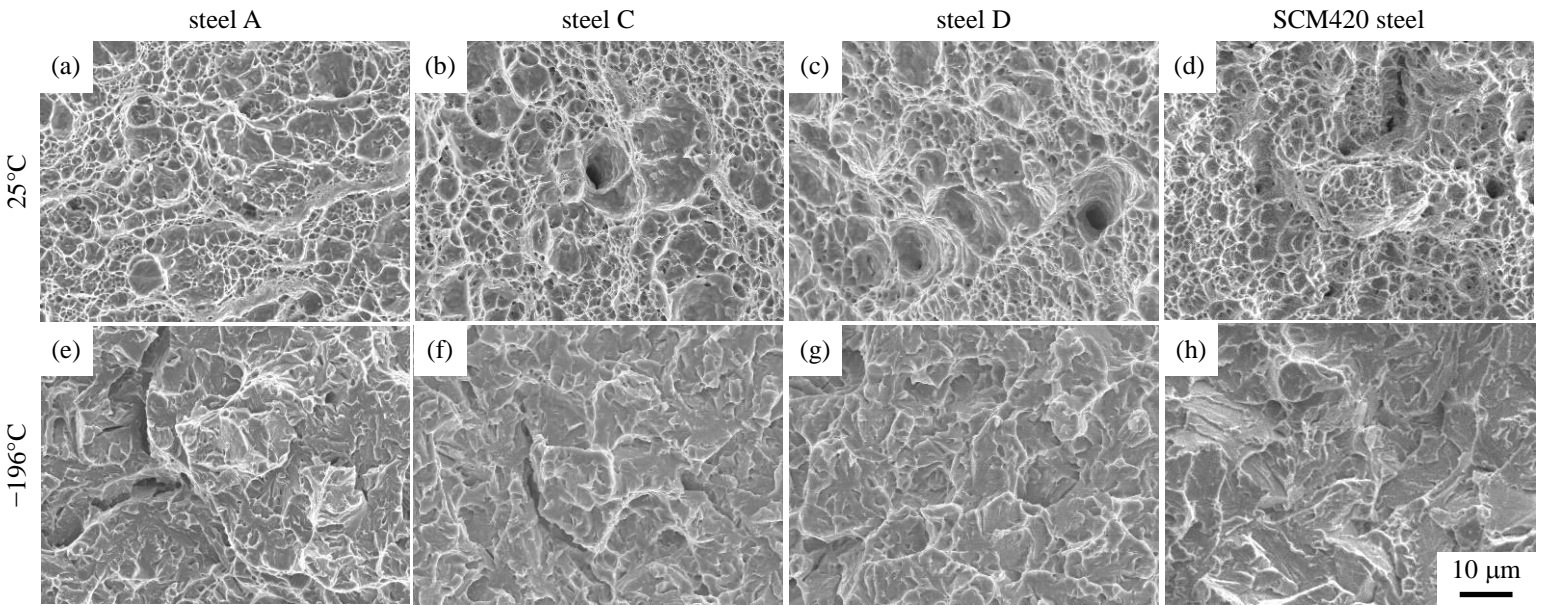


Fig. 7-12. Typical fractographs of the steels A, C and D and of the SCM420 steel tempered at 200°C. The steels were tested at 25°C or at -196°C.

7.4 Discussion

In the present work, the addition of Cr, Mo, and/or Ni to a 0.2%C-1.5%Si-1.5%Mn-0.05%Nb TM steel increased the volume fraction of the MA-like phase and decreased the carbon concentration of the retained austenite in the MA-like phase, with there being a small variation in the volume fraction of the retained austenite phase as well. The formation of the pro-eutectoid ferrite was also suppressed. The carbide volume fractions of the resulting alloyed steels were much lower than that of SCM420 steel. These metallurgical characteristics are expected to influence the impact properties of the steels B through E. To this effect, the relationships between the two are discussed below.

7.4.1 High upper-shelf Charpy impact absorbed values

The steels A through E possessed tensile strengths and *US-CIAV*s superior to those of SCM420 steel, as can be seen from **Fig. 7-13(a)**. As shown in the figure, these values in the case of the steels A through E were nearly the same as those of TBF steel, which has the same chemical composition as the steels A through E.⁴⁾ In general, the *US-CIAV* of TRIP-aided steel is principally controlled by its matrix structure (*i.e.*, its size, morphology, and other such parameters), the characteristics of its carbide (*i.e.*, its volume fraction and size, among other parameters), and the characteristics of its retained austenite phase (*i.e.*, its volume fraction, carbon concentration, and morphology).¹⁸⁾ In addition, it is known that the initiation, growth and coalescence behavior of voids is influenced by the interparticle paths of the second phases (MA-like

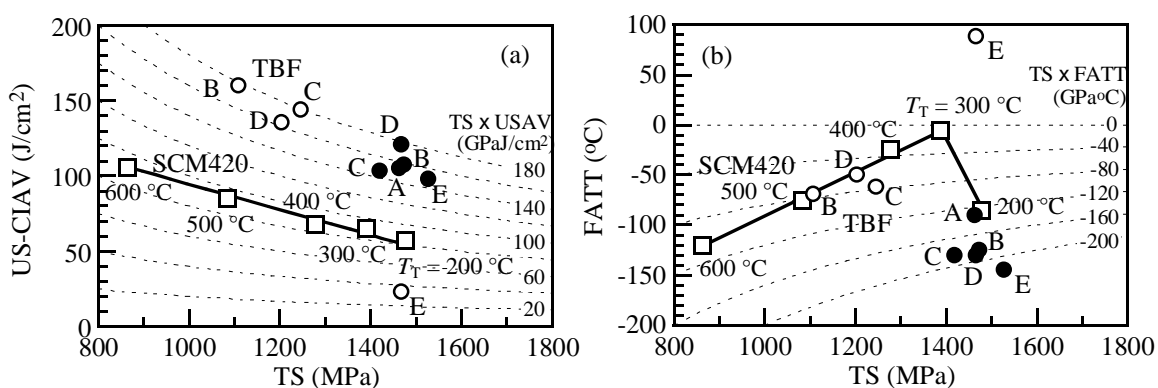


Fig. 7-13. Relationships between tensile strength (*TS*) and (a) the upper-shelf Charpy impact absorbed value (*US-CIAV*) and (b) the ductile-brittle fracture appearance transition temperature (*FATT*) for the steels A through E (●), the SCM420 steel (□) tempered at 200–600 °C, and TRIP-aided bainitic ferrite (TBF) steels⁴⁾ (○), which had the compositions as those of the present steels A through E and were austempered at 400 °C for 1000 s.

phases) or the carbides. According to Horn and Ritchie¹⁹⁾ and Sarikaya *et al.*,²⁰⁾ the carbide precipitates in tempered martensitic steel are located on the prior austenitic grain, packet, and block boundaries, as well as in the wide lath-martensite structure. These carbide precipitates generally act as void-initiation sites in martensitic steels.

Keeping in mind the above-cited studies, the void-initiation and void-coalescence behavior of the steels B through E is illustrated in **Fig. 7-14(a)**. Most of the voids originated at the interface of the MA-like phase and the wide lath-martensite structure (Fig. 7-11(b)). Observations of the cross-sections of the tensile-tested specimens showed that voids in SCM420 steel had originated at a strain of approximately 3.6% (before necking). On the other hand, those in the steel D (1.0Cr-0.2Mo steel) had originated at approximately 6.0% (after necking). These results may be attributed to the fact that the softening of the wide lath-martensite structure and the strain-induced transformation of the metastable retained austenite phase both suppressed the formation of voids in the steel D.

According to the McClintock model for the coalescence of voids, which consists of cylindrical holes with an initial radius b_0 , with the average distance between the holes being l_0 ,^{21,22)} the strain to fracture (ε_f) is given by

$$\varepsilon_f = (1 - n) \ln(l_0/2b_0) / \{ \sinh[(1 - n)(\sigma_a + \sigma_b)/(2\sigma/\sqrt{3})] \}, \quad (7-3)$$

for a material with a stress-strain curve that follows the expression $\sigma = K\varepsilon^n$ (K: strength coefficient; n : strain hardening coefficient). In Eq. (7-3), σ_a and σ_b are the stresses parallel and perpendicular to the axis of the cylindrical holes, respectively, and σ is the true flow stress. It can be seen from Fig. 7-11 that the radius b_0 of the voids in the steel D (1.0 Cr-0.2 Mo steel) was almost the same as that of the voids in SCM420 steel. On the other hand, the average distance between the voids (l_0) for the steel D (l_0 was the same as the size of the prior austenitic grains) was greater than that for SCM420 steel (much shorter than the size of the prior austenitic grains). In this study, it can be considered that *US-CIAVs* of steels A through E are mainly controlled by the average distance between the voids. Actually, when the fracture strains ($\varepsilon_f = \ln(1/(1 - RA))$) were calculated using the reduction in area (*RA*) values listed in Table 7-2, it was found that the fracture strains for the steels A through E were greater than that for SCM420 steel, although the n or n^{4-7} of SCM420 steel was almost the same as those of the steels A through E (Table 7-2). Thus, a large fracture strain was expected to result in the absorption of a large amount of energy after the application of the peak load (E_P ; Fig. 7-8). This large absorbed energy was related to the facts that the number of voids (Fig. 7-11(a)) in the steels A through E were fewer than those in SCM420 steel and that the steels A through E contained a greater number of coarse dimples (Figs. 7-12(b) and

7-12(c)) than the SCM420 steel.

When the *US-CIAVs* of the steels B through E were correlated to the characteristics of their retained austenite phases, the values exhibited a positive relationship with the volume fractions of the retained austenite phases, as shown in **Fig. 7-15(a)**. This was similar to what was noticed for the carbon concentrations of the steels. The microstructures of the steels B through E were characterized by (i) a wide lath-martensite structure matrix with only a small amount of carbide and a lowered carbon concentration and (ii) a large amount of finely dispersed MA-like phases, which contained metastable retained austenite at the prior austenitic grain, packet, and block boundaries. The *US-CIAVs* of these steels were negatively correlated with the volume fractions of their carbide (**Fig. 7-15(c)**). As can be seen from **Figs. 7-11(a)** and **7-11(b)**, a small number of voids were formed mainly at the MA-like phase/wide lath-martensite structure interface in these steels. In SCM420 steel, a large number of voids originated in the wide lath-martensite structure, and these decreased the deformability of the steel owing to the increase in the volume fraction of the carbide (**Figs. 7-11(c)** and **7-11(d)**).

Therefore, on the basis of these results, it was assumed that the high *US-CIAVs* of the steels B through E were caused by presence of the metastable retained austenite of 2–4 vol% and the softened wide lath-martensite structure. In this case, it was assumed that the metastable retained austenite phase effectively lowered the concentration of localized stress near the MA-like phase by plastic relaxation owing to a strain-induced transformation. In addition, only some of the carbide precipitates in the wide lath-martensite contributed to the decrease in the number of void-initiation sites. In this regard, it is not reveal which metallurgical factor is more effective on impact toughness of TM steel.

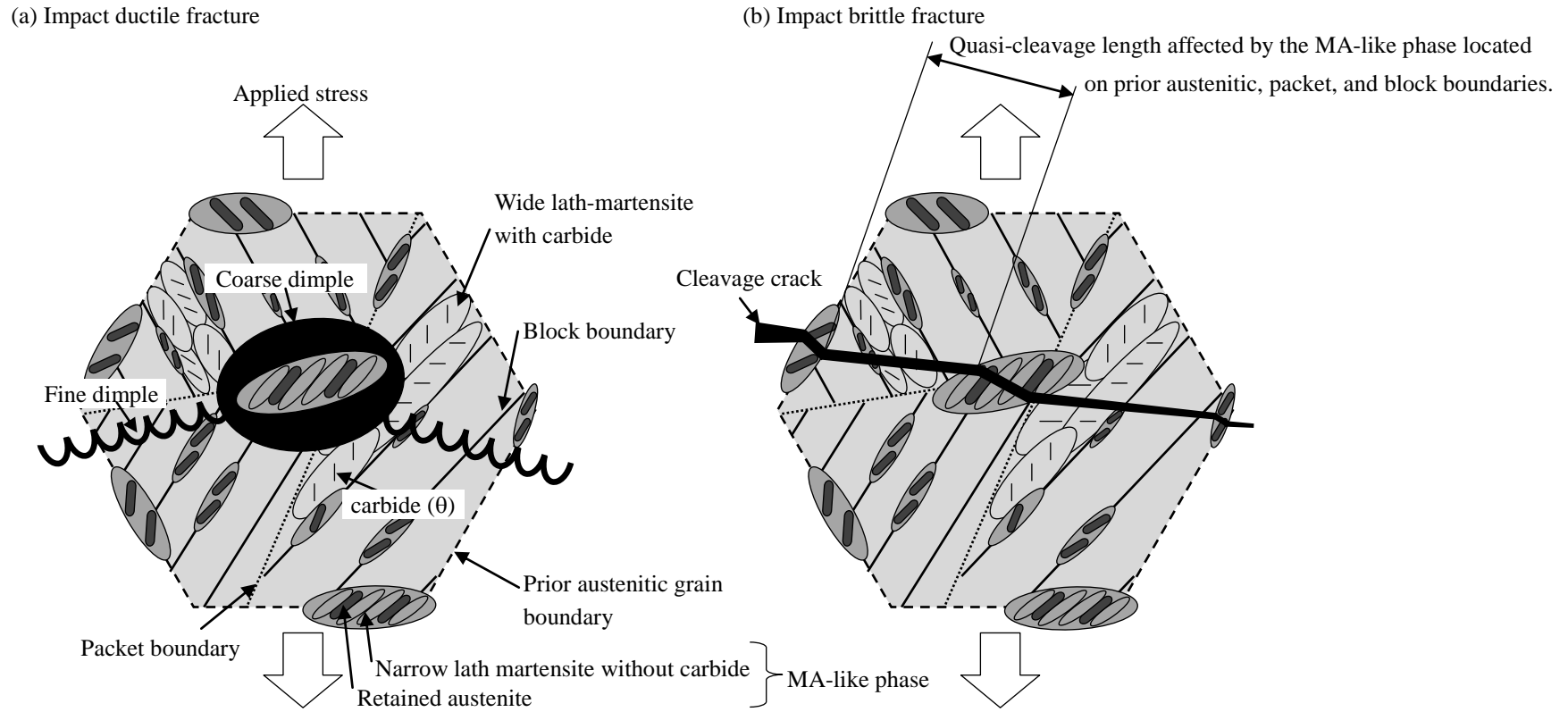


Fig. 7-14. Illustrations showing (a) an impact ductile fracture and (b) a brittle fracture that resulted from the impact test to which the steels B through E were subjected.

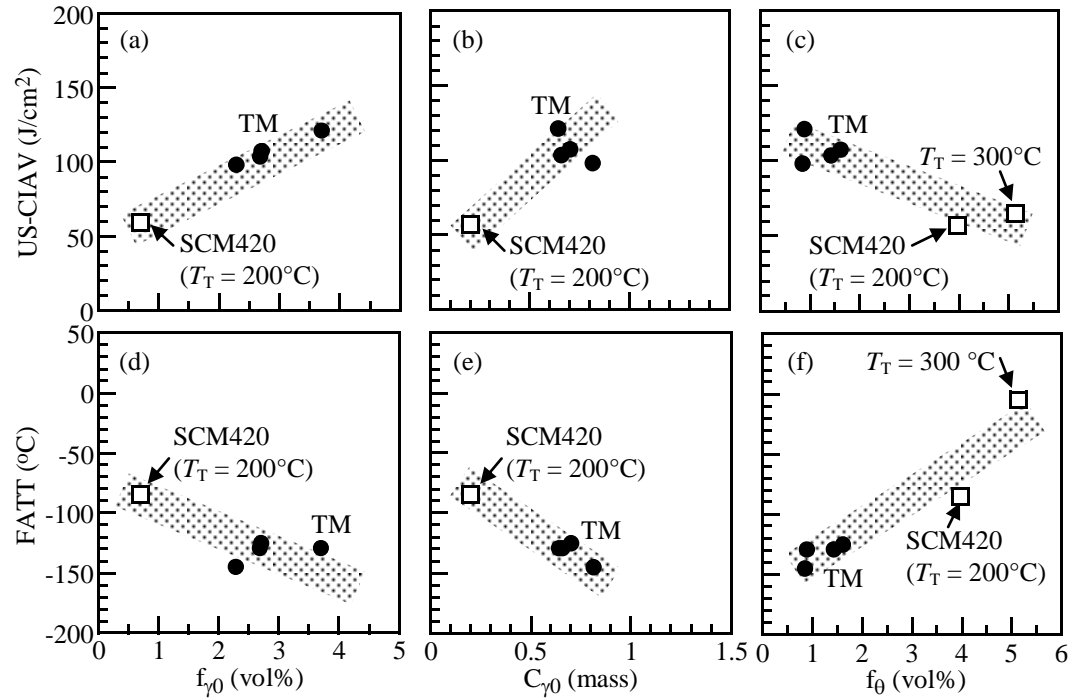


Fig. 7-15. Correlations between (a–c) the upper-shelf Charpy impact absorbed value (*US-CIAV*) and (d–f) ductile-brittle fracture appearance transition temperature (*FATT*) and the initial retained austenite characteristics ($f_{\gamma 0}$ and $C_{\gamma 0}$) or volume fraction of the carbide (f_{θ}) for the steels B through E (●) and for SCM420 steel (□).

7.4.2 Low ductile-brittle fracture appearance transition temperature

When the *FATTs* of the steels B through E were compared with that of SCM420 steel and the previously described TBF steel⁴⁾, the steels B through E were found to exhibit lower *FATTs*, despite exhibiting higher tensile strengths (Fig. 7-13(b)). According to Kunitake *et al.*²³⁾, the *FATTs* of low-carbon martensitic and martensitic/bainitic steels are mainly correlated with the packet size (*d*) of the quasi-cleavage fracture surfaces as per the following relationship.

$$FATT \propto d^{-1/2} \quad (7-4)$$

Figure 7-16 shows the relationship between *FATTs* and the packet sizes for the steels A through E. A linear relation existed between the *FATTs* and the packet sizes for the steels B through E. The slopes of these *FATT* vs. $d^{-1/2}$ curves were similar to or lower than those for low-carbon martensitic and martensitic/bainitic steels containing only a small amount of carbide as reported by Kunitake *et al.*²³⁾ This indicates that the small quasi-cleavage crack size of steels B through E was resulted from increase of quasi-cleavage crack deflections due to finely dispersed MA-like phase on prior austenitic grain, packet and block boundaries in matrix structure.

When the *FATTs* of the steels B through E were compared with that of SCM420 steel tempered at 200°C, the *FATTs* of the steels B through E were found to be lower than that of SCM420 steel by $\Delta FATT$. According to Song *et al.*¹⁸⁾, the *FATT* of TBF steel is significantly lowered by the high volume fraction and carbon concentration of the retained austenite phase. As can be seen from Figs. 7-15(d) and 7-15(e), in this study, the *FATTs* of the steels B through E exhibited the same tendency as that reported by Song *et al.* for TBF steel. This indicated that the strain-induced transformation of the retained austenite phase in the present alloyed steels played a role in lowering their *FATTs* by $\Delta FATT$ via plastic relaxation during the propagation of quasi-cleavage cracks, as shown in Fig. 7-14(b). It was assumed that the cleavage cracks originated in the MA-like phase because of the presence of the much softened wide lath-martensite matrix.

On the basis of the above-mentioned facts, it could be concluded that the decrease in the *FATT* ($\Delta FATT$) of the steels B through E was owing to the presence of (i) decrease of the size of quasi-cleavage fracture facet due to a large amount of finely dispersed MA-like phase and (ii) the plastic relaxation of the metastable retained austenite phase by a strain-induced transformation, which played an important role in the suppression of the initiation and propagation of quasi-cleavage cracks.

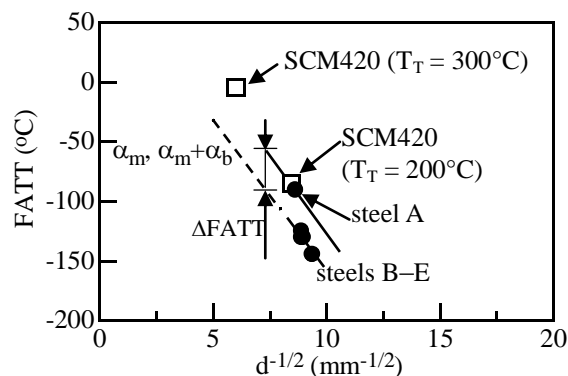


Fig. 7-16. Relationship between the ductile-brittle fracture appearance transition temperature (*FATT*) and the size (*d*) of the packets on the quasi-cleavage fracture surfaces in the steels A through E and in the SCM420 steel tempered at 200°C and at 300°C. The dotted line represents the data for the 0.12%C-0.30%Si-0.83%Mn-0.30%Cu-1.11%Ni-0.53%Cr-0.49%Mo-0.03%V (mass%) steel, whose microstructure comprised martensitic (α_m) or martensitic/bainitic ($\alpha_m+\alpha_b$) structures.²³⁾

It should be noted that the decrease in the *FATT* owing to low-temperature tempering embrittlement did not occur in the steels A through E, in contrast to the SCM420 steel tempered at 300°C. This may have also been due to the presence of the deformable softened wide lath-martensite structure, which had a smaller amount of carbide and because of the plastic relaxation of the strain-induced transformation of the metastable retained austenite phase.

7.5 Summary

The effects of the addition of Cr, Mo, and/or Ni on the Charpy impact absorbed value and ductile-brittle fracture appearance transition temperature of a 0.2%C-1.5%Si-1.5%Mn-0.05%Nb (in mass%) TM steel were investigated. The results can be summarized as follows.

- (1) The microstructures of the alloyed TM steels consisted of a wide lath-martensite structure that contained only a small amount of carbide and a narrow lath-martensite-metastable retained austenite complex phase (MA-like phase) at the prior austenitic grain, packet, and block boundaries. The addition of Cr, Mo and/or Ni refined the microstructure of the TM steel and increased the volume fraction of the MA-like phase by decreasing the M_S temperature of the steel. On the other hand, the alloying elements also decreased the carbon concentration of the retained austenite phase of the steel.
- (2) The upper-shelf Charpy impact absorbed value and ductile-brittle fracture appearance transition temperature of the TM steel were increased and decreased, respectively, by the addition of Cr, Mo and/or Ni. This was particularly true for

the complex addition of Cr and Mo. The impact properties of the resulting alloyed steels were superior to those of SCM420 and TBF steels.

- (3) The high upper-shelf Charpy impact absorbed value was caused by the presence of (i) a softened wide lath-martensite matrix, which contained only a small amount of carbide and had a lower carbon concentration, (ii) a large amount of finely dispersed MA-like phase, and (iii) a metastable retained austenite phase of 2–4 vol% in the MA-like phase, which lead to plastic relaxation by a strain-induced transformation and played an important role in the suppression of the initiation, growth and coalescence of voids.
- (4) The low ductile-brittle fracture appearance transition temperature was associated with the presence of above mentioned (ii) and (iii) which suppressed the initiation and propagation of quasi-cleavage cracks.

REFERENCES

- (1) V.F. Zackay, E.R. Parker, D. Fahr and B. Bush: The Enhancement of Ductility in High-strength Steels, *Trans. Am. Soc. Met.*, **60** (1967), pp. 252–259.
- (2) K. Sugimoto, J. Sakaguchi, T. Iida and T. Kashima: Stretch-flangeability of a High-strength TRIP Type Bainitic Sheet Steel, *ISIJ Int.*, **40** (2000), pp. 920–926.
- (3) T. Hojo, T. Kajiyama, and K. Sugimoto: Impact Properties of C-Si-Mn-Al and C-Si-Mn-Al-Nb Ultra High-Strength Low Alloy TRIP-Aided Bainitic Ferrite Steels, *Proc. of Asia Steel Int. Conf. 2009*, The Korean Institute of Metals and Materials, Seoul, South Korea, (2009), S7-09 (9 pages).
- (4) K. Sugimoto, D. Ina, and J. Kobayashi: Toughness of Advanced Ultra High-Strength TRIP-Aided Steels with Good Hardenability, *Proc. of ICAS 2010*, Metall. Ind. Press, Beijing, 2010, CD-R (14 pages).
- (5) K. Sugimoto, M. Murata and S-M. Song: Formability of Al–Nb Bearing Ultra High-strength TRIP-aided Sheet Steels with Bainitic Ferrite and/or Martensite Matrix, *ISIJ Int.*, **50** (2010), pp. 162–168.
- (6) D.W. Suh, S.J. Park, T.H. Lee, C.S. Oh, and S.J. Kim: Influence of Al on the Microstructural Evolution and Mechanical Behavior of Low-Carbon, Manganese Transformation-Induced-Plasticity Steel, *Metall. Mater. Trans. A*, **41A** (2010), pp. 397–408.
- (7) A. Grajcar, R. Kuziak, and W. Zalecki: Third generation of AHSS with increased fraction of retained austenite for the automotive industry, *Arch. Civ. Mec. Eng.*, **12** (2012), pp. 334–341.
- (8) H. Aydin, E. Essadiqi, I. Jung, and S. Yue: Development of 3rd generation AHSS with medium Mn content alloying compositions, *Mater. Sci. Eng. A*, **564** (2013), pp. 501–508.
- (9) J.G. Speer, D.V. Edmonds, F.C. Rizzo and D.K. Matlock: Partitioning of carbon from supersaturated plates of ferrite, with application to steel processing and fundamentals of the bainite transformation, *Solid State Mater. Sci.*, **8** (2004), pp. 219–237.
- (10) N. Zhong, X.D. Wang, L. Wang, and Y.H. Rong: Enhancement of the mechanical properties of a Nb-microalloyed advanced high-strength steel treated by quenching–partitioning–tempering process, *Mater. Sci. Eng. A*, **506** (2009), pp. 111–116.
- (11) X.D. Wang, N. Zhong, Y.H. Rong, T.Y. Hsu (Z.Y. Xu) and L. Wang: Novel ultrahigh-strength nanolath martensitic steel by quenching–partitioning–tempering process, *J. Mater. Res.*, **24** (2009), pp. 260–267.
- (12) K. Sugimoto and J. Kobayashi: Newly developed TRIP-aided martensitic steels, *Materials Science & Technology 2010 Conference & Exhibition* (Recent

Chapter 7. Effects of Microalloying on the Impact Toughness of Ultrahigh-strength TRIP-aided Martensitic Steels

- Developments in Steel Processing) October 17-21, 2010, Houston, Texas, pp. 1639–1649.
- (13) J. Kobayashi, D.V. Pham and K. Sugimoto: Stretch-flangeability of 1.5GPa Grade TRIP-aided Martensitic Cold Rolled Sheet Steels, *Steel Res. Int.* **2011**, (2011), pp. 598–603.
- (14) M.A. Grossman: Hardenability Calculated from Chemical Composition, *Trans. Am. Inst. Min. Metall. Eng.*, **150** (1942), pp. 227–257.
- (15) J.H. Hollomon and L.D. Jaffe: The Hardenability Concept, *Trans. Am. Inst. Min. Metall. Eng.*, **167** (1946), pp. 601–616.
- (16) H. Maruyama: X-ray measuring method of retained austenite, *J. Jpn. Soc. Heat Treat.*, **17** (1977), pp. 198–204 (in Japanese).
- (17) D.J. Dyson and B. Holmes: Effect of Alloying Additions on the Lattice Parameter of Austenite, *J. Iron Steel Inst.*, **208** (1970), pp. 469–474.
- (18) S-M. Song, K. Sugimoto, M. Kobayashi, H. Matsubara and T. Kashima: Impact Properties of Low Alloy TRIP Steels, *Tetsu-to-Hagane*, **86** (2000), pp. 563–569 (in Japanese).
- (19) R.M. Horn and R.O. Ritchie: Mechanisms of tempered martensite embrittlement in low alloy steels, *Metall. Trans. A*, **9A** (1978), pp. 1039–1053.
- (20) M. Sarikaya, A.K. Jhingan, and G. Thomas: Retained Austenite and Tempered Martensite Embrittlement in Medium Carbon Steels, *Metall. Trans. A*, **14A** (1983), pp. 1121–1133.
- (21) G.E. Dieter: *Mechanical Metallurgy* (SI Metric Edition), McGraw-Hill Book Co., London, U.K., 1988, pp. 262–265.
- (22) F.A. McClintock: A Criterion for Ductile Fracture by the Growth of Holes, *J. Appl. Mech.*, **35** (1968), pp. 363–371.
- (23) T. Kunitake, F. Terasaki, Y. Ohmori, and H. Ohtani: *Toward Improved Ductility and Toughness*, Climax Molybdenum Develop. Co., Kyoto, Japan, (1971), pp. 83–100.

Chapter 8. Notch-fatigue strength of advanced TRIP-aided martensitic steels

8.1 Introduction

For the past decade, second- and third-generation advanced high-strength steels such as 5–25%Mn transformation-induced plasticity (TRIP)/twinning-induced plasticity steels¹⁻³⁾, C-Si-Mn quench and partitioning steels⁴⁾, and C-Si-Mn TRIP-aided bainitic ferrite (TBF) steels^{5,6)} have been developed to reduce the weight of automotive bodies in white and to improve impact safety. In order to enhance the tensile strength further, C-Si-Mn ultrahigh-strength TRIP-aided steels with a martensitic matrix (*TRIP-aided martensitic steel*; TM steel)⁷⁻⁹⁾ have recently been developed for automotive applications. These TM steels can be produced by an isothermal transformation (IT) process below the martensite-finish temperature (M_f) after austenitizing and a subsequent partitioning (P) process at temperatures below 350°C (hereafter a combination of the IT and P processes is called an ITP process). Resultantly, the TM steels are characterized not only by good sheet formability, but also by high impact toughness¹⁰⁾ and fracture toughness.¹¹⁾ If the TM steel possesses a high notch-fatigue strength, it has potential applications such as in precision driving parts and in ultrahigh-pressure common rails for diesel engines. However, such a notch-fatigue strength has not yet been investigated.

In the present study, the notch-fatigue properties of 0.1–0.6%C-1.5%Si-1.5%Mn TM steels were investigated and compared with those of commercial Cr-Mo-containing structural steels (SCM420, SCM435 and SCM440 steels). In addition, the notch-fatigue limit and notch sensitivity were related to metallurgical factors such as microstructural and retained austenite characteristics.

8.2 Experimental procedure

In the current work, five kinds of steel bars, A through E, with different carbon contents were prepared by vacuum melting, followed by hot forging and hot rolling to a diameter of 13 mm. The chemical compositions and estimated martensite-start temperatures (M_{sS})¹²⁾ are listed in **Table 8-1**. For comparison, commercial SCM420 (steel F) and SCM435 (steel G) steel bars, and a vacuum-melted SCM440 (steel H) steel bar of diameter 13 mm were used.

After smooth and notched specimens for tension and fatigue tests (**Fig. 8-1**) were machined from these steel bars, the ITP process illustrated in **Fig. 8-2** (isothermal transformation at $T_{IT} = 50^\circ\text{C}$ and then partitioning at $T_P = 250^\circ\text{C}$) was conducted in salt baths for steels A through E. Partitioning was conducted for further carbon-enrichment in the retained austenite. For steels F–H, quenching in oil at 50°C after austenitizing at

900°C and then tempering at 200 to 600°C for 3600 s were carried out.

Table 8-1. Chemical composition (mass%) and martensite transformation-start temperature (M_s , °C) of a steel used.

Steel		C	Si	Mn	P	S	Cr	Mo	Al	O	N	M_s
TM	A	0.10	1.49	1.50	0.015	0.0015	< 0.01	< 0.01	0.039	0.0007	0.0007	457
	B	0.20	1.51	1.51	0.015	0.0011	< 0.01	< 0.01	0.040	0.0012	0.0012	420
	C	0.29	1.50	1.50	0.014	0.0012	< 0.01	< 0.01	0.040	0.0014	0.0013	388
	D	0.40	1.49	1.50	0.015	0.0012	< 0.01	< 0.01	0.043	0.0015	0.0010	348
	E	0.61	1.50	1.53	0.015	0.0011	< 0.01	< 0.01	0.034	0.0009	0.0014	270
SCM	F	0.21	0.21	0.86	0.016	0.018	1.12	0.16	0.035	*	0.0031	416
	G	0.35	0.17	0.78	0.012	0.019	1.12	0.16	0.033	*	0.0029	369
	H	0.41	0.19	0.80	< 0.005	0.0009	1.00	0.20	0.044	0.0018	0.0009	351

The retained austenite characteristics of steels A through E were investigated by X-ray diffractometry (XRD; Rigaku Co., RINT2100). The specimens were electro-polished after grinding with Emery paper (#1200). The volume fraction of retained austenite (f_γ , vol%) was quantified from the integrated intensity of the (200) $_\alpha$, (211) $_\alpha$, (200) $_\gamma$, (220) $_\gamma$ and (311) $_\gamma$ X-ray diffraction peaks, using Mo-K α radiation.¹³⁾ The carbon concentration (C_γ , mass%) was estimated from the empirical equation¹⁴⁾ shown below. In this case, the lattice constant (a_γ , $\times 10^{-1}$ nm) was measured from the (200) $_\gamma$, (220) $_\gamma$ and (311) $_\gamma$ peaks using Cu-K α radiation.

$$\begin{aligned}
 a_\gamma = & 3.5780 + 0.0330\%C_\gamma + 0.00095\%Mn_\gamma - 0.0002\%Ni_\gamma + 0.0006\%Cr_\gamma \\
 & + 0.0220\%N_\gamma + 0.0056\%Al_\gamma - 0.0004\%Co_\gamma + 0.0015\%Cu_\gamma + 0.0031\%Mo_\gamma \\
 & + 0.0051\%Nb_\gamma + 0.0039\%Ti_\gamma + 0.0018\%V_\gamma + 0.0018\%W_\gamma, \quad (8-1)
 \end{aligned}$$

where $\%Mn_\gamma$, $\%Ni_\gamma$, $\%Cr_\gamma$, $\%N_\gamma$, $\%Al_\gamma$, $\%Co_\gamma$, $\%Cu_\gamma$, $\%Mo_\gamma$, $\%Nb_\gamma$, $\%Ti_\gamma$, $\%V_\gamma$ and $\%W_\gamma$ represent the concentrations of individual elements (mass%) in retained austenite. As an approximation, the added contents of the above alloying elements were substituted for these concentrations in this study.

The microstructures of the steels were observed using a field-emission scanning electron microscope (FE-SEM; Hitachi Co., S-4100 and FE-SEM-EBSP; JEOL Ltd., JSM-6500F) with electron backscattering diffraction (EBSP) system and a transmission electron microscope (TEM; JEOL Ltd., JEM-2010). Samples for FE-SEM-EBSP analysis taken from the grip section of the tensile and fatigue specimens were ground using colloidal silicon after alumina grinding. The volume fraction of the second phase was estimated from the SEM image and the image quality map from EBSP analysis. Vickers hardness tests were carried out using a micro Vickers hardness tester (Shimadzu

Co., HMV-1, load: 4.9 N ($HV0.5$) at 25°C.

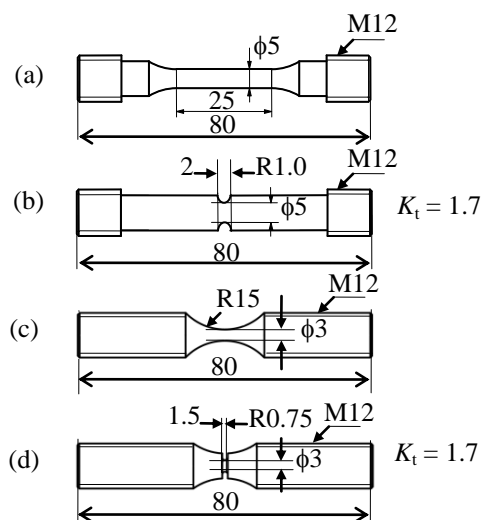


Fig. 8-1. Dimensions of (a, c) smooth and (b, d) notched specimens for (a, b) tensile and (c, d) fatigue tests. Notch root radii of (b) and (d) are 1 mm and 0.75 mm, respectively.

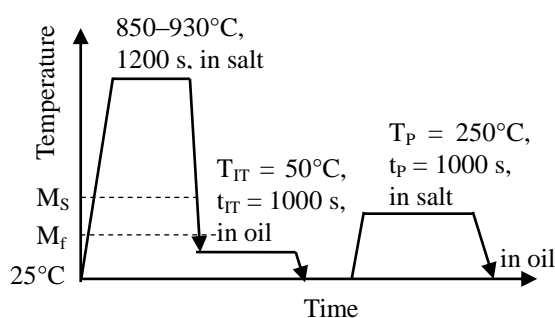


Fig. 8-2. Heat treatment diagram for steels A through E; T_{IT} , t_{IT} , T_P and t_p represent isothermal transformation temperature, isothermal transformation time, partitioning temperature and partitioning time, respectively.

The surfaces of all the specimens for tension and fatigue tests were ground using #600 Emery paper before testing. Tension tests were conducted using a tensile testing machine (Shimadzu Co., Japan, AG-10TD) at 25°C and at a cross-head speed of 1 mm/min. In order to measure precisely yield stress (0.2% offset proof stress), strain gauge (gauge length: 10 mm, Kyowa Electronic Instruments Co., Ltd) was attached on surface of specimen. The displacement was measured from the position of the cross head and the load was measured by the load cell. Fatigue tests were carried out using a multi-type fatigue testing machine (Tokyo Koki Co. Ltd., Japan, PMF4-10, **Fig. 8-3(a)**) at 25°C, with a sinusoidal wave of 80 Hz. The stress ratio, defined as the ratio of minimum stress (σ_{\min}) to maximum stress (σ_{\max}) was $R = 0.1$ (**Fig. 8-3(b)**). The fatigue limit was defined by the maximum value of the stress amplitude ($\sigma_R = \sigma_{\max} - \sigma_{\min}$)

without failure up to 1.0×10^7 cycles.

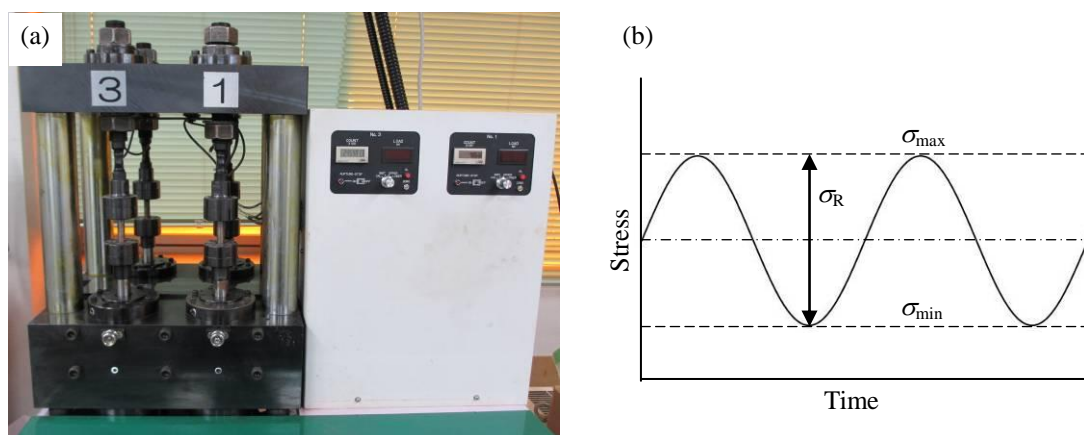


Fig. 8-3. (a) Image of a multi-type fatigue testing machine (Tokyo Koki Co. Ltd., Japan, PMF4-10) and (b) sinusoidal curve of fatigue test. σ_R : stress amplitude, σ_{\max} : maximum stress, σ_{\min} : minimum stress. Stress ratio ($R = \sigma_{\max}/\sigma_{\min}$) is 0.1.

8.3 Results

8.3.1 Microstructure and retained austenite characteristics

Figure 8-4 shows image quality (IQ) maps and orientation maps of steels B, D and E. The microstructures of steels B through E principally consist of a wide lath-martensite structure matrix or martensite block structure (dark-yellow phase) and a blocky second phase (yellowish-green phase) (Figs. 8-4(a)–8-4(c)), although the steel A possesses a large amount of polygonal ferrite located on the prior austenitic grain boundary because of its low hardenability. Steel C possesses the almost same microstructure of steel B. The blocky second phases of steels B through E, which are located on prior austenitic grain, packet and block boundaries, are characterized by lower IQ indexes, indicating that the second phases possess higher dislocation densities and/or finer microstructures¹⁵⁾. With increasing carbon content, block size decreases and the blocky second phase fraction increases. Also, most of the retained austenite phases are very fine and exist mainly in the blocky second phase. The microstructures of steels F–H also consist of a wide lath-martensite structure matrix and a blocky second phase, like steel B through E. However, the steels F through H are characterized by an absence of the retained austenite.

As shown in **Fig. 8-5(a)**, a large amount of fine and needle-shaped carbide seems to precipitate only in the wider lath-martensite structure. It is expected that the needle-shaped carbides are precipitated by auto-tempering on quenching. Most of the blocky second phases are found to consist of narrow lath-martensite structures and retained austenite (Fig. 8-5(b)). Although the retained austenite morphology in the blocky second phase is indistinct, it seems that the retained austenite, observed as a

dotted phase in the second phase (Figs. 8-4(a)–8-4(c)) is located along the narrow lath-martensite boundary. These results suggest that the blocky second phase seems to a martensite-austenite constituent or phase which is observed in martensitic steel of the prior studies.^{9,16)} Hereafter, the blocky second phase is called an “*MA-like phase*”.

Figure 8-6 shows the variations in the initial volume fraction and carbon concentration of the retained austenite and volume fractions of the MA-like phase and carbide, as a function of the carbon content in steels A–E. It is seen in Fig. 8-6(a) that the carbon concentration reaches peak value in steels B and C. Note that the carbon concentrations in steels D and E are lower than the added carbon contents. In contrast, the volume fraction of retained austenite increases with increasing carbon content. In particular, steel E has a significant volume fraction of retained austenite.

The volume fraction of the MA-like phase increases monotonically with increasing carbon content (Fig. 8-6(b)). However, the volume fraction of carbide becomes maximum in steel B, although the carbide fraction ($f_0 = 1.77$ vol%) is much lower than that (4.20 vol%) in steel F.

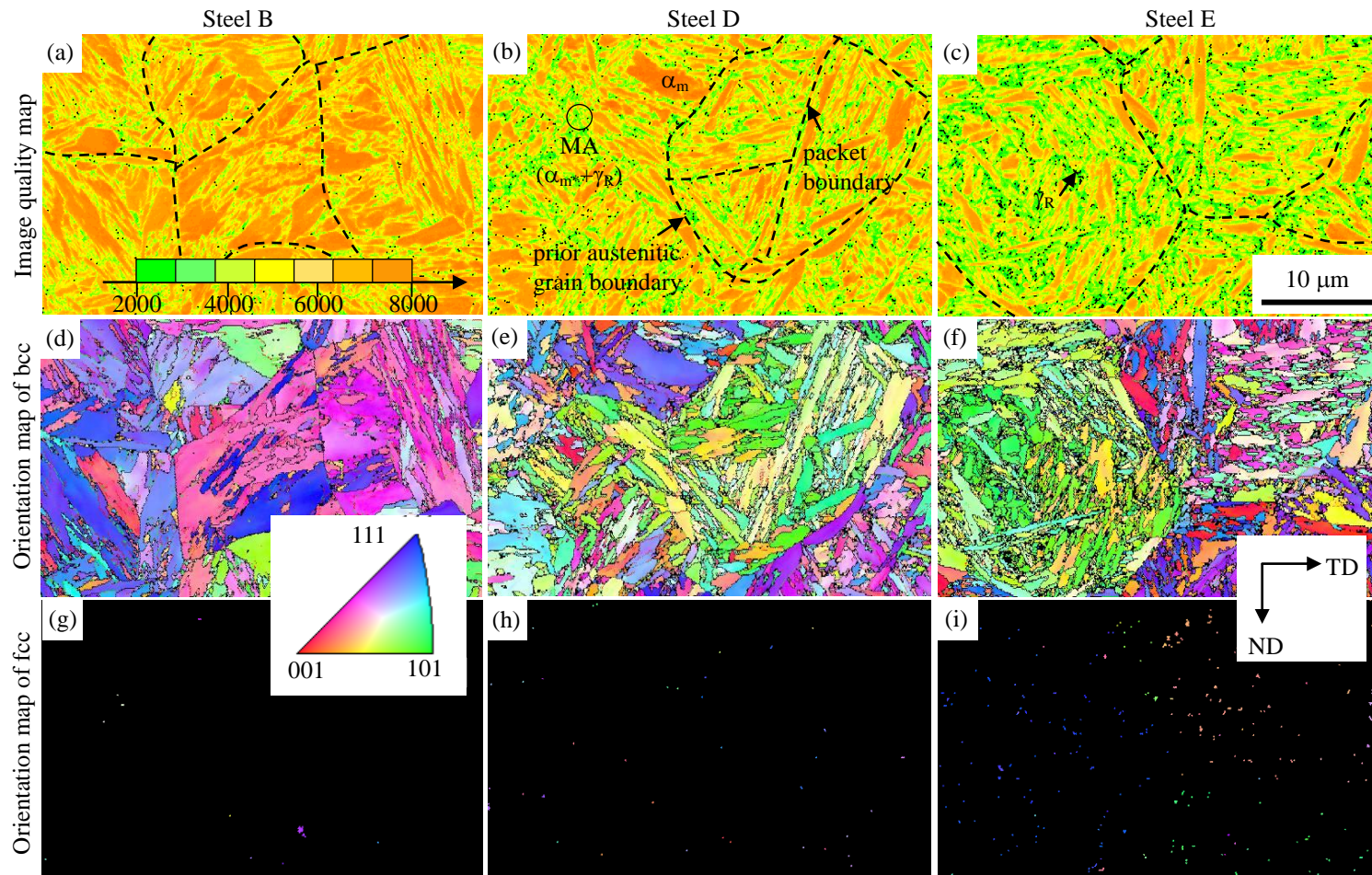


Fig. 8-4. Image quality distribution maps of body-centered cubic (bcc) phase and orientation maps of bcc and face-centered cubic (fcc) phases in steels B, D and E. In (a)–(c), α_m , α_m^* and γ_R represent wide lath-martensite (dark yellow), narrow lath-martensite (yellowish green) and retained austenite (dotted black).

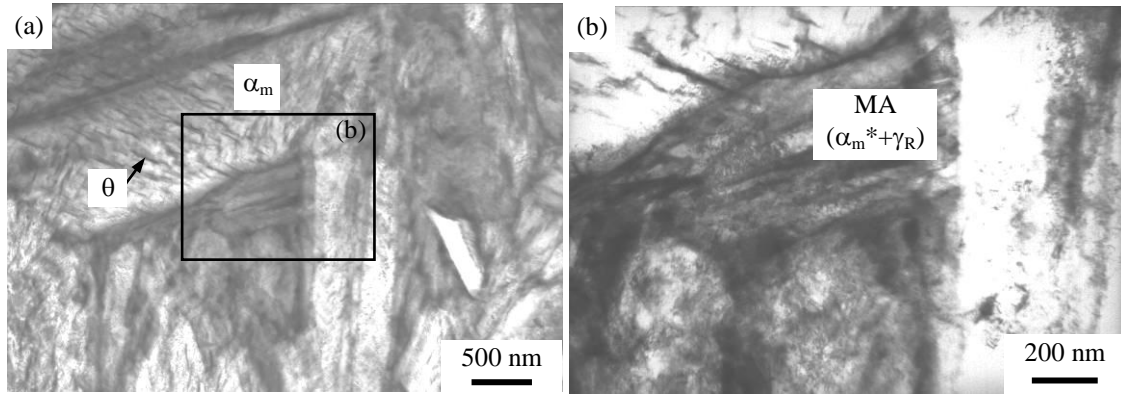


Fig. 8-5. Transition electron microscopy images of steel D, in which α_m , α_m^* , γ_R and θ represent wide lath-martensite, narrow lath-martensite, retained austenite and carbide, respectively.

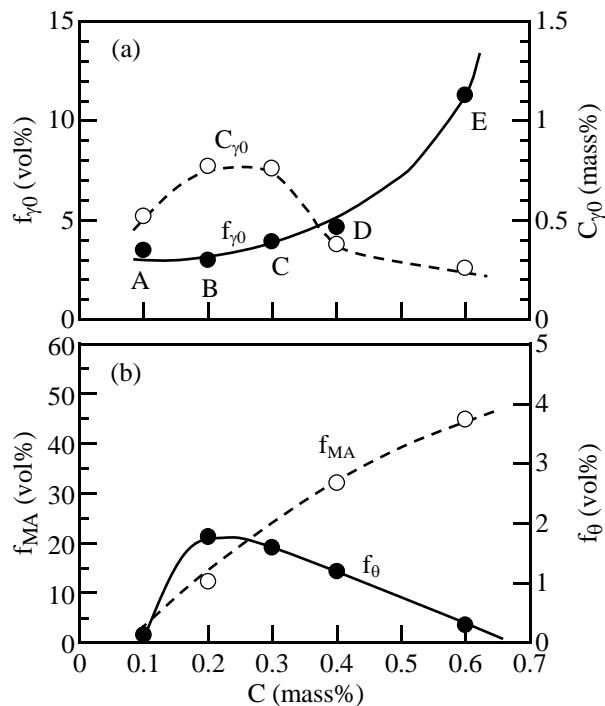


Fig. 8-6. Variations in (a) initial volume fraction ($f_{\gamma 0}$) and carbon concentration ($C_{\gamma 0}$) of retained austenite and (b) volume fractions of MA-like phase (f_{MA}) and carbide (f_{θ}) as a function of carbon content (C) in steels A through E.

8.3.2 Vickers hardness and tensile properties

Figure 8-7 shows flow curves of smooth and notched specimens of steels A through E. Table 8-2 shows the Vickers hardness and tensile properties of these steels. The Vickers hardness values of steels A through E are between 284HV and 717HV, and increase with increasing carbon content. Similarly, both the yield stress or 0.2% offset proof stress and tensile strength increase with increasing carbon content. In contrast, the total elongation decreases with increasing carbon content, except for steel E.

The notch-tensile strength (TS_N) increases with increasing carbon content in the same way as the tensile strength (TS). As a result, steels B through D exhibit high notch-tensile strength ratios ($NSR = TS_N/TS$), except for steels A and E, although these notch-tensile strength ratios are somewhat lower than those of steels F–H.¹⁷⁾

Table 8-2. Vickers hardness, tensile properties, and fatigue properties of steels A–E.

Steel	HV0.5	YS	TS	TS_N	NSR	UEI	TEI	LEI/TEI	FL	FL_N	q
A	284	713	1046	1338	1.28	7.3	17.0	0.57	847	453	1.24
B	457	1193	1495	2214	1.48	3.7	14.0	0.74	969	645	0.72
C	535	1448	1786	2771	1.55	3.4	12.8	0.73	1141	807	0.59
D	600	1620	2009	3042	1.51	4.0	11.7	0.66	1300	847	0.77
E	717	1830	1845	874	0.47	0.0	0.0	0.00	1067	619	1.03

HV: Vickers hardness number; YS (MPa): 0.2% offset proof stress or yield strength; TS (MPa): tensile strength; TS_N (MPa): notch-tensile strength; NSR: notch-tensile strength ratio; UEI (%): uniform elongation; TEI (%): total elongation; FL (MPa): fatigue limit of smooth specimen; FL_N (MPa): fatigue limit of notched specimen; q : notch-sensitivity factor; *: not measured.

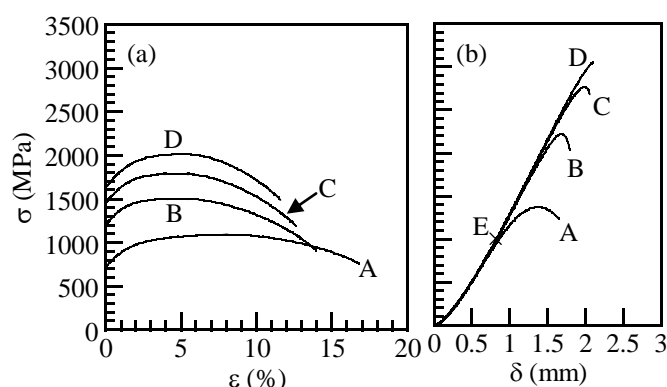


Fig. 8-7. (a) Nominal stress-plastic strain (σ - ε) curves of smooth specimens and (b) nominal stress-displacement (σ - δ) curves of notched specimens in steels A through E.

8.3.3 Notch-fatigue limit and notch sensitivity for fatigue

Figure 8-8 shows stress amplitude-number of cycles (S - N) curves of steels A through E. **Figure 8-9** shows the fatigue limits of smooth and notched specimens and the “notch sensitivity factor q ”¹⁸⁾, defined by the following equation:

$$q = (K_f - 1)/(K_t - 1), \quad (8-2)$$

where K_f and K_t are the fatigue-notch factor ($= FL/FL_N$) and stress concentration factor (1.7 in this study), respectively.

The fatigue limits of both smooth and notched specimens increase linearly with

carbon content (or Vickers hardness) in steels A through D. The notch sensitivity becomes minimum in steel C. When the notch-fatigue limits of steels B through D were compared with those of steels F through H, they were found to be higher and the notch sensitivities were lower.

132

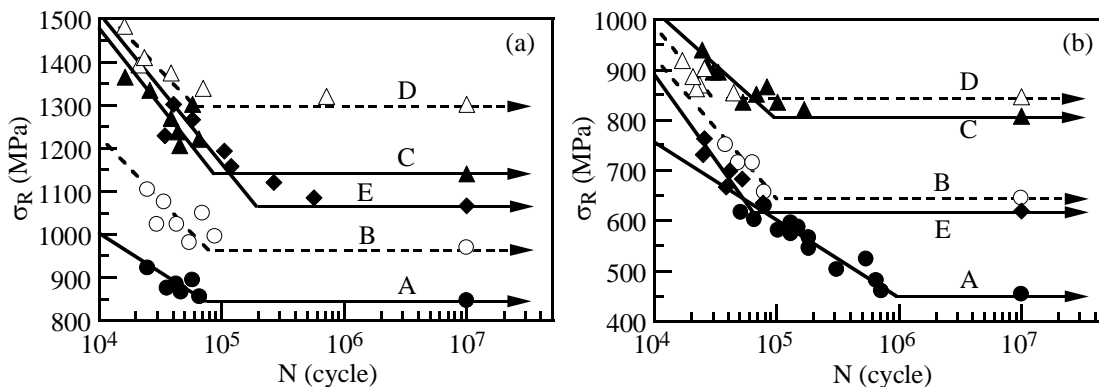


Fig. 8-8. Stress amplitude-number of cycles ($S-N$) curves of (a) smooth and (b) notched specimens in steels A through E.

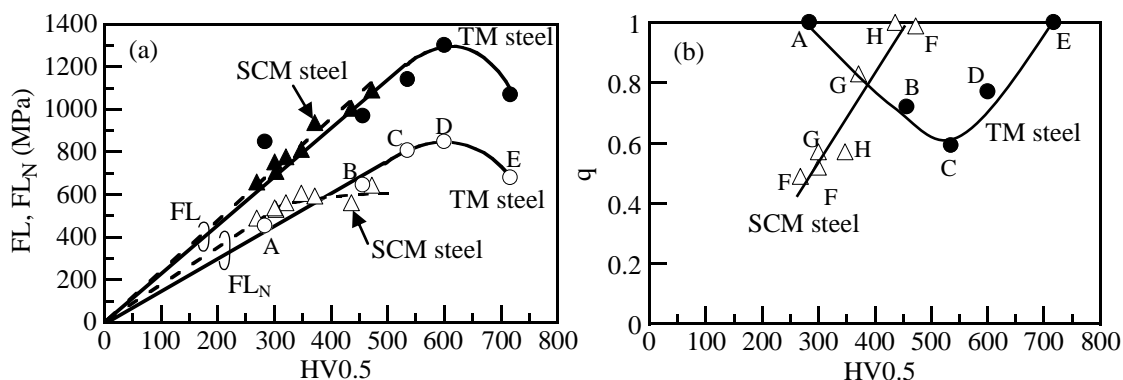


Fig. 8-9. Variations in (a) fatigue limits (FL , FL_N) and (b) notch sensitivity (q) of smooth and notched specimens as a function of Vickers hardness ($HV0.5$) in steels A–E ($\circ\bullet$; TM) and steels F–H ($\Delta\blacktriangle$; SCM).

Figure 8-10(a) shows a typical SEM image of a fatigue crack on a notch root surface of steel D failed at $N_f = 5.0 \times 10^4$ cycles. The fatigue crack is originated mainly in the wide lath-martensite structure. Also, propagation of the crack is disturbed by the MA-like phase. In this case, inclusions such as Al_2O_3 are not likely to be crack initiation sites at the surface in the current study (Fig. 8-10(b)).

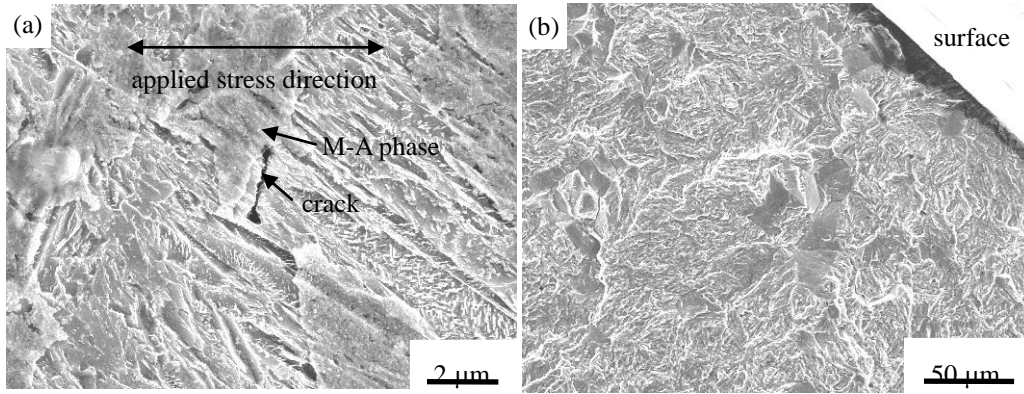


Fig. 8-10. Scanning electron microscopy images of (a) initial crack and (b) failure surface of notched specimen in steel D, fractured at $N_f = 5.0 \times 10^4$ cycles.

8.4 Discussion

8.4.1 Microstructure and retained austenite characteristics of steels B through D

According to Kobayashi et al.⁹⁾, the microstructural changes in TM steels subjected to an ITP process at temperatures lower than the M_f temperature can be illustrated as shown in **Fig. 8-11(d)**, and summarized as follows.

Stages 1–3: When the steel is cooled to a T_3 temperature lower than the M_s temperature, the austenite first transforms to a wide lath-martensite structure (stages 2–3 in Figs. 8-11(a), 8-11(c) and 8-11(d)). In this stage, carbide does not precipitate in the wide lath-martensite structure. According to Koistinen and Marburger¹⁹⁾, the amount of wide lath-martensite structure ($f\alpha_m$) is given by the following equation:

$$f\alpha_m = 1 - \exp\{-1.10 \times 10^{-2}(M_s - T_3)\} \quad (8-3)$$

Stages 3–5: On subsequent continuous cooling to the isothermal transformation temperature ($T_{IT} = 50^\circ\text{C}$) below the M_f temperature, the wide lath-martensite structure is auto-tempered, that is, a small amount of carbide precipitates only in the wider lath-martensite structure. Simultaneously, some supersaturated solute carbon diffuses into the untransformed austenite. Then, most of the untransformed austenite is transformed into a narrow lath-martensite structure, with a little retained austenite on the lath boundary (stages 3–5 in Figs. 8-11(c) and 8-11(d)). No carbide precipitates in the narrow lath-martensite structure.

Stages 5–7: During isothermal transformation holding, supersaturated solute carbon in wide and narrow lath-martensite structures diffuses into the retained austenite (stages 5–7 in Fig. 8-11(d)).

Stages 8–11: The retained austenite phase is further carbon-enriched by diffusion of

supersaturated carbon in the wide and narrow lath-martensite structures, without further carbide precipitation in these lath-martensite structures and a decrease in the retained austenite volume fraction.

As shown in Figs. 8-4 and 8-6 and Table 8-2, the volume fraction of the MA-like phase increased with increasing carbon content in steels B through D, with refining of the wide lath-martensite structure and a small increase in the retained austenite fraction. The carbon concentration of the retained austenite and carbide fractions became maximum in steels B and C. In general, the higher the carbon content (the lower the M_s temperature) of a steel, the greater the increase in the volume fraction of untransformed austenite, accompanied by a subsequent increase in the MA-like phase fraction (Fig. 8-11(b)), as well as a decrease in the carbide fraction in the wide lath-martensite. This may control the volume fraction of the MA-like phase in steels B through D, leading to a high carbon concentration in the retained austenite and carbide fractions in steels B and C. The decreased carbon concentrations of the retained austenite in steels D and E may be influenced by transformation expansion strain of narrow lath-martensite surrounding the retained austenite, which reduces the lattice constant of the retained austenite.

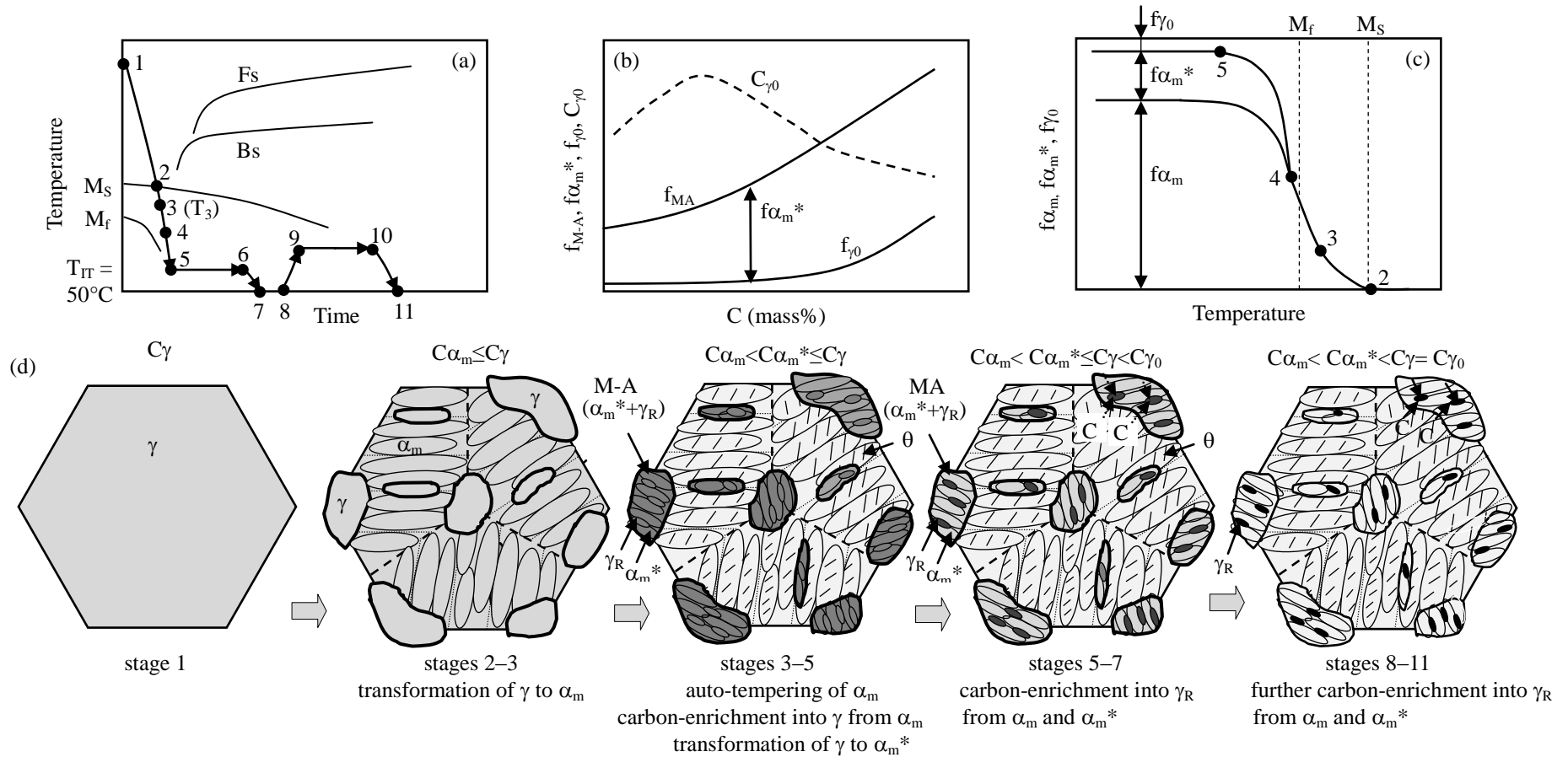


Fig. 8-11. Illustration of (a) heat treatment diagram, (b) carbon content dependences of initial volume fraction (f_{γ_0}) and carbon concentration (C_{γ_0}) of retained austenite and volume fractions of MA-like phase (f_{MA}) and narrow lath-martensite ($f_{\alpha_m^*}$), (c) variations in martensitic transformation volume (f_{α_m}), $f_{\alpha_m^*}$ and f_{γ_0} with temperature and (d) microstructural changes at stages 1–11 during heat treatment in steel D, in which α_m , α_m^* , γ , γ_R , MA and θ represent wide lath-martensite, narrow lath-martensite, austenite, retained austenite, MA-like phase and carbide, respectively. C_γ , C_{α_m} and $C_{\alpha_m^*}$ are carbon concentrations of austenite, wide lath-martensite and narrow lath-martensite, respectively.

8.4.2 Low notch-tensile strength ratios of steels B through D

According to Majima et al.²⁰⁾, the notch-tensile strength ratio of a ductile metal is mainly controlled by two primary factors, namely (i) the stress triaxiality factor and (ii) the ratio of local elongation to total elongation (LEI/TEI). The larger the values of these two factors, the higher the notch-tensile strength ratio because of an increase in plastic notch constraint. **Figure 8-12(a)** shows the notch-tensile strength ratios of steels A through D and steels F through H as a function of LEI/TEI , with those of 0.2%C-1.5%Si-1.5%Mn-0–1.0%Cr-0–0.2%Mo-0–1.5%Ni-0.05%Nb (in mass%) TBF steels.¹⁷⁾ In the figure, these notch-tensile strength ratios tend to increase with increasing LEI/TEI , although steel A exhibits a lower notch-tensile strength ratio. So, it is considered that the higher notch-tensile strength ratios of steels B through D are caused by larger LEI/TEI values under a constant stress triaxiality factor, similar to steels F through H and the TBF steels.

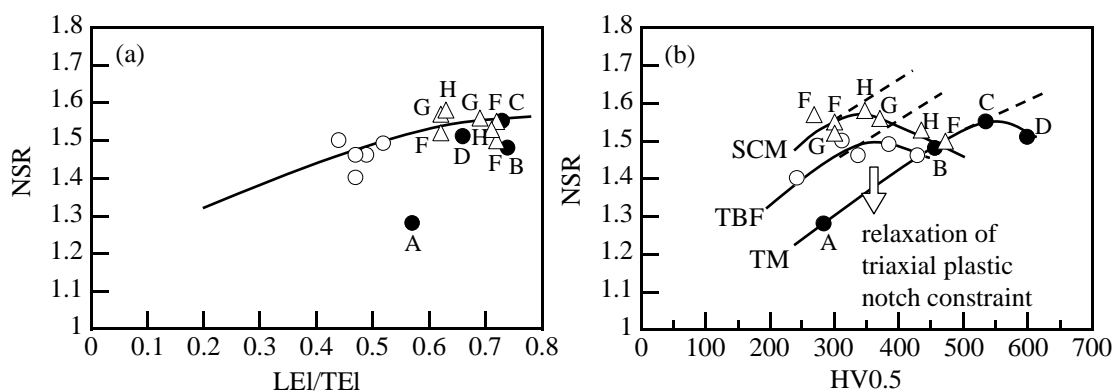


Fig. 8-12. Relationships between notch-tensile strength ratio ($NSR = TS_N/TS$) and (a) LEI/TEI and (b) Vickers hardness (HV) in steels A–D (●; TM), 0.2%C-1.5%Si-1.5%Mn-0–1.0%Cr-0–0.2%Mo-0–1.5%Ni-0.05%Nb (in mass%) TRIP-aided bainitic ferrite steels (○; TBF) and steels F–H (Δ; SCM).

If the above-mentioned notch-tensile strength ratios are plotted as a function of Vickers hardness, steels A through D belong to a group with lower notch-tensile strength ratios than steels F through H, in the same way as for the TBF steels (Fig. 8-12(b)). This result indicates that the retained austenite in the MA-like phase plays a role in reducing the notch-tensile strength ratio through a plastic relaxation of the strain-induced transformation to martensite, as well as the softened wide lath-martensite, which increases the uniform elongation or decreases local elongation. In other words, it is expected that the strain-induced transformation of the retained austenite effectively relaxes triaxial plastic notch constraint in steels B through D.

8.4.3 High notch-fatigue limits of steels B through D

In general, the notch-fatigue limit of a conventional ultrahigh-strength structural steel is saturated in the high Vickers hardness range, as shown in steels F through H (Fig. 8-9(a)). However, the notch-fatigue limits of steels B and D linearly increased with Vickers hardness, even in the Vickers hardness range between 457HV and 600HV.

In section 8.4.2, it was suggested that the strain-induced transformation of the retained austenite plastically relaxes a triaxial plastic notch constraint in steels B through D, compared with steels F through H. In addition, the growth of fatigue cracks was disturbed by the blocky MA-like phase, as shown in Fig. 8-10(a). According to Knott²¹⁾, the plastic zone size (d_Y) at a small crack tip can be estimated using the following equation:

$$d_Y = K^2 / (3\pi Y S^2), \quad (8-4)$$

where K is the stress intensity factor, defined by $\sigma(\pi c)^{1/2}$, σ is the applied stress, and c is the crack length. In steel D, the plastic zone size is estimated to be about 4.0 μm if the fatigue crack length at the first stage is $2c = 30 \mu\text{m}$, equivalent to the prior austenitic grain size, and the applied stress is the maximum stress ($\sigma = \sigma_{\text{max}} = FL/0.9 = 1444 \text{ MPa}$), corresponding to the fatigue limit. The plastic zone always includes some retained austenite particles in MA-like phase (see **Fig. 8-13**) because the interparticle path of MA-like phase is 0.5–2.0 μm (Fig. 8-4(b)). Therefore, the plastic relaxation by the strain-induced transformation of retained austenite can be expected to take place always in the plastic zone during fatigue deformation. From these facts and the metallurgical characteristics of steels B through D, it is considered that the followings contribute to the high notch-fatigue limit and low notch sensitivity through the suppression of crack initiation and propagation in steels B through D:

- (1) a plastic relaxation of localized stress concentration as a result of the strain-induced transformation of 3–5 vol% metastable retained austenite;
- (2) a large amount of finely dispersed MA-like phase along prior austenitic, packet and block boundaries;
- (3) a small amount of carbide, precipitated only in the wide lath-martensites structure

In (1), the transformed martensite also decreases the triaxial plastic notch constraint and plays a role in suppressing crack initiation and propagation. Regarding (2), a difference in flow stress between the wide lath-martensite structure and the MA-like phase may produce a high compressive long-range internal stress in the wide lath-martensite structure matrix, suppressing crack initiation.²²⁾ Factor (3) decreases the number of crack initiation sites and therefore suppresses crack initiation.

According to previous studies^{8,11)}, the mechanical stability of retained austenite in TM steels is hardly influenced by the carbon concentration, because most of the retained austenite phases are surrounded or constrained by hard narrow lath-martensite structures. So, a high volume fraction of retained austenite in steels B through D may further increase the contribution of (1) to fatigue deformation.

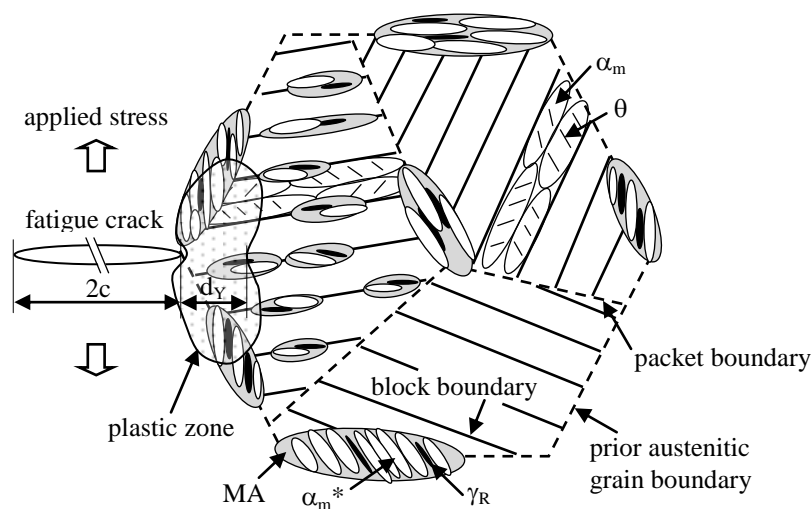


Fig.8-13. Illustration of plastic zone size (d_Y) in steel D at crack tip and distribution of MA-like phases; α_m , α_m^* , γ_R and θ represent wide lath-martensite, narrow lath-martensite, retained austenite and carbide, respectively.

8.5 Summary

The notch-fatigue strengths and notch sensitivities of 0.1–0.6% C-1.5% Si-1.5% Mn (in mass%) TM steels were investigated for automotive applications. Also, the notch-fatigue properties were related to the microstructural and retained austenite characteristics. The main results are summarized as follows.

- (1) If TM steels containing 0.2%, 0.3% or 0.4% C were subjected to an ITP process, consisting of isothermal transformation and partitioning processes, they achieved much higher notch-fatigue limits and lower notch sensitivities than conventional 0.2–0.4% C-1.0% Cr-0.2% Mo structural steels without retained austenite.
- (2) It was expected that high notch-fatigue limits were principally associated with
 - (i) plastic relaxation of localized stress concentration as a result of the strain-induced transformation of 3–5 vol% metastable retained austenite and
 - (ii) a large amount of finely dispersed MA-like phase along prior austenitic, packet and block boundaries, as well as
 - (iii) a small amount of carbide only in the wide lath-martensite structure, which contribute to difficult fatigue crack initiation and/or propagation.

REFERENCES

- (1) T. Furukawa: Dependence of strength-ductility characteristics on thermal history in low carbon, 5 wt%-Mn steels, *Mater. Sci. Technol.*, **5** (1989), pp. 465–470.
- (2) U. Brux, G. Frommeyer, O. Grassel, L.W. Meyer and A. Weise: Development and characterization of high strength impact resistant Fe-Mn-(Al, Si) TRIP/TWIP steels, *Steel Res.*, **73** (2002), pp. 294–298.
- (3) W. Cao, J. Shi, C. Wang, L. Xu, M. Wang, Y. Weng and H. Dong: The 3rd Generation Automobile Sheet Steels Presenting with Ultrahigh Strength and High Ductility, *Proc. of ICAS 2010*, Metall. Ind. Press, Beijing, (2010), pp. 196–215.
- (4) J.G. Speer, D.V. Edmonds, F.C. Rizzo and D.K. Matlock: Partitioning of carbon from supersaturated plates of ferrite, with application to steel processing and fundamentals of the bainite transformation, *Solid State Mater. Sci.*, **8** (2004), pp. 219–237.
- (5) K. Sugimoto, J. Sakaguchi, T. Iida and T. Kashima: Stretch-flangeability of a High-strength TRIP Type Bainitic Sheet Steel, *ISIJ Int.*, **40** (2000), pp. 920–926.
- (6) K. Sugimoto, M. Murata and S-M. Song: Formability of Al–Nb Bearing Ultra High-strength TRIP-aided Sheet Steels with Bainitic Ferrite and/or Martensite Matrix, *ISIJ Int.*, **50** (2010), pp. 162–168.
- (7) K. Sugimoto and J. Kobayashi: Newly developed TRIP-aided martensitic steels, Materials Science & Technology 2010 Conference & Exhibition (Recent Developments in Steel Processing) October 17-21, 2010, Houston, Texas, pp. 1639–1649.
- (8) J. Kobayashi, D.V. Pham and K. Sugimoto: Stretch-flangeability of 1.5GPa Grade TRIP-aided Martensitic Cold Rolled Sheet Steels, *Steel Res. Int. 2011*, (2011), pp. 598–603.
- (9) J. Kobayashi, S. Song and K. Sugimoto: Microstructure and Retained Austenite Characteristics of Ultra High-Strength TRIP-aided Martensitic Steels, *ISIJ Int.*, **52** (2012), pp. 1124–1129.
- (10) K. Sugimoto, D. Ina, and J. Kobayashi: Toughness of Advanced Ultra High-Strength TRIP-Aided Steels with Good Hardenability, *Proc. of ICAS 2010*, Metall. Ind. Press, Beijing, (2010), CD-R(14 pages).
- (11) Junya Kobayashi, Daiki Ina and Koh-ichi Sugimoto: Fracture Toughness of a 1.5GPa Grade C-Si-Mn-Cr-Nb TRIP-Aided Martensitic Steels, *Proc. of Materials Science and Technology 2012 (MS&T2012)*, MS&T Partner Societies, Pittsburgh, PA, USA, (2012), pp. 937–944.
- (12) I. Tamura: *Steel Material Study on the Strength*, Nikkan Kogyo Shinbun Ltd., Tokyo, (1970), p. 40 (in Japanese).
- (13) H. Maruyama: X-ray measuring method of retained austenite, *J. Jpn. Soc. Heat*

- Treat.*, **17** (1977), pp. 198–204 (in Japanese).
- (14) D.J. Dyson and B. Holmes: Effect of Alloying Additions on the Lattice Parameter of Austenite, *J. Iron Steel Inst.*, **208** (1970), pp. 469–474.
- (15) O. Umezawa: Practical application of SEM-EBSP analysis, *J. Jpn. Inst. Light Met.*, **50** (2000), pp. 86–93 (in Japanese).
- (16) C. Wang, Y. Zhang, W. Cao, J. Shi, M. Wang and H. Dong: Austenite/martensite structure and corresponding ultrahigh strength and high ductility of steels processed by Q&P techniques, *Sci. China Technol. Sci.*, **55** (2012), pp. 1844–1851.
- (17) N. Yoshikawa, J. Kobayashi and K. Sugimoto: Notch-Fatigue Properties of Advanced TRIP-Aided Bainitic Ferrite Steels, *Metall. Mater. Trans. A*, **43** (2012), pp. 4129–4136.
- (18) G.E. Dieter: *Mechanical Metallurgy* (SI Metric Edition), McGraw-Hill Book Co., London, (1988), p. 403.
- (19) D.P. Koistinen and R.E. Marburger: A general equation prescribing the extent of the austenite-martensite transformation in pure iron-carbon alloys and plain carbon steels, *Acta Metall.*, **7** (1959), pp. 59–60.
- (20) T. Majima, M. Anzai and H. Nakazawa: Notch Tensile Strength of Ductile Materials, *Bull. JSME*, **29** (1986), pp. 4000–4004.
- (21) J.F. Knott: *Fundamentals of Fracture Mechanics*, Baifukan, Tokyo, (1977), p. 127.
- (22) K. Sugimoto, M. Kobayashi and S. Hashimoto: Ductility and strain-induced transformation in a high-strength transformation-induced plasticity-aided dual-phase steel, *Metall. Trans. A*, **23A** (1992), pp. 3085–3091.

Chapter 9. Conclusions

In the present study, the microstructure, tensile properties, formabilities, impact toughness, and fatigue properties of transformation-induced plasticity (TRIP)-aided martensitic (TM) steel were investigated and are discussed in this thesis. The results obtained in this study are summarized below:

In **Chapter 1**, the background of advanced high-strength steels (AHSSs) and the aim of this study are introduced. AHSSs have been developed to improve the fuel efficiency and impact safety of automobiles. For the production of vehicles made primarily of steel in the future, light-weight automobile bodies can be fabricated by the application of newly developed AHSSs (e.g., TRIP steels). Focusing on the TRIP effect that improves the mechanical properties of steels, the mechanism of TRIP was introduced.

In **Chapter 2**, the effect of partitioning temperature after quenching on the microstructure and retained austenite characteristics of 0.2%C-1.5%Si-1.5%Mn (in mass%) TM steel are presented and discussed. The presence of a carbon-enrichment mechanism during partitioning is proposed in this chapter. TM steel consisting of wide and narrow lath-martensite structures contained about 3 vol% of retained austenite after quenching in oil, with 1.7–2.0 vol% of carbides only in wider lath-martensite structures. With partitioning at temperatures lower than 250°C for times shorter than 1000 s, the volume fractions of the retained austenite and carbide were maintained, although the carbon concentration of the retained austenite increased. In this case, high mechanical properties of TM steel for automotive application can be expected due to a superior TRIP effect.

In **Chapter 3**, the effect of alloying elements on the microstructure and retained austenite characteristics of 0.2%C-1.5%Si-1.5%Mn TM steel are given and discussed. Addition of Cr and Mo to the base steel raised the upper limit of partitioning temperature to 400°C, although the carbon concentration in retained austenite decreased slightly. Further, Ni addition decreased the volume fraction of retained austenite and increased the carbon concentration.

In **Chapter 4**, the effects of quenching or isothermal transformation processes on the tensile properties and formability of 0.2%C-1.5%Si-1.5%Mn-0.05%Nb TM steels are presented and discussed. When isothermally transformed at temperatures below M_f , TM steel showed a tensile strength of 1.5 GPa and a total elongation of 8%. The hole-expanding ratio ($\lambda = 30\text{--}50\%$) was higher than that in steel obtained after quench and partitioning (QP). As a result, steel obtained after the IT process possessed a superior combination of tensile strength and stretch flangeability. It is considered that the excellent combination of IT process steel is mainly caused by a uniform and fine

martensite lath structure matrix and a smaller amount of carbides that suppress the damage caused by punching and cracking on hole expanding, as well as by the presence of metastable retained austenite.

In **Chapter 5**, the effect of partitioning temperature after the IT process on the tensile properties and formabilities of 0.2%C-1.5%Si-1.5%Mn-0.05%Nb TM steel are presented and discussed. Partitioning after the IT process significantly enhanced the formability, especially stretch flangeability, of TM steel as compared to that obtained from partitioning after the quenching process. The excellent stretch flangeability was associated with softening of a mixed uniform wide and narrow lath martensitic structure matrix and an increase in the stability of the retained austenite, which suppressed the damage caused by punching and crack propagation on hole expansion through the partitioning process.

In **Chapter 6**, the effect of the addition of Cr, Mo, and/or Ni on the tensile properties and formabilities of 0.2%C-1.5%Si-1.5%Mn-0.05%Nb TM steel are given and discussed. The addition of 0.5%Cr and 1.0%Cr significantly improved the combination of tensile strength and stretch flangeability of TM steel. This was mainly caused by the refinement of the size of voids and cracks at the interface of an MA-like phase upon punching and suppression of void coalescence on hole expanding.

In **Chapter 7**, the effects of the addition of Cr, Mo and/or Ni on the Charpy impact absorbed value and ductile-brittle fracture appearance transition temperature of 0.2%C-1.5%Si-1.5%Mn-0.05%Nb TM steel are presented and discussed, and are compared with those for TRIP-aided bainitic ferrite (TBF) steel and conventional martensitic steel. When Cr, Cr-Mo, or Cr-Mo-Ni was added to the base steel, TM steel exhibited a high upper-shelf Charpy impact absorbed value that ranged from 100 J/cm² to 120 J/cm² and a low fracture appearance transition temperature that ranged from -150°C to -130°C, while also exhibiting a tensile strength of about 1.5 GPa. This impact toughness of the alloyed steel was far superior to that of conventional martensitic steel and was caused by the presence of a softened wide lath-martensite matrix. This matrix contained only a small amount of carbide and hence had a lower carbon concentration, a large amount of finely dispersed martensite-retained austenite complex phase, and a metastable retained austenite phase of 2–4 vol% in the complex phase, which led to plastic relaxation via a strain-induced transformation and played an important role in the suppression of the initiation and propagation of voids and/or cleavage cracks.

In **Chapter 8**, notch-fatigue strengths and notch sensitivities of 0.1–0.6%C-1.5%Si-1.5%Mn TM steel are given and discussed. If TM steel containing 0.2%, 0.3% or 0.4%C were subjected to an ITP process, comprising isothermal transformation and partitioning processes, much higher notch-fatigue limits and lower

notch sensitivities than those in the case of conventional martensitic steels (SCM steels) without retained austenite were achieved. It was expected that high notch-fatigue limits were principally associated with the plastic relaxation of localized stress concentration as a result of the strain-induced transformation of metastable retained austenite and a large amount of a finely dispersed MA-like phase along prior austenitic, packet, and block boundaries, as well as a small amount of carbide only in the wide lath-martensite structure, which contributed to difficult fatigue crack initiation and/or propagation.

In this thesis, the microstructure, retained austenite characteristics, tensile properties, formabilities, impact toughness and fatigue properties of TM steel were systematically investigated and discussed on various heating processes and chemical compositions. TM steel showed not only ultrahigh strength but also high formability, impact energy absorption capacity, and fatigue strength that are necessary to improve the fuel efficiency and impact safety of automobiles. Although TM steel has possessed some challenges (manufacturability, shape controllability, corrosion resistance, etc.) in putting into practical use, it can be expected that the applications of TM steel would improve the global environment and our lives in the future.

List of Papers

Papers

- (1) Muneo Murata, Junya Kobayashi and Koh-ichi Sugimoto: Stretch-flangeability of Ultra High-strength Low Alloy TRIP-aided Sheet Steels with Mixed Structure Matrix of Bainitic Ferrite and Martensite, *Tetsu-to-Hagane*, Vol. 96, No. 2, 2010, pp. 84–92 (in Japanese).
- (2) Koh-ichi Sugimoto, Junya Kobayashi, Goro Arai: Development of Ultra High-Strength Low Alloy TRIP-Aided Steel for Hot-Forging Parts, *Steel Research International*, vol.81, No. 9, 2010, pp. 254–257.
- (3) Junya Kobayashi, Koh-ichi Sugimoto, Goro Arai: Effects of Hot-Forging Process on Combination of Strength and Toughness in Ultra High-Strength TRIP-Aided Martensitic Steels, *Advanced Materials Research*, Trans Tech Publications, vol. 409, 2012, pp. 696–701.
- (4) Junya Kobayashi, Sung-Moo Song, Koh-ichi Sugimoto: Microstructure and Retained Austenite Characteristics of Ultra High-Strength TRIP-aided Martensitic Steels, *ISIJ International*, Vol. 52, No. 6, 2012, pp. 1124–1129.
- (5) Nobuo Yoshikawa, Junya Kobayashi, Koh-ichi Sugimoto: Notch-Fatigue Properties of Advanced TRIP-Aided Bainitic Ferrite Steels, *Metallurgical and Materials Transactions A*, Vol. 43A, No. 11, 2012, pp. 4129–4136.
- (6) Junya Kobayashi, Daiki Ina, Nobuo Yoshikawa, Koh-ichi Sugimoto: Effects of the Addition of Cr, Mo and Ni on the Microstructure and Retained Austenite Characteristics of 0.2%C-Si-Mn-Nb Ultrahigh-Strength TRIP-aided Bainitic Ferrite Steels, *ISIJ International*, Vol. 52, No. 10, 2012, pp. 1894–1901.
- (7) Junya Kobayashi, Nobuo Yoshikawa and Koh-ichi Sugimoto: Effects of Cr and Mo on Retained Austenite Characteristics and Tensile Properties of TRIP-aided Annealed Martensitic Steel, *Tetsu-to-Hagane*, Vol. 98, No. 11, 2012, pp. 610–617 (in Japanese).
- (8) Junya Kobayashi, Nobuo Yoshikawa and Koh-ichi Sugimoto: Notch-Fatigue Strength of Advanced TRIP-aided Martensitic Steels, *ISIJ International*, Vol. 53, No. 8, 2013, pp. 1479–1486.
- (9) Junya Kobayashi, Daiki Ina, Yuji Nakajima and Koh-ichi Sugimoto: Effects of Microalloying on the Impact Toughness of Ultrahigh-Strength TRIP-Aided Steels, *Metallurgical and Materials Transactions A*, Vol. 44A, No. 11, 2013, pp. 5006–5017.
- (10) Duc Van Pham, Junya Kobayashi and Koh-ichi Sugimoto: Effects of Microalloying on Stretch-flangeability of TRIP-aided Martensitic Sheet Steel, *Tetsu-to-Hagane*, Vol. 99, No. 11, 2013, pp. 659–668 (in Japanese).

- (11) Koh-ichi Sugimoto, Junya Kobayashi and Daiki Ina: Fracture Toughness of Advanced TRIP-aided Martensitic Steels, Key Engineering Materials (Advances in Fracture and Damage Mechanics XII), Vol. 577–578, 2014, pp. 97–100.
- (12) Junya Kobayashi, Daiki Ina, Asahiko Futamura and Koh-ichi Sugimoto: Fracture Toughness of an Advanced Ultrahigh-strength TRIP-aided Steel, ISIJ International, 2014. (in print)

Proceedings of International Conference

- (1) Koh-ichi Sugimoto and Junya Kobayashi: Newly Developed TRIP-aided Martensitic Steels, Materials Science & Technology 2010 Conference & Exhibition (Recent Developments in Steel Processing), The Minerals, Metals & Materials Society (TMS), Warrendale, PA, USA, CD-R, 2010, pp.1639-1649.
- (2) Koh-ichi Sugimoto, Junya Kobayashi and Daiki Ina: Toughness of Ultra High-Strength TRIP-Aided Steels with high Hardenability, The International Conference on Advanced Steels 2010 (ICAS 2010), Metallurgical Industry Press, Beijing, China, Abstract and Manuscript No.FR004, 2010, CD-R (14 pages).
- (3) Junya Kobayashi, Duc Van Pham and Koh-ichi Sugimoto: Stretch-flangeability of 1.5GPa Grade TRIP-aided Martensitic Cold Rolled Sheet Steels", Steel Research International Special Edition: ICTP2011, Wiley-VCH Verlag GmbH & Co. KGaA, Weinheim, Germany, 2011, pp. 598–603.
- (4) Junya Kobayashi, Duc Van Pham, Koh-ichi Sugimoto: Stretch Flangeability and Bendability of a 0.2C-1.5Si-1.5Mn-0.05Nb Ultrahigh-Strength TRIP-Aided Martensitic Sheet Steel, Steel Research International Special Edition: Metal Forming 2012, Wiley-VCH Verlag GmbH & Co. KGaA, Weinheim, Germany, 2012, pp. 883–886.
- (5) Junya Kobayashi, Daiki Ina and Koh-ichi Sugimoto: Fracture Toughness of a 1.5GPa Grade C-Si-Mn-Cr-Nb TRIP-Aided Martensitic Steels, Proc. of Materials Science and Technology 2012 (MS&T2012), MS&T Partner Societies, Pittsburgh, PA, USA, 2012, pp. 937–944.
- (6) Tomohiko Hojo, Junya Kobayashi and Koh-ichi Sugimoto: Hydrogen Embrittlement Resistances of Alloying Elements Adding Ultra High Strength Low Alloy TRIP-aided Steels, Proc. of Materials Science and Technology 2012 (MS&T2012), MS&T Partner Societies, Pittsburgh, PA, USA, 2012, pp. 1186–1192.
- (7) Koh-ichi Sugimoto, Junya Kobayashi and Duc Van Pham: Advanced Ultrahigh-Strength TRIP-aided Martensitic Sheet Steels for Automotive Applications, Proceedings on the International Symposium on New Developments in Advanced High Strength Sheet Steels (AIST 2013), Association for Iron & Steel

List of Papers

Technology, Warrendale, PA, USA, 2013, pp. 175–184.

- (8) Tomohiko Hojo, Junya Kobayashi, Kousuke Yamamoto, Akihiko Nagasaka, Koh-ichi Sugimoto, Takehide Senuma and Yoshito Takemoto: Hydrogen Embrittlement Properties of Ultra High-Strength Low Alloy TRIP-Aided Steels with Hot Forging Process, The 2nd International Symposium on Automobile Steel (ISAS2013), The Chinese for Metals, China, 2013, pp. 169–172.
- (9) Tomohiko Hojo, Junya Kobayashi and Koh-ichi Sugimoto: Fatigue Properties of Nitrogen Added Ultra High-Strength Low Alloy TRIP-Aided Steels, Materials Science & Technology 2013 Conference (MS&T'2013) Proceedings, Montreal, Canada, 2013, pp. 169–176.
- (10) Junya Kobayashi, Yuji Nakajima and Koh-ichi Sugimoto: Effects of Cooling Rate on Impact Toughness of an Ultrahigh-Strength TRIP-aided Martensitic Steel, Proceedings of 8th International Conference on Processing & Manufacturing on Advanced Materials (Thermec' 2013), Las Vegas, USA, December 2-6, 2013, 6 pages. (in print)
- (11) Koh-ichi Sugimoto, Junya Kobayashi and Yuji Nakajima: The Effects of Cooling Rate on Retained Austenite Characteristics of a 0.2C-1.5Si-1.5Mn-1.0Cr-0.05Nb TRIP-aided Martensitic Steel, Proceedings of 8th International Conference on Processing & Manufacturing on Advanced Materials (Thermec' 2013), Las Vegas, USA, December 2-6, 2013, 6 pages. (in print)

Reviews

- (1) Koh-ichi Sugimoto and Junya Kobayashi : Advanced Ultrahigh-strength TRIP-aided Sheet Steel with Excellent Cold Formability, Journal of the Japan Society for Technology of Plasticity, Vol. 54, No. 634, 2013, pp. 949–953

Relationship between this thesis and published papers

Chapter 2: Junya Kobayashi, Sung-Moo Song, Koh-ichi Sugimoto: Microstructure and Retained Austenite Characteristics of Ultra High-Strength TRIP-aided Martensitic Steels, ISIJ International, Vol. 52, No. 6, 2012, pp. 1124–1129. **(Papers No. (4))**

Chapter 3: Koh-ichi Sugimoto and Junya Kobayashi: Newly Developed TRIP-aided Martensitic Steels, Materials Science & Technology 2010 Conference & Exhibition (Recent Developments in Steel Processing), The Minerals, Metals & Materials Society (TMS), Warrendale, PA, USA, CD-R, 2010, pp.1639-1649. **(Proceedings No. (2))**

Chapter 4: Junya Kobayashi, Duc Van Pham and Koh-ichi Sugimoto: Stretch-flangeability of 1.5GPa Grade TRIP-aided Martensitic Cold Rolled

List of Papers

Sheet Steels", Steel Research International Special Edition: ICTP2011, Wiley-VCH Verlag GmbH & Co. KGaA, Weinheim, Germany, 2011, pp. 598–603. **(Proceedings No. (3))**

Chapter 5: Junya Kobayashi, Duc Van Pham, Koh-ichi Sugimoto: Stretch Flangeability and Bendability of a 0.2C-1.5Si-1.5Mn-0.05Nb Ultrahigh-Strength TRIP-Aided Martensitic Sheet Steel, Steel Research International Special Edition: Metal Forming 2012, Wiley-VCH Verlag GmbH & Co. KGaA, Weinheim, Germany, 2012, pp. 883–886. **(Proceedings No. (4))**

Chapter 6: Duc Van Pham, Junya Kobayashi and Koh-ichi Sugimoto: Effects of Microalloying on Stretch-flangeability of TRIP-aided Martensitic Sheet Steel, *Tetsu-to-Hagane*, Vol. 99, No. 11, 2013, pp. 659–668 (in Japanese). **(Papers No. (10))**

Chapter 7: Junya Kobayashi, Daiki Ina, Yuji Nakajima and Koh-ichi Sugimoto: Effects of Microalloying on the Impact Toughness of Ultrahigh-Strength TRIP-Aided Steels, Metallurgical and Materials Transactions A, Vol. 44A, No. 11, 2013, pp. 5006–5017. **(Papers No. (9))**

Chapter 8: Junya Kobayashi, Nobuo Yoshikawa and Koh-ichi Sugimoto: Notch-Fatigue Strength of Advanced TRIP-aided Martensitic Steels, ISIJ International, Vol. 53, No. 8, 2013, pp. 1479–1486. **(Papers No. (8))**

Acknowledgement

I would thank all the people who have supported me on researching and writing this thesis.

I would like to express my sincere gratitude to Prof. Koh-ichi Sugimoto of Shinshu University for providing me an opportunity to study at Sugimoto laboratory and for his excellent tutelage, supervision and encouragement during the course of this doctoral research. And I would also like to acknowledge Prof. Sachihiko Isogawa of Daido University, Prof. Susumu Arai, Assoc. Prof. Kazuhiko Sakaki and Assoc. Prof. Noboru Nakayama of Shinshu University for their useful advises which improved this thesis.

I am grateful to Japan Society for the Promotion of Science (JSPS) for providing me financial support.

I would like to express my heartfelt gratitude to Assist. Prof. Song-Moo Song of Shinshu University and Assist. Prof. Tomohiko Hojo of Iwate University for their useful advises and encouragement during the course of this doctoral research.

I am very much thankful to my seniors and juniors for some supports and carrying experimental works on this study.

Finally, I would like to thank to my family for their encouragement and support all throughout the course of this doctoral research.

Thank you very much again,

Junya Kobayashi